SEGREGATION AND REACTIVITY AT BRASS SURFACES IN METHANOL SYNTHESIS CATALYSIS

by

CHARLES EDWARD CAWTHORNE

Department of Chemical Engineering and Chemical Technology
Imperial College, London.

A Thesis submitted for the Degree of Doctor of Philosophy to the University of London and for the Diploma of Imperial College.

December, 1983.

SEGREGATION AND REACTIVITY AT BRASS SURFACES IN METHANOL SYNTHESIS CATALYSIS

Catalysts based on Cu/ZnO have been widely used in the low temperature (L.T.) shift and low pressure methanol synthesis reactions. It has been shown that brass can be formed in these catalysts and that this results in the de-activation of the L.T. shift reaction. The objective of this work was to establish the effect of brass formation on methanol synthesis.

The problem was approached in two ways. Model studies of the adsorptive properties of clean brass surfaces with differing zinc contents were carried out under UHV conditions using XPS and TPD. It was necessary to study the segregation of zinc in Cu/Zn alloys so that the surface compositions of the alloys could be established. The segregation study revealed that significant surface zinc enrichment occurred upon annealing several different bulk composition alloys. A 2% bulk Zn alloy gave up to 30% Zn in the surface whilst a maximum of 60-65% Zn was possible for a 30% bulk Zn alloy. It was also found that annealing above 250°C caused zinc evaporation from the surface, so affecting the surface concentration. The presence of zinc in a copper substrate did not significantly affect the amount of CO taken up for low surface zinc contents (below 10%) compared with a pure copper surface. However, the presence of zinc in a copper substrate did appear to create new lower energy adsorption sites.

In the second approach, $Cu/ZnO/Al_2O_3$ catalysts were prepared and pre-treated to induce brass formation, and the activity for methanol synthesis investigated. Up to 6.5% Zn in solid solution in copper could be formed, but the presence of brass had no net affect on the activity for methanol synthesis. The inter-relation of the results and their implications for methanol synthesis are discussed.

TO MY PARENTS

ACKNOWLEDGEMENTS

I must express my sincere thanks to Dr. Dave Chadwick, my supervisor at College, for his continued enthusiasm and guidance during this work. I must also thank Dr. Pat. Denny and Dr. Ken Waugh of ICI for their supervision during the industrial periods at Agricultural Division and at the Corporate Laboratory, and for their invaluable contributions outside the industrial periods.

I must also express my gratitude to the Departmental Workshop, especially Terry Stephenson and Bob King for making the components of the high and low temperature probe and for willingly repairing the regular mechanical failures on the ESCA instrument. Malcolm Dix and Dick Wood of the Electronic Workshop must be thanked for keeping the electrical side of the ESCA in working order, and the latter again for designing and constructing the temperature control unit used in the desorption experiments. My thanks are also due to Dr. Howard Stone of the Physics Department for preparing the Cu/Zn alloys. I wish to express my gratitude to ICI Agricultural Division for a substantial contribution towards the research project. I must thank the following staff at ICI Ag. Div., Billingham for their invaluable assistance during my industrial period of the summer of 1982 :

Mike Arvidson and Mickey Shann - for their instruction on catalyst preparation.

Bernie Hill - for letting me loose on her micro-reactor units.

Pat Allon, Colin Bartlett and Sue Kipling - for coping with a continuum of samples for XRD over a four week period and their assistance in the analysis of the results.

T. Singh and Mrs. C. M. Hay - for producing the surface area results.

I would like to thank Professor D. A. Dowden, Dr. M. Bowker and Dr. M. Spencer of ICI for their valuable contributions, and Dr. Karol Senkiw and Marcus Karolewski, my colleagues in the 'LAB' at College for putting up with me and providing useful discussions.

I must also express my appreciation to my parents for supporting me during the final months of this project.

Finally, I must thank Karen Slade-Pluck for her careful and patient typing of the manuscript, and my father and Len Osborne for arranging the duplication of the manuscript.

CONTENTS

	Page
ABSTRACT	ii
ACKNOWLEDGEMENTS	iv
CONTENTS	vi
CHAPTER 1 INTRODUCTION	1
CHAPTER 2 REVIEW OF THE LITERATURE	
2.1 SEGREGATION IN AND CATALYSIS BY BINARY ALLOYS	11
2.1.2. Important concepts connected with Binary alloys	11
2.1.2. Review of work done on binary alloy systems	14
2.2 THE ADSORPTION AND DESORPTION OF CO ON AND FROM COPPER SURFACES	24
2.2.1 Adsorption temperature and rate of uptake	24
2.2.2. Nature of Chemisorbed CO on Copper surfaces	27
2.2.3 Desorption of CO from Copper surfaces	42
2.3 ADSORPTION OF HYDROGEN ON COPPER	50
2.4 THE ADSORPTION OF METHANOL, FORMALDEHYDE AND FORMIC ACID ON COPPER SURFACES	53
2.5 CHEMISORPTION ON ZINC METAL SURFACES	58
2.6 REVIEW OF RELEVANT WORK ON Cu/ZnO CATALYSTS	60
CHAPTER 3 THE PRINCIPLES OF PHOTO-ELECTRON SPECTROSCOPY AND TEMPERATURE PROGRAMMED DESORPTION	
3.1 PHOTO-ELECTRON SPECTROSCOPY	65
3.1.1 The principle and types of photo-electron spectroscopy	65
3.1.2 Photo-electron spectometer	67
3.1.3 Inelastic mean free path	68
3.1.4 The use of XPS for quantitative analysis	73
3.1.5 The chemical shift	75

3.1.6 Relaxation 76

3.1.7 Shake-up 76

3.1.8 The use of UPS 76

3.2 TEMPERATURE PROGRAMMED DESORPTION 77

3.2.1 Theory and analyses 79

3.2.2 Some more recent methods of analysis 82

3.2.3 Initial interpretation of desorption spectra 87

CHAPTER 4 EXPERIMENTAL

4.1 DESCRIPTION OF THE UHV SYSTEM 89

4.2 THE HIGH AND LOW TEMPERATURE PROBE 94

4.2.1 Design and construction 94

4.2.2 Use of the probe 104

4.2.3. Performance 104

4.3 ARRANGEMENT USED TO CARRY OUT TPD EXPERIMENTS 106

4.4 EXPERIMENTAL PROCEDURES 110

4.4.1 Sample mounting and preparation 110

4.4.2 Gas dosing 112

CHAPTER 5 SEGREGATION IN COPPER/ZINC ALLOYS

5.1 SAMPLE PREPARATION 113

5.2 RESULTS 115

5.2.1 Effect of sputtering on the surface composition 116

5.2.2 Effect of annealing temperature on the surface composition 117

5.2.3 Effect of lead impurities on the segregation in Cu/Zn alloys 123

5.3 DEVELOPMENT OF A BASIC EQUATION TO RELATE THE MEASURED PEAK AREA RATIOS TO THE COMPOSITION OF THE UPPERMOST ATOMIC LAYERS IN A BINARY ALLOY 127

5.4 DETERMINATION OF THE SURFACE COMPOSITION BY THE ASSUMPTION OF POSSIBLE COMPOSITION PROFILES 139

5.4.1 Average surface composition 140

5.4.2 Top layer model 144

5.4.3 Linear concentration profile model 146

5.4.4 Exponential concentration profile model 150

5.4.5 Discussion of the top layer, linear and exponential profile models 151

5.4.6 Linear concentration profile with depletion layers 154

5.4.7 Exponential concentration profile with depletion layers 157

5.4.8 Discussion of the depletion models 158

CHAPTER 6 CO CHEMISORPTION ON POLYCRYSTALLINE COPPER, ZINC AND BRASS SURFACES

6.1 CHEMISORPTION OF CO ON POLYCRYSTALLINE COPPER 165

6.1.1 Uptake of CO 165

6.1.2 Photo-electron spectra of chemisorbed CO 166

6.1.3 Desorption of CO from polycrystalline copper surfaces 171

6.2 CHEMISORPTION OF CO ON ZINC 180

6.3 CHEMISORPTION OF CO ON A 30% BULK ZN BRASS 180

6.4 CHEMISORPTION OF CO ON A 5% BULK ZN BRASS 181

6.4.1 Uptake of CO 181

6.4.2 Photo-electron spectra of adsorbed CO 181

6.4.3 Desorption of CO from a 5% Bulk Zn brass 187

6.5 CHEMISORPTION OF CO ON A 10% BULK ZN BRASS 190

6.6 " " " " 2% " " " 190

6.7 EFFECT OF SURFACE ZINC ON THE AMOUNT OF CO ADSORBED 191

6.8 EVIDENCE FOR DISSOCIATION OF CO ON BRASS SURFACES 194

6.8.1 Quantification of the dissociation 204

6.8.2 Discussion 216

CHAPTER 7 THE ADSORPTION OF HYDROGEN, CARBON DIOXIDE AND METHANOL

7.1 HYDROGEN ADSORPTION 218

7.2 CARBON DIOXIDE ADSORPTION 218

7.3 METHANOL ADSORPTION 219

7.3.1 Methanol adsorption on polycrystalline copper 219

7.3.2 Methanol adsorption on a brass surface 220

CHAPTER 8 BRASS FORMATION IN Cu-ZnO-Al_2O_3 CATALYSTS AND ITS EFFECT ON METHANOL SYNTHESIS

8.1 PREPARATION AND CHARACTERISATION OF THE BRASSY CATALYSTS 224

8.1.1 Preparation and conditioning 224

8.1.2 Surface areas 234

8.1.3 Discussion 235

8.2 ACTIVITIES OF THE BRASSY CATALYSTS 245

8.3 RELATIONSHIP BETWEEN CATALYST ACTIVITY, SURFACE AREA AND BRASS FORMATION 257

8.3.1 Activity against total area 259

8.3.2 Activity against metal area 259

8.3.3 Activity against oxide area 263

8.3.4 Effect of brass formation on the activity 265

8.3.5 Dependence of the activity on a function involving both the metal and oxide areas 269

8.4 FINAL DISCUSSION AND SUMMARY 275

CHAPTER 9 DISCUSSION OF RESULTS

9.1 SEGREGATION IN BRASSES AND ITS IMPLICATION ON THE CATALYST COMPOSITION 277

9.2 DEPENDENCE OF THE ACTIVITY ON METAL AREA 279

9.3 EFFECT OF BRASS FORMATION AND CONDITIONING OF THE ACTIVITY 282

9.3.1 Metallic phase 282

9.3.2 Cu (I) in ZnO 283

9.4 MECHANISTIC IMPLICATIONS FROM THE BRASSY CATALYSTS FOR METHANOL SYNTHESIS AND THE L.T. SHIFT 284

9.4.1 Other mechanistic implications 289

9.5 DISSOCIATION OF CO BY BRASS SURFACES AND ITS IMPLICATIONS IN METHANOL SYNTHESIS 290

9.6 FINAL SUMMARY AND CONCLUSIONS 291

9.6.1 Segregation in brasses 291

9.6.2 Adsorption of CO on polycrystalline Cu, Zn, and Cu/Zn surfaces 292

9.6.3 Conditioning of $Cu/ZnO/Al_2O_3$ catalysts to form brass 294

ADDENDUM 297

REFERENCES 298

APPENDICES 305

Appendix I 306

Appendix II 308

Appendix III 326

CHAPTER 1

INTRODUCTION

Methanol, chemical formula CH_3OH, is a basic industrial chemical which is produced at an annual rate of 10 million tonnes[1]. As well as being used as a solvent in many industrial processes[2], it is also a starting point for the production of many other materials. A further potential application of the alcohol is its use in the direct generation of energy, and the possibility that it could be used as an engine fuel[1]. Although the use of methanol in these latter two fields is not completely new, it has not yet been fully developed on the large scale. However, it could become much more important in the future as the world's existing oil supplies become exhausted, thus necessitating a new source of fuel. It has also been shown that aromatic compounds can be formed from methanol using zeolite catalysts[3], therefore the alcohol has an important part to play both now and in the future. At present, much of the methanol produced is converted into formaldehyde which is also a starting point for the production of other materials[4]. A breakdown of the current uses of methanol has been presented[1] and is shown in Table 1.1.

TABLE 1.1

BREAKDOWN OF THE PRESENT DAY USES OF METHANOL

Formaldehyde	50%
Dimethyl terephthalate	9%
Methyl amines and methyl halides	8%
Methyl methacrylate	7%
Solvents	7%
Others (including acetic acid)	19%

Methanol was originally produced by the destructive distillation of wood, and this was the principal source of the alcohol until the early 1920s when BASF (Badische Anilin und Soda Fabrik)

developed a process which synthesised methanol from carbon monoxide and hydrogen. This is now the adopted route for the production of methanol and has almost totally replaced the wood distillation process.

The reaction between carbon monoxide and hydrogen is not simple however, and the interaction of these two gases can produce several products[5,6] and some possible reaction pathways are shown below:

$$(n + 1)H_2 + 2nCO \rightleftharpoons C_nH_{2n+2} + nCO_2 \qquad (1.1)$$

$$(2n + 1)H_2 + nCO \rightleftharpoons C_nH_{2n+2} + nH_2O \qquad (1.2)$$

$$2nH_2 + nCO \rightleftharpoons C_nH_{2n+2}O + (n-1)H_2O \qquad (1.3)$$

$$2(n - 1)H_2 + nCO \rightleftharpoons C_nH_{2n}O_2 + (n-1)H_2O \qquad (1.4)$$

Reactions (1.1) and (1.2) are associated with the formation of alkanes (with n = 1 these reactions correspond to methanation), whilst reactions (1.3) and (1.4) are associated with the formation of alcohols and ethers and of aldehydes and ketones respectively. With n = 1, reaction (1.3) corresponds to the formation of methanol, as given below :

$$2H_2 + CO \rightleftharpoons CH_3OH \qquad (1.5)$$

Although the reaction between CO and H_2 looks complicated, a particular reaction product can be achieved by using a catalyst which is selective towards that reaction. The reaction of CO and H_2 is therefore a good example of where not only catalyst activity, but also catalyst selectivity is important. Catalysts

based on cobalt, iron and nickel, for example, are associated with the methanation type reaction[5,6]. Methanol synthesis has been achieved by the use of zinc based and more recently copper and zinc based catalysts with a good selectivity and these will be described in more detail.

Before considering the catalysts used in the synthesis of methanol, it is important to consider the thermodynamics of reaction (1.5). Figure 1.1 shows a plot of the standard free energy of formation of methanol from carbon monoxide and hydrogen against temperature, based on thermodynamic data presented by Stull, Westrum and Sinke [7]. As can been seen from Figure 1.1, the methanol synthesis reaction is thermodynamically most favourable at temperatures which are as low as possible. In addition, increasing pressure will shift the equilibrium in reaction (1.5) to the right.

The first catalytic synthesis of methanol from CO and H_2 developed by BASF in the 1920s used a catalyst based on zinc oxide and chromia, the latter component being present to act as a promoter. This catalyst was found to be highly active, but a significant activity could only be achieved by using reaction temperatures which were in the region of 570-720K. At these temperatures, the free energy of methanol formation from CO and H_2 (syn-gas) is positive from the data in Figure 1.1, and consequently only a low equilibrium yield of methanol would be possible. As a result, fairly high reaction pressures between 100 and 500 atmospheres were found to be necessary to give a reasonable equilibrium yield at temperatures of 570-720K[8].

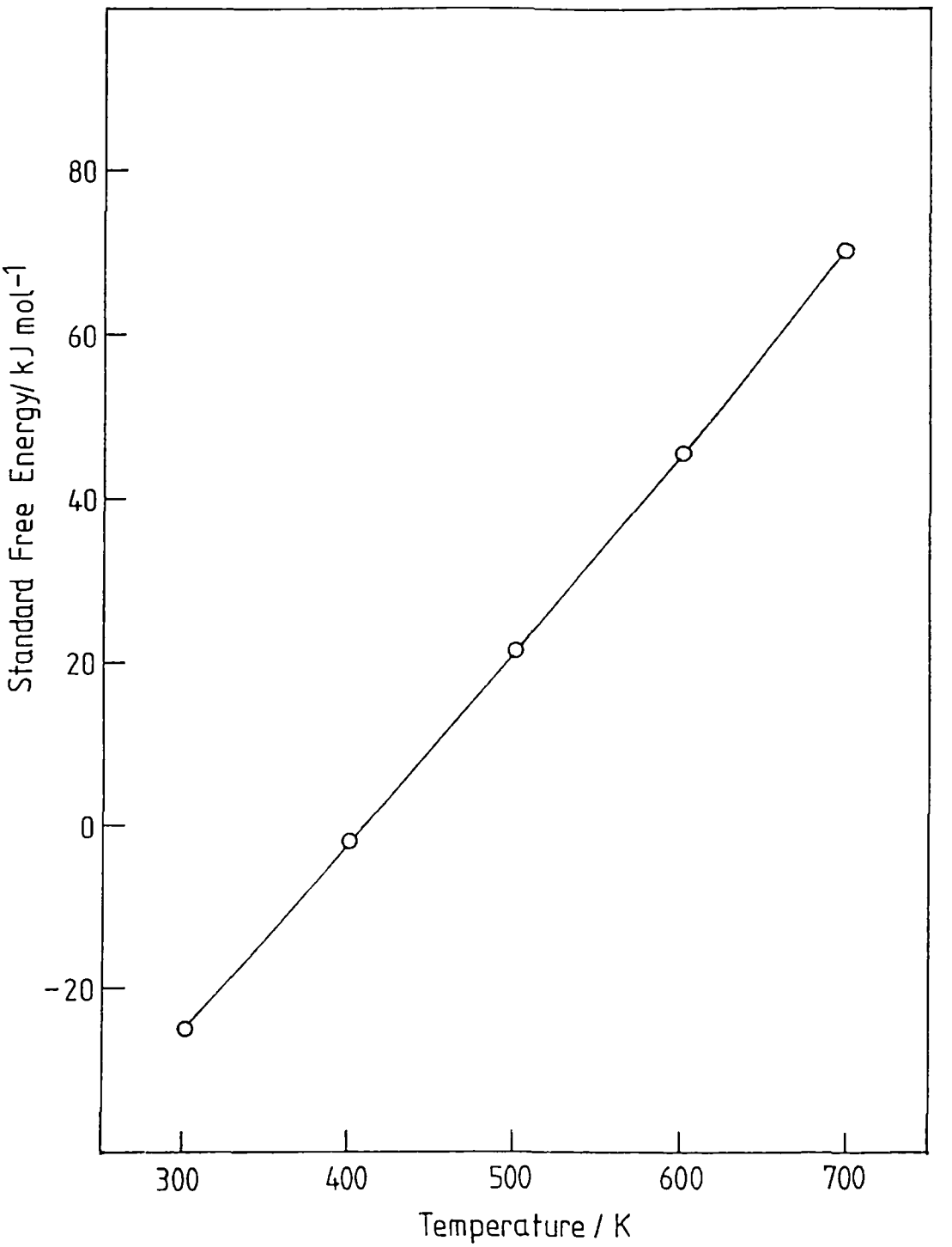


Figure 1.1. Standard free energies of formation of methanol from CO and H_2

In his review on methanol synthesis, Natta[8] mentioned that catalysts based on copper, zinc and chromia could give an even better activity than the zinc oxide-chromia types. However, the copper based catalysts had little resistance to ageing and were very susceptible to poisoning by sulphur for example. The poisoning occurred because the reaction gases used earlier in the twentieth century were much more impure than those used in the present day.

In the 1960s, a new catalyst was developed by ICI which was based on a copper-zinc oxide-alumina ternary mixture. Chromia can be used instead of alumina. This catalyst gave an improved activity compared with that of the zinc oxide-chromia types[5]. The important aspect of this ternary mixture catalyst was that its activity was still good at a lower temperature compared with that of the zinc oxide-chromia types which meant that the reaction temperature could be dropped, giving a higher equilibrium methanol yield (see Figure 1.1). In addition, the synthesis could be carried out at a lower pressure because of the improved equilibrium yield. The synthesis of methanol using the copper zinc oxide-alumina catalysts has become known as the low pressure process and typical reaction conditions used for this process are temperatures between 493K and 573K and a pressure of between 50 and 100 atmospheres. Besides having a good activity, the copper-zinc oxide-alumina catalyst is also very selective towards methanol formation from syn-gas. A selectivity of better than 99% can be achieved by this catalyst at the reaction conditions employed for the low pressure process, and this too is an improvement on the previous zinc oxide-chromia catalysts[3]. Consequently, the low pressure process is the current method used to produce methanol from syn-gas using a copper-zinc oxide-alumina

ternary mixture as the catalyst.

Although a good catalyst has been developed for methanol synthesis, the actual reaction mechanism on the copper-zinc oxide-alumina system system is not fully understood at all. Two possible mechanisms have been proposed and are presented by Kung[2] in his review of methanol synthesis, and are shown in Figure 1.2. The first mechanism, A, involves the formation of a formyl intermediate during successive hydrogenation of adsorbed carbon monoxide. The second mechanism, B, proceeds via formate and methoxy type intermediates following the insertion of carbon monoxide into a surface hydroxyl to form the formate and then subsequent hydrogenation and dehydration to form the methoxy species and the product. The principal difference between the two mechanisms is that the first mechanism (A) involves the bonding of a carbon atom to the catalyst surface, whilst the second mechanism (B) involves the bonding of an oxygen atom to the catalyst surface. Although these two mechanisms have been proposed, there is no clear cut evidence yet to support either one or the other and it is possible that some other mechanism may exist.

Another important aspect of methanol synthesis using Cu-ZnO-Al_2O_3 type catalysts that has not been resolved to date is concerned with the catalyst itself. It has been suggested that some of the zinc oxide component in the catalyst is reduced in an atmosphere containing hydrogen and the dissolution of the resulting zinc in the copper phase results in the formation an an α-phase brass in the catalyst. Experiments have been carried out which show that some brass can be formed during the final preparation stage of the catalyst[9], and these experiments are discussed in more detail

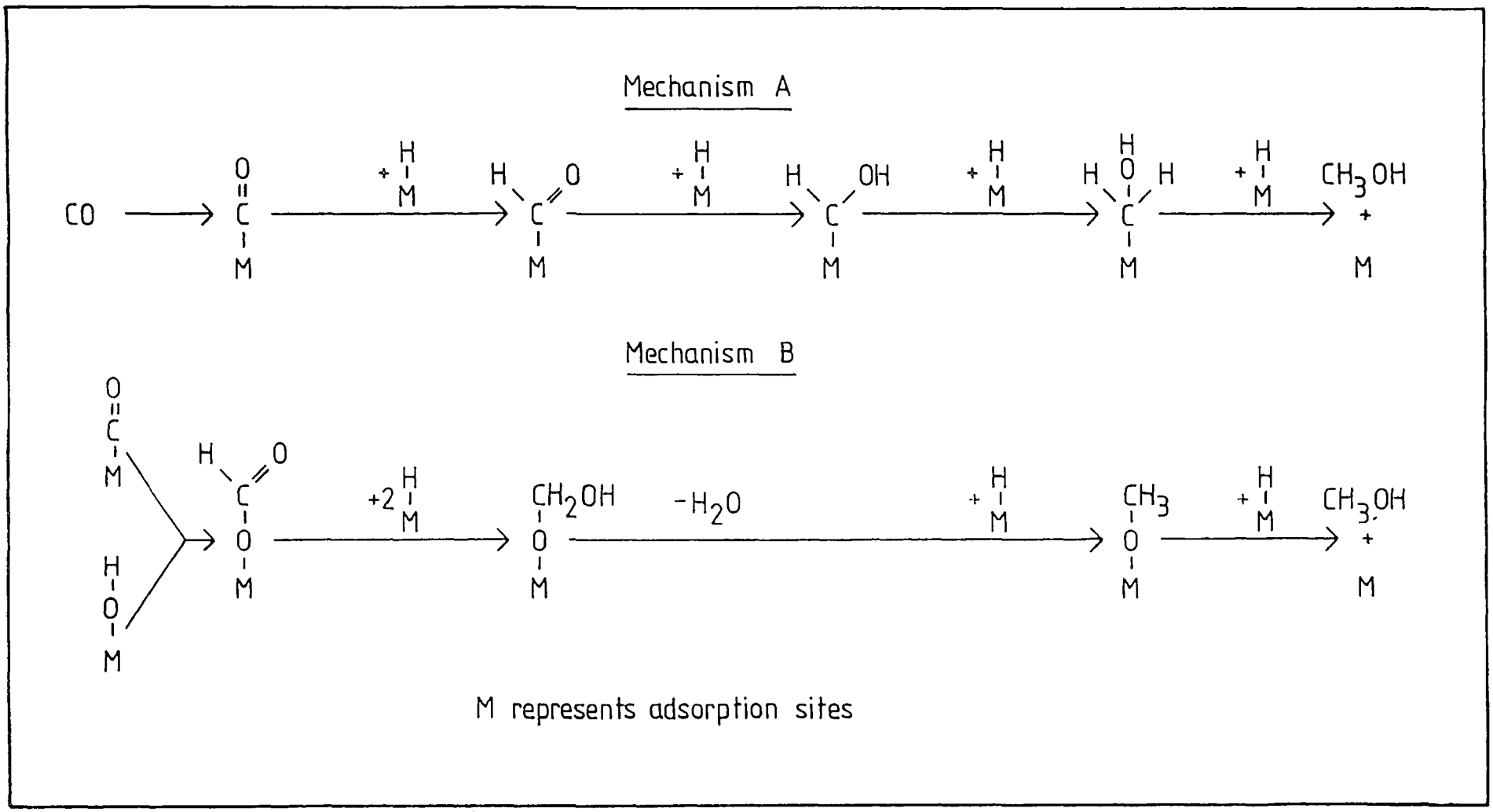


Figure 1.2. Two possible reaction mechanisms as presented by Kung[2]

in Chapter 2, section 2.6. At present, it is not clear whether the presence of a low zinc content brass (<5% Zn) in the $Cu-ZnO-Al_2O_3$ system would play any part in the methanol synthesis reaction. It is possible that the presence of brass in the catalyst may simply deactivate the catalyst through a loss of active surface area. On the other hand, it may be that a form of Cu-Zn site in the catalyst could be an important part of the methanol synthesis mechanism.

The basic aim of this work is to study the reactivity of brass surfaces and to elucidate their role, if any, in the methanol synthesis reaction.

The majority of the studies in this work were made on clean brass surfaces in an ultra-high vacuum (UHV) environment. Although the conditions of the UHV environment (a pressure below 10^{-9} torr) do not resemble those of the real catalyst, the use of the UHV methods are important in the study of heterogeneous catalysis. In general, the rate of reaction of a species is dependent on the concentration of the species on the surface and also on the temperature. Under UHV conditions, surface coverages up to a complete monolayer can be formed, so that the dependence of reaction rate on the species concentration on the surface is still preserved even at pressures of 10^{-10} torr. So, providing the surface being studied simulates that of a real catalyst under the reaction operating conditions as far as surface concentration and composition are concerned, chemisorption studies made in UHV conditions should be representative of the real conditions[10]. However, in order to obtain coverages of up to one monolayer on the surface of samples studied under UHV conditions, temperatures which are much lower than those of the real reaction conditions must be used

for the UHV studies (e.g. the adsorption of carbon monoxide on copper is studied at 80K - see Chapter 2). The study of adsorbed species on surfaces in UHV conditions at lower temperatures has an added advantage. By lowering the temperature, the surface lifetime of adsorbed species can be extended to such an extent that any intermediate species may be identified. This is not possible on catalysts operating at normal reaction conditions because intermediates may have a surface lifetime of microseconds or shorter. Hence the use of UHV studies can be used to aid the understanding of the principles involved in heterogeneous catalysis.

In order to carry out the experiments required to study the reactivity of brass surfaces, it was necessary to construct a special probe which could allow a sample to be warmed or cooled between 100K and 700K. The reasons for this are discussed in Chapter 4. In addition, a system for obtaining temperature programmed desorption (TPD) spectra had to be set up - this too is discussed in Chapter 4.

In order to understand the reactivity of brass surfaces, it was necessary to obtain the surface composition of the brass, so that the reactivity could be studied as a function of the surface zinc content. However, alloys often have the property that one component segregates to the surface upon annealing, so a study was made to determine the dependence of the surface composition on annealing temperature. This was done for several bulk composition brasses.

The reactivity studies were made by using the techniques of X-ray photo-electron spectroscopy and temperature programmed

desorption. The two techniques were used to study the adsorption of carbon monoxide and some initial work on the adsorption of hydrogen and methanol.

The reactivity studies were complemented by studying the effect of brass formation in $Cu-ZnO-Al_2O_3$ catalysts on the activity for methanol synthesis. By consideration of both of these pieces of work, the effect of brass formation in the methanol synthesis catalyst can be quantified and it may be possible to draw some conclusions about the reaction mechanism.

CHAPTER 2

REVIEW OF THE LITERATURE

2.1 Segregation in and Catalysis by Binary Alloys

2.1.1 Important concepts connected with Binary Alloys

Until the mid 1960s, any catalysis and chemisorption work on alloys was, in general, based on the assumption that the surface composition of the alloy was similar to that of the bulk. However, studies made by Sachtler and his co-workers[11,12] in the mid 1960s argued that the surface composition could be very different from that of the bulk, and they put forward two main points. Their first point was that many homogeneous alloys which were prepared at high temperatures became thermodynamically unstable at much lower temperatures. This instability led to a rearrangement of the surface atoms which could separate into two phases, one rich in component A and one rich in component B for an alloy A_xB_{1-x} where x is the bulk composition. Secondly, if a thermodynamic equilibrium were eventually established throughout the alloy, the surface would assume a composition which had a minimum surface energy. They performed some experiments on the Cu-Ni system which confirmed these views[11]. As a result, it can immediately be seen that the surface composition of a binary alloy is not necessarily the same as that of the bulk.

For the Cu-Ni system below 322°C, a miscibility gap exists[13] and under certain conditions it is possible to get two phases in the surface layer, one enriched in copper and one enriched in nickel. This is the first condition mentioned earlier. The Cu-Zn system however, has no miscibility gap in the bulk

composition range of interest (i.e. between 0 -30% zinc) above 150°C, so the formation of more than one phase in the surface layer will not occur. Over the composition range of interest, the Cu-Zn alloy is monophasic (α -phase) with a face centred cubic structure and is formed by substitutional solid solution of the zinc atoms in the copper lattice. The heats of sublimation for copper and zinc and are 339kJ/mol and 130kJ/mol respectively[15], and consequently it would be expected that there would be segregation of zinc to the surface, so that the surface energy was minimised[16] because zinc has the lower heat of sublimation.

Surface enrichment of an alloy can also be caused by two other phenomena[13,16]. Argon ion sputtering, a destructive cleaning technique which is used in HV/UHV conditions, can preferentially remove one component from an alloy, this component being the one with the lower heat of sublimation. This leads to surface enrichment of the higher sublimation heat component. This effect has been seen in several systems, and a few examples are quoted in the next section. Chemisorption induced surface enrichment can also occur if there is a gas in contact with the alloy surface. If the heat of adsorption of the gas on each alloy component is significantly different, then surface enrichment of the component with the higher heat of adsorption occurs.

The surface composition of alloys can now be determined by several methods, as listed below :

(i) Work function measurements

(ii) Selective chemisorption

(iii) Auger-electron spectroscopy

(iv) Photo-electron spectroscopy

These methods are of a less surface sensitive nature going down the list and so become less suitable for determining the surface composition, but on the other hand, the methods are easier to interpret going down the list[16]. Methods (iii) and (iv) are most commonly used to estimate surface compositions of alloys, and possible analyses of the spectra obtained using these two methods to find the surface composition are described in the next section.

Adsorption on a pure metal surface may not necessarily involve the bonding of the adsorbate to one substrate atom. It is possible that the active site will involve two or more atoms. This group of atoms which form the active site is usually known as an ensemble. Alloying of the pure metal, A, with a second component, B, will create two effects. Firstly, the number of ensembles of pure A will decrease, and secondly, the introduction of component B will create new ensembles, involving mixtures of atoms from A and B. This latter effect can lead to the creation of new active sites. In addition to these, of course, ensembles of pure B will also be formed. This is the case for a Cu-Ni alloy and this was shown experimentally by Yu et al[18] from a thermal desorption study of CO from this alloy. The authors have shown that there were four adsorption states resulting from four different active sites. Two states were associated with ensembles of pure Cu and pure Ni, but the other two states were

associated with two new active sites, present because of the alloying. These new sites were made from ensembles of a mixture of copper and nickel, the two sites having different compositions of the two components. In the case of the Cu-Zn system, it would be expected that the zinc would act as a diluent of active sites in the surface of the alloy owing to its inactivity, rather than forming a set of different active sites.

2.1.2 Review of Work done on Binary Alloy Systems

Until mid 1983, no work has been reported on segregation in the Cu-Zn system. Although the surface will probably become zinc enriched through segregation, accurate surface compositions remain to be established. In order to understand chemisorption on brass surfaces, it is necessary to know the composition of the surface layer of the alloy. It is proposed to review some of the methods used by previous workers to calculate alloy surface compositions and concentration profiles.

Quinto et al[19] made a partial study of the Cu-Ni system by Auger Electron Spectroscopy (AES). They found that copper was preferentially sputtered from the surface so leading to nickel enrichment. This result is to be expected. They also found that the normalised derivative amplitudes of the Auger Spectra at ∿900eV. were proportional to the average alloy concentration (i.e. the concentration averaged over the first few atomic layers). This is a result which was also found by Mathieu and Landolt[20] for both Ag-Pd and Ni-Pd alloys. Quinto et al found that no significant excess concentration of either component appeared in the surface

layer, and consequently no analysis was made to determine surface compositions.

In contrast to the findings of Quinto et al, evidence was presented by Helms[21] and Helms and Yu[22] that there was a difference between the relative Auger transitions of copper and nickel at approximately 100eV and those at approximately 900eV. This difference showed that Cu segregation to the surface on annealing did occur. The authors studied samples with different bulk compositions ranging from 10% Cu to 50% Cu, and all of these gave the same result (i.e. copper enrichment). The authors calculated the surface composition of the alloy after annealing by simply taking the ratio of the low energy copper and nickel Auger transitions so that :

$$X_{Cu} = \frac{y}{1 + y}$$

where X_{Cu} is the mole fraction of copper in the surface layer and $y = I_{Cu}/I_{Ni}$

where I_{Ni}, I_{Cu} are the measured Auger peak intensities. The authors calculated that for the 10% bulk Cu alloy, up to 65% Cu was present in the surface after annealing, whilst almost 100% surface Cu could exist in the case of the 50% bulk Cu alloy. The authors found, in agreement with Quinto et al however, that copper was preferentially sputtered, giving nickel enrichment in the surface after ion bombardment.

Bouwman et al[23] studied the surface composition of Pt/Sn alloys again by AES. They found that the surface became enriched with Sn and that the surface composition was a function of annealing

temperature, the surface tin content increasing with temperature over the range studied. The surface composition was determined by directly using the peak height ratios of tin to platin um :

$$X_{Sn} = \frac{ay}{1 + ay}$$

where X_{Sn} is the mole fraction of tin in the surface layer and

$$y = \frac{\text{Height of Sn Peak}}{\text{Height of Pt Peak}}$$

The term a is the observed elemental yield ratio Pt/Sn of the same Pt and Sn peaks for equiatomic amounts of Pt and Sn. This term is used to correct for the slightly different sensitivity of the Auger peaks obtained from tin and platin um. This method of analysis along with that of Helms and Yu[22] relies on the peaks being surface sensitive, i.e. the peaks must be based on the contributions from atoms in the topmost layer only. This is a reasonable method of determining surface compositions if the energy of the emitted electrons is low (approximately 100eV). At this electron energy, the electron escape depth is small (see Chapter 3), so that the second and subsequent layers will not contribute much to the signal. However, at higher electron energies, the escape depth is greater and the resulting peaks become more sensitive to the composition of layers below the surface.

Maire et al[24] also used the low energy Auger electron peaks to study chemisorption induced segregation. Their method of obtaining the surface composition of the alloy following adsorption (in this case of oxygen) was the same as that described previously for the Pt/Sn system. The results obtained were as

expected. The component which formed the stronger bond with the adsorbate was enriched in the surface, this component being Pd. The authors pointed out that their method for calculating the surface compositions strictly resulted in the mean composition of the first uppermost layers being determined rather than the composition of the surface layer itself. They came to the conclusion that it would be necessary to use information from both the high and low energy Auger transitions to calculate a more accurate value for the surface composition. In this particular piece of work, it was not possible to obtain the high energy transition, so the authors did not attempt to make the more accurate calculation which they suggested as being necessary.

The difference in the calculated surface composition resulting from either the high energy or low energy Auger transitions only, is further illustrated by Stoddart et al[25] in their work on Pd-Ni alloys. They too found that using the high energy transitions, the surface composition was similar to that of the bulk throughout the bulk composition range 0 - 100% Ni. However, the low energy transitions showed that surface enrichment of Pd resulted. The calculation method was assumed to be similar to that used by Bouwman et al[23] as described previously because Stoddart et al did not describe a method in their paper. The authors then presented a method for determining the bulk composition for forming a monolayer of Pd (the component which segregated to the surface) at the surface. This was done by using a relation developed by Seah[26] for studying overlayers on a substrate of a different material by AES. This expression is given below :

$$\frac{I_L}{I_H} = \frac{\exp\ (-m/N_L)}{\exp\ (-m/N_H)} \qquad (2.1)$$

where m is the overlayer thickness and N_L and N_H are the attenuation layer thicknesses (electron escape depths) of the substrate low energy and high energy electrons. I_L and I_H are the measured Auger intensities of the low and high energy transitions of the substrate material (or in the case of the alloy analysis, the nickel transitions). The authors found that for a bulk composition of 65% Pd or greater, a monolayer of Pd was formed at the surface. However, an accurate attempt to determine the surface composition was not presented.

Somorjai and Overbury[27] presented their own expression which related the ratio of the high and low energy Auger transitions for one component of the alloy and for the same component as pure to a composition profile for the alloy. Their expression is given below :

$$\frac{R_{E,E'}}{R^{o}_{E,E'}} = \frac{\lambda_{E'}\int_{o}^{\infty} X(z)\exp(-z/\lambda_E)\ dz}{\lambda_E\int_{o}^{\infty} X(z)\exp(-z/\lambda_{E'})dz} \qquad (2.2)$$

where $R_{E,E'}$ is the ratio of high and low energy transitions for one of the components of the alloy

$R^{o}_{E,E'}$ is the ratio of high and low energy transitions for the same component as pure

$\lambda_E, \lambda_{E'}$ are the escape depths of electrons having kinetic energies of E and E' respectively.

X(z) is the composition at a depth, z.

This method was based on summing the contributions from each atomic layer at an increasing depth below the surface so as to obtain the total Auger intensity. The authors presented an expression which related the total Auger signal intensity, I_E, to the signal contribution from each layer, and this is shown below:

$$I_E = \int_0^\infty K(E, ...) \exp(-z/\lambda_E) \qquad (2.3)$$

where K(E, ...) is a complicated function involving properties of the solid, the electron scattering within it and other experimental parameters.

Expression (2.2) was derived so as to eliminate the term K(E,...) and this is shown in the paper. Some assumptions were also made. These were that there were no matrix effects on the Auger signals (i.e. the presence of neighbouring atoms did not affect the signal), and that the sampling depth of the incident electron beam was much greater than the longest electron escape depth. The former assumption means that the signal at a particular depth can be made to be directly proportional to the number of atoms in that layer. The latter assumption means that there is a uniform excitation with depth as far as the measured Auger signal is concerned. This is a good approximation, as electron beams are usually at an energy level of 2000eV or greater. The authors did not use expression

(2.2) to obtain surface compositions in their paper, and probably made the derivation to show that changes in the two Auger peak ratios from the same component would indicate surface enrichment.

In their study of Pt/Sn alloys by AES and XPS, Bouwman and Biloen[28] presented a method for obtaining a more accurate determination of the surface composition. This method was similar to that of Somorjai and Overbury in that it used an expression to relate the total Auger/XPS signal intensities to contributions from successive layers at and below the surface. Bouwman and Biloen derived an expression relating the average surface composition to the composition of successive layers at and below the surface. This is shown below :

$$\bar{X}_A = \frac{I_{E_A}}{I'_{E_A}} = \frac{I_o(E_A) \int_o^{\infty} \exp(-z/\lambda_{E_A})\, X_A(z)dz}{I_o(E_A)\, \lambda_{E_A}} \qquad (2.4)$$

where $\bar{X}_A$ is the average surface composition

I_{E_A} is the measured signal intensity of component A in the alloy

I'_{E_A} is the measured signal intensity of the same peak from an alloy of known composition

λ_{E_A} is the escape depth for electrons with kinetic energy, E_A

$X_A(z)$ is a composition profile

$I_o(E_A)$ is an element-characteristic constant

The basis behind the method was to create a composition profile, in a parametric form which best fitted the experimental data. The experimental data was obtained in the form of average surface compositions from the Auger/XPS peak intensities as illustrated in equation (2.4). The authors obtained two average surface compositions by using the peak intensities of the low energy Auger transitions and of the high energy XPS peaks. The difference in kinetic energy of these peaks resulted in the two average surface compositions being different, because of the difference in electron escape depth (see Chapter 3, section 3.1.3). The I'_{E_A} term was found by fracturing the alloy sample in vacuo and analysing the exposed face. The face would be a better representation of the bulk alloy composition because it was clean, so eliminating the segregation effects through ion bombardment and annealing. The procedure used by Bouwman and Biloen is described below :

(1) $X_A(z)$ had to be formulated in a parametric form,
$X_A = X_A(z, P_1 \ldots P_n)$

(2) Integration of this parametric expression according to equation (2.4). For each measured value of I_{E_A}/I'_{E_A}, an equation for the parameters P_1, P_2 ...P_n was obtained.

(3) The equations obtained in (2) were solved to give the values of the parameters P_1 .. P_n. From the profile, the surface concentration could be found.

The authors presented two profiles, an exponential and a block type profile to which they tried to fit their data. These profiles

are illustrated in Figure 2.1. The authors found that a block type profile with depletion of a few atomic layers below the surface gave the best fit to their experimental data. The subject of composition profiles will be discussed more fully in Chapter 5 when applied to the Cu-Zn results.

Webber et al[29] studied the Cu-Ni alloy system by AES and XPS. They used a similar expression to define the average surface composition as Bouwman and Biloen (equation (2.4)), but tried to fit a profile to a series of layers of constant composition, as they obtained many more data points. The authors in this case obtained the measured average surface composition of Cu as given below :

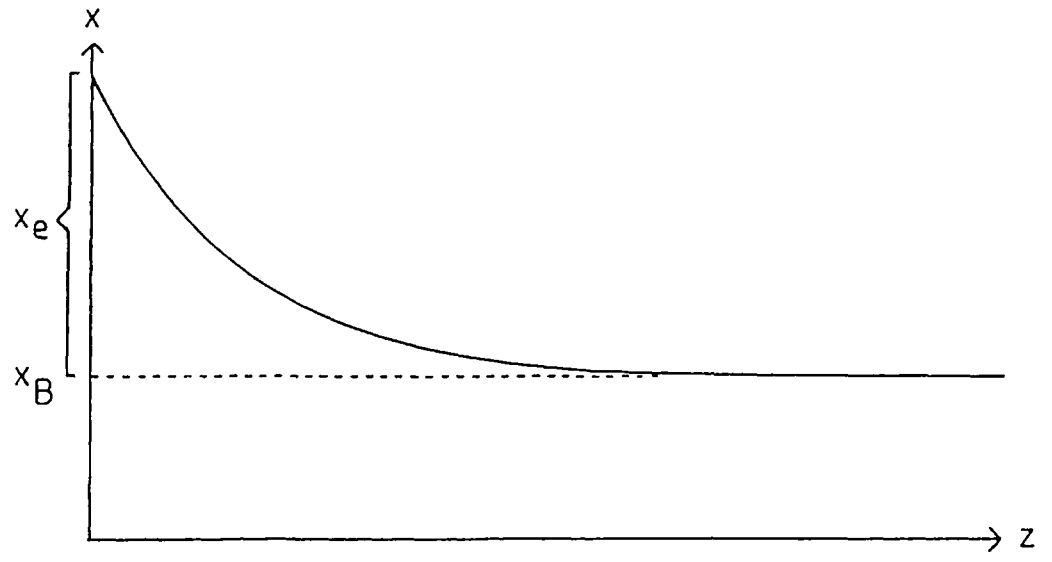
$$\bar{X}_{Cu} = I_{Cu}/(I_{Cu} + kI_{Ni}) \qquad (2.5)$$

where $\bar{X}_{Cu}$ is the average surface composition of Cu.

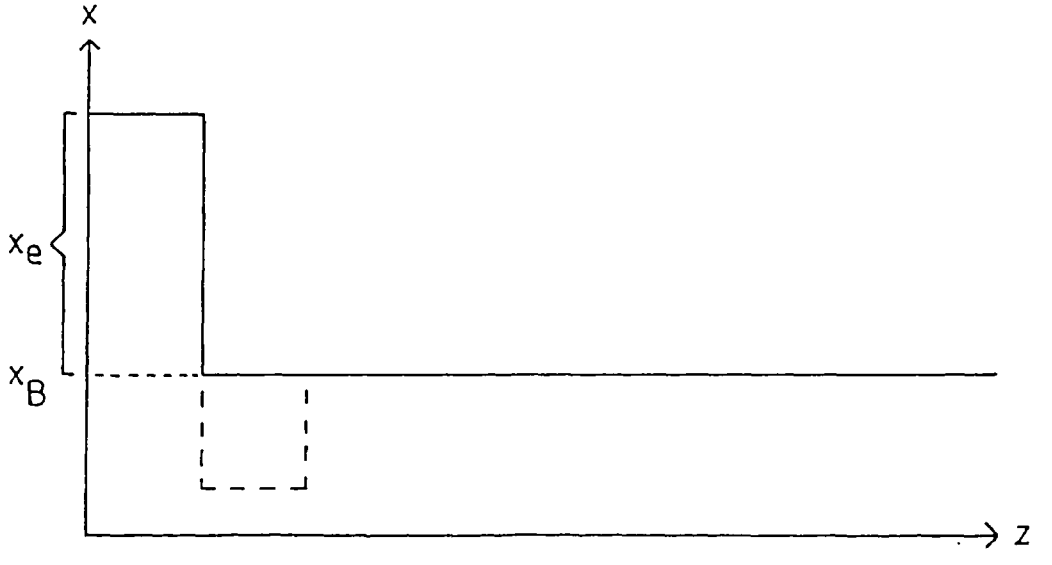
I_{Ni}, I_{Cu} are the measured signal intensities of nickel and copper respectively from the alloy.

k is a relative elemental sensitivity factor.

The factor k, was obtained by measuring the intensities of the copper and nickel peaks from pure copper and nickel under the same experimental conditions. Each average surface composition was determined by using Cu and Ni peak pairs at similar kinetic energies, whilst a series of average surface compositions were found by measuring the Cu/Ni peak pairs at different kinetic energies. The authors found that there was heavy copper segregation to the surface in a 5% and in a 50% bulk Cu alloy,



(a). Exponential type profile



(b). Block type profile (dashed section represents the case where depletion occurs below the surface)

z is the depth
x is the mole fraction of segregant
x_B is the bulk composition
x_e is the surface excess of segregant

Figure 2.1. Possible composition depth profiles suggested by Bouwman and Biloen [28] to model segregation in their Pt/Sn alloy system

giving a surface composition of almost 100% Cu in both cases. However, below the surface, a depletion layer was also formed before the profile returned to bulk in the case of the 5% bulk Cu alloy.

2.2 The Adsorption and Desorption of CO on and from copper surfaces

The adsorption of CO on copper surfaces has been studied by many workers in recent years. Much of the earlier work was carried out using surface potential measurements, infra-red spectroscopy (i.r.s.) and low energy electron diffraction (LEED) on poly-crystalline and the low index (i.e. (100), (110), (111)) single crystal copper surfaces. Work function variations as a function of coverage have also been used to study CO adsorption. More recently, electron spectroscopic techniques in the form of X-ray photoelectron spectroscopy (XPS), Ultra-violet photoelectron spectroscopy (UPS) and Auger-electron spectroscopy (AES) have become more readily available, and these techniques, especially XPS and UPS, have been employed in addition to study CO adsorption. The reverse process, desorption, can also provide important information on the nature of adsorbed species and has also been used in the past to complement adsorption studies. It is proposed to review the principal work carried out on the adsorption and desorption of CO on copper surfaces and to present the results and various interpretations which have been given in the literature to date.

2.2.1 Adsorption Temperature and Rate of Uptake

The vast majority of the studies carried out on CO adsorption

have been done with the copper surface at a temperature between 77K (liquid nitrogen temperature) and approximately 150K. At this temperature, CO is adsorbed rapidly with a high sticking probability. This is illustrated by several workers. Tracy[31] found that work function changes for a Cu (100) surface on adsorbing CO at 77K indicated a rapid initial uptake. He quoted that a CO dose of 1.7L(1L = 1 langmuir = 10^{-6} torr-sec) was required to form almost a complete overlayer. Isa et al[32] reported an uptake with a sticking probability of almost unity at 80K. They quoted the O1s to $Cu2p_{3/2}$ X-ray photo-electron spectra intensity ratios for two CO doses on a Cu(100) surface. At 1.5L CO dose, the ratio was found to be 0.020 (± 0.002) whilst at 30L, this ratio had increased by a small amount to 0.024 (± 0.002) showing that the majority of the adsorption sites were covered following a 1.5L dose. The additional uptake following a 30L dose is discussed later in section 2.2.2.

On a Cu(111) surface (formed by epitaxial growth on mica), Kessler and Thieme[50] found that a CO overlayer was formed at 150K following a 3L dose. This is in general agreement with the results quoted above.

Horn et al[33] suggested that the sticking probability of CO on copper was high for all of the crystal faces at 77K. This generalisation appears to be justified considering the results obtained above and following the report of the authors that saturation occurred on a Cu(110) surface between 3L and 4L.

It can now be seen that on all low index copper surfaces, CO is rapidly taken up at low temperatures. There seems to be some

disagreement however, as to whether CO is adsorbed on copper at room temperature (295K). In 1971, Joyner et al[34] reported the adsorption of CO on a Cu (100) surface at 295K. They used low energy electron diffraction (LEED) and AES techniques to make the study. Subsequently, Tracy[31] and Chesters and Pritchard[35] suggested that impurities or electron beam effects may have created apparent CO uptake at 295K. Indeed, Tracy[31] found that the adsorption of CO at 77K was completely reversible from LEED and work function measurements. Thurston[36] found that no CO was adsorbed at room temperature following dosing pressures of up to 10^{-6} torr.

Further work by Isa, Joyner and Roberts[32] on the adsorption of CO on a Cu(100) surface at 295K was carried out using XPS and UPS. They found that CO was adsorbed with a sticking probability of approximately 10^{-6} at 295K. They also found that the XPS and UPS characteristics were different from those at 80K, as will be described later. Joyner et al appear to be the only workers to observe this phenomenon as no other reports have been made. Consequently, this speculation over adsorption of CO at 295K still remains today.

CO is found to exist in a physisorbed state on polycrystalline copper at 20K. This result was presented by Norton et al[37]. The authors found that the physisorbed CO changed to a chemisorbed species at 30K, where it showed the characteristics of adsorbed CO found by most workers between 77K and 150K.

2.2.2. Nature of Chemisorbed CO on Copper Surfaces

In this section, a review of ideas as to how CO is chemisorbed on copper surfaces will be presented. This review will consider the variety of views as to whether there is one adsorption state of CO on copper or whether multiple adsorption states exist. In addition, the various interpretations of the C1s and O1s photo-electron spectra and the ultra-violet photo-electron spectra will be presented.

Pritchard, in his paper on chemisorption on copper[38] showed that CO was adsorbed on polycrystalline and single crystal copper surfaces in two stages. This was demonstrated by the presence of a maximum in the surface potential as a function of coverage, and by the change in the infra-red (i.r.) spectrum. He showed by a LEED investigation that on both the Cu(100) and Cu (111) surfaces, CO adsorption formed single structures during the first stage of adsorption. For the Cu (100) surface a c(2 x 2) pattern was formed, whilst on the Cu (111) surface a ($\sqrt{3}$x $\sqrt{3}$)R30^{o} pattern was formed. At the end of the first stage of the adsorption, these patterns corresponded to coverages of 1/2 and 1/3 for the Cu (100) and the Cu (111) surfaces respectively. In the second stage of adsorption, Pritchard reported that a much more complex pattern was formed on both the (100) and (111) surfaces. For the (100) surface, he found that the final coverage would be 4/7 of a monolayer. For the (111) surface, he stated that the resulting structure was much more complex, and suggests that the final coverage would be about 1/2 monolayer. Pritchard suggested that the second stage of adsorption resulted from the formation of a compression structure on the copper surface on both the (100) and (111) surfaces.

The original work on the Cu (100) surface as described above, was presented by Chesters and Pritchard[35]. In this paper, they described the compression phase as limited additional chemisorption involving the mutual displacement of the already chemisorbed CO molecules. At the start of the compression phase up to saturation, the CO molecules which were already bound moved from the adsorption sites in such a way as to enable further CO molecules to be adsorbed. The overlayer at this stage was an array which was approximately close packed but was no longer simply related to the substrate structure. The formation of the compression phase resulted in a small increase in coverage, but the heat of adsorption was greatly reduced.

A further description of the compression structure was given by Tracy[31]. He obtained very similar results for CO adsorption on the (100) surface to those of Pritchard and Chesters. Again, he found that CO was adsorbed in two stages. The first stage formed a c(2 x 2) LEED pattern up to 1/2 monolayer coverage. Above 1/2 monolayer, he found a compression structure which he illustrated. Tracy determined that at the 1/2 monolayer point there were 0.77×10^{15} CO molecules/cm^2, whilst at saturation this increased to 0.9×10^{15} CO molecules/cm^2 at 77K. The adsorption sites for CO on copper surfaces will be considered further after the results and interpretations of photo-emission studies of chemisorbed CO have been considered.

There are differences in opinions regarding the interpretation of the C1s and O1s photo-electron spectra and the ultra-violet photo-electron spectra resulting from the adsorption of CO on

copper surfaces. The results and interpretations of different workers will be considered in turn.

Norton and Tapping[39] studied the adsorption of CO on a polycrystalline copper surface. From the UPS studies, they obtained peaks at 8.0eV, 8.8eV and 11.9eV, using a 40.8eV source. In addition, they obtained a possible fourth peak at 13.6eV, but this peak was not very well defined. The binding energy of the peak at 8.0eV was approximate, as this peak was poorly resolved in the UPS spectrum. Both the C1s and O1s spectra showed two peaks. In the C1s spectrum, the binding energies were found to be 286.3eV and 288.4eV, whilst those of the O1s spectrum were 532.8eV and 535.1eV. The lower binding energy peak in both spectra was $2\frac{1}{2}$ times more intense than the higher binding energy peak. This led the authors to interpret the lower binding energy peaks of the C1s and O1s spectra to be associated with the CO adsorption. The interpretation of the higher binding energy peaks is not as clear and the authors suggested that they could be due to shake-up events[40]. Norton and Tapping interpreted the presence of the fourth peak at 13.6eV as being part of two overlapping spectra, each one containing two peaks. They suggested that this could represent two distinct species on the surface, but they did not go into any more detail.

Ertl et al[41] studied the adsorption of CO on a Cu (111) surface by UPS. The results of these workers were similar to those of Norton and Tapping, and they obtained two main peaks at 8.5eV and 11.6eV below the Fermi level. In addition, they again obtained a weak peak centred at 13.5eV below the Fermi level. The authors interpreted this spectrum as resulting from

one adsorption state forming the two peaks with the lowest binding energies, and a shake-up satellite forming the remaining peak. A LEED pattern of the adsorbed CO was also obtained by these workers. They found that on the Cu (111) surface a ($\sqrt{3}$x $\sqrt{3}$)R30^{o} pattern was formed, which is in agreement with the result obtained by Pritchard as described earlier.

Allyn et al[42] studied the chemisorption of CO on a Cu (100) surface, using angle resolved UPS. These workers obtained a three peak structure UPS spectrum, the peaks having binding energies of 8.5, 11.7 and 13.5eV below the Fermi level, which is almost identical to that found by Ertl et al, as described above. Allyn et al came to the same conclusion as Ertl et al.

It would appear that the chemisorption of CO on either the (100), (111) or polycrystalline copper surfaces, results in one main adsorbed phase, being formed. However, work has been published which suggests the existence of two adsorbed phases and this will be considered next.

Evidence for the existence of two adsorbed phases of CO on a copper surface was presented by Demuth and Eastman[43]. They carried out adsorption on a Cu (100) surface. They found that there were four peaks in the UPS spectrum at low CO coverages which they compared to the spectra obtained by Norton and Tapping and by Ertl et al. The authors designated this phase as Phase 1. On increasing the CO coverage, the phase 1 spectral features intensified and a new peak appeared at approximately 7eV below the Fermi level. On further exposure to CO, the peaks at approximately 7eV and 13eV intensified whilst the phase 1

spectral features levelled off in intensity. These results suggest that one adsorbed phase exists at a low coverage of CO (phase 1), whilst a second phase begins to appear and intensify at higher coverages. The second phase resulted in the appearance of the peaks at approximately 7eV and 13eV. The authors estimated that the coverage of phase 1 on the Cu (100) surface was between 1/8 and1/4 monolayer whereas the total coverage before the onset of compression on a Cu (100) surface is 1/2 monolayer. So the second phase seemed to form a significant part of the adsorbed species. The authors, however, found that on polycrystalline and (111) surfaces only phase 1 was observed. This latter result agrees reasonably with the work of Norton and Tapping[39] and of Ertl et al[41].

Demuth and Eastman interpreted their UPS spectra for the phase 1 state as a CO molecule bonded skew to the surface. They supported this interpretation by comparing the relaxation/screening shifts of the C1s and O1s X-ray spectra of CO adsorbed on copper and on nickel. For the CO on Cu, they found that the O1s shift was approximately 1eV greater than the C1s shift. For CO adsorption on Ni, these shifts are identical. They attributed the difference in the copper case to a smaller oxygen to copper substrate distance which suggests possible binding of the CO molecule at an angle. The interpretation of the phase 11 state was much more complex and the authors were unable to successfully determine how the CO moleculeswere adsorbed in this phase. The authors stated that the second phase took the coverage up to the 1/2 monolayer level, but the total coverage was kept below this point. If this was the case, the additional peaks in the UPS spectrum could not be attributed to compression structures, as these are formed above 1/2 monolayer coverage

on the (100) surface.

Jugnet et al[44] have also claimed that they have observed two adsorbed phases of CO on a Cu (111) surface. Their UPS results were almost identical to those obtained previously for Cu (111) and polycrystalline copper surfaces. At higher coverages above 0.3L CO dose, they saw peaks at 8.7eV, 9.6eV, 11.7eV and 13.7eV below the Fermi level. However, at low coverages (equivalent to a dose 0.3L or less), they reported that only the peaks at 8.7eV and 11.7eV appeared and that on increasing the CO coverage the intensity of the peaks at 9.6eV and 13.7eV became enhanced. They concluded from this that the two sets of peaks were from two adsorbed states of CO which were superimposed. They associated these two states to the presence of two different crystallographic sites, but they did not describe the different sites in any more detail. The authors also found that the O1s spectrum had a single peak with a binding energy of 532.9eV at low CO coverages. However, on increasing the coverage, a second peak appeared at 534.9eV. These two binding energies are almost identical to those obtained by Norton and Tapping for a polycrystalline surface. The authors interpreted the lower binding energy peak of the O1s spectrum (532.9eV) and the UPS peaks at 8.7eV and 11.7eV to CO bonding on "on top of" adsorption sites, whilst the second adsorbed phase was attributed to "bridge sites ". This interpretation implies that the "on top of" sites were populated first, and were the more reactive sites compared with the "bridge sites" which were populated at higher CO coverages.

Further UPS studies have been made on the Cu (111) surface by Kanski et al[45]. These workers obtained a UPS spectrum with four peaks. These peaks were located at 8.5eV, 9.8eV, 12.0eV and 13.5eV below the Fermi level. These results are very similar to those obtained by Ertl et al and by Jugnet et al (at higher CO coverages) for their Cu (111) surfaces. The results also agree with the peaks that Demuth and Eastman assigned to their phase 1 type adsorption, described earlier. The results obtained by Norton and Tapping for their polycrystalline surface also agree with the spectrum obtained by Kanski et al. The authors reported that no coverage dependence of the peaks was observed (except for uniform increases in intensity with coverage) although the authors did not say how low their smallest dose was. As a consequence of this, it is difficult to tell whether the coverage independence of the UPS spectrum extends right down to very small CO coverages or whether the authors did not record the UPS spectrum at very low CO coverages. Therefore it cannot be confirmed whether the result obtained by Jugnet et al as described earlier (i.e. the superposition of two adsorption states in the UPS spectrum) was a real effect or not. The authors obtained a similar UPS spectrum for the Cu (100) surface, again with no coverage dependence. The authors interpreted their spectra as showing that the CO molecule was bound to the Cu (111) surface at an angle of about 35°. This result is in agreement with the interpretation presented by Demuth and Eastman[43] for their (111) surface.

Norton et al[37] performed some studies of CO adsorption on a polycrystalline copper surface. The authors obtained a UPS spectrum with a four peak structure which agreed with that

obtained by other workers for the Cu (111) and polycrystalline copper surfaces, and the data is presented in Table 2.1. The C1s and O1s spectra were also taken, and these could be easily deconvolved into three peaks. In the C1s spectrum, the binding energies of the three peaks were 286.6eV, 289.4eV and 294.0eV whilst for the O1s spectrum, the binding energies of the three peaks were 533.7eV, 536.0eV and 541.0eV. These spectra do not compare very favourably with those of Norton and Tapping or those of Jugnet et al (the agreement between these two sets of work was good). Firstly, there was an additional peak in both the C1s and the O1s spectra with binding energies of 294.0eV and 541.0eV respectively, and secondly, the two lower binding energy peaks were in a different position to those obtained by Norton and Tapping and Jugnet et al. No indication as to why the shift occurred was given by the authors. In addition, no experiments to determine the coverage dependence of the UPS and XPS spectra were carried out, so again, it cannot be seen whether the multiple adsorption state effect proposed by Jugnet et al was reproducible or not. Norton et al interpreted the three peak structure of the XPS spectra as resulting from shake up processes in addition to the adsorbed CO. They suggested that there was one main peak at the lowest binding energy in the C1s and O1s spectra and that the remaining peaks were associated with shake up. The authors estimated that the coverage of the surface was approximately 0.3 monolayers which agrees favourably with other work carried out on the (111) surfaces.

TABLE 2.1 SUMMARY OF THE UPS DATA OBTAINED BY VARIOUS WORKERS FOR ADSORBED CO ON COPPER SURFACES.

Peak binding energy (in eV below the Fermi level)					Copper Surface	Temp	Comments	Ref
	(8.0)	8.8		11.9 (13.6)	Polyx	80K		39
		8.5		11.6 (13.5)	(111)	80K		41
		8.5		11.7 13.5	(100)	80K		42
		8.5	10.0	11.7 13.5	(100)	180K	Low coverage	43
7.0		8.5	10.0	11.7 13.0	(100)	180K	High coverage	43
		8.7		11.7	(111)	80K	Low coverage	44
		8.7	9.6	11.7 13.7	(111)	80K	High coverage	44
		8.5		11.8 13.5	Polyx	80K		37
	8.3		9.7	11.8 13.5	Polyx	80K	Deconvolving the peak at 8.5eV	37
		8.5	9.8	12.0 13.5	(111)	80K		45
		8.6	(9.8)	11.8 13.7	(100)	80K	1.5L	32
6.9		8.7	10.0	11.9 13.4	(100)	80K	30L	32
6.9		8.7		11.9 13.5	(100)	120K		32
		8.7		11.9 13.5	(100)	140K		32
		8.1		11.1	(100)	295K		32
			9.9	12.6 15.5	-	-	Gas phase CO	37

N.B. (i) Gas phase CO binding energies w.r.t. vacuum level.

Fuggle et al[46] in their work on the (100) and polycrystalline copper surfaces have also found that both the C1s and O1s spectra are three peak structures. They reported that these three peak structures were almost the same following adsorption on both types of surface. Consequently this suggests that adsorption on different crystal faces does not result in a multiple peak structure for the C1s or the O1s spectra. The authors suggested that there was only one adsorbed state of CO on the copper surface, giving rise to one main peak in the C1s and O1s spectra, whilst the remaining pair of peaks were induced by the photo-emission process. This is a similar conclusion to that of Norton et al[37]. It is also in agreement with the conclusion of Norton and Tapping[39], Ertl et al[41] and Allyn et al[42].

Some theoretical work has been carried out to try to model the C1s and O1s spectra, and explain their structure. Messmer et al[47] presented a method whereby they could calculate the intensities of the individual peaks in each of the C1s and O1s spectra. They successfully modelled the spectra by assuming that there was one adsorbed state of CO which gave rise to the lowest binding energy peaks, whilst the remaining peaks were due to shake up transitions within the orbitals of the carbon and oxygen atoms.

A different explanation of the cause of the multiple peaks in the C1s and O1s spectra has been given by Gunnarsson and Schonhammer[48] and by Messmer et al in a more recent paper[49]. These workers have suggested that core hole screening causes multiple peaks to

to occur. The core hole screening results when valence electron orbitals are modified when a core hole is created. The modification of the valence orbitals results in their having a slightly different binding energy. In both pieces of work, the authors attributed the pair of peaks with the highest binding energies in both the C1s and O1s spectra to the core hole screening effect. Consequently, the conclusion was that there was only one adsorbed phase of CO.

TABLE 2.2 SUMMARY OF THE XPS DATA OBTAINED BY VARIOUS WORKERS FOR ADSORBED CO ON COPPER SURFACES.

C1s peak binding energies (eV)			O1s peak binding energies (eV)			Copper Surface	Temp	Comments	Ref
286.3	288.4		532.8	535.1		Polyx	80K		39
			532.9	534.9		(111)	80K		44
286.6	289.4	294.0	533.7	536.0	541.0	Polyx	80K		37
	289.0	293.8	534.1			(100)	80K		32
286.6			532.8			(100)	295K		32
		291.3			537.5			Gas phase CO	37

N.B. (i) All binding energies referred to the Fermi level except for the gaseous CO data which are referred to vacuum level.

In their work on the adsorption of CO on Cu (100) at 80K, Isa et al[32] obtained a two peak structure for their C1s spectrum and only one peak in their O1s spectrum. In the C1s spectrum, the lowest binding energy peak was at 289.0eV, whilst the higher one was at 293.8eV. These two peak positions agreed reasonably with those of Norton et al[37]. However, the peak which has been detected at 286.6eV by other workers (see Table 2.2 above) has not apparently been detected by Isa et al. In the O1s spectrum,

the authors quoted a binding energy of 534.1eV which compared reasonably with the lowest binding energy peak obtained by Norton et al. However, the authors did not appear to have seen, or taken into account, any higher binding energy peaks in the O1s spectrum. In their paper, Isa et al presented the C1s and O1s spectra which they obtained following adsorption of CO. It would appear from the spectra that the C1s spectrum was sufficiently broad to include a third peak at approximately 287eV. If the C1s spectrum was interpreted in this way, then the result would agree with the results of the other workers. In the case of the O1s spectrum, the peak quoted at 534eV was again sufficiently broad (approximately 4eV) for a second peak to exist at a higher binding energy(at approximately 536eV). If this was so , then this too would agree with previous results. The O1s spectrum was not continued above 540eV, so it is difficult to determine whether the third peak at 541eV which has been seen by other workers was present or not. If the interpretation of the peak positions by Isa et al was correct, then the absence of the lowest binding energy peak at 286.6eV in the C1s spectrum would be more difficult to explain. Isa et al concluded that there was only one adsorbed phase of CO and that the peak at 293.8eV in the C1s spectrum was probably associated with a shake-up satellite. The intensities of the C1s and O1s peaks were measured at two coverages, one corresponding to a 1.5L dose and a second corresponding to a 30L dose. No real changes occurred, except that the intensities increased by about 1/5. The UPS results were also recorded at these two coverages. Following a 1.5L dose, the familiar four

peak structure appeared with peak positions which agreed well with those presented earlier. The data is shown in Table 2.1. At 30L an additional peak appeared at 6.9eV below the Fermi level and this agrees with the findings of Demuth and Eastman for their Cu (100) surface. However, Isa et al suggested that this additional peak was a result of the onset of the compression structures, having performed a LEED observation at the same time. As a result the authors interpreted the phase II adsorption of Demuth and Eastman[43] as the formation of the compression structures and they stated that the possibility of a distinct second adsorbed species did not exist. It has also been suggested (a view which the authors share with Norton et al) that the peak at 13.5eV in the UPS spectrum could also be due to shake up, but this is not completely clear and it would appear that more work needs to be done to determine whether this is the case or not.

Isa et al[32] also studied the adsorption of CO on a Cu (100) surface at 295K. The results for the UPS and XPS spectra appear in tables 2.1 and 2.2 respectively. This result seems to be something of an anomaly, as it has not been reproduced by any other workers, and so it has been included for completeness. It can be seen from the tables that both the C1s and O1s spectra had single peaks at binding energies of 286.6eV and 532.8eV respectively. Peaks with these binding energies were not observed by Isa et al themselves at 80K, whilst the higher binding energy peaks seen at 80K were not observed at 295K. At 295K, the UPS spectrum was a three peak structure, whilst at 80K, a four peak structure formed the UPS spectrum.

Further work has been carried out on the structure of CO adlayers on copper surfaces. Horn et al[33] studied the adsorption of CO on the Cu (110) surface, by LEED and surface potentials (and also i.r. spectroscopy). They found that there was a surface potential maximum after which the compression structures began to form. At the surface potential maximum, the LEED pattern gave a p(2x1) structure, and this changed to c(1.3x2) upon formation of the compression structure. These structures are illustrated in Figure 2.2. Horn et al also determined that the heat of adsorption up to the surface potential maximum was approximately constant at 55kJ/mol. On formation of the compression structure, this fell rapidly.

In some later work, Pritchard[111] studied the structure of CO adlayers on the Cu (100) and Cu (111) surfaces by considering the results from LEED patterns and from i.r. spectroscopy. On the Cu (100) surface up to 1/2 monolayer CO coverage he found that a c(2x2) structure was formed. This is in agreement with Isa et al[32]. For the Cu (111) surface he confirmed the $(\sqrt{3}x\sqrt{3})R30^{\circ}$ structure of the adlayer up to 1/3 monolayer coverage. Kessler and Thieme[50] also obtained similar LEED results, and found that at saturation the coverage was 3/7 monolayer.

Pritchard in his paper on the CO adlayers also considered the question as to whether CO was attached to the copper surface via bridge or linear (on top of) sites. He preferred the view of CO being linearly bonded before the onset of compression, after considering results obtained by i.r. spectroscopy and other work done by Andersson using EELS[51]. However work done by Anderson [52] using a molecular orbital study implies that CO is bridge bound

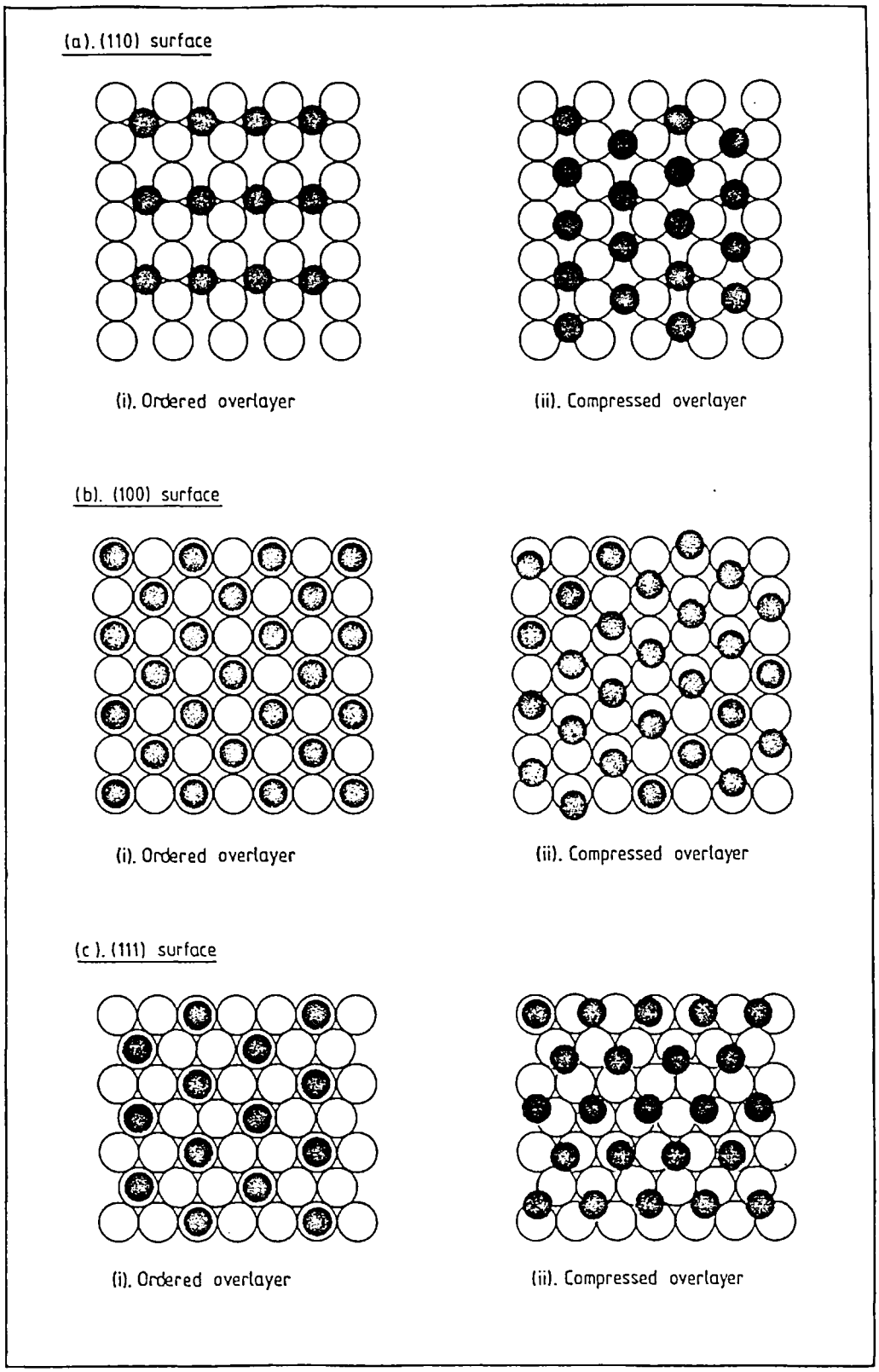


Figure 2.2. Possible overlayer structures for chemisorbed CO on Cu (110), (100) and (111) surfaces - in this diagram it has been assumed that CO is linearly bound before compression

to copper surfaces. Pritchard illustrated possible overlayer models for the (100) and (111) surfaces and these are shown in Figure 2.2. He suggested that the compression structure on both surfaces was composed of adsorbed CO on a mixture of linear and bridge sites. This could explain the two adsorbed CO phases suggested by Jugnet et al[44] as described earlier, where they interpreted the two phases to adsorption on linear and bridge sites. However, the development of the second phase in Jugnet's work occurs at 0.3L and above which may correspond to too low a coverage for the onset of compression unless the pressure measurement by Jugnet was inaccurate.

Hollins and Pritchard[53] found that a surface potential maximum occurred whilst adsorbing CO on a Cu (111) surface. At the maximum, the LEED pattern was ($\sqrt{3}$x $\sqrt{3}$) R30°, and represented a coverage of 1/3 monolayer which is in agreement with previous results. The heat of adsorption was found to be 50kJ/mol up to the surface potential maximum, but dropped abruptly to 38kJ/mol at the onset of compression of the adsorbed CO. The workers imply that CO is also linearly bound up to the surface potential maximum.

2.2.3 Desorption of CO from Copper Surfaces

Little work has been published where successful thermal desorption spectra have been obtained. Indeed, little accurate information is available in the literature concerning activation energies of desorption or any temperatures at which peak maxima occur. However, it would appear that some workers have attempted

to produce thermal desorption spectra but have not succeeded in getting any reasonable results. These attempts will now be summarised.

In their work on CO on polycrystalline copper, Norton et al[39] reported that their attempt to obtain a reasonable desorption spectrum was unsuccessful. They were trying to use the technique to determine whether they could attribute the two peaks that they found in the C1s and O1s X-ray photo-electron spectra to two adsorbed molecular species. However, this did not work, and no further details of any reason for the failure were given.

Kessler and Thieme[50] attempted to obtain thermal desorption spectra from their Cu (111) surfaces. Again, no successful results were obtained, because in this case, the authors had difficulties with background CO. This problem was associated with desorption of CO from the sample holder which resulted in a background desorption spectrum from the holder being superimposed on the main desorption spectrum. The degradation of the spectrum must have been very significant, because the authors stated that its evaluation was very difficult and they decided not to use the results. Again, no more details were given.

In a subsequent paper[37], Norton and co-workers stated that they had no success in obtaining two separate desorption peaks. On this occasion, a spectrum appears to have been observed, but only with a single peak. However, no spectrum was presented by the authors so it is difficult to tell whether they succeeded in obtaining a reasonable spectrum.

There have been three cases where thermal desorption spectra of CO from copper surfaces have been obtained, up to mid 1983, but only two of them were published. Spicer et al[18] obtained a first order line shape peak from the desorption of CO from a Cu (110) surface showing that CO was molecularly adsorbed at low temperatures. This is a result which is well accepted from photo-emission studies. The authors also found that the temperature at which the peak was a maximum (T_{max}) was below or at 220K. However, T_{max} does not appear to have been determined any more accurately. Unfortunately, Spicer et al could not cool their sample below -110°C (163K), and as a result they could not resolve the desorption peak completely. This last comment from the authors seems to suggest that there could be a second more weakly bound state desorbing at a lower temperature but if this is a real effect is unclear. A value for the activation energy of desorption for the major peak was not given.

Another desorption spectrum of CO from a Cu (110) surface was obtained by Bowker[54]. He dosed the crystal with the surface temperature at 140K, and from this he obtained a first order line shape peak with a T_{max} of approximately 210K. No other peaks were observed at any temperature between 140K and 210K. This results agrees favourably with the main peak obtained by Spicer et al[18], as described earlier, but throws some doubt as to whether a second more weakly bound state exists on this surface. The activation energy for desorption was not determined accurately for this desorption spectrum, but was estimated to be in the region of 60-70kJ/mol.

Madix has given further details of the activation energy for desorption, pre-exponential factor and T_{max} for the desorption of CO from a Cu (110) surface[55-57]. He found that the value of T_{max} was 223K. The activation energy was found to be 13.5kcal/mol ($\sim$ 56kJ/mol) and the pre-exp. factor was quoted as 4×10^{13} sec^{-1}.

Ertl et al[58] obtained a desorption spectrum for CO from a Cu (111) surface. This surface was created by evaporating an excess of copper onto a Ru(0001) substrate (the Cu/Ru system was being studied). They obtained two peaks with T_{max} of 170K and 200K and also gave very rough estimates of the activation energies, which were 40kJ/mol and 65kJ/mol. An accurate determination of the activation energy was not made, because some of the lower energy state CO had already been pumped off before the thermal desorption run was performed. The authors interpreted the lower energy state as the desorption of the CO which formed the compression structures on the Cu (111) surface.

Additional information can be obtained from other work where desorption has been carried out, <u>but</u>, where no mention has been made of desorption spectra at all. These papers give some idea of desorption temperatures and the activation energies of desorption.

Kessler and Thieme[50] used work function-temperature spectra to evaluate activation energies of desorption. They found that on a surface where copper was evaporated onto a Cu (111) substrate, giving a polycrystalline surface, there were three differently bound states of CO. The activation energies for

desorption of these states were 54kJ/mol, 45kJ/mol and 34kJ/mol. They attributed the highest activation energy to the Cu (100) surface and the intermediate activation energy to the Cu (111) surface. This follows since the (100) face is more reactive than the (111) face[38,59]. The lowest activation energy was attributed to a weakly bound state and the authors suggested that this state was related to the transition between 1/3 coverage and 3/7 coverage. This coverage change was associated with a LEED pattern change, the latter showing a CO compression structure on the copper surface. Hence the state with an E_d of 34kJ/mol could be interpreted as the desorption of the CO which formed the compression structure.

Ertl et al[41] reported that following adsorption of CO on a Cu (111) surface at -130°C (143K), they could desorb the CO at - 100°C (173K). From this they estimated an adsorption energy of 12kcal/mole, which approximates to an activation energy of desorption of 48kJ/mole. This figure is close to that obtained by Kessler and Thieme for a Cu (111) surface, as mentioned earlier.

Norton et al[37] reported that CO completely desorbed from a polycrystalline copper surface by a temperature of approximately 170K. They obtained this result by monitoring the intensity changes of the peaks in the UPS spectra at different temperatures. Desorption started at approximately 100K. Similarly, Jugnet et al[44] found that CO desorbed at around 100K, and the result was also established by monitoring the UPS spectra at different temperatures. However, this result was obtained from a Cu (111) surface.

Isa et al[32] found that CO desorption from a Cu (100) surface commenced below 145K, and was completed by 200K. This too was determined by monitoring the UPS spectra as a function of temperature. It was found that at 145K, the additional peak at 6.9eV in the UPS spectrum disappeared which suggests that the additional CO forming the compression structure had desorbed.

Chesters and Pritchard[35] monitored the desorption of CO from a Cu (100) surface using potential measurements. They reported that there were two stages of desorption. The first stage was complete by 195K and was attributed to the desorption of the CO forming the compression structure on the copper surface. The authors then stated that all of the remaining CO had desorbed at room temperature. This second stage was the adsorbed CO which was held on the copper surface in an ordered manner, forming the first 1/2 monolayer coverage.

Apart from these papers, there has been very little other information regarding the desorption of CO from copper surfaces. Thermal desorption spectra themselves are rarely published (only two have actually appeared in the literature), which suggests that obtaining a thermal desorption spectrum of CO from copper is not an easy task. It would seem that desorption of CO from sample holders or other nearby surfaces could be an important consideration in setting up an experiment to carry out thermal desorption, following remarks made by Kessler and Thieme[50].

From the results of the various workers who have tried to obtain desorption spectra or monitor the desorption by some other technique, it can be seen that CO desorbs from copper surfaces in a temperature range of approximately 140-220K. Variations in the temperature where CO desorption is completed could be attributed to the various authors using different heating rates for warming their samples. A faster sample heating rate will shift T_{max} for a desorption peak to a higher temperature. This can be seen from equations (3.9) and (3.10) in Chapter 3.

It seems likely that there could be two desorption peaks of CO from copper surfaces. Two different experiments which have just been described[32, 35] have revealed two desorption states, with the lower energy state being attributed to CO compression structures on the copper surfaces. However, only the experiment by Ertl et al[58] showed a lower energy state by thermal desorption, but this peak was not accurately determined because the adsorption temperature was too high. This problem was also highlighted by Spicer et al for their thermal desorption spectrum from a Cu (110) surface. It would seem necessary therefore to attempt to perform a thermal desorption experiment with an adsorption temperature which is much lower than 150K, preferably as near liquid nitrogen temperature as possible. This is an experiment which does not appear to have been successfully carried out to date. Part of the objective of this work was to obtain a thermal desorption spectrum of CO from polycrystalline copper and to attempt to get the sample temperature as low as possible (in the region of 100K), so that any weakly bound states could be detected without the difficulties of the lowest sample

temperature attainable being too high as was the case for Spicer et al[18] and Ertl et al[58], for example.

In summary, CO appears to be desorbed in two stages, over the temperature range 140-220K. The first stage has been interpreted as the desorption of the CO adsorbed in the compression structure, whilst the second stage is attributed to the desorption of the remaining (the majority) adsorbed CO. The activation energies for desorption of CO from the (100), (110) and (111) single crystal surfaces of copper which have been quoted in the literature are shown in Table 2.3.

TABLE 2.3 ACTIVATION ENERGIES REPORTED FOR DESORPTION OF CO FROM COPPER

Copper single crystal Surface	Activation Energy E_d
Cu (111)	45kJ/mol
Cu (100)	54kJ/mol
Cu (110)	55-65kJ/mol

A fourth activation energy for desorption of 34kJ/mol was quoted by Kessler and Thieme[50] which is probably associated with CO desorption from the compression structure.

2.3 Adsorption of Hydrogen on Copper

Many experiments have been carried out on the adsorption of hydrogen on copper, but the majority of the work has been done on reduced copper powders. It has been shown that hydrogen is readily chemisorbed on these reduced copper powders[14,60].

However, a suggestion was made that the adsorption of hydrogen on reduced copper powders was due to the presence of some residual contamination[61]. Kwan[62] produced evidence that supported the latter view, because he found only a slight activated chemisorption at high temperature on a carefully reduced copper powder.

Initial investigations of the adsorption of hydrogen on clean copper films have indicated that there is little or no hydrogen chemisorbed on these films[63-65]. In their work on the adsorption of hydrogen on evaporated copper films by surface potential measurements, Pritchard and Tompkins[66] found that no molecular hydrogen was chemisorbed on the copper surface below a temperature of 300°K.
However, further work by Pritchard[68] has shown that copper can dissociatively adsorb hydrogen in the temperature range 273-313K. The inability of copper to dissociatively adsorb hydrogen at low temperatures below 273K has been attributed to the presence of an appreciable activation energy of adsorption[67]. Alexander and Pritchard[67] found that the heat of adsorption of hydrogen on copper was 40kJ/mol and that the activation energy for desorption was $\sim$ 75kJ/mol so that the activation energy

for adsorption would be around 30-40kJ/mol. In contrast to this, Kwan[62] and some other workers, as described by Pritchard[67] found that much higher temperatures were required before chemisorption of hydrogen from the gas phase occurred. This resulted in activation energies for adsorption of around 100kJ/mol. The significant difference was attributed to an inconsistency in the experimental work by the different investigators. This inconsistency was probably as a result of different surface structures of copper being investigated[67].

The adsorption of atomic hydrogen, which is achieved in practice by dissociating the molecule at a hot tungsten filament held near to the sample, occurs more readily on a copper surface. The uptake of atomic hydrogen has been studied by Pritchard and Tompkins[66], again using surface potential measurements. They found that atomic hydrogen was adsorbed at low temperatures between 90K and approximately 300K. At around 90K, the adsorbed hydrogen was immobile on the surface, but an increase in temperature towards 195K led to an increase in the mobility of the adatoms, which eventually desorbed at higher temperatures around 300K. Further details of the adsorption of atomic hydrogen on copper were given by Alexander and Pritchard[67] where they looked at hydrogen chemisorption on evaporated copper films, again using surface potential measurements. They established that hydrogen desorption was rapid at room temperature, except at low coverage, with complete desorption being achieved at around 330K.

The adsorption of hydrogen on copper was studied by Kojima et al[69] using thermal desorption. The authors performed their

experiments using a polycrystalline copper plate in a UHV system. The sample was exposed to different doses of hydrogen between 30L and 30000L at room temperature, and the subsequent desorption spectra produced almost symmetrical peaks which had a T_{max} that was coverage dependent. At low coverage T_{max} was approximately 355K, but as the coverage increased, T_{max} decreased towards 325K. This is a characteristic of a second order desorption process, and this would be expected since the process involves recombination of two single H atoms and then their subsequent desorption. The authors determined the activation energy for desorption as 68.6 (± 8.0) kJ/mol which is similar to that from Pritchard's work[67]. Although the authors did not mention whether the hydrogen was pre-dissociated before adsorption, this certainly may have been possible. This is because there was a Bayard-Alpert type ionisation gauge very near the sample, and the filament on this gauge could easily be a source of dissociated hydrogen. Experiments will be carried out in this work to determine whether polycrystalline copper does adsorb hydrogen from the molecular gas, the results being given in Chapter 7.

Wachs and Madix[57] have also obtained a hydrogen desorption spectrum from a Cu (110) surface, following adsorption of formaldehyde and its subsequent oxidation. The authors observed similar spectra to that of Kojima, and again found that T_{max} was coverage dependent. However, a lower value for E_d, was quoted, this being approximately 60kJ/mol.

Bowker[70] too obtained a similar set of desorption spectra to those described above. In this case, the sample was dosed with between 3L and 30L of hydrogen, which had been pre-dissociated by a local mass spectrometer filament. The sample had been held at a temperature of approximately 160K during dosing. However, no values for the kinetic parameters were available.

2.4 The Adsorption of Methanol, Formaldehyde and Formic Acid on Copper Surfaces

It has been suggested that methoxy or formate intermediate species may be important in the mechanism of methanol synthesis from CO and H_2. Therefore in this section it is proposed to present the principal results of the adsorption of methanol, formic acid and also formaldehyde on Cu surfaces, so that these intermediate species can be characterised. The majority of this work has been carried out by Madix, Bowker and co-workers and their results will be reviewed.

Madix and Bowker[71] studied the adsorption of methanol on Cu (110). Methanol was found to adsorb at 140K giving a five peak UPS structure, which indicated that the methanol was molecularly adsorbed to the copper surface via the oxygen atom in the molecule. The XPS results showed that there was a single oxygen peak at 532.4eV and a single carbon peak at 286.2eV. On warming the sample to 270K, a significant amount of methanol desorbed at approximately 200K, leaving a new species behind on the copper surface at 270K. The UPS spectrum changed to a

three peak structure which was characteristic of the presence of a methoxy species adsorbed on the surface. The XPS spectra showed a shift in the O1s peak to 531.2eV whilst the C1s peak remained at 286.2eV. The change in the O1s peak indicated that ∿ 60% of the methanol adsorbed at 140K was lost. However, it is not completely clear whether the methoxy species was formed at 140K or whether it was formed on warming to 270K. The authors suggested that some methoxy was formed at 140K, and was ther enhanced by warming to 270K. Methanol was also adsorbed on the Cu (110) surface at 270K. The UPS spectra again showed a three peak structure which was characteristic of the presence of methoxy species on the surface. The XPS spectra showed that the C1s peak remained invariant at 286.2eV, but the O1s peak was at 530.7eV. The difference between this and the previous peak at 531.2eV, could probably be attributed to readsorption of background methanol at 140K in the previous experiment (after warming to 270K, the sample re-cooled to 140K) which gave a much broader O1s peak at 531.2eV. Adsorption at 270K resulted in almost twice as much methanol being taken up, compared with the amount of adsorbed material remaining on the surface following warming of the adsorbed layer at 140K to 270K. The authors suggested that there was competition for adsorption sites between the methoxy species and the low temperature molecularly adsorbed state. The adsorbed methoxy species desorbed at ∿ 370K as methanol, following adsorption at either 140K or 270K. Hence, it can be seen that a methoxy species is formed on the Cu (110) surface and that it is stable up to ∿ 370K. The species can be formed either by direct adsorption of methanol at 270K or by adsorbing methanol at 140K and warming to 270K.

The adsorption of CH_3OH after pre-dosing oxygen on a Cu (110) surface has been studied by Wachs and Madix[56] and by Bowker and Madix[71]. Wachs and Madix found that there was coincident desorption of methanol, hydrogen and formaldehyde at 370K from their flash desorption studies. The coincidence of two or more desorption peaks with the same shape (order) implies that the desorbing species originate from the same surface intermediate[56,72]. The coincident hydrogen, methanol and formaldehyde were interpreted as resulting from the methoxy species either decomposing to form formaldehyde and hydrogen or recombining with a neighbouring hydrogen atom to recreate methanol. Wachs and Madix also observed coincident desorption of CO_2 and H_2 at 470K which is indicative of the presence of formate species on the surface. Bowker and Madix reproduced the desorption spectrum described above, but did not observe the desorption of CO_2 and H_2 at 470K. They explained the presence of the extra peaks in Wachs and Madix work as resulting from the adsorption of formaldehyde impurity in the methanol forming a formate species. Bowker and Madix also studied the pre-dosed oxygen system using XPS and UPS. In their XPS results, they found that at 130K the pre-dosed oxygen which was equivalent to a 1/4 of a monolayer coverage, gave an O1s peak at 530.0eV. This peak broadened and shifted to 531.7eV upon adsorption of methanol, whilst the component based at 530.0eV became indistinct, indicating that there was some interaction between the pre-adsorbed oxygen and the methanol. Upon warming of the adlayer to 270K, some water and methanol were desorbed which gave a 35% decrease in the O1s peak intensity, the majority of this loss resulting from the originally

dosed oxygen at 140K being desorbed as water. The water was formed by the reaction of this oxygen with adsorbed hydrogen atoms which were released from the methanol hydroxyl group on formation of the methoxy species. The surface coverage of methoxy species at 270K following pre-adsorption of oxygen and methanol adsorption at 140K was much greater than for the case where methanol was dosed at 140K in the absence of oxygen. This was due to the formation of the more stable methoxy species, even at 140K, in the presence of oxygen. The authors also pre-dosed the surface with oxygen and adsorbed methanol at 270K. The O1s peak which resulted had a binding energy of 530.8eV and was similar to the peak obtained by warming the oxygen/ methanol adlayer from 140K to 270K, indicating the presence of the methoxy species on the surface. In every case, there was one C1s peak at 286.2eV.

Hofmann et al[73] studied methanol adsorption on a Cu (100) surface. In this case, the methoxy intermediate was not formed on the surface following methanol adsorption at 85K and warming to room temperature. The adsorbed methanol desorbed intact at 165K. Only by predosing with oxygen could the authors obtain the methoxy species, this being recognised from a characteristic UPS spectrum. The authors found that the methoxy decomposed at $\sim$ 370K on the (100) surface to give formaldehyde and hydrogen.

The adsorption of formic acid on a Cu (110) surface has been studied by Ying and Madix[74] and by Bowker and Madix[75]. The former pair found that following adsorption of formic acid at

190K, the desorption spectrum contained a hydrogen peak at 273K and coincident CO_2 and H_2 peaks in a ratio of 2 : 1 at 475K. The intermediate in this case was a formate. The hydrogen peak at 273K resulted from the dissociation of the formic acid upon adsorption at 190K releasing the acidic hydrogen atom and its subsequent desorption. The difference between the evolution of hydrogen at 273K and the decomposition of the formate at 475K indicates that the formate is a stable intermediate. Bowker and Madix found that adsorption of formic acid at 140K gave a C1s peak at 289.5eV and an O1s peak at 532.5eV, representing molecularly adsorbed formic acid. On warming to 375K, it was found that $\sim$ 50% of the adsorbed formic acid desorbed at 180K, whilst the remainder dissociated into the formate species which was characterised by a C1s peak at 287.7eV, and an O1s peak at 531.5eV. The UPS spectrum showed a four peak structure which also characterised the formate. Predosing the copper surface with oxygen resulted in the formate being formed at a lower temperature giving approximately twice the coverage of formate at 375K compared with that of clean copper.

Wachs and Madix[57] and Bowker and Madix[76] have also studied the adsorption of formaldehyde on a Cu (110) surface. It was found that following adsorption of formaldehyde only at 140K, the desorption spectrum contained just one peak at 230K which corresponded to molecular formaldehyde. However, oxygen pre-adsorption created a formate intermediate, which was characterised

by the coincident desorption of CO_2 and H_2 at 475K. Adsorption of oxygen/formaldehyde on the Cu (110) surface at 140K resulted in a two peak O1s structure with binding energies at 531.1eV and 532.8eV. A single C1s peak at 287.7eV was also observed. The original atomic oxygen XPS peak from the predosing was lost, indicating interaction between the two adsorbed species, which gave the peak at 531.1eV, whilst the peak at 532.8eV was due to parent formaldehyde. On warming to 400K, the parent formaldehyde desorbed at 230K and the O1s peak at 532.8eV disappeared, hydrogen was desorbed at around 340°C, and the O1s peak at 531.1eV shifted to 531.5eV. The C1s peak remained unchanged. The mechanism suggested to explain the events described above, was that formaldehyde was oxidised to a H_2CO_2 complex which gave an O1s peak at 531.1eV. On raising the temperature, the H_2CO_2 complex dissociated, releasing one hydrogen atom, so giving the hydrogen desorption peak at $\sim$ 340°C and shifting the O1s peak to 531.5eV which is characteristic of the formate.

A summary of the binding energies of the XPS and UPS peaks following adsorption of methanol, formic acid and formaldehyde on a Cu (110) surface is presented in Table 2.4.

2.5 Chemisorption on Zinc Metal Surfaces

Although some studies have been made on the reactivity of ZnO (e.g. Nagarjunan et al[77], Bowker et al[78] and Baranski et al[79] no studies have been made at all as regards the adsorption of CO, H_2, CO_2 and methanol on zinc metal.

TABLE 2.4 BINDING ENERGIES FOR METHANOL, FORMIC ACID, AND FORMALDEHYDE ADSORBED ON Cu(110)

Adsorbed species and conditions	Binding Energies w.r.t. Fermi level (eV) C1s	O1s	UPS Peaks	Remarks
1a) MeOH adsorbed at 140K	286.2	532.4	5.5,7.0,9.0,11.5,16.0	
b) After warming layer 1a) to 270K	286.2	531.2	5.0,8.5, 15.5	
c) MeOH adsorbed at 270K	286.2	530.7	5.0,8.5,15.5	
2a) 1/4 monolayer O adsorbed at 300K	-	530.0	5.8	
b) MeOH adsorbed onto layer 2a) at 140K	286.2	531.7	5.0,8.5,11.0,15.5	
c) After warming layer 2b) to 270K	286.2	530.8	5.0,8.5,15.5	
d) MeOH adsorbed onto layer 2a) at 270K	286.2	530.8	5.0,8.5,15.5	
3a) HCOOH adsorbed at 140K	289.5	532.5	5.6,8.2,9.9,13.4	
b) After warming layer 3a) to 375K	287.7	531.5	4.9,7.5,9.2,12.7	
4a) HCOOH adsorbed at 140K following pre-adsorption of O at 300K	287.7	531.6	-	
5a) HCHO adsorbed at 140K	287.7	533.1	5.6,9.2,11.8	Peak at 9.2 eV is broad
6a) HCHO adsorbed at 140K following pre-adsorption of 1/4 monolayer of O at 300K	287.7	(531.1 (532.8	-	
b) After warming layer 6a) to 400K	287.7	531.5	4.9,7.5,9.2,12.7	

2.6 Review of Relevant Work on Cu/ZnO Catalysts

As stated in the Introduction, the mechanism of the methanol synthesis reaction over $Cu/ZnO/Al_2O_3$ catalysts is not fully understood. A possible set of mechanisms, described by Kung[2] in his review on methanol synthesis were presented in the Introduction.

Klier et al[80,81] suggested that a Cu(1) solution in ZnO formed an active component in the $Cu/ZnO/Al_2O_3$ catalyst. They proposed an initial mechanism whereby the Cu(I) centres non-dissociatively chemisorbed and activated CO, and the ZnO centres activated hydrogen. The reaction proceeded via a series of hydrogenation steps to form methanol. Klier et al[82] have also found that the presence of CO_2 in the reaction gas mixture increases the catalyst activity. The presence of the CO_2 is thought to be as a reaction promoting role, because for a reaction mixture of CO_2 and H_2 only the methanol synthesis reaction is heavily retarded. It has been found that in the absence of CO_2, catalyst deactivation is rapid. However, by gradually replacing the CO by CO_2, a maximum methanol synthesis rate is achieved. In addition the rate of deactivation is also drastically reduced by increasing the amount of CO_2 present. On further replacement of CO by CO_2, however, the rate of methanol production decreases again. The optimum syn-gas ratio was found to be 2/28/70 by volume for CO_2, CO and H_2 respectively. Klier et al have attributed the promotion role of CO_2 to its ability to keep the catalyst in the intermediate oxidation state (i.e. to maintain

the Cu(I) active centres), because it is able to re-oxidise any Cu(I) centres that have been reduced to copper metal. In the absence of CO_2 the authors interpreted the deactivation of the catalyst to the reduction of the Cu(I) centres to copper metal because of the presence of the H_2/CO reducing atmosphere. At high concentrations, the CO_2 essentially acts as a poison, because it does not take part in the methanol synthesis reaction itself, but it is adsorbed on the catalyst.

The other important aspect of Cu/ZnO catalysis, as mentioned in the Introduction, is the possible formation of α-phase brass in the Cu/ZnO catalyst by the reduction of the ZnO, and the subsequent dissolution of the resulting zinc in the copper phase. Herwijnen and De Jong[9] showed that thermal treatment of Cu/ZnO shift catalysts in a reducing atmosphere caused a decrease in the BET surface area and they detected brass formation by the use of X-ray diffraction. The treatment used by the authors in their catalyst was firstly a standard reduction procedure, using a 5% by volume hydrogen in nitrogen reducing gas at $\sim 200^{\circ}C$. The second part of the treatment involved raising the reduction temperature and conditioning with a hydrogen stream containing 1 or 100 ppmv of water. At a reducing temperature of $300^{\circ}C$, it was found that the BET area decreased significantly and at the same time, the XRD results showed that brass was present in the catalyst. The authors found that the brass phase could contain anything up to 8% zinc, and that the amount of brass formed at $300^{\circ}C$ could be varied by having differing amounts of water present in the reducing gas as trace

quantities. This can be illustrated by considering the thermodynamics of brass formation. In their paper, Herwijnen and De Jong showed that it was thermodynamically possible to form α-brass via the following reaction :

$$yCu + ZnO + H_2 \rightleftharpoons \alpha\text{-}Cu_yZn + H_2O \qquad (2.6)$$

The equilibrium composition of the zinc in the brass formed by the reduction of ZnO increased with increasing temperature. The equilibrium also moved to the right of equation (2.6) for increasing ratios of the partial pressure of hydrogen to the partial pressure of water (P_{H_2}/P_{H_2O}). For example, at 300°C and P_{H_2}/P_{H_2O} = 1000, it was thermodynamically possible to form a brass containing 10% zinc. The effect of temperature and the ratio P_{H_2}/P_{H_2O} on the formation of brass is illustrated in Figure 2.3. It was found experimentally that increasing the P_{H_2}/P_{H_2O} ratio resulted in an increase in the amount of zinc in the brass phase - this is in agreement with the thermodynamics of the system. The authors came to the conclusion that the observed amount of dissolved zinc in copper would be lower than that predicted thermodynamically, because the diffusion of zinc in the copper rich phase would be rate-limiting at 250-300°C.

After treating to form brass, the catalysts were activity tested to find out how the brass formation affected the rate of CO conversion in the shift reaction. It was found that a dramatic de-activation occurred following brass formation with a significant zinc content. Although the BET area decreased

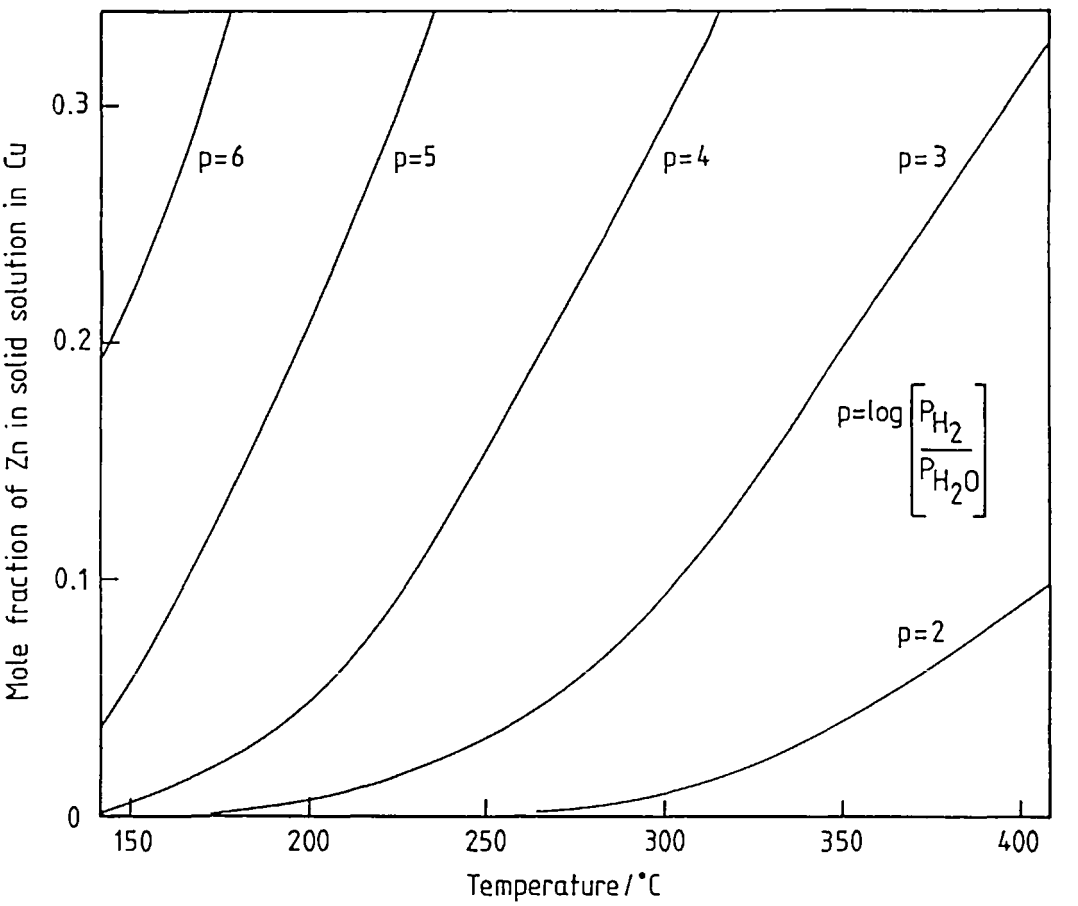


Figure 2.3. Equilibrium composition for the reaction $y\,Cu + ZnO + H_2 \rightleftharpoons \alpha Cu_y Zn + H_2O$ [9]

during the thermal treatment, Herwijnen and De Jong could not account for the continuing decline in activity with increasing zinc content brass from BET area losses alone. They came to the conclusion that the presence of brass had a strong negative affect on the activity of the shift reaction.

To date, no reports have been made as to how brass formation in Cu/ZnO catalysts affects their activity towards methanol synthesis. This is an experiment which was carried out in this work, and the results are presented in Chapter 8.

CHAPTER 3

THE PRINCIPLES OF PHOTO-ELECTRON SPECTROSCOPY AND TEMPERATURE PROGRAMMED DESORPTION

3.1 Photo-Electron Spectroscopy

In the last ten years or so, the application of photo-electron spectroscopy (PES) has been extensively developed. This development has made PES an important tool in the understanding of reactions at solid surfaces and has a significant role to play in catalysis research[55,83-85]. The technique enables the solid surface both in a clean state and with an adsorbed layer to be probed at an atomic level. Much of the pioneering work on electron spectroscopy was done by K. Siegbahn and his various co-workers[86]. Since then much work has been done on the adsorption of a variety of gases on different solid surfaces, so that details of bonding for example could be determined.

3.1.1. The principle and types of Photo-Electron Spectroscopy

In a photo-electron experiment, a sample (either gaseous, liquid or solid) is exposed to monochromatic electro-magnetic radiation. If the energy of this radiation is high enough, it will ionise the atoms in the sample. The ionisation causes a photo-electron to be emitted. This electron will be ejected with a particular kinetic energy which depends on the energy of the exciting radiation and the binding energy of the electron as given below :

$$E_K = h\nu - E_B \qquad (3.1)$$

where E_K is the kinetic energy of the electron emitted
E_B is the electron binding energy
$h\nu$ is the energy of the exciting radiation.

A plot of the number of electrons emitted against electron kinetic energy gives the photo-electron spectrum. In most cases, electron binding energy is used rather than electron kinetic energy for recording spectra. As most atoms have electrons in several different discrete energy levels, there will be a kinetic energy distribution made up of a series of peaks in the photo-electron spectrum reflecting the electronic structure of the sample. In practice, the kinetic energies of photo-electrons are detected by an electron analyser (spectrometer).

There are two types of photo-electron spectroscopy. X-ray photo-electron spectroscopy (XPS) uses, as the name suggests, an X-ray source to excite the electrons in a sample. Typically, the excitation energy is around 1-2KeV. At this energy it is possible to excite both the core and valence levels of atoms in a sample. However, the valence peaks are difficult to obtain in practice because they have a low photo-ionisation cross-section. XPS can be used to identify elements in a substance as each element has a characteristic set of binding energies. It can also be used to quantify an effective sample composition (as would be required for the study of surface segregation), and to determine chemical shifts of adsorbates on solid surfaces

which can give information of the nature of adsorption (see section 3.1.5).

The second type of photo-electron spectroscopy is ultra-violet photo-electron spectroscopy (UPS), which uses a U.V. radiation source of up to 40eV, depending on the type. UPS is used to study the valence levels of solids and gases and an important use of the technique is for the study of adsorbates on solid surfaces.

3.1.2 Photo-electron spectrometer

If the photo-electron spectrum of the gas phase is being measured then equation (3.1) applies with $E_B = E_B^V$, where E_B^V is the electron binding energy referred to the vacuum level. In a gas experiment, an electron at rest in the vacuum is the reference for zero energy[85]. However, for solids the situation is more complicated[83, 85, 87] because a certain amount of energy, the work function, is required to remove a photo-electron from the solid to the vacuum level. An energy level diagram for a conducting (metallic) sample, shown in Figure 3.1, illustrates this point. In most PES instruments, the sample and the spectrometer (electron-analyser) are electrically connected, so that the Fermi levels of both the sample and the spectrometer are equal at equilibrium. This is the system shown in Figure 3.1. The sample vacuum level, ϕ_{sa}, is not a convenient reference point for zero binding energy point in a conducting solid, because it varies from sample to sample, since

the work function is not necessarily the same for different samples. A convenient binding energy reference point is the Fermi level of the sample. If the sample and spectrometer are connected electrically, then the binding energies of the core levels in the sample w.r.t. the Fermi level can be determined without knowing the work function of the sample itself, as illustrated in Figure 3.1. It can be seen that the binding energy w.r.t. to the Fermi level (BE_F) is related to the spectrometer work function, ϕ_{sp}, and the measured electron kinetic energy (E_K). This is shown below in equation (3.2) :

$$BE_F = h\nu - E_K - \phi_{sp} \qquad (3.2)$$

where $h\nu$ is the energy of the incident radiation.

The spectrometer work function can be assumed to be constant from experiment to experiment for a particular electron analyser. The spectrometer work function can be determined by measuring the kinetic energy of a strong photo-electron peak of a sample where the binding energy of that peak is well known and tabulations are available[88,89]. Hence, once the spectrometer work function has been found, it is possible to determine binding energies in any sample with a common reference point.

3.1.3 Inelastic mean free path

Photo-electrons produced by the ionisation of atoms in a sample have to travel through the sample until they reach the vacuum. In travelling through a material, some of these electrons will suffer inelastic collisions with locally

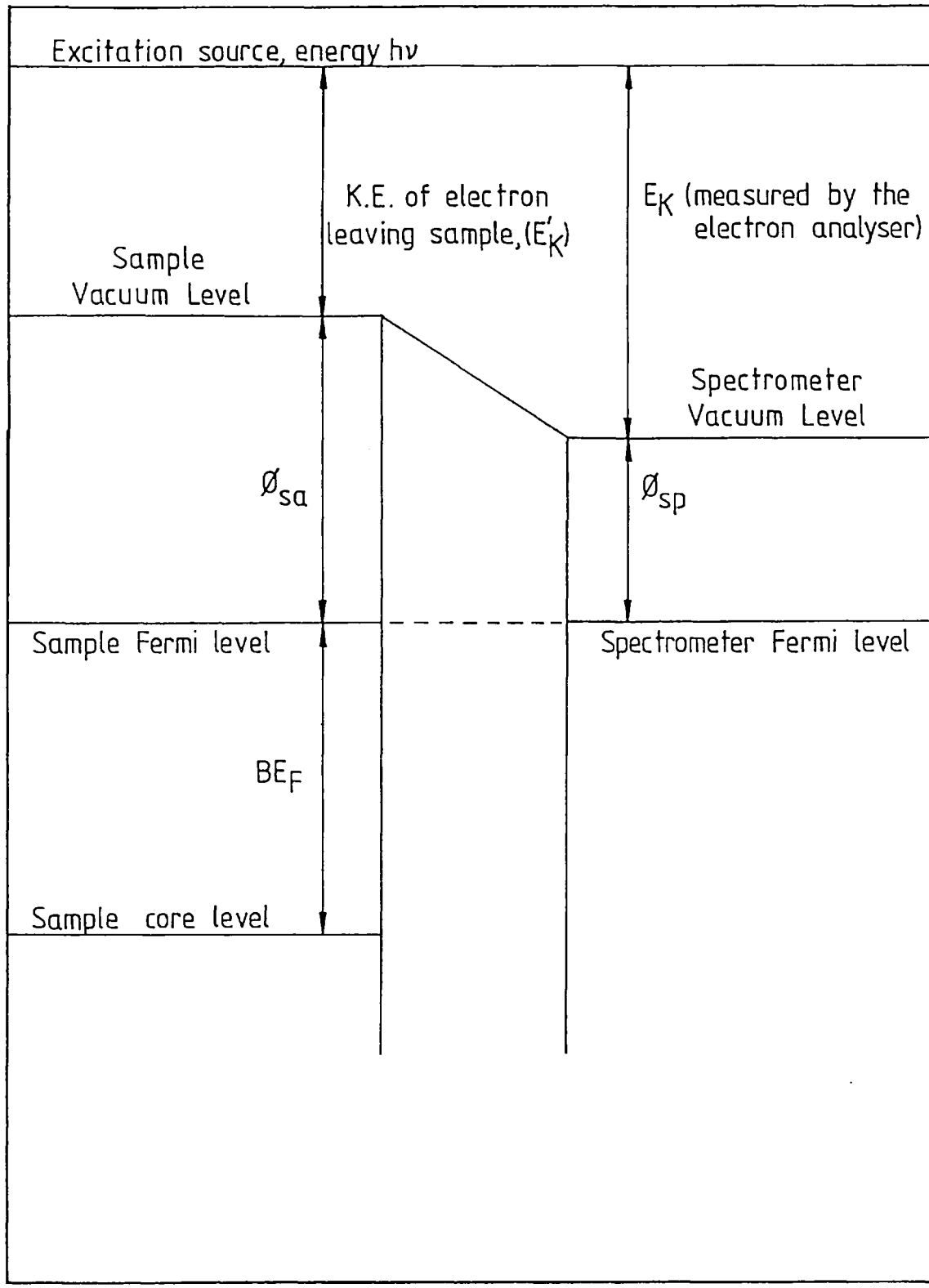


Figure 3.1. Energy level diagram for a conducting sample in a photoelectron spectrometer, with the sample in electrical equilibrium with the spectrometer (note: $\emptyset_{sa}$ is much exaggerated compared with BE_F)

bound electrons. These collisions will result in a loss of kinetic energy of the photo-electron. This effect is not significant in gas phase photo-electron spectroscopy. However, for solid samples, the density of the constituent atoms is very much greater than that of the gas phase, and the effect of inelastic collisions becomes very significant. In a solid a photo-electron will only travel a very short distance before experiencing an inelastic collision which is in the order of angstroms. The effect of the IMFP can be represented mathematically as follows.

If $I_o(x,E)$ is the total PE flux with a kinetic energy, E, originating at a depth, x, below the surface, then the flux of photo-electrons $I(x,E)$ emerging at the surface with kinetic energy, E, which originated at a depth, x, is given by the following expression[90] :

$$I(x,E) = I_o(x,E) \exp(-x/\lambda(E)) \qquad (3.3)$$

The term $\lambda(E)$ in equation (3.3) is referred to as the inelastic mean free path (IMFP) of an electron with a kinetic energy,E. This term is also known as the mean electron escape depth or the attenuation length. The IMFP represents the depth from which 1/e of the photo-electrons produced at that depth escape from the solid surface with the same kinetic energy.

The IMFP of an electron is a function of both the electron kinetic energy and of the sample material. The dependence of the IMFP on kinetic energy is not monotonic, but goes through a minimum at an electron kinetic energy of approximately 100eV.

A generalised curve showing this dependence for all of the elements is presented in Figure 3.2. IMFPs have been determined experimentally for most elements over the energy range 10-2000eV. Indeed, Seah and Dench[91] have used experimental IMFPs to form a universal curve to predict IMFPs at different kinetic energies for different elements. Attempts were made by Penn[92] to theoretically predict IMFPs but the accuracy of these results is unclear.

As a consequence of the inelastic scattering of electrons in a solid, the photo-electron spectrum will be made up of peaks superimposed on a significant background. This background results from electrons emerging from the surface with a distribution of energies following differing extents of inelastic collisions, and originating with different kinetic energies. As the kinetic energy is decreased the recorded background signal from the PE spectrum increases because more electrons can emerge with a lower kinetic energy. This background has to be subtracted out before peaks can be used in a quantitative manner.

The most important consequence of the IMFP is the fact that only electrons originating from a relatively short depth below the surface will escape from the solid sample and form a photo-electron spectrum. As can be seen from Figure 3.2, typical IMFPs range from a few angstroms to about 20Å for electron kinetic energies between 10 and 2000eV. These distances respresent up to only approximately 10 monolayers, so photo-electron spectroscopy is a surface sensitive technique. The surface sensitivity of the technique increases with decreasing kinetic energy (down to ~100eV). Any photo-electron peaks made

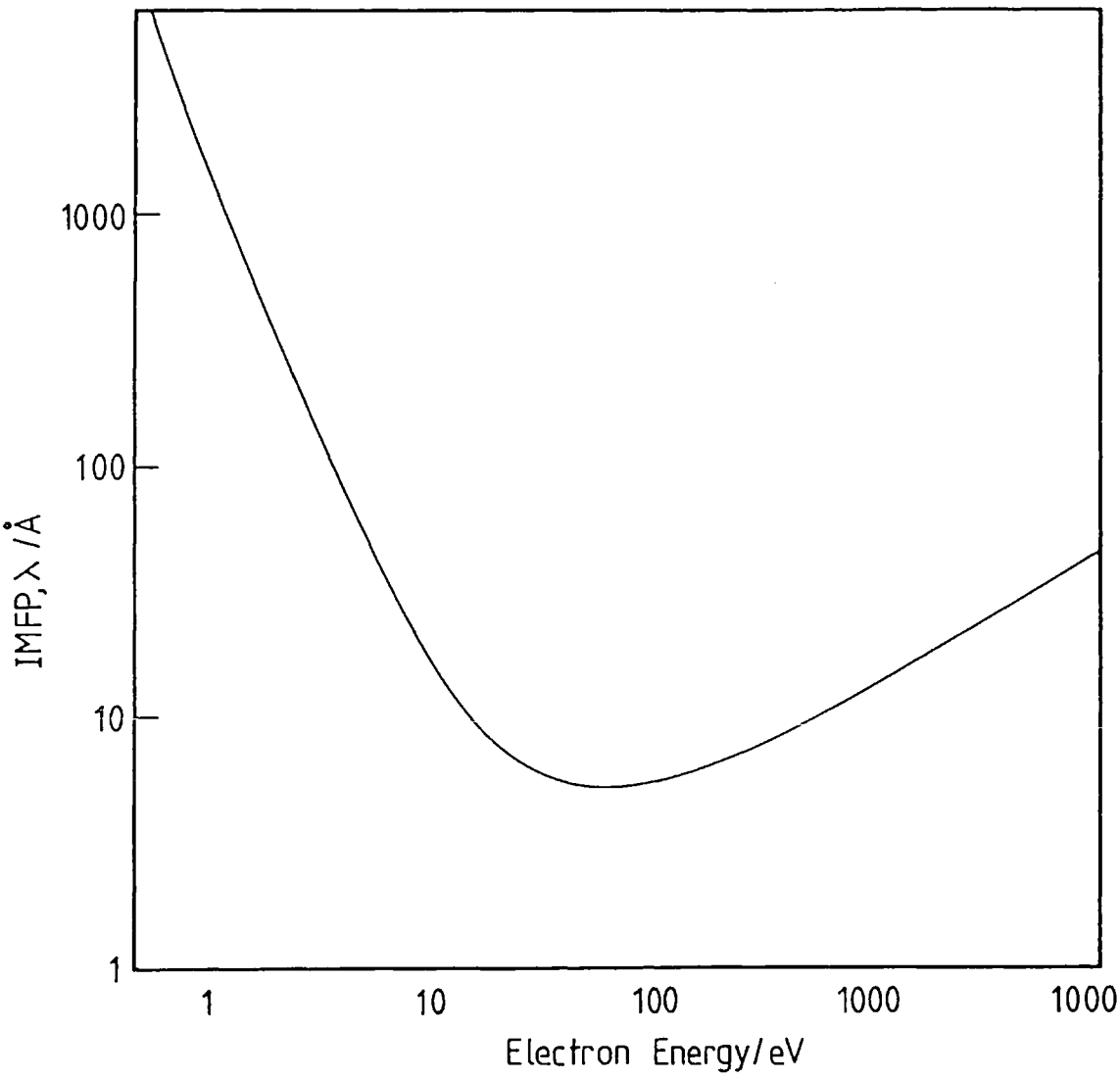


Figure 3.2. A typical curve illustrating the dependence of the IMFP on electron energy

up from electrons with a kinetic energy of ~100eV will be representative of the top 2 or 3 monolayers of the sample only, and will be principally composed of electrons from the surface layer. Even at kinetic energies of around 1000eV, photo-electron peaks will only be representative of the top 10 monolayers (approximately). Consequently, photo-electron spectroscopy has become an important tool in the field of surface science.

3.1.4 The use of XPS for quantitative analysis

The peak intensities obtained from a photo-electron spectrum can be used for quantitative analysis. For example, in this work, peak intensities are used to determine the surface composition of an alloy sample. The photo-electron peak intensity can be related to parameters associated with the sample and of the instrument, as shown below[93]:

$$I_j(x) = \frac{K\sigma_j N_j}{S_j} \qquad (3.4)$$

where $I_j(x)$ is the intensity of photo-electron j, originating at a depth, x,

N_j is the number of j atoms per unit volume

σ_j is the photo-ionization cross-section of atom, j,

S_j is the total photo-electron scattering coefficient

K is an instrument response function.

The photo-electron scattering coefficient for most XPS applications is inversely related to the IMFP. An expression was developed by Powell[94] which related the photo-electron peak intensity to parameters associated with the sample and with the instrument and is shown below :

$$I(E_A,x) = I(h\nu)N_A\sigma_A(h\nu,x)\alpha_A(E_A)H(E_A,E) \qquad (3.5)$$

where $I(E_A,x)$ is the measured intensity of photo-electrons from atoms of species A, with kinetic energy E_A, originating at a depth of, x,

$I(h\nu)$ is the X-ray flux incident on the sample, with a characteristic energy, $h\nu$,

N_A is the density of species A in the sample

$\sigma_A(h\nu,x)$ is the photo-ionization cross-section of atoms of species A, as a function of incident radiation energy and depth.

$\alpha_A(E_A)$ is a function involving the IMFP

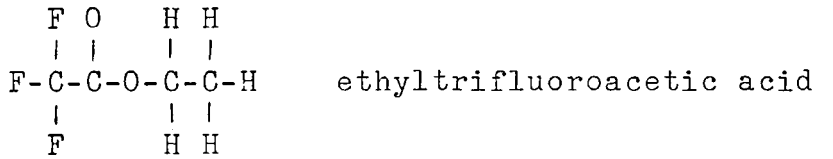
$H(E_A,E)$ is a function involving the analyser transmission function, the detector efficiency and the extent of electron retardation in an analyser with pass energy, E.

The term $H(E_A,E)$ represents the instrument response function.

Another application of XPS is the analysis of the amount of a material which is adsorbed on a substrate. In addition to being able to obtain a photo-electron spectrum of a solid sample, it is also possible to obtain a spectrum from the adsorbed material. This is important in the study of metal overlayers on a substrate (see Briggs[93] and Seah[26] for example) and in the chemisorption of gases on metal surfaces because it allows the extent of the coverage to be determined.

3.1.5 The Chemical Shift

An important qualitative aspect of XPS which has become important in the study of adsorption is a phenomenon known as the chemical shift. It was found by Siegbahn[86] that the binding energy of an electron in a given level was dependent on the chemical environment of the atom from which the electron originated. For example, an X-ray photo-electron spectrum of ethyltrifluoroacetic acid, obtained by Siegbahn and co-workers, produced four different binding energies for electrons originating from the Cls level over a range of approximately 9eV. There are four carbon atoms in this molecule and each carbon atom is in a different chemical environment. The molecule is shown below to illustrate this :



ethyltrifluoroacetic acid

The chemical shift is reviewed by Orchard[90].

3.1.6 Relaxation

The chemical shift does not necessarily account for binding energy changes between molecules in the gas phase and adsorbed molecules. A process known as relaxation can also cause a binding energy shift. This process increases the kinetic energy of electrons surrounding a core-hole because these electrons are polarised towards the hole. It has been suggested that relaxation due to adsorption may alter binding energies of adsorbates by up to 3eV compared with the gas phase[83].

3.1.7 Shake-Up

A process known as shake-up can create additional peaks in photo-electron spectra. These result from valence electrons being excited to higher energy levels and the additional energy being lost to the photo-electron[83]. Shake-up peaks can appear in photo-electron spectra for adsorbates, and it has been suggested that the two higher binding energy peaks in both the C1s and O1s spectra for CO on a copper surface are both shake-up satellites. Consequently, care needs to be exercised in the interpretation of multiple peak structures from adsorbed species. The shake-up process is described in more detail in the literature[40].

3.1.8 The use of UPS

As stated previously, ultra-violet photo-electron spectroscopy can be used to study valence bands and can be used to help the

understanding of surface bonding, and as a method of finger-printing adsorbed species. Shifts also occur in the UPS spectrum on changing the adsorbate from the gas phase to an adsorbed phase, and different shifts occur again for different chemical situations and/or from relaxation effects. In practice, the UPS spectrum for an adsorbate is compared with that for the gas phase and orbital assignments are made for each peak in the adsorbate spectrum based on this comparison (e.g. 4σ, 1π, 5σ orbitals may be assigned to the peaks)[55]. As a finger-printing method for surface species, UPS can be very useful. It has been shown that intermediates have characteristic spectra which do not change appreciably from surface to surface[55]. The importance of this is that once an adsorbed or intermediate species has been identified on a surface by some technique, a characteristic UPS spectrum can be obtained for that particular state, and hence used to identify the state if the characteristic spectrum appears in any other work. An example of this is the adsorption of methanol on a Cu (110) surface[71].

3.2 Temperature Programmed Desorption

In recent years, the technique of thermal desorption has become a very important additional tool in the study of adlayers on various surfaces in relation to catalysis[30, 55, 95, 96]. The technique can be used to measure surface concentration and any differences in adsorption states that may exist on adsorbing single simple gases (e.g. CO, H_2). More importantly, the technique can be used to identify any surface intermediates

that may be formed following adsorption of two or more gases or of more complex molecules by observing the species which desorb during a desorption run (e.g. the formation of a formate after adsorption of formic acid on Cu (110) - the intermediate desorbed as CO_2 and H_2 in the appropriate ratio[56, 75]). The results of the technique, if analysed carefully, can also be used to determine the kinetics of desorption processes. This ability to obtain kinetic information and to identify possible surface intermediates is very important in the elucidation of reaction mechanisms involved in catalytic processes.

The principle behind thermal desorption is that after creating an adlayer by adsorption of a species at a given temperature, the sample is heated and at a characteristic temperature, the adlayer desorbs from the surface forming a "pressure burst". This pressure burst, if detected as a function of temperature forms the desorption spectrum. To obtain a successful desorption spectrum, the adsorption temperature must be well below the desorption temperature. The most common way to create a thermal desorption spectrum is to monitor the pressure burst caused by raising the temperature of the sample with the adsorbed layer with an ion gauge or with a mass spectrometer. The temperature is normally raised in a programmed manner (this method is usually referred to as temperature programmed desorption, or TPD) which makes analysis of the results easier - see section 3.2.1. An experimental method to obtain thermal desorption spectra is described in Chapter 4.

3.2.1 Theory and Analyses

The desorption process can be described by a Polyani-Wigner (Arrhenius) type equation[95, 98]:

$$\frac{d\sigma}{dt} = k_d\sigma^n = \nu\sigma^n \exp(-E_d/RT) \qquad (3.6)$$

where σ is the surface concentration of the desorbing species

$\frac{d\sigma}{dt}$ is the rate of desorption

ν is the pre-exponential or frequency factor

E_d is the activation energy for desorption

n is the order of desorption

The rate of desorption can also be related to the pumping speed of the system[95,98]:

$$-\frac{d\sigma}{dt} = \frac{V}{AkT}\frac{dp}{dt} + \frac{p}{\tau} \qquad (3.7)$$

where A is the sample area

V is the volume of the system

τ is a characteristic pumping time, $\tau = V/S$

S is the pumping speed of the system

If the characteristic pumping time is high, the pumping speed S is low and the desorption rate is proportional to the rate of change of pressure. However, if the pumping speed is high so that $P/\tau >> dP/dt$, then the desorption rate is conveniently

proportional to the pressure change through desorption. Ehrlich[97] used the former method in his pioneering work on directly measuring kinetics of desorption. He used a "flash desorption" technique with a very rapid sample heating rate of approximately 10^3K/sec. Redhead[98] on the other hand developed the first full analysis of desorption spectra obtained in high pumping speed equipment, so that the reaction order, activation energy for desorption and the pre-exponential factor could be determined. Redhead's analysis used heating rates in the order of 1-10K/sec, unlike that of Ehrlich. As it is proposed to carry out the desorption experiments in this work with a heating rate of approximately 1K/sec with a high pumping speed instrument, the analysis by Redhead will be reviewed.

From equation (3.6) it can be seen that the desorption rate increases with temperature, but decreases with surface coverage. During a thermal desorption run, the desorption rate will therefore pass through a maximum. By considering the maximum rate of desorption, a relation can be established between the activation energy for desorption (E_d), the pre-exponential factor (ν) and the temperature at which the desorption rate is a maximum (T_{max}). This relation is found by taking the derivative of the desorption rate w.r.t. time and setting the derivative equal to zero. If a temperature programme is used such that the temperature can be determined at a time, t, then the relation can be found easily. The most commonly used temperature programme is a linear one, of the form :

$$T(t) = T_o + \beta t \qquad (3.8)$$

where $T(t)$ is the sample temperature at time, t,

T_o is the initial temperature

β is the heating rate in K/sec

In this work, a linear heating rate was used in the experiments and will therefore be incorporated into the analysis. The relation between the activation energy of desorption, the pre-exp. factor and T_{max} is given by :

$$\frac{E_d}{RT_{max}^2} = \frac{\nu}{\beta} \exp(-E_d/RT_{max}) \text{ for a 1st order process} \quad (3.9)$$

$$\frac{E_d}{RT_{max}^2} = \frac{2\sigma_m \nu}{\beta} \exp(-E_d/RT_{max}) \text{ for a 2nd order process} \quad (3.10)$$

$$= \frac{\sigma_o \nu}{\beta} \exp(-E_d/RT_{max})$$

where σ_o is the initial coverage

σ_m is the coverage at T_{max}

The relations are derived by assuming that E_d and ν are coverage independent. It can be seen that for a first order process T_{max} is independent of coverage, whilst for a second order process a desorption peak will shift to a lower T_{max} on increasing the initial surface coverage. These are important in the initial identification of orders of desorption (see also section 3.2.3). If a process is known to be first order, then an estimate of the activation energy can be made if a value

of 10^{13} is assumed for the pre-exp. factor[95, 98].

Redhead presented a method of obtaining the activation energy without assuming a value for the pre-exp. factor. For a first order peak, this is done by using a relation derived from the manipulation of equation (3.9):

$$\frac{E_d}{RT_{max}} + 2 = \frac{d(\log \beta)}{d(\log T_{max})} \qquad (3.11)$$

The method involves varying the heating rate, and plotting log β against log T_{max}. Use of equation (3.11) gives E_d, and back-substitution in equation (3.9) gives the pre-exp. factor. Redhead suggested that the heating rate should be varied by at least two orders of magnitude to give reliable results.

For a second order process, a plot of log $(\sigma_o T_{max}^2)$ against log $(1/T_{max})$ is made which should result in a straight line of slope E_d/R hence giving the activation energy. Backsubstitution of E_d in equation (3.10) gives the pre-exp. factor.

3.2.2. Some More Recent Methods of Analysis

Since Redhead's analysis, more recent analyses have been developed which overcame some of the difficulties encountered by using Redhead's method. The difficulties are revealed during the course of this section.

Falconer and Madix[99] produced a method of obtaining the activation energy without previous knowledge of either the pre-exp. factor or the desorption order by using equation (3.6). They replaced the σ^n term with $g(\sigma)$, where $g(\sigma)$ is an arbitrary, non-negative expression for the desorption rate dependence on surface coverage , and found that :

$$\ln(\beta/T_{max}^2) = \ln\left[\frac{R\nu}{E_d}\left[\frac{dg(\sigma)}{d\sigma}\right]_{T_{max}}\right] - (E_d/RT_{max}) \qquad (3.12$$

By plotting $\ln(\beta/T_{max})$ against $(1/T_{max})$ for a series of heating rates, a straight line of slope $(-E_d/R)$ is obtained hence giving E_d. The authors preferred this method of analysis to that of Redhead as they came to the conclusion that the method of Redhead described above did not result in straight line being formed, as the slope is dependent on T_{max} and as a result, an accurate determinatation of E_d was made very difficult.

Falconer and Madix presented a second method of obtaining E_d. This second method used a series of desorption curves obtained using a variety of heating rates but with the same initial surface coverage in each case. This method was devised in case the heating rates were unknown. By putting $N = -d\sigma/dt$, equation (3.6) could be used to derive the equation below (at the peak maximum) :

$$\ln(N_{max}) = (\nu g(\sigma_{max})) - (E_d/RT_{max}) \qquad (3.13)$$

where N_{max} is the height of the desorption peak at its maximum.

A plot of N_{max} against $1/T_{max}$ gives a straight line with slope $(-E_d/R)$ providing σ_{max} is independent of the heating rate. This method and the one involving $g(\sigma)$ above have been used successfully by the authors giving excellent agreement where tested.

Another method of analysis has been devised to obtain E_d without knowledge of the pre-exp. factor. This method used the height and area of the desorption peak to determine E_d and is described below :

$$\text{Rate of desorption} = N = -\frac{d\sigma}{dt} = \nu\sigma^n \exp(-E_d/RT) \qquad (3.14)$$

$$= k_d \sigma^n$$

The peak height is proportional to the desorption rate N. At a given temperature T, the coverage is proportional to the area under the desorption curve to the right of the temperature T.

Mathematically : $N = K_1 (Ht)$ (3.15)

$$\sigma = K_2 A \qquad (3.16)$$

where Ht is the peak height at temperature T

A is the coverage at temperature T

K_1, K_2 are constants of proportionality

In the case of a first order peak, by substituting (3.15) and (3.16) into equation (3.14) the following expressions are obtained :

$$K_1(Ht) = K_2 A\nu \exp(-E_d/RT)$$

$$\frac{K_1(Ht)}{K_2 \quad A} = \nu\exp(-E_d/RT)$$

$$\ln \frac{K_1}{K_2} + \ln \frac{(Ht)}{A} = \ln\nu - (E_d/RT)$$

$$\ln \frac{(Ht)}{A} = \ln Z - (E_d/RT)$$

where Z is $\frac{(K_2\nu)}{K_1}$

A plot of ln (Ht)/A against 1/T gives a straight line of slope $(-E_d/R)$.

This method is solely a lineshape analysis at one initial coverage and for a single heating rate. Its disadvantage is that the order of desorption must be known.

In all the methods of analysis described so far, it has been assumed that the activation energy E_d has been independent of coverage. This is the ideal case but is not always so in practice. Coverage dependent activation energies in first order desorption spectra result in a change in the position of T_{max} with changes in the initial coverage[95,98].

In a separate paper, Falconer and Madix[100] presented a novel method of analysing desorption spectra which used desorption rate isotherms. This method could show any dependence

of activation energy on coverage and give a quantitative determination of this effect. Furthermore, the method could give the order of the desorption process.

The desorption rate isotherm method requires a series of desorption spectra taken with the same heating rate but with different initial coverages. On each of the resulting spectra, the amplitude at a temperature T (this is proportional to the desorption rate N) and the area under the desorption curve to the right of that temperature T (this is proportional to the coverage at temperature T) are both measured. This process is repeated at several different temperatures so that a plot of ln (Ht) against ln A (where (Ht) and A are defined previously) can be made at several different fixed temperatures. From manipulation of equation (3.6) it can be shown that these plots should have a slope n (the order). From the plot of ln (Ht) against ln A, at constant temperatures, a number of points are obtained for ln (Ht) as a function of temperature at a fixed coverage. These are plotted as ln (Ht) against 1/T and result in several straight lines each at different fixed coverage. The activation energy can then be obtained from the slope of these plots. If the slope of a plot at one coverage is different from that at a second coverage, then the activation energy is coverage dependent. If ln (Ht) against (1/T) has been plotted for several different coverages, then a quantitative determination of the coverage dependence of the activation energy can be obtained.

Many more analyses have been developed which take into account additional complications such as effects of the pumping speed, lateral interactions, and the effects of readsorption[76,101-105, 109, 134] but these will not be reviewed here.

3.2.3 Initial Interpretation of Desorption Spectra

In this section, some rules of thumb which can be employed in the initial interpretation of thermal desorption spectra[55] will be presented. As mentioned in 3.2.1, the order of a desorption process can be judged from the characteristics of the lineshapes obtained. The lineshapes associated with different order desorption processes have different shapes[119]. The zero order curve is characteristic in its rapid, almost instantaneous decay at T_{max}. The half order and first order desorption peaks are asymmetric. For the first order curve, the ratio of the area under the desorption curve to the right of the maximum to the total area is equal to 1/e. The second order curve is almost symmetrical.

The variation of lineshape position with initial coverage is a useful indicator of the order. First order processes exhibit desorption peaks that grow in magnitude with increasing dosage of adsorbate, whilst the position of T_{max} remains constant. In a second order process, the position of T_{max} will move to a lower temperature with increasing coverage.

Rough estimates of the activation energy in kcal/mol can be obtained from :

$$E_d = \frac{T_{max}}{16}$$

As mentioned earlier, by assuming a pre-exp factor of $10^{13} sec^{-1}$ it is possible to obtain another estimate of E_d using Redhead's relations between activation energy, pre-exp. factor and T_{max} (see 3.2.1).

CHAPTER 4

EXPERIMENTAL

4.1 Description of the UHV system

The majority of the experimental results obtained in this work were found using a Vacuum Generators ESCA3 instrument[106]. The ESCA3 is a dual chamber UHV system which has one chamber containing the electron spectrometer and a second chamber in which samples can be prepared. The samples themselves were mounted onto the end of a probe and transfer between the two chambers was achieved by horizontal translation of the probe using a linear drive system which was attached to the preparation chamber. Instrument probes are covered in more detail in the next section. The ESCA3 is illustrated in Figure 4.1. Pumping on this system was by oil vapour diffusion pumps, each chamber having its own pump so that the two chambers could be isolated from one another. The pumping system was capable of creating base pressures of the order of 10^{-10} torr in both chambers following bakeout of the instrument.

The sample preparation chamber had several accessories attached to it to enable experiments to be carried out. An AGS2 type argon ion gun was fitted for specimen cleaning (see section 4.4.1), and a tungsten filament was also available for sample heating, which was required for the purposes of cleaning, annealing to achieve segragation in the alloy samples (see section 4.4 and Chapter 5) and to obtain thermal desorption spectra (see section 4.3). A problem arose in that the filament had to be moved away from the sample before the probe could be

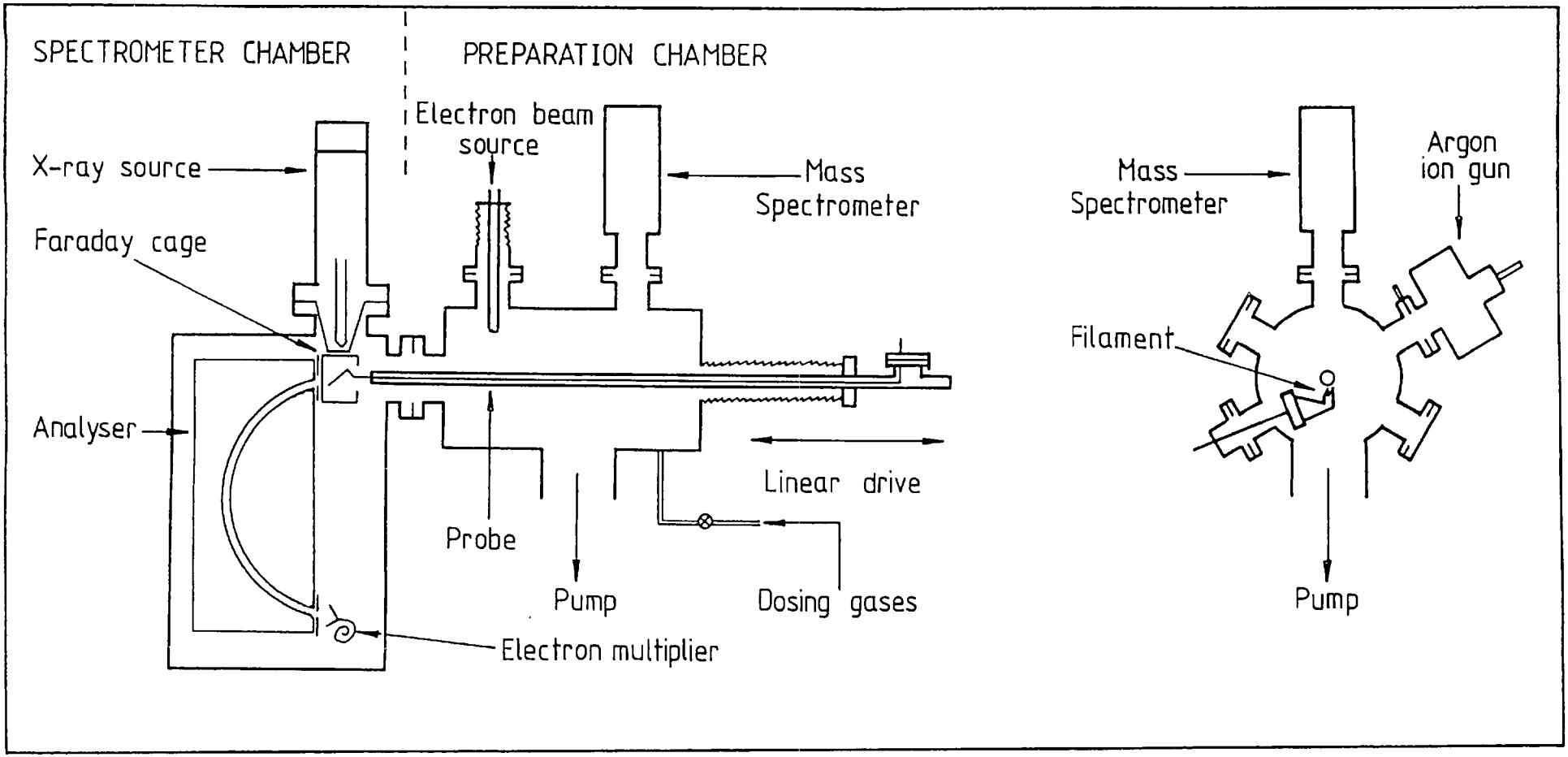


Figure 4.1. The ESCA3 instrument

moved to a different part of the instrument. This problem was easily overcome by mounting the filament on a wobble stick - this is discussed more fully in section 4.3. A Vacuum Generators Q8 mass spectrometer was fitted to the preparation chamber so that it was possible to monitor the composition of the residual vacuum and the gases being dosed on the sample and to detect desorbing species during thermal desorption experiments (see section 4.3). The relative positions of the sample heating filament and the mass spectrometer are discussed in section 4.3.

The spectrometer chamber had two principal excitation sources. Photons of energies in the region of 1.2-1.5KeV were derived from an X-ray gun mounted at 90° to the analyser entrance. The X-ray gun had two anode faces, one coated with magnesium (1253.6eV) and the second coated with aluminium (1486.6eV). The X-ray gun was differentially pumped using an ion pump. The second source was from a gas discharge U.V. lamp which was mounted at 90° to both the analyser entrance and the X-ray gun.

The electron analyser in the ESCA3 instrument was of the hemispherical type[107], with the electrons travelling through an angle of 150°. The analyser used a fixed transmission energy, so that it acted as a narrow energy pass filter, allowing through electrons which had a pre-selected kinetic energy. This pre-selected kinetic energy could be changed to give increasing resolution (decreasing the analysing energy increases the resolution). Electrons leaving the sample were not at the same

kinetic energy as the analyser, so some form of retardation was required to bring the electron kinetic energy to that of the analyser pass energy. This was achieved in the ESCA3 by applying a retardation voltage, R, between the sample and the electrical centre point of the electron energy analyser itself. The voltages on the two hemispheres of the analyser were arranged so that the electrical centre point was at earth potential. Whilst photo-electron spectra were being taken, the sample was held inside a Faraday cage which was electrically connected to the sample. This connection was used to make the Fermi levels of both the sample and the spectrometer equivalent, as discussed in Chapter 3, section 3.1.2. The electrical arrangement of the sample and the analyser is shown in Figure 4.2, and the Faraday cage and the analyser entrance are illustrated in Figure 4.3. In the ESCA3 system, a DVM was used to indicate the kinetic energy of an electron at the Fermi level of the sample, this energy being equivalent to $E_k + \phi_{sp}$, the measured kinetic energy and the spectrometer work function respectively in Figure 3.1 in Chapter 3. The measurement point for the DVM was across the retard potential, but as the retard potential did not take into account the analyser pass energy or the spectrometer work function, an additional voltage HV + W was injected in series with the DVM using the HV + W supply as shown in Figure 4.2. The voltage HV was equivalent to the analyser pass energy whilst W corrected for the work function. The DVM reading for the kinetic energy may not be accurate if the spectrometer work function drifts, unless the voltage W changes so as to compensate for these variations. However, the method used in this work to calibrate the binding

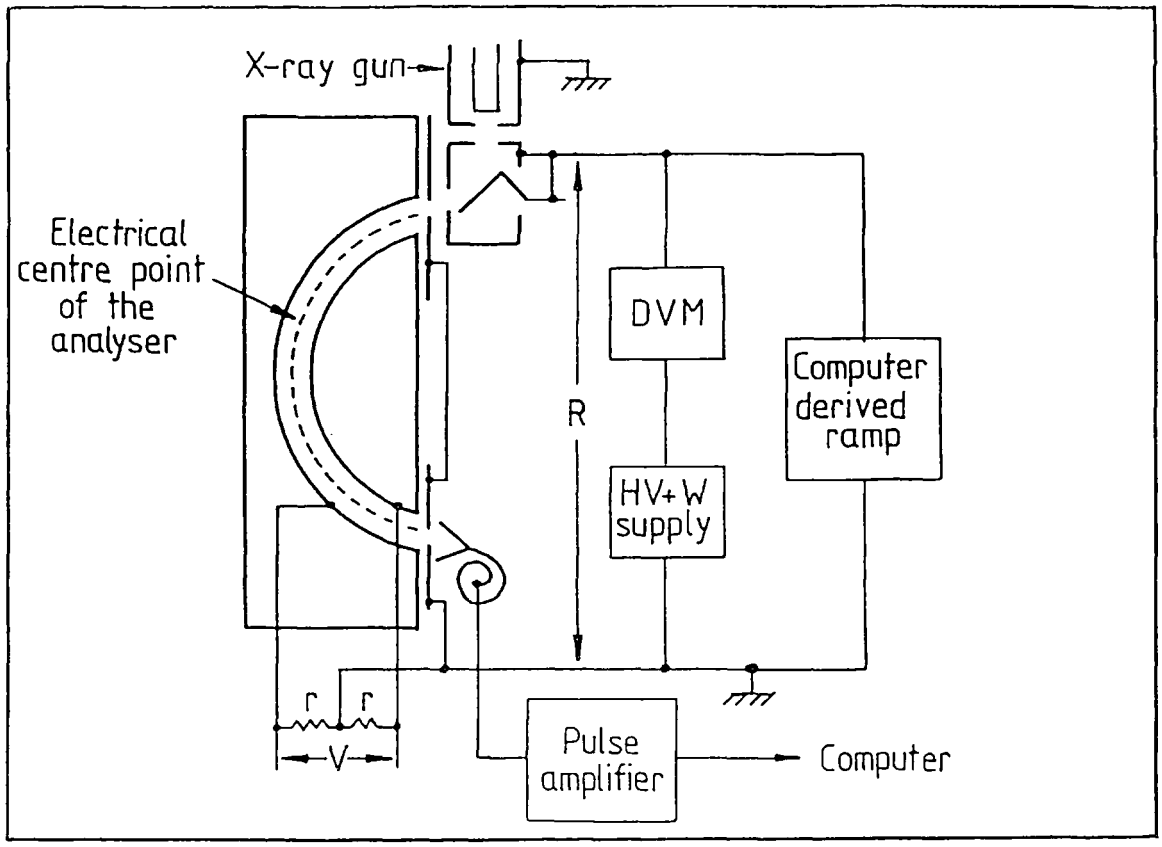


Figure 4.2. Electrical arrangement of the ESCA3 spectrometer

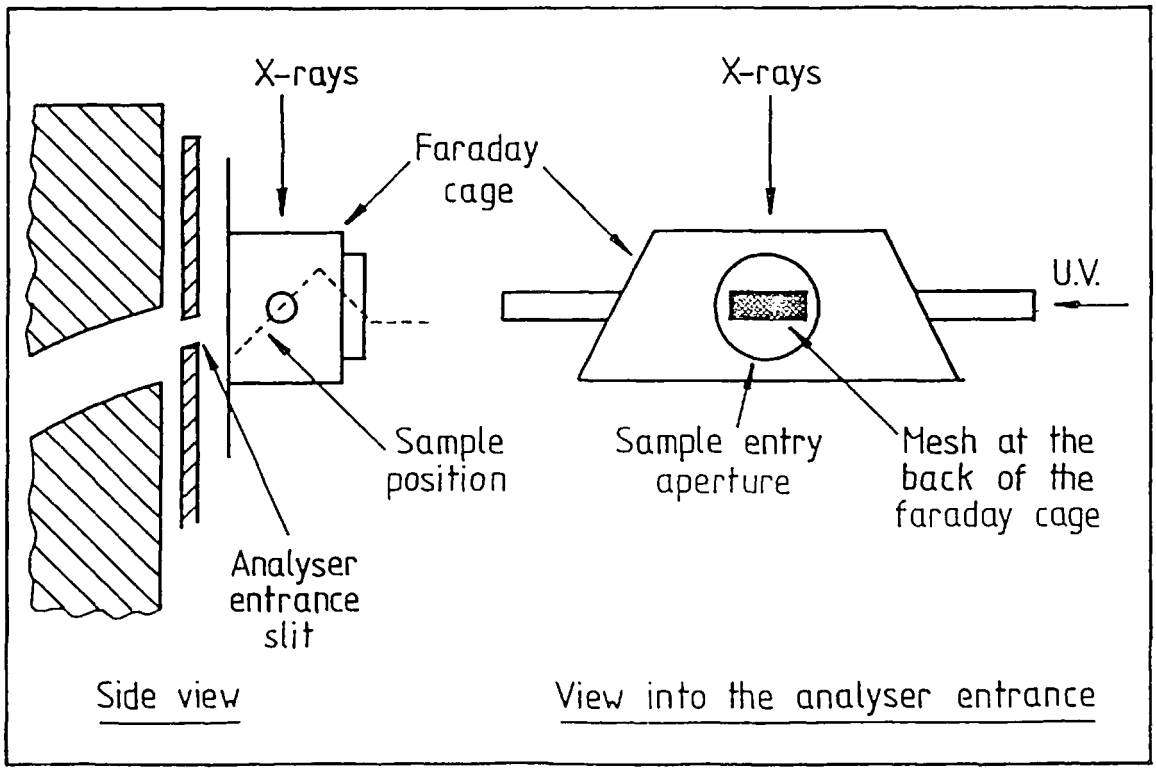


Figure 4.3. Configuration of the sample, analyser entrance and excitation sources

energy scale automatically eliminated possible work function drift as will become apparent below.

A photo-electron spectrum was obtained by using a voltage ramp between two set end points as the retard potential. The spectra were then stored digitally on a PDP8 computer, which allowed easy manipulation of the spectra. The DVM gave the kinetic energy range of the spectrum, and the binding energy scale was calibrated by measuring the kinetic energy of a peak with a well known binding energy. In this work, the $Cu2p_{3/2}$ peak was used to calibrate the binding energy scale, and this peak typically gave a kinetic energy of 322.35eV (±0.05eV) on the instrument DVM. The binding energy of the $Cu2p_{3/2}$ peak has been given as 932.8eV[88], giving an effective source energy of 1255.15eV (±0.05eV) which includes the spectrometer work function. The binding energy of other peaks could then be determined exactly by subtracting the measured kinetic energy from the effective source energy.

4.2 The high and low temperature probe

4.2.1 Design and Construction

As a consequence of the design of the ESCA3 having two separate chambers as described in section 4.1, any sample which was to be studied in the instrument had to be mounted at the end of a probe. In order to carry out segregation and thermal desorption studies on copper based samples, it was necessary

to use a probe where the sample temperature could be varied. A typical commercial temperature variable probe is illustrated in Figure 4.4.

The probe had to be of this type of construction to enable the sample to be transferred between the preparation chamber and the spectrometer chamber. The important aspects of construction other than that the probe matched the instrument geometry and sizes (e.g. the sample and its holder had to be small enough to fit into the Faraday cage in the spectrometer chamber) was that the sample had to have a direct electrical connection to a pin on the outside of the probe. This was necessary so that the retard potential could be applied to the sample.

This connection could be made in two ways. An insulated wire could be connected between the sample and the pin at the end of the probe with the sample and connecting pin being electrically isolated from the barrel of the probe. Alternatively, the sample could be directly attached to the barrel of the probe, to which the retard potential connection pin was also connected.

In order to carry out the planned experiments in this work, it was necessary to be able to reduce the sample temperature to as near liquid nitrogen temperature as possible so that the adsorption experiments could be carried out. It was also necessary to be able to heat the sample up to 500^{o}C to enable

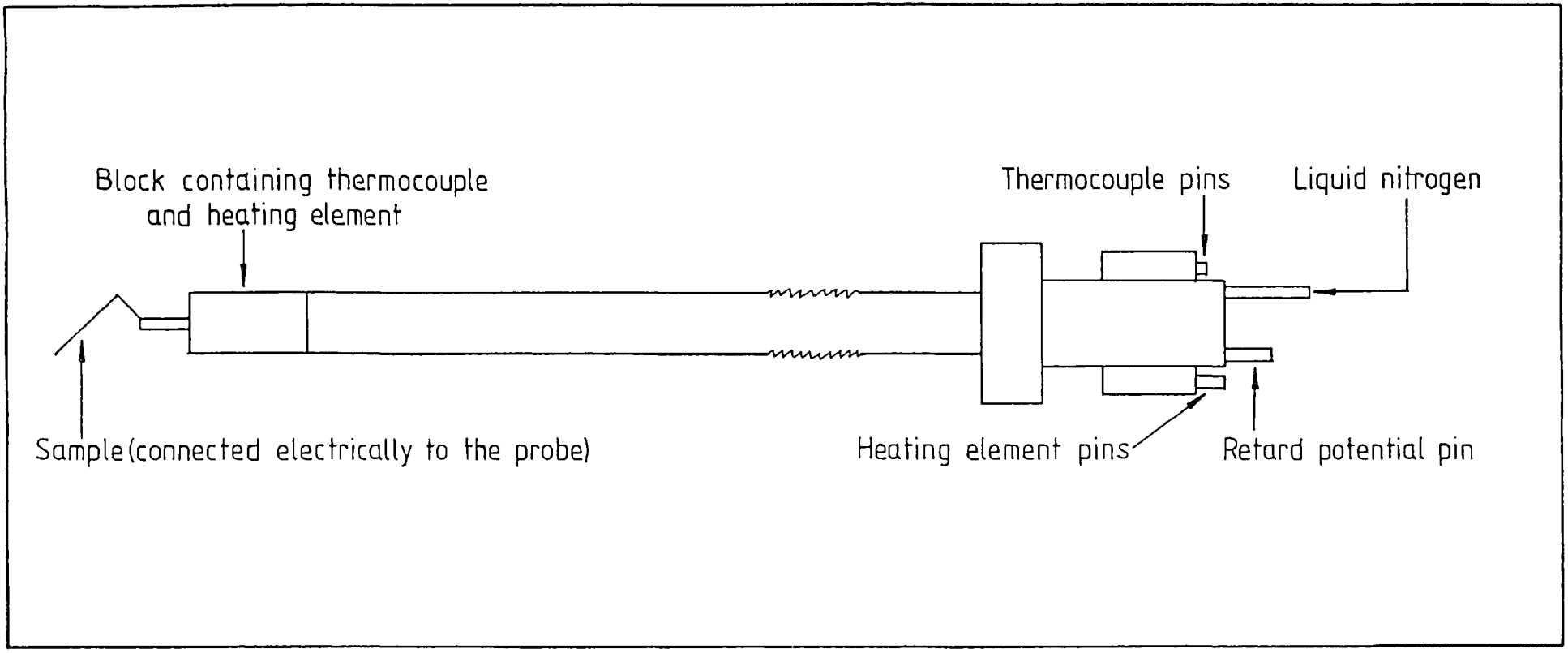


Figure 4.4. A typical commercial temperature variable probe

sample cleaning and the segregation and thermal desorption experiments to be carried out. The commercial probe could achieve these requirements, but it had some important disadvantages. The heating element was contained inside the end of the barrel of the probe. This design had a significant thermal inertia, as the barrel and the whole of the sample support was being heated, making it unsuitable for TPD or segregation studies. Another problem was that the sample temperature on the commercial probe was measured at the end of the barrel of the probe, adjacent to the heating element. This design resulted in a significant difference between the measured temperature and the real sample temperature. An experiment was carried out to determine the accuracy of the measured temperature on the commercial probe. The difference between the temperature measured by the probe and the actual sample temperature was found to be as high as 20-25^{o}C. This discrepancy was too great for accurate segregation or TPD studies.

It was decided to build a probe which was capable of achieving high and low temperatures with a low thermal inertia and with a system for measuring the sample temperature accurately. The former could be achieved by heating the sample directly using a tungsten filament, whilst the latter could be realised by attaching a thermocouple directly to the sample. Several constrainsts were placed on the design. As the probe moved through a horizontal range of approximately 0.5 metre, the thermocouple wires from the sample could not be taken directly

to a port on the preparation chamber. These wires had to go inside the barrel of the probe to feedthroughs at the other end. The major constraint was physical size. The probe could only have a diameter of 13mm, whilst the sample and its mounting assembly had to fit into the Faraday cage through a 12mm diameter hole. A further constraint was that the sample had to be electrically isolated from the main body of the probe in order to prevent high retard potential voltages appearing on the barrel and consequently a significant section of stainless steel work on the outside of the instrument also being at high voltage.

The final design of the probe is shown in Figure 4.5 and Figure 4.6 where its construction is illustrated. A 6mm O.D. stainless steel tube formed the cooling mechanism, and this tube was fitted through a FC19 comflat and welded to it to make a vacuum tight joint. The sample end of the cooling tube was blanked off again with a vacuum tight seal. The cooling tube was bolted to a FC19 T-piece, to which a set of feedthroughs were also attached. Two of these feedthroughs were used as the attachment point for two thermocouple wires from the sample. The wires running down the middle of the probe had a diameter of 0.19mm, and were covered in fine glass tubing to provide electrical insulation from the stainless steel work of the probe. A diameter of 0.19mm was chosen for for these wires to provide wire strength which was necessary whilst constructing the probe.

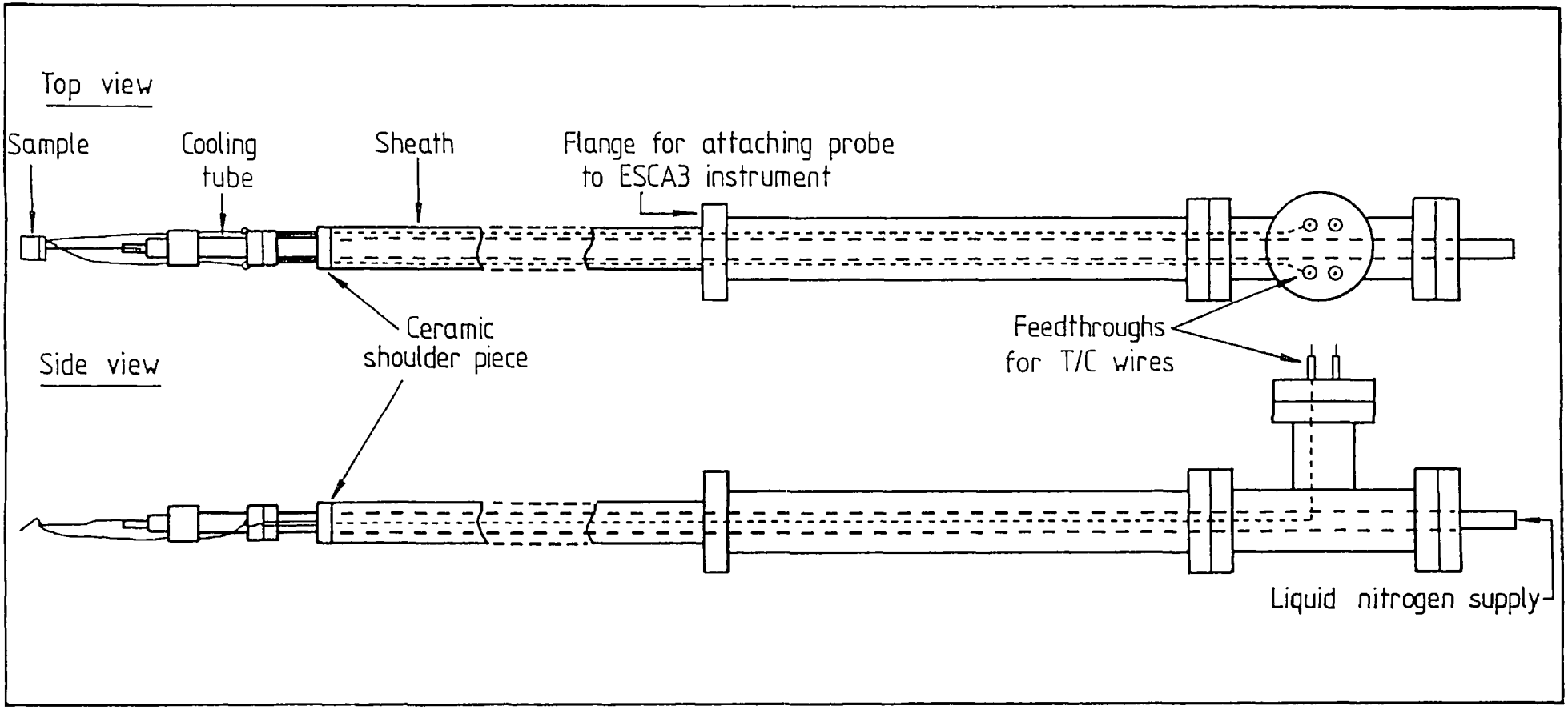


Figure 4.5. The complete high and low temperature probe

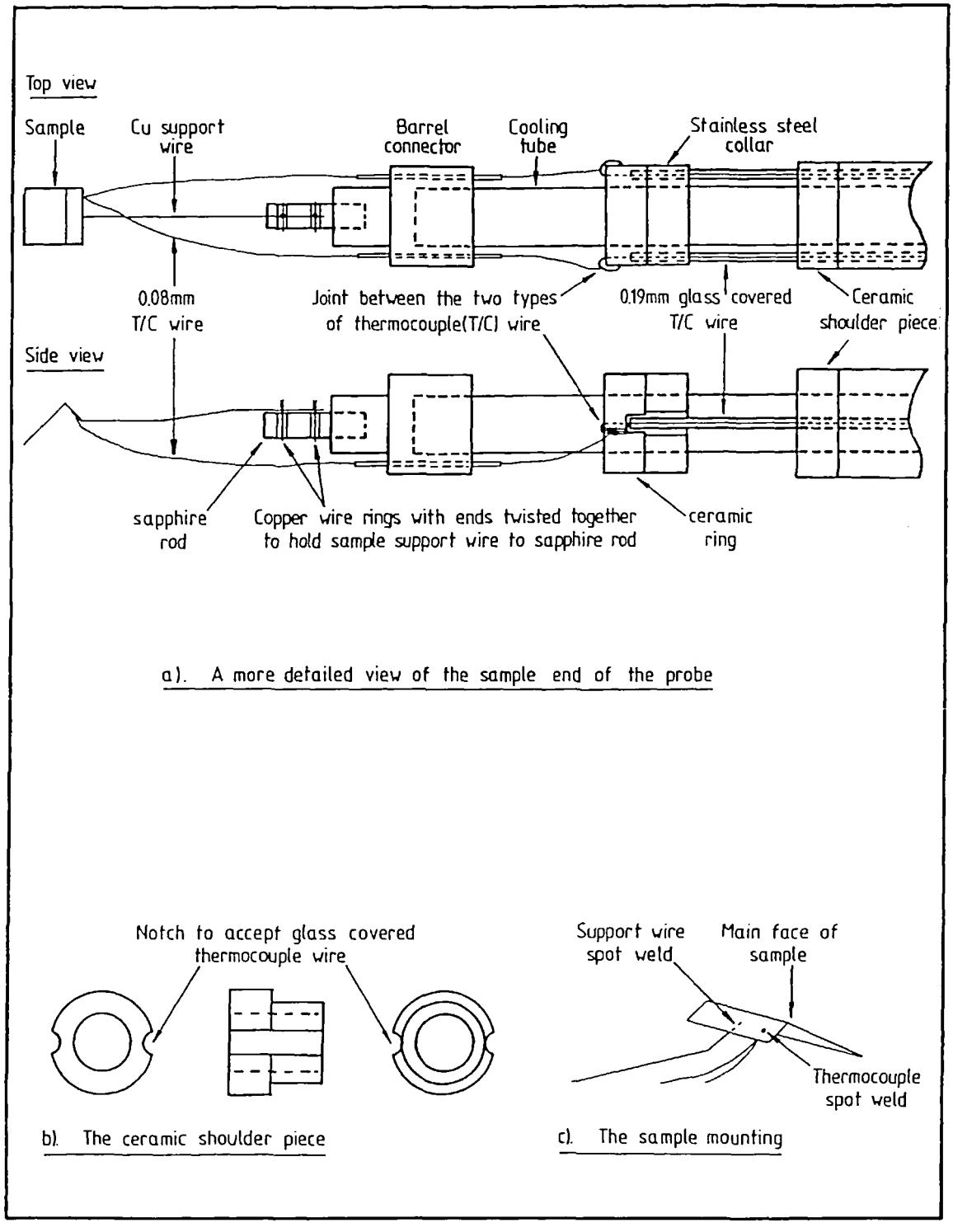


Figure 4.6. Diagram showing specific parts of the high and low temperature probe

The majority of the cooling tube was surrounded by a stainless steel sheath as illustrated. This sheath section served two purposes. Firstly, it formed a means of attaching the probe to the instrument itself. Secondly, a ceramic shoulder piece was mounted on the cooling tube and fitted into the sample end of the sheath. This was necessary to ensure that the cooling tube, and hence the sample remained reasonably immobile. This ceramic shoulder piece is shown in Figure 4.6.b. The ceramic piece was made from pyrophyllite and was fired at 1000^{o}C before use on the probe. The sheath also had a couple of holes drilled through it to assist pumping out the inside of the probe. The sample mounting assembly was then attached to the end of the cooling tube. An exposed section of the cooling tube was left between the end of the sheath and the sample mounting system. The reason for this is two-fold. Firstly, any differential contraction between the sheath and the cooling tube could be allowed for, because in practice the cooling tube contracted 2-3mm on cooling from ambient to near liquid nitrogen temperature. Secondly, an attachment point for the thermocouple wires from the sample was required to assist easy sample changing.

The sample mounting assembly consisted of a stainless steel barrel connector, a short piece of sapphire rod and the sample itself. The barrel connector was fitted onto the end of the cooling tube and had two grub screws which enabled it to be firmly attached to the cooling tube and also easily removeable for the purposes of sample changing. The sample end of the

barrel connector had the sapphire rod fitted into it and this provided the necessary electrical isolation, as mentioned earlier. The thermal properties of the sapphire rod were suitable, as its thermal conductivity increases with decreasing temperature, so no cooling difficulties were anticipated. The sample itself was spot welded to a fine copper support wire which was attached to the sapphire rod by twisting together the ends of a copper wire forming a ring around the support wire and the sapphire rod. Small grooves were cut in the sapphire rod for these attachment rings to copper wire to sit in. Two tightening rings were used. The copper support wire was made as fine as possible, without losing strength, so that background effects in thermal desorption owing to sample supports[50] could be avoided. The support was eventually made with two pieces of 0.2mm copper wire which were twisted together.

The sample temperature was measured using a chromel-alumel thermocouple made from 0.08mm wires spot-welded to the sample. Fine wires were used on the sample to reduce thermal conduction between the sample and the surrounds via the wires to a minimum. As a result of using a fine thermocouple wire on the sample, and a thicker thermocouple wire in the main body of the probe, some sort of joint between the two types of thermocouple wire was required. This joint needed to be made in such a way that the sample thermocouple wires could be detached and re-attached to enable easy sample changing. A stainless steel collar and a ceramic ring were mounted on the exposed section of the cooling tube, and these were used to "tie off" the thicker thermocouple

wire from the feedthroughs. The stainless steel collar was firmly attached to the cooling tube with grub screws with the ceramic ring being fitted loosely against the collar on the sample side. The ceramic ring was held in position by tying off the thicker thermocouple wires under a slight tension. By tying off the thicker thermocouple wire, loops of each wire were formed on opposite sides of the ceramic ring. It was on these loops that the fine thermocouple wires from the sample were wrapped around to form the connection between the two types of wire. To prevent difficulties resulting from the formation of additional thermocouple junctions, the T1 wire from the sample had to be connected to the T1 wire from the feedthroughs, and similarly the T2 wire from the sample had to be connected to the T2 wire from the feedthroughs.

The sample itself was formed from a 11 x 7mm piece of foil which had a 3mm x 7mm section bent round so that it was at 90^{o} to the remainder of the sample (8mm x 7mm) as shown in Figure 4.6.c. The 8mm x 7mm face formed tha main part of the sample, whilst the smaller section was used to spot weld the copper support wire and the thermocouple to the sample so preventing damage to the main surface after preparation (see section 4.4.1). In the spectrometer chamber, only the main part of the sample was irradiated with X-rays if the sample was positioned correctly inside the Faraday cage, so that the spot weld damage on the sample would not affect the results.

4.2.2 Use of the Probe

Sample cooling was achieved by forcing liquid nitrogen down a PTFE tube which was fed down to the sample end of the cooling tube. The free end of the PTFE tube was connected to a liquid nitrogen reservoir which was slightly pressurised with nitrogen. Warming of the sample was achieved by radiative heating from a tungsten filament held a few millimetres behind the sample. This will be described further in the next section.

4.2.3 Performance

The sample temperature could easily be reduced to - 170°C (103K). This temperature could be reached in about 15 minutes following cooling from ambient. On warming from this low temperature, a linear heating rate of better than 1 K/sec could be maintained up to 30°C (303K) whilst the liquid nitrogen supply was continued. A plot of sample temperature against time for a typical linear heating schedule of approximately 1K/sec is shown in Figure 4.7. The plot is essentially linear over the majority of the temperature range, but at the low temperature end of the schedule, the heating rate was more rapid. This initial rapid temperature increase before the linear increase should not cause any difficulties in the interpretation of the desorption spectra, as the linear increase starts at around 140K. After heating the sample to ambient from $\sim$ 100K, a temperature of less than -160°C (113K) could

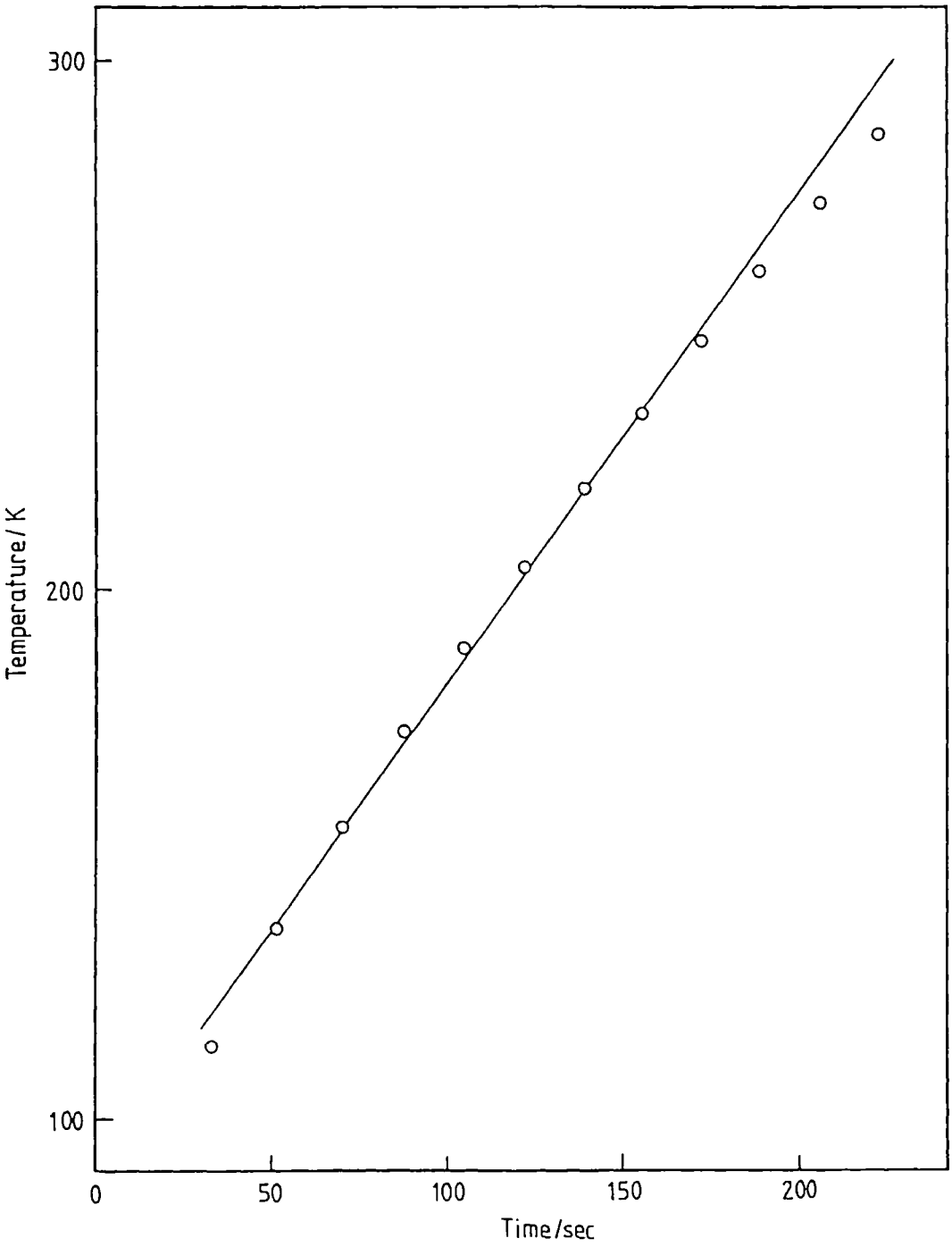


Figure 4.7. A typical temperature/time plot from a linear heating schedule of approx. 1K/sec

be reattained in approximately a minute. On warming from ambient, a sample temperature of around 300°C could be achieved using the tungsten filament. This temperature could be made much greater using electron bombardment. On heating radiatively, to 300°C, the sample temperature fell back to 50-75°C within a minute of switching off the tungsten filament. It can be seen that the probe satisfied the requirements to carry out the experiments planned for this work.

4.3 Arrangement used to carry out TPD experiments

The method of carrying out the thermal desorption experiments was based on that described by McCarty, Falconer and Madix[108]. To obtain thermal desorption spectra, the sample was held in front of the mass spectrometer so that any desorbing species could travel "line of sight" into the mass spectrometer. In the ESCA3 the preparation chamber was used for TPD.
As mentioned in Section 4.1, the sample heating filament needed to be moveable. This was achieved by mounting the filament and its supports on a ceramic block which was attached to a wobble stick. The arrangement of this is shown in Figure 4.8. This system enabled the filament to be brought up behind the sample with a gap of 2-3mm, but also enabled the filament to be dropped completely away to enable the sample to be transferred to other parts of the instrument.

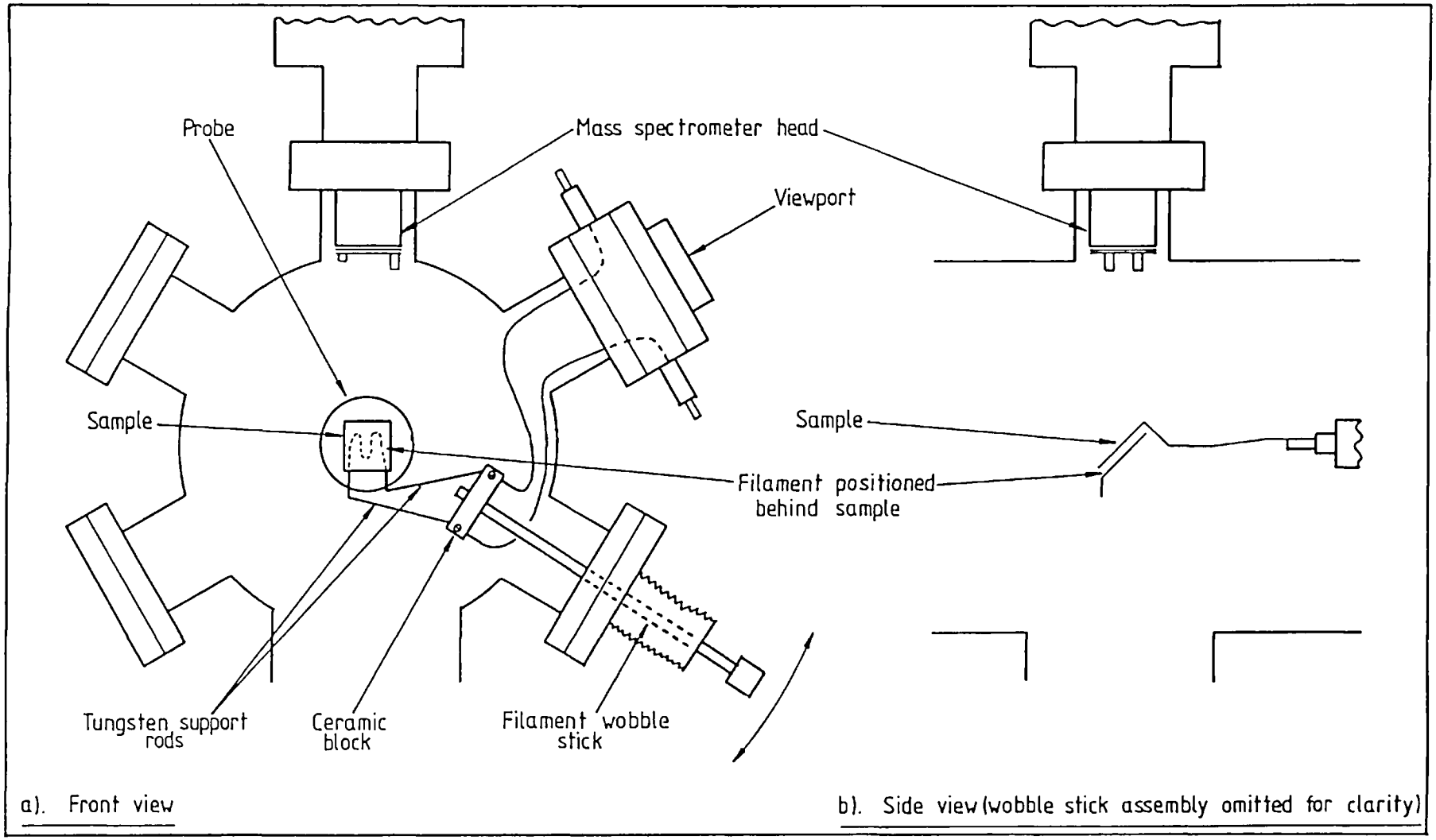


Figure 4.8. Relative positions of the heating filament, sample and mass spectrometer for TPD

Typical distances between the sample and the mass spectrometer head, as used by Madix and co-workers[70] were in the order of 2cm. Owing to the geometry of the ESCA3, a minimum sample to mass spectrometer head distance of only 7cm could be achieved. The angle of the sample was fixed at 45° to suit the XPS work, consequently the mass spectrometer would only detect those species desorbing at $\sim 45^{\circ}$ to the surface normal by line of sight. This would result in a decrease in sensitivity compared with desorption normal to the surface as fewer desorbing species would be seen because of the cosine distribution law. The horizontal position of the sample where desorption was carried out could have been adjusted but this would have required the corresponding adjustment of the filament position which practically is an inconvenient action.

As described in Chapter 3, a linear heating rate is usually used as the programme in running a TPD experiment. Linear heating was achieved by using a specially built temperature control unit which was basically a comparator which compared the signal from the thermocouple on the sample with a reference voltage, and used the difference to control the heating filament. To obtain a linear heating rate, the reference voltage appeared as a linear voltage ramp. Obviously, by changing the reference ramp rate, the sample heating rate changed accordingly. By changing the voltage range of the reference ramp, the start and final temperature of the heating schedule could be altered. For example a 1-9½ volt ramp gave a possible temperature range of approximately $-200^{\circ}C$ to $+30^{\circ}C$ which was adequate for CO desorption.

As described in section 4.1, the data collection system on the particular instrument used was by digitising the spectra and storing and manipulating them in digital form. It was proposed to collect the thermal desorption spectra in a similar way. The computer system ramp output (which was used to control the kinetic energy range on the electron analyser in XPS mode) was employed as the reference for the heating schedule. The signal output from the mass spectrometer was first fed into an amplifier before being converted into digital form by an analogue to digital converter. The output from the A/D converter was then taken to the computer system.

TPD experiments were carried out by arranging the sample and filament in the position shown in Figure 4.8. Whilst obtaining spectra between near liquid nitrogen temperature and ambient, the supply of liquid nitrogen to the probe was maintained. This was done so that radiation from the heating filament did not desorb any condensed material on the nearby cold stainless steel work of the probe.

In their work, McCarty, Falconer and Madix[108] used a sample of 0.05mm thickness, presumably to keep an even temperature distribution across the sample and to keep the filament power as low as possible whilst achieving a reasonable heating rate (in their case it was $\sim$ 10K/sec) so that filament outgassing and radiative heating of the cold surroundings leading to

unwanted desorption could be eliminated. In this work, sample thicknesses of around 0.05 to 0.1mm were used for similar reasons.

4.4 Experimental procedures

4.4.1 Sample mounting and preparation

The samples which were studied were pure copper, pure zinc and a variety of different bulk composition brasses in the range 2% - 30% bulk zinc. The pure copper and zinc samples were obtained from Goodfellow Metals as spec. pure(99.99%) 0.05mm thick foils. A 30% bulk zinc brass sample was also obtained from Goodfellow Metals as a 99.9% pure 0.05mm thick foil. Three other brass samples with bulk compositions of 2%, 5% and 10% zinc were prepared by the Solid State Physics Group of Imperial College from spec. pure components. An additional 5% sample was made by the Metallurgy Department of Imperial College, but this brass was found to have an excessive lead content - this is described in the segregation results in Chapter 5. This was probably as a result of non spec. pure zinc being used in the alloy preparation. The alloys after preparation had to be rolled and polished down to $\sim$0.05mm thickness.

Every sample which was used in the ESCA instrument was cut to size and polished, the final polish being made with 1μ lapping compound. The samples were then shaped and mounted in the way described in section 4.2.1.

Before any experimentation could be started, the samples had to be cleaned in vacuo. This was necessary to remove all surface contamination, principally carbon. The cleaning procedures for pure copper, pure zinc and the brasses differed as a result of the highly volatile zinc, and are described below.

The pure copper sample was cleaned in a manner similar to that in the literature[110]. The only difference was that the high temperature annealing at $\sim 400^{\circ}C$ was carried out separately from the ion bombardment because of the instrument geometry. Cleaning was achieved by successive cycles of argon ion bombardment and electron bombardment annealing at $\sim$ 400-500°C. This cycling followed an overnight annealing at a similar temperature. The final anneal of the sample to remove argon ion damage of the surface and was done using a radiative filament, and annealing at $\sim 300^{\circ}C$ for a few minutes. The estimated carbon contamination after cleaning was about 2% of a monolayer. There was no detectable oxygen contamination (see also Chapter 6).

No record exists in the literature as regards the cleaning of zinc samples. By baking the instrument at 140°C, the sample was annealed at a reasonable temperature to cause segregation of carbon from the bulk to the surface (the melting point of zinc is 419°C). Only a few argon ion bombardment/anneal cycles were required to obtain a clean surface with $< 2\%$ of a monolayer of carbon. The annealing was carried out at a temperature of $\sim$ 175°C. No detectable oxygen was seen.

The brass samples had to be treated with care. The annealing temperature had to be made high enough to remove bulk carbon but not too high as to result in significant zinc loss. The samples were cleaned in a similar style to the pure copper samples except that the annealing temperature was restricted to $\sim 200^{\circ}C$. The final anneal determined the composition of the surface to be studied, and was carried out at a desired temperature for approximately 15 minutes (see also Chapter 5 on segregation). The surface cleanliness was approximately 5% of a monolayer of carbon. No oxygen contamination was observed.

4.4.2 Gas dosing

Dosing gases were admitted to the preparation chamber via an all metal leak valve, and originated from BOC research grade gas bottles (99.9998% pure) via a H.V. bakeable gas handling line. For dosing methanol, a glass bulb which was partially filled with the alcohol was attached to the gas handling line. Before dosing, the methanol was purified to remove dissolved gases. This was done by subjecting the alcohol to successive freeze/thaw cycles until no gas evolution occurred on thawing under vacuum. During dosing, the methanol was held at a temperature of $\sim -60^{\circ}C$ by immersing the glass bulb in a slurry of acetone, so that a constant pressure of approximately 0.5 torr was maintained behind the leak valve. This vapour pressure was used to avoid freezing in the leak valve. The temperature rise of the slurry during the dosing period was insignificant.

CHAPTER 5

SEGREGATION IN COPPER/ZINC ALLOYS

In order to understand the reactivity of brass surfaces, it was necessary to determine the composition of the surface layer of the alloys as accurately as possible. As described in Chapter 2, alloys often have the property that the surface composition is temperature dependent, and it would be expected that the surface composition of a brass would be a function of annealing temperature because copper and zinc have different heats of sublimation. As a result of this, it was necessary to study the segregation in brasses as a function of temperature and bulk composition, with bulk zinc contents of 2%, 5%, 10% and 30% Zn being chosen. From these results, the surface composition of the alloy could be determined and in addition, an attempt could be made to obtain an approximate form of the composition profile with depth below the surface. With this analysis, a quantitative assessment could be made of the effect of zinc in the surface layer on the adsorption of CO and also of H_2, CO_2 and CH_3OH. This latter effect is covered in Chapters 6 and 7.

5.1 Sample Preparation

The brass samples which were studied were cleaned as described in Chapter 4. Before the final anneal to establish the surface composition, the samples were given a long sputter to recreate a similar composition profile before each final anneal. The final anneal in each case was made at every temperature for

approximately 15 minutes. The reasons behind the use of this procedure will be discussed after the results have been presented in section 5.2.2. Following the final anneal, the samples were essentially quenched to near room temperature. Even from high temperatures of above 300°C, the sample temperature could drop back to below 75°C in less than 30 seconds, and could reach less than 50°C in under a minute. The photo-electron spectra which are described in the next section, were then measured with the sample temperature at between room temperature and 50°C. It was not possible to record spectra whilst the segregation process was taking place because the sample could not be annealed inside the spectrometer chamber of the ESCA3. Zinc contamination of the spectrometer might have occurred through evaporation during annealing.

Surface contamination following the anneal period was mainly carbon, which was estimated to be 5% of a monolayer at worst (C1s : $Cu2p_{3/2}$ peak area ratio of better than 1 : 1000). In addition to carbon, other surface contaminants were checked for after the 15 minute annealing period. It was found that there were no detectable levels of oxygen or sulphur in the surface, the O1s and $S2p_{3/2}$ peaks being scanned to test for contamination. Lead is frequently an impurity in zinc, so the lead 4f peaks were monitored following the annealing period to check for any lead segregation in the brass samples. As described in Chapter 4, two 5% bulk Zn alloys were prepared, because it was found that one of the

samples was made from impure zinc, and this impurity resulted in lead segregation to the surface in addition to the zinc. The presence of the lead had an adverse effect on the segregation characterisitcs and this will be described in section 5.2.3. Apart from this sample, no detectable lead contamination was observed in the alloys, even at high annealing temperatures.

5.2 Results

The segregation in the alloys was analysed by measuring the intensities of three pairs of copper and zinc photo-electron peaks. The copper and zinc peaks in each pair resulted from photo-electrons with similar kinetic energies and are presented in the results as a ratio of the zinc intensity to the copper intensity. The intensities were found by measuring the area under the appropriate peaks after taking a linear background subtraction. The three Zn/Cu peak pairs were chosen to give measurements with differing surface sensitivities. The most surface sensitive peak pair was formed from the Cu and Zn $2p_{3/2}$ peaks derived from the Mg-Kα source which represented approximately the top four atomic layers (see section 5.3). A second peak pair was formed from the Cu and Zn3p peaks, again derived from the Mg-Kα source, and these were formed from photo-electrons originating from the top nine or ten atomic lavers. The third pair was the Cu and Zn $2p_{3/2}$ peaks derived from the Al-Kα source which represented an intermediate depth. The low

kinetic energy XPS peaks of less than 150eV were not used in the analysis because the peaks were both weak and superimposed on a steeply ascending background. Similarly, the low energy Auger peaks were not used. The 3p peaks were used in preference to the 3s peaks because the former had a higher cross section, and consequently gave a better defined zinc peak when the 2% bulk Zn alloy was studied. The high energy Auger peaks at approximately 920eV and 1000eV were not used because it was difficult to define an accurate peak area.

5.2.1 Effect of Sputtering on the surface composition

The effect of sputtering on brasses is illustrated in Table 5.1, where the Zn/Cu peak area ratios for the $2p_{3/2}$ (Mg-Kα) peaks are in general smaller than the corresponding theoretical ratios for bulk composition throughout the sample.

TABLE 5.1

Alloy Bulk Composition (% Zn)	2	5	10	30
$2p_{3/2}$ (Mg-Kα) peak area ratio	0.016	0.047	0.06	0.15
Theoretical peak area ratio for bulk composition	0.021	0.054	0.11	0.43

This illustrates that zinc is preferentially sputtered which is in qualitative agreement with the results of Szymonski[118] who studied the sputtering of brass samples using a time-of-flight analysis.

5.2.2 Effect of annealing temperature on surface composition

The dependence of the $2p_{3/2}$(Mg-Kα), $2p_{3/2}$(Al-Kα) and the 3p peak area ratios with annealing temperature and bulk composition are shown in Table 5.2. The variation of the $2p_{3/2}$ (Mg-Kα) ratio, the most surface sensitive ratio, is presented in Figure 5.1 so that an approximate surface zinc concentration variation with annealing temperature and bulk composition can be illustrated. The results show that there is surface enrichment in zinc upon annealing Cu/Zn alloys in vacuo. This is completely consistent with the"segregation rules" described by Ponec[16] which were outlined in Chapter 2. The results are also consistent with the findings of other workers who have studied alloy systems with components of different volatilities.

An important aspect of the segregation of zinc in the Cu/Zn alloy system is that there is a particular annealing temperature at which the surface zinc concentration passes through a maximum. This is a common feature in each of the four different bulk alloys, with the maximum occurring between 200 and 250°C. The interpretation of this phenomenom is that at temperatures below 200°C, zinc principally segregates to the surface of the alloy creating enrichment. Up to 200°C the surface zinc concentration increased with annealing temperature, probably

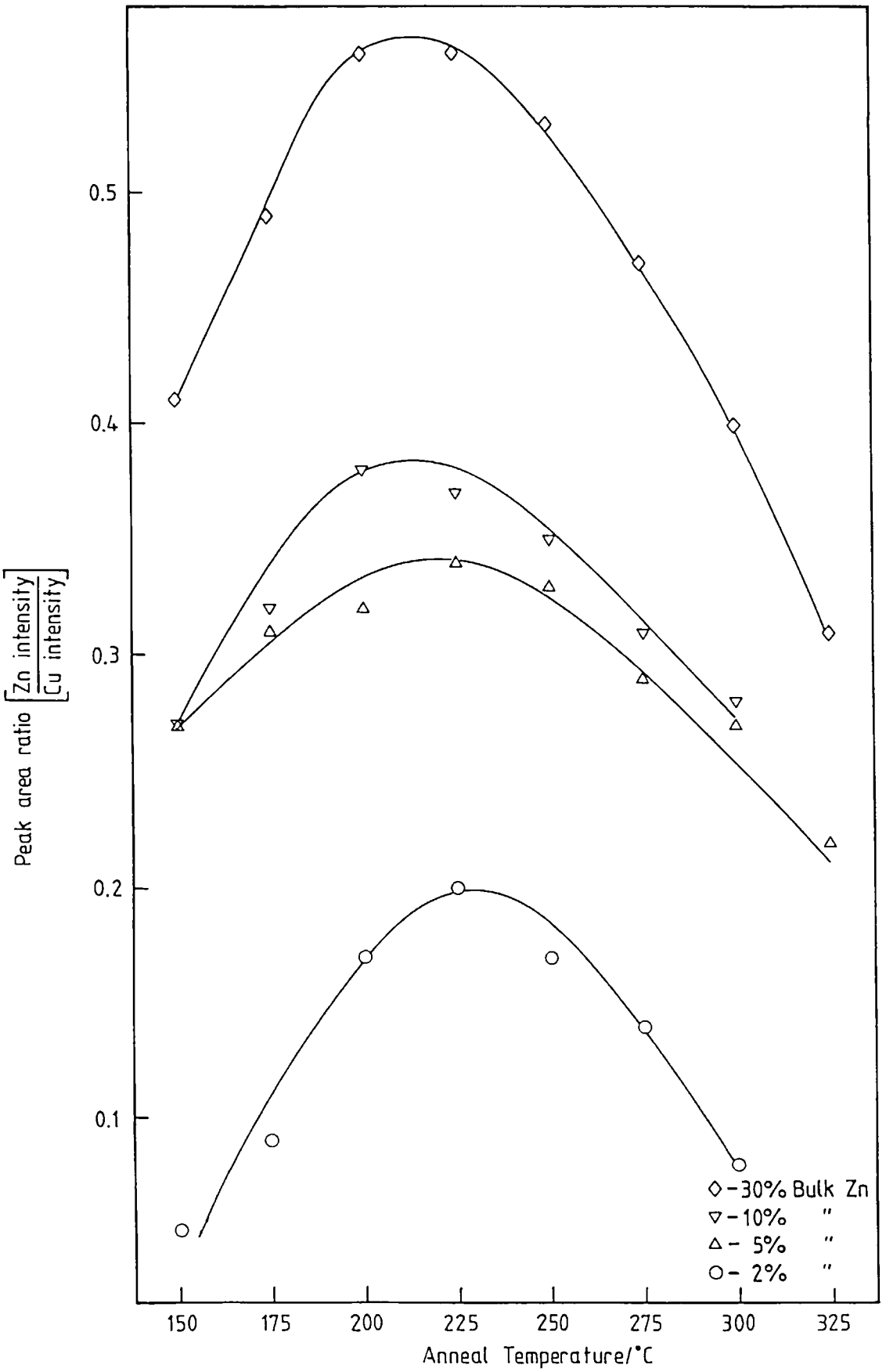


Figure 5.1. Variation of the $2p_{3/2}$ (Mg Kα) peak area ratios with annealing temperature

TABLE 5.2 Zn/Cu peak area ratios as a function of bulk composition and annealing temperature

Anneal temp.	Peak	Source	Zn/Cu Peak area ratios			
			2% bulk Zn	5% bulk Zn	10% bulk Zn	30% bulk Zn
150°C	2p	Mg-Kα	0.05	0.27	0.27	0.41
	2p	Al-Kα	0.04	0.19	0.24	0.42
	3p	Mg-Kα	0.01	0.08	0.12	0.36
175°C	2p	Mg-Kα	0.09	0.31	0.32	0.49
	2p	Al-Kα	0.07	0.24	0.26	0.48
	3p	Mg-Kα	0.03	0.10	0.13	0.38
200°C	2p	Mg-Kα	0.17	0.32	0.38	0.56
	2p	Al -Kα	0.12	0.26	0.29	0.54
	3p	Mg-Kα	0.03	0.12	0.14	0.43
225°C	2p	Mg-Kα	0.20	0.35	0.37	0.56
	2p	Al-Kα	0.13	0.27	0.28	0.52
	3p	Mg-Kα	0.04	0.13	0.16	0.46
250°C	2p	Mg-Kα	0.17	0.33	0.35	0.53
	2p	Al-Kα	0.13	0.26	0.28	0.47
	3p	Mg-Kα	0.04	0.12	0.15	0.38
275°C	2p	Mg-Kα	0.14	0.29	0.31	0.47
	2p	Al-Kα	0.11	0.23	0.23	0.42
	3p	Mg-Kα	0.03	0.09	0.13	0.33
300°C	2p	Mg-Kα	0.08	0.27	0.28	0.40
	2p	Al-Kα	0.06	0.21	0.22	0.35
	3p	Mg-Kα	0.01	0.08	0.09	0.29
325°C	2p	Mg-Kα	-	0.22	-	0.31
	2p	Al-Kα	-	0.16	-	0.34
	3p	Mg-Kα	-	0.06	-	0.25

because of an increase in the rate of solid state diffusion. However, owing to the volatility of zinc (its melting point is 419°C), evaporation of the zinc from the enriched surface started to become significant above 200°C, and the surface concentration of zinc became affected by this in addition to the segregation. The final surface composition after annealing at temperatures above 200°C was probably determined by a balance between segregation of zinc from the bulk and evaporation of segregant from the surface, as suggested by Webber and Chadwick in their communication on evaporation limited segregation in Cu/Ni alloys[112]. Zinc evaporation was confirmed by annealing a test 5% bulk zinc sample at well above 325°C. This resulted in a peak at mass 65 appearing on a mass spectrum of the residual vacuum which disappeared on removing the sample heating source. It was therefore concluded that annealing of the brasses at high temperature resulted in heavy zinc loss from the brass.

The experiments on the four different bulk composition alloys were terminated at either 300°C or 325°C. These temperatures were the maximum that could be reached by radiative annealing. It was found that at the highest annealing temperatures of 300°C and 325°C, the system pressure remained below 2×10^{-9} torr.

As can be seen from Figure 5.1, the position of the maximum surface zinc content changed with bulk composition. The position of this maximum moved to a lower temperature with

increasing zinc content in the bulk. For the 30% bulk Zn alloy, the maximum was between 200°C and 225°C but the maximum for the 2% bulk Zn alloy was between 225°C and 250°C. This reflects the longer diffusion pathway for the Zn atoms in the 2% alloy.

The annealing period described in section 5.1 was chosen to be long enough to give a steady surface composition but not too long so that carbon began to appear in the surface through segregation from the bulk. The long sputter which was applied just before the final anneal followed by the anneal was able to recreate a similar set of peak area ratios implying that the surface composition and depth profile for a given bulk alloy was reproducible to a reasonable extent. This was the case when the alloys were sputtered after annealing at their temperature of maximum surface zinc content or higher temperatures. However, this was not checked after annealing the 2% bulk Zn alloy at 300°C. The system of sputter/anneal was used to obtain the surface composition as a function of temperature in preference to a system of successive annealing. It was possible to reproduce the peak area ratios within an error of 10%. Sample to sample reproducibility was not as easy to obtain however. A comparison was made between the segregation in two 2% bulk Zn alloys. As this alloy contained only a small amount of zinc, then this comparison represented the severest test of sample to sample reproducibility. The comparison is illustrated in Table 5.3.

TABLE 5.3 Comparison of the segregation results in two different 2% bulk Zn alloys for a selection of annealing temperatures

Anneal Temp.	Peak	Excitation source	Zn/Cu peak area ratios	
			Sample I	Sample II
200°C	$2p_{3/2}$	MgKα	0.18	0.13
	$2p_{3/2}$	AlKα	0.12	0.09
	3p	MgKα	0.03	0.03
225°C	$2p_{3/2}$	MgKα	0.20	0.15
	$2p_{3/2}$	AlKα	0.13	0.11
	3p	MgKα	0.04	0.04
250°C	$2p_{3/2}$	MgKα	0.17	0.15
	$2p_{3/2}$	AlKα	0.13	0.11
	3p	MgKα	0.04	0.04

The difference in the results can immediately be seen, and the results imply that sample I had a greater surface zinc content. There are two possible reasons for the discrepancy. It is not safe to state that both samples were given a similar number of sputter/anneal cycles. Addition cycles would result in further zinc depletion of the bulk, and a significant difference in the number of cycles would result in one sample becoming less surface enriched in zinc upon annealing because of the depletion. However, a glance at Table 5.3 shows that the 3p peak area ratios were similar suggesting that additional bulk depletion of sample II

may not be the cause of the discrepancy. A second possibility was that the sample angles were not identical which would lead to the emission angles and hence the peak area ratios being different. This would account for the difference in the surface sensitive peak area ratios, whilst the 3p ratios were similar. However, the extent of the error seems much too large for small variations in the sample mounting angle, unless this angle was significantly modified when the sample entered the Faraday cage and relaxed upon withdrawal. However, sample to sample reproducibility is not critical for establishing the CO uptake as a function of the amount of Zn in the brass because the surface composition of the brass was always determined before performing any adsorption experiments.

In section 5.1, a description was given of how the sample was essentially quenched to room temperature. Although the quenching was fairly rapid, it was assumed that no significant relaxation of the surface composition and depth profile occurred following cooling from 275°C and higher when the sample temperature passed through 200°C to 225°C. It was not possible to check whether any relaxation occurred or not.

5.2.3 Effect of lead impurity on the segregation in Cu/Zn alloys

In the previous section, a brief description was given about the presence of lead impurities in one of the 5% bulk Zn alloys. The lead contamination was found when two addition peaks appeared

in the Zn 3s spectral region. These two peaks were established as Pb 4f. There was a dramatic increase in the lead contamination after annealing at 300°C compared with that after annealing at 200°C, as can be seen in Figure 5.2 where the Zn3s(+Pb 4f) spectra are shown. The amount of lead present in the surface layer was estimated at 4%, based on the simplifying assumption that all of the lead was present in the surface layer. A similar set of segregation experiments were carried out on both the pure and contaminated 5% bulk Zn alloys. The comparison between the segregation results for these two alloys are shown in Table 5.4, where the values for the $2p_{3/2}$(Mg-Kα) and the $2p_{3/2}$(Al-Kα) peak area ratios are presented. It can immediately be seen that the surface enrichment in the impure alloy was very much less than that for the pure alloy. Differences in bulk composition can be discounted as a possible cause of this result because an analysis of both samples showed that each had a bulk composition of 5% Zn. Clearly the presence of the lead in the alloy strongly inhibits the segregation of zinc, but consideration of the heat of sublimation of Pb and Zn shows that in a Pb/Zn system, lead enrichment should not occur, as lead has a heat of sublimation of 197kJ/mol compared with 130kJ/mol for zinc. Copper and lead are not known to alloy, so the appearance of lead in the surface must be as a result of its presence leading to a reduction in the surface energy.

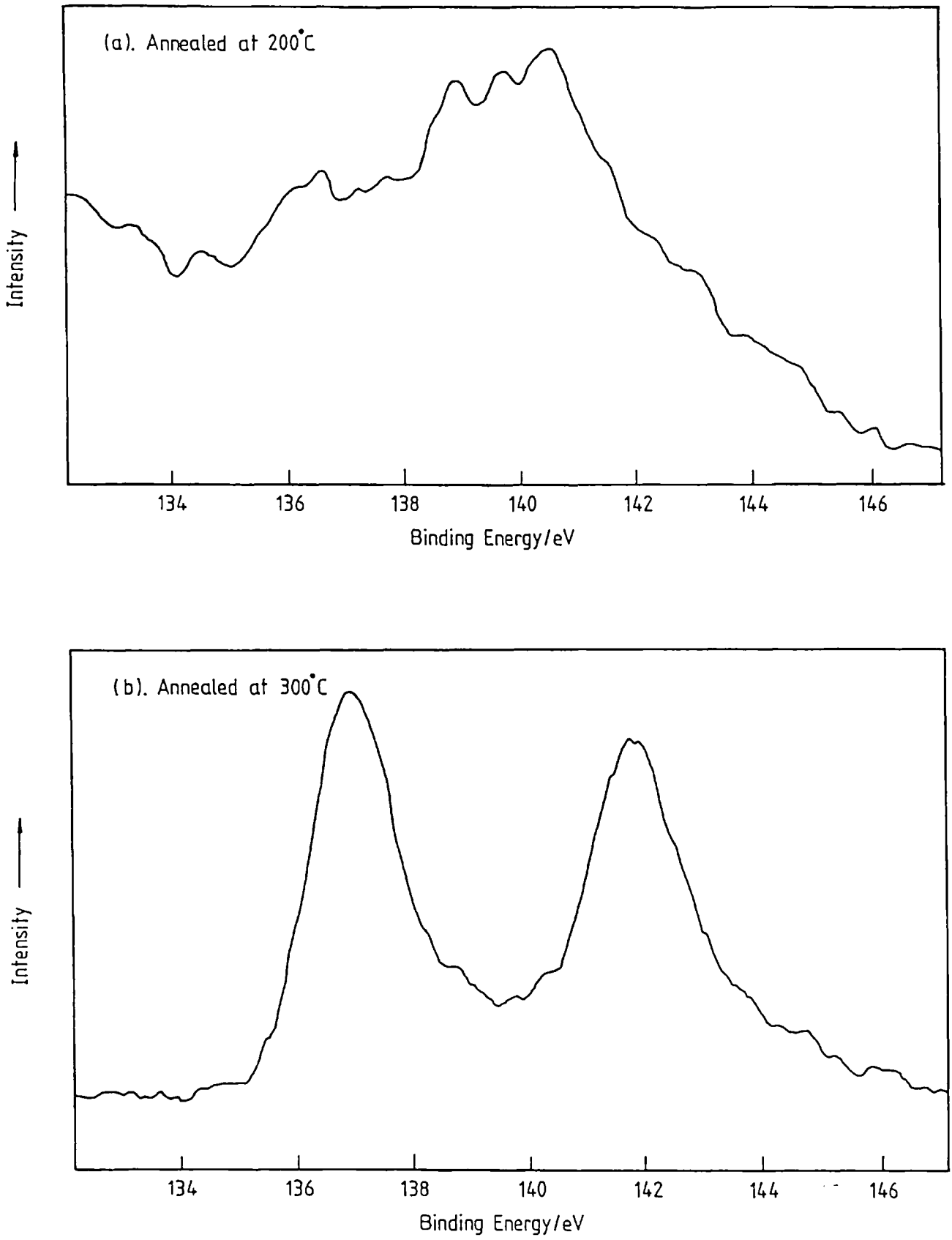


Figure 5.2. Zn 3s spectral region showing the appearance of Pb 4f peaks following annealing of a lead contaminated 5% bulk Zn brass

TABLE 5.4 The effect of lead impurities on the segregation results in a 5% bulk Zn brass

Anneal Temp.	Peak	Excitation source	Zn/Cu peak area ratios	
			Pure sample	Impure sample
150°C	$2p_{3/2}$	MgKα	0.27	0.08
	$2p_{3/2}$	AlKα	0.19	0.08
175°C	$2p_{3/2}$	MgKα	0.31	0.12
	$2p_{3/2}$	AlKα	0.24	0.12
200°C	$2p_{3/2}$	MgKα	0.32	0.17
	$2p_{3/2}$	AlKα	0.26	0.16
225°C	$2p_{3/2}$	MgKα	0.35	0.17
	$2p_{3/2}$	AlKα	0.27	0.16
250°C	$2p_{3/2}$	MgKα	0.33	0.15
	$2p_{3/2}$	AlKα	0.26	0.14
275°C	$2p_{3/2}$	MgKα	0.29	0.12
	$2p_{3/2}$	AlKα	0.23	0.11
300°C	$2p_{3/2}$	MgKα	0.27	0.07
	$2p_{3/2}$	AlKα	0.21	0.06

5.3 Development of a basic equation to relate the measured peak area ratios to the composition of the uppermost atomic layers in a binary alloy.

In section 5.2.2, the segregation results were presented as ratios of the zinc and copper peak intensities energies. As will be shown in section 5.4, these peak area ratios can be used directly to calculate an approximate surface composition. However, this composition will not be exact because the use of the peak area ratios only gives an average composition of the uppermost layers of the alloy. The average composition results because the Cu and Zn photo-electron peaks are made up from electrons originating from not only the top layer, but from layers below the surface. The contributions from successive layers to the total Cu and Zn peaks are weighted, this weighting being related to the photo-electron IMFPs associated with the kinetic energy of the photo-electrons which form the Cu and Zn peaks. In order to obtain a better estimate of the surface composition, a calculation procedure is required which takes into account the effect of the IMFP and the composition depth profile. This will be the objective of this section and also of the next section.

As described in Chapter 3, section 3.1.3, if $I_o(E_A,x)$ represents the photo-electron (P.E.) flux with kinetic energy E_A originating from species A at a depth x below the surface, then the P.E. flux emerging at the surface as a consequence of the flux from a depth x below the surface will be given by :

$$I_s(E_A,x) = I_o(E_A,x) \exp(-x/\lambda_A(E_A)) \qquad (5.1)$$

where $\lambda_A(E_A)$ is the electron IMFP at a kinetic energy, E_A in species A.

If the P.E. flux emerging at the surface is summed for all depths then the total P.E.flux will be given by :

$$I_s(E_A) = \int_o^\infty I_o(E_A,x) \exp(-x/\lambda_A(E_A))dx \qquad (5.2)$$

However, $I_s(E_A)$ represents the total P.E. flux emerging at the surface rather than the true measured peak intensity. Powell[94] presented an expression which related the measured peak intensity of a P.E. flux of kinetic energy E_A from species A at a depth x below the surface to a set of parameters, and this is reproduced below :

$$I_A(E_A,x) = I(h\nu)\, N_A\, \sigma_A(h\nu,x)\, \alpha_A(E_A) H(E_A,E) \qquad (5.3)$$

The parameters $I(h\nu)$, N_A, $\sigma_A(h\nu,x)$, $\alpha_A(E_A)$ and $H(E_A,E)$ were described in Chapter 3, section 3.1.4. Equation (5.3) can be integrated to give the total measured peak intensity of a P.E. flux from species A with kinetic energy E_A, and this is shown below:

$$I_A(E_A) = \int_o^\infty I(h\nu) N_A\, \sigma_A(h\nu,x) \alpha_A(E_A)\, H(E_A,E)\, dx \qquad (5.4)$$

This expression can be compared with equation (5.2) and the following parameters in equation (5.4) can be regarded as equivalent to those in equation (5.2) :

$$I_A(E_A) = I_s(E_A)H(E_A,E)$$

$$I(h\nu)N_A\sigma_A(h\nu,x) = I_o(E_A,x)$$

$$\alpha_A(E_A) = \exp(-x/\lambda_A(E_A)) \qquad (5.5)$$

Equation (5.4) can therefore be written as :

$$I_A(E_A) = \int_o^\infty I(h\nu)N_A\ \sigma_A(h\nu,x)\exp(-x/\lambda_A(E_A))H(E_A,E)dx \qquad (5.6)$$

If the alloy can be considered as a series of discrete atomic layers, and if it assumed that there are no matrix effects, then the total measured peak intensity, $I_A(E_A)$, can be re-written as a summation of the individual measured peak intensities from the layers at and below the surface as shown below :

$$I_A(E_A) = \sum_{i=0}^{\infty} I(h\nu)N_{A,i}\sigma_A(h\nu,i)\exp(-id/\lambda_A(E_A))\ H(E_A,E) \qquad (5.7)$$

where $N_{A,i}$ is the number of atoms of species A in the i^{th} layer below the surface

d is the inter-layer spacing

In an alloy there is more than one species present. The measured peak intensity of a species B be expressed in a similar

way to that in equation (5.7). This expression is :

$$I_B(E_B) = \sum_{i=0}^{\infty} I(h\nu) N_{B,i} \sigma_B(h\nu,i) \exp(-id/\lambda_B(E_B))\ H(E_B,E) \qquad (5.8)$$

where the parameters $I_B(E_B)$, $N_{B,i}$, $\sigma_B(h\nu,i)$, $\lambda_B(E_B)$ and $H(E_B,E)$ are similar to those in equation (5.7) but refer to species B.

If the ratio of equations (5.7) and (5.8) are taken, then this will result in an expression which defines $I_A(E_A)/I_B(E_B)$ which is equivalent to a peak area ratio determined in the experiments. This ratio is given below :

$$\frac{I_A(E_A)}{I_B(E_B)} \equiv R = \frac{\sum_{i=0}^{\infty} N_{A,i}\ \sigma_A(h\nu,i) \exp(-id/\lambda_A(E_A))\ H(E_A,E)}{\sum_{i=0}^{\infty} N_{B,i} \sigma_B(h\nu,i) \exp(-id/\lambda_B(E_B))\ H(E_B,E)} \qquad (5.9)$$

The incident X-ray flux $I(h\nu)$ term will cancel because the same X-ray source and conditions were used in obtaining each peak area ratio. The terms $H(E_A, E)$ and $H(E_B, E)$ are, as described in Chapter 3, formed from three parameters - the transmission function, the detector efficiency and the electron optical factor. As the peak area ratios were measured with Cu and Zn peaks of a similar kinetic energy, the transmission functions and the detector efficiencies in $H(E_A, E)$ and $H(E_B, E)$ can be cancelled when the ratio of these instrument response functions are taken. Similarly, the electron optical factor, the third

term in the instrument response function will cancel out in equation (5.9) because the electron deceleration from the sample to the hemispherical analyser itself (i.e. over the retardation stage) will be similar for Cu and Zn photo-electrons forming a particular ratio.

The $N_{A,i}$ and $N_{B,i}$ terms in equation (5.9) can be related to the mole fractions of species A and B in layer i, so that

$$N_i \theta_i^A = N_{A,i}$$

$$N_i \theta_i^B = N_{B,i}$$

where θ_i^A and θ_i^B are the mole fractions of species A and B in layer, i, respectively

N_i is the total number of atoms in layer, i.

If it is assumed that the total number of atoms in each layer is approximately equal, then N_i will not appear in the final expression.

The photo-ionisation cross-sections, $\sigma_A(h\nu,i)$ and $\sigma_B(h\nu,i)$ were obtained from the data presented by Schofield[113], where the cross-sections were calculated using a Hartree-Slater model. Cross-sections are given for individual subshells and for ionization resulting from irradiation from both the Mg-Kα and AlKα sources, unlike the data of Evans et al[114].

However, there is good agreement between the ratio of the copper and zinc total photo-ionization cross-sections for the 2p shell calculated by Schofield and that obtained experimentally by Evans et al, giving reasonable confidence in the data of Schofield. The photo-ionization cross-sections for the Cu and Zn subshells to be used in the analysis which will follow are shown in Table 5.6. It was assumed that the cross-section was independent of depth.

In the ESCA3 instrument, the sample is mounted at an angle of 45^{o} to the horizontal plane as shown in Figure 4.3 in Chapter 4. As can be seen from Figure 4.3, the entrance to the hemispheres of the analyser is at an angle of 15^{o} to the horizontal axis. Consequently, the electrons which are detected by the analyser are collected over a narrow band of angles about 30^{o} to the plane of the sample. This will result in an effective electron IMFP of $\lambda(E)\sin\phi$, where ϕ is 30^{o}.

The IMFP of the photo-electrons was determined using the universal curve of Seah and Dench[91]. These were chosen in preference to the theoretical data of Penn[92] as some doubts have been cast over the accuracy of Penn's results by Karolewski[115]. The latter obtained IMFPs for photo-electrons passing through lead which were approximately twice those obtained by Penn. The universal curve of Seah and Dench was also preferred because it was based on a least squares fit to experimental data. The universal relation is given by :

$$\lambda_m = \frac{A}{E^2} + B(mE)^{\frac{1}{2}} \qquad (5.10)$$

where λ_m is the IMFP in monolayers

m is the monolayer thickness in nanometres

E is the electron kinetic energy

A,B are constants

Conversion of equation (5.10) from λ_m to λ_n, the IMFP in nanometres is effected the relation :

$$\lambda_n = m\lambda_m \qquad (5.11)$$

From their fit, Seah and Dench established that A was 538 and B was 0.41. For the kinetic energy range of interest, i.e. 230-1200eV, the term A/E^2 is small compared to $B(mE)^{\frac{1}{2}}$. Consequently, equation (5.10) can be reduced to :

$$\lambda_m = 0.41(mE)^{\frac{1}{2}} \qquad (5.12)$$

This equation can be expressed in angstroms as :

$$\lambda_n = 0.13\ a^{1.5}\ E^{\frac{1}{2}} \qquad (5.13)$$

The parameter, a, the monolayer thickness in angstroms, was assumed to be equivalent the inter-layer spacing, as the conversion from the IMFP in monolayers (λ_m) to the IMFP in units of distance must be dependent on the separation of the

monolayers. Consequently, it was necessary to determine the inter-layer spacing of the samples which were used. The inter-layer spacing can be derived from the lattice constant for α-brasses, but these are dependent on the amount of zinc dissolved in the brass phase. As a simplification to overcome the fact that the thermally treated brass samples would be composed of layers with different compositions, the lattice constants were determined by assuming that all of the layers in the brass samples were at their bulk compositions. This simplification will not cause drastic errors as will be shown later. All of the samples which were studied were polycrystalline, and in practice there was no easy way of determining the inter-layer spacing. It was assumed that the surface would be principally formed from either the (100) or the (111) faces or a balance between these two, and that the inter-layer spacing would be based on these two faces. In the analysis to determine the surface composition which will be presented in the next section, it was decided to do the analysis twice, one analysis being based on the samples being predominantly formed from the (100) face, and the second being based on the (111) face. An average of these two is a third possibility, but there is no information available as to how the two faces should be weighted. The inter-layer spacing, d, for the (100) and (111) faces are given by :

$$d = \ell/2 \quad \text{for the (100) face}$$

$$d = \ell/\sqrt{3} \quad \text{for the (111) face}$$

where ℓ is the lattice constant for a brass.

The lattice constant for α-brasses was obtained from data by Pearson[116], and these constants and the resulting values for the inter-layer spacings are given for the four different bulk compositions in Table 5.5

TABLE 5.5 Lattice constants and layer spacings in different bulk brasses

Bulk zinc content	Lattice constant (Å)	Inter-layer spacings (110) face (Å)	(111) face (Å)
2%	3.618	1.81	2.09
5%	3.625	1.81	2.09
10%	3.635	1.82	2.10
30%	3.682	1.84	2.13

The IMFP of an electron of kinetic energy, E, in a brass sample will now be given by :

$$\lambda_{Br}(E) = 0.13\, d^{1.5}\, E^{\frac{1}{2}} \qquad (5.14)$$

Consequently, equation (5.9) which related the measured peak area ratio to the composition depth profile and the IMFPs can be re-written as follows, if species A and B are replaced by

Zn and Cu respectively :

$$R = \frac{\sum_{i=0}^{\infty} \theta_i^{Zn} \sigma_{Zn}(h\nu) \exp(-id/\lambda_{Br}(E_{Zn})\sin\phi)}{\sum_{i=0}^{\infty} \theta_i^{Cu} \sigma_{Cu}(h\nu) \exp(-id/\lambda_{Br}(E_{Cu})\sin\phi)} \qquad (5.15)$$

where E_{Cu}, E_{Zn} are the kinetic energies of the copper and zinc peaks forming the measured peak area ratio.

In equation (5.15), the same function is used to calculate the IMFP in both the numerator and the denominator. The term $\exp(-id/\lambda_{Br}(E_{Cu})\sin\phi)$ can be conveniently re-written as :

$$[\alpha(E_{Cu})]^i = \exp(-id/\lambda_{Br}(E_{Cu})\sin\phi) \qquad (5.16)$$

where $\alpha(E_{Cu}) = \exp(-d/\lambda_{Br}(E_{Cu})\sin\phi)$

Similarly,

$$[\alpha(E_{Zn})]^i = \exp(-id/\lambda_{Br}(E_{Zn})\sin\phi) \qquad (5.17)$$

where

$$\alpha(E_{Zn}) = \exp(-d/\lambda_{Br}(E_{Zn})\sin\phi)$$

The energy dependence of the α terms has been retained because there is a kinetic energy difference of almost 100eV between the Cu and Zn peaks. At low energies this will give

significantly different values for the IMFP and hence for α. As a result of this, two values of α have been calculated for each peak area ratio.

It was found that the IMFPs calculated from equation (5.14) only varied slightly with bulk composition for a given electron kinetic energy. This means that the simplification of calculating the lattice constants assuming that the layers of the brass were all at bulk composition would not lead to significant errors. Appropriate values for the effective IMFP for each peak obtained in the experiments are presented in Table 5.6.

TABLE 5.6 Kinetic Energies, photo-ionization cross-sections, IMFPs and α(E) values for the peaks recorded in the segregation experiments

Peak	Excitation source	Kinetic energy	Cross Section	IMFP/Å (100) face	IMFP/Å (111) face	α(E) (100) face	α(E) (111) face
$Cu\ 2p_{3/2}$	MgKα	322.4eV	15.9	2.9	3.6	0.53	0.55
$Zn\ 2p_{3/2}$	MgKα	233.7eV	18.0	2.5	3.0	0.47	0.50
$Cu\ 2p_{3/2}$	AlKα	555.2eV	16.7	3.7	4.7	0.62	0.64
$Zn\ 2p_{3/2}$	AlKα	466.5eV	18.9	3.4	4.3	0.59	0.61
Cu3p	MgKα	1179eV	2.3	5.5	6.8	0.72	0.73
Zn3p	MgKα	1166eV	2.6	5.5	6.8	0.72	0.73

Notes: (i) The photo-ionization cross-sections are relative to the Cls cross-section reference of 1.0

(ii) The IMFPs quoted are the effective values based on the photo-electron flux being detected at 30^{o} to the plane of the sample surface.

The parameters $\alpha(E_{Cu})$ and $\alpha(E_{Zn})$ can now be found for each peak obtained in the experiments. It was found that $\alpha(E)$ was essentially independent of small changes in the lattice constant and the IMFP. As a result of this the same set of six $\alpha(E)$ values could be used for a particular crystal face for all four different bulk composition alloys. These values of $\alpha(E)$ are shown for the (100) and (111) faces in Table 5.6.

If the ratios of the photo-ionization cross-sections for similar copper and zinc peaks are taken using the values presented in Table 5.6, it is found that the ratio $\sigma_{Zn}(h\nu)/\sigma_{Cu}(h\nu)$ is the same for all three peak pairs. This constant, to be denoted as σ, has a value of 1.13. Equation (5.15) will now become :

$$R = \frac{\sigma \sum_{i=0}^{\infty} \theta_i^{Zn} \left[\alpha(E_{Zn})\right]^i}{\sum_{i=0}^{\infty} \theta_i^{Cu} \left[\alpha(E_{Cu})\right]^i} \qquad (5.18)$$

where R is a measured peak area ratio, and E_{Cu} and E_{Zn} are the K.E.'s associated with the ratio.

Equation (5.18) is the basic equation which will be used in the next section to provide a more accurate result for the surface composition of the alloy. From the experiments, three peak

area ratios were found, and there will be a characteristic value of $\alpha(E_{Cu})$ and $\alpha(E_{Zn})$ associated with each of these ratios as shown in Table 5.6. This will lead to three different equations involving the composition of the uppermost layers. By manipulation of these three equations, the surface composition can be derived and this will be described in Section 5.4.

5.4 Determination of the surface composition by the assumption of possible composition profiles

In section 5.3, a basic equation was developed which related the measured peak intensity ratios to the surface composition and to the composition of successive layers below the surface. The objective of this section is to suggest possible composition profiles and use them to obtain a surface composition.

If a particular composition profile is assumed, a relation can usually be developed between the surface mole fraction of one component and the mole fractions of the same component in the successive layers below the surface. By doing this, it is possible to eliminate all of the mole fraction terms in equation (5.18) except for θ_o^{Cu} and θ_o^{Zn} which are the surface mole fractions of copper and zinc respectively, and the bulk mole fractions of copper and zinc, θ_B^{Cu} and θ_B^{Zn}. As these two terms are not independent, then by putting $\theta_o^{Cu} = 1-\theta_o^{Zn}$ and $\theta_B^{Cu} = 1-\theta_B^{Zn}$ there will only be one unknown in equation (5.18) and the surface mole fraction of zinc can be

quickly obtained. As three different peak area ratios were found in the experiments, it is possible to determine three different answers for the surface composition. By making a comparison between these three surface compositions, it is possible to judge whether a suggested composition profile is a good fit or not, the closer the agreement, the better the fit. This process of assuming a profile and examination of the agreement of the resulting surface compositions was the approach adopted.

5.4.1 Average surface composition

Before considering possible composition profiles, the surface composition which is found directly from the peak area ratios was determined. This surface composition is only a first approximation, because the calculation gives a result which is in reality an average composition over the uppermost layers of the alloy. The surface mole fraction of zinc, θ_o^{Zn}, will be given by :

$$\theta_o^{Zn} = \frac{R}{1+R} \qquad (5.19)$$

where R is the Zn/Cu peak area ratio.

The surface compositions have been calculated using each of the three available peak area ratios for all four bulk composition alloys at every annealing temperature, and the results are shown in Table 5.7. These results are also shown graphically in Figure 5.3. Except for the 30% bulk Zn alloy, it can be seen that there are significant differences in the surface compositions calculated from the $2p_{3/2}$ (MgKα) peak area ratios and those calculated from the 3p peak area ratios at a fixed bulk composition and annealing temperature.

For the 30% bulk Zn alloy, a similar situation exists but the difference is not nearly as large. This suggests that the atomic layers immediately below the surface in the 30% bulk Zn alloy are enriched to a greater extent than in the 2%, 5% and 10% bulk Zn alloys, but this will be discussed later in the chapter when possible concentration profiles have been tried and their results have been discussed.

TABLE 5.7 Average surface mole fractions of zinc calculated from each peak area ratio for all four bulk composition alloys at each anneal temperature

Anneal Temp.	Peak	Source	Surface mole fraction of Zn			
			2% bulk Zn	5% bulk Zn	10% bulk Zn	30% bulk Zn
150°C	$2p_{3/2}$	MgKα	0.05	0.21	0.21	0.29
	$2p_{3/2}$	AlKα	0.04	0.16	0.19	0.30
	3p	MgKα	0.01	0.08	0.11	0.26
175°C	$2p_{3/2}$	MgKα	0.08	0.24	0.24	0.33
	$2p_{3/2}$	AlKα	0.07	0.20	0.21	0.32
	3p	MgKα	0.03	0.10	0.12	0.27
200°C	$2p_{3/2}$	MgKα	0.15	0.25	0.28	0.36
	$2p_{3/2}$	AlKα	0.11	0.21	0.23	0.35
	3p	MgKα	0.03	0.11	0.12	0.30
225°C	$2p_{3/2}$	MgKα	0.16	0.26	0.27	0.36
	$2p_{3/2}$	AlKα	0.11	0.21	0.21	0.34
	3p	MgKα	0.04	0.11	0.14	0.31
250°C	$2p_{3/2}$	MgKα	0.14	0.25	0.26	0.35
	$2p_{3/2}$	AlKα	0.11	0.21	0.22	0.32
	3p	MgKα	0.04	0.11	0.13	0.28
275°C	$2p_{3/2}$	MgKα	0.12	0.23	0.24	0.32
	$2p_{3/2}$	AlKα	0.10	0.19	0.19	0.30
	3p	MgKα	0.03	0.09	0.12	0.25
300°C	$2p_{3/2}$	MgKα	0.08	0.21	0.22	0.29
	$2p_{3/2}$	AlKα	0.06	0.17	0.18	0.26
	3p	MgKα	0.01	0.08	0.08	0.23
325°C	$2p_{3/2}$	MgKα	-	0.18	-	0.24
	$2p_{3/2}$	AlKα	-	0.14	-	0.25
	3p	MgKα	-	0.05	-	0.20

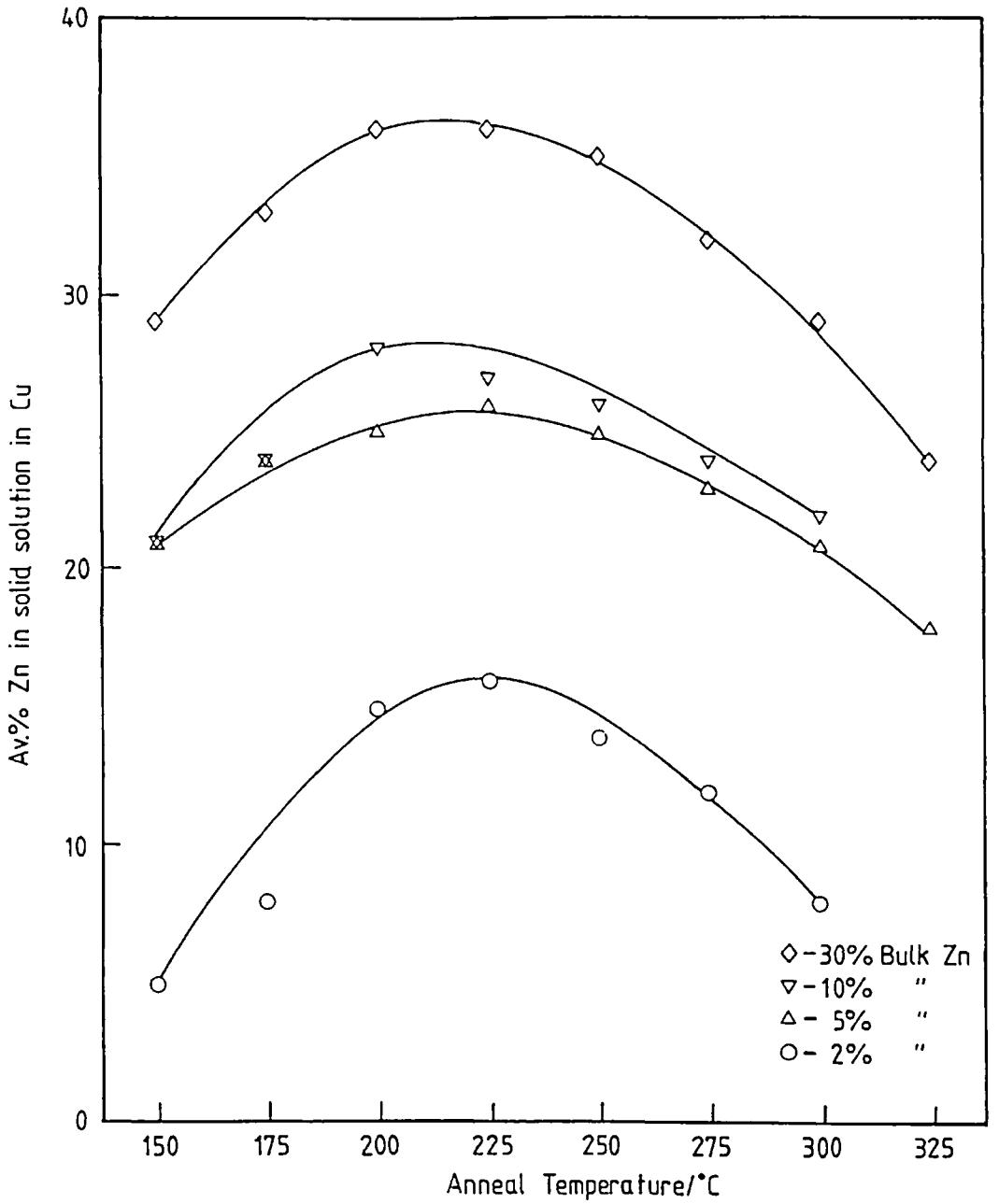


Figure 5.3. Average surface compositions as a function of annealing temperature

5.4.2 Top Layer Model

A simple advancement from calculating the average surface compositions is to assume a profile where all of the enrichment is confined to the surface layer only and all of the sub-surface layers are at bulk composition. This profile is illustrated in Figure 5.4 as a series of atomic layers. This model enables the maximum possible zinc content of the surface layer to be found, on the assumption that there is no depletion of the layers below the surface. This latter aspect will be discussed later in this section. The top layer model can be represented mathematically as :

$$\theta_i^{Zn} = \theta_o^{Zn} \quad \text{for } i = 0 \tag{5.20}$$

$$\theta_i^{Zn} = \theta_B^{Zn} \quad \text{for } i > 0 \tag{5.21}$$

By expanding equation (5.18), and substituting in the equations for the top layer model (equations (5.20) and (5.21)) and noting that $\theta_i^{Cu} = 1-\theta_i^{Zn}$ for any i, the following expression is obtained :

$$R = \frac{\sigma\left[\theta_o^{Zn} + \sum_{i=1}^{\infty} [\alpha(E_{Zn})]^i \theta_B^{Zn}\right]}{(1-\theta_o^{Zn}) + \sum_{i=1}^{\infty} [\alpha\ (E_{Cu})]^i\ (1-\theta_B^{Zn})} \tag{5.22}$$

In addition, by the binomial theorem :

$$\sum_{i=0}^{\infty} a^i = \frac{1}{1-a} \quad \text{for } 0 < a < 1$$

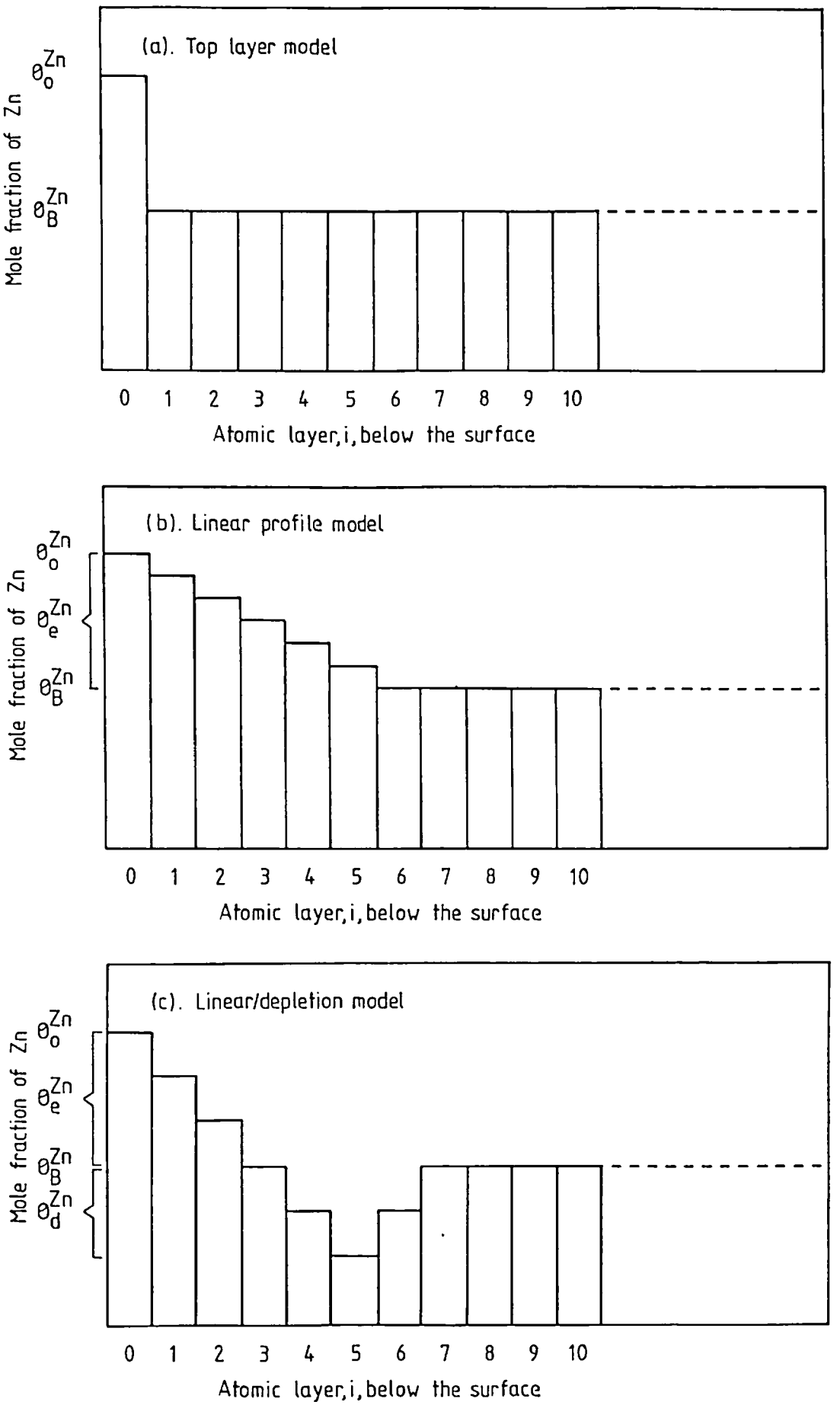


Figure 5.4. Layer by layer diagrams illustrating the different composition depth profile models used to establish the alloy surface compositions

Consequently, equation (5.22) can be written as :

$$\frac{R}{\sigma} = \frac{\theta_o^{Zn} - \theta_B^{Zn} + (\theta_B^{Zn}/(1-\alpha(E_{Zn}))}{\theta_B^{Zn} - \theta_o^{Zn} + (1-\theta_B^{Zn})/(1-\alpha(E_{Cu}))} \qquad (5.23)$$

This equation can be re-arranged to give the surface zinc mole fraction :

$$\theta_o^{Zn} = \frac{R\theta_B^{Zn} + \sigma\theta_B^{Zn} - \frac{\sigma\theta_B^{Zn}}{1-\alpha(E_{Zn})} + \frac{R(1-\theta_B^{Zn})}{1-\alpha(E_{Cu})}}{(R + \sigma)} \qquad (5.24)$$

Equation (5.24) can be used to calculate three values for the surface zinc mole fraction in a similar manner to that in the average surface composition calculation. The calculated surface zinc mole fractions using each of the three peak area ratios for all four bulk composition alloys at every annealing temperature are shown in Table 5.8. Two mole fractions are given for each peak area ratio, one corresponding to the calculation being based on the surface being predominantly composed of (100) faces and the second being based on the surface being mainly composed of (111) faces. The surface compositions found using the top layer profile will be discussed after other profiles have been presented.

5.4.3 Linear concentration profile model

In this model, there is a linear decrease in the zinc content of the atomic layers from the surface layer down to the bulk.

TABLE 5.8 Surface mole fractions of zinc calculated from the top layer model

	2% Bulk Zn Brass					
	(100) Face			(111) Face		
Peak Pair	2p(MgKα)	2p(AlKα)	3p(MgKα)	2p(MgKα)	2p(AlKα)	3p(MgKα)
Anneal Temp.						
150°C	0.08	0.06	-0.02	0.08	0.07	-0.02
175°C	0.14	0.12	0.04	0.14	0.13	0.04
200°C	0.26	0.22	0.04	0.27	0.24	0.05
225°C	0.30	0.23	0.06	0.31	0.25	0.07
250°C	0.26	0.23	0.06	0.27	0.25	0.07
275°C	0.22	0.20	0.04	0.22	0.22	0.04
300°C	0.13	0.10	-0.01	0.13	0.11	-0.02

	10% Bulk Zn Brass					
	(100) Face			(111) Face		
Peak Pair	2p(MgKα)	2p(AlKα)	3p(MgKα)	2p(MgKα)	2p(AlKα)	3p(MgKα)
Anneal Temp.						
150°C	0.31	0.30	0.08	0.32	0.32	0.08
175°C	0.37	0.33	0.11	0.38	0.36	0.11
200°C	0.44	0.38	0.14	0.46	0.41	0.14
225°C	0.43	0.36	0.18	0.44	0.39	0.18
250°C	0.41	0.36	0.15	0.42	0.39	0.15
275°C	0.36	0.29	0.11	0.37	0.31	0.11
300°C	0.33	0.27	0.08	0.34	0.29	0.01

	5% Bulk Zn Brass					
	(100) Face			(111) Face		
Peak Pair	2p(MgKα)	2p(AlKα)	3p(MgKα)	2p(MgKα)	2p(AlKα)	3p(MgKα)
Anneal Temp.						
150°C	0.36	0.30	0.11	0.37	0.32	0.11
175°C	0.41	0.38	0.17	0.43	0.41	0.18
200°C	0.43	0.41	0.22	0.44	0.44	0.23
225°C	0.45	0.41	0.23	0.47	0.45	0.23
250°C	0.43	0.41	0.22	0.45	0.44	0.23
275°C	0.39	0.36	0.14	0.40	0.39	0.15
300°C	0.36	0.32	0.12	0.38	0.35	0.12
325°C	0.30	0.24	0.04	0.31	0.26	0.04

	30% Bulk Zn Brass					
	(100) Face			(111) Face		
Peak Pair	2p(MgKα)	2p(AlKα)	3p(MgKα)	2p(MgKα)	2p(AlKα)	3p(MgKα)
Anneal Temp.						
150°C	0.28	0.25	0.08	0.27	0.26	0.07
175°C	0.36	0.32	0.12	0.35	0.34	0.11
200°C	0.42	0.39	0.22	0.42	0.41	0.21
225°C	0.41	0.37	0.25	0.41	0.39	0.25
250°C	0.39	0.31	0.12	0.38	0.33	0.12
275°C	0.33	0.26	0.03	0.33	0.27	0.02
300°C	0.27	0.16	-0.04	0.26	0.17	-0.05
325°C	0.18	0.15	-0.13	0.16	0.15	-0.14

The rate of decrease can be varied by adjusting the layer number, n, at which the bulk composition is reached. This model can be represented mathematically as :

$$\theta_i^{Zn} = \theta_B^{Zn} + \theta_e^{Zn} \left(\frac{n-i}{n} \right) \qquad \text{for } 0 \leqslant i \leqslant n \qquad (5.25)$$

$$\theta_i^{Zn} = \theta_B^{Zn} \qquad \text{for } i > n \qquad (5.26)$$

where θ_e^{Zn} is the excess mole fraction of zinc in the surface layer (i.e. $\theta_e^{Zn} = \theta_o^{Zn} - \theta_B^{Zn}$)

i is the layer number (i=0 represents the surface layer).

This model is illustrated in Figure 5.4. Equations (5.25) and (5.26) can be substituted into the basic equation , (5.18) and from this a relation can be found defining the excess mole fraction of zinc in the surface. This relation is given below:

$$\theta_o^{Zn} = \frac{B(1-\theta_B^{Zn})\alpha cs - \theta_B^{Zn} . \alpha zs}{B.cf + zf} + \theta_B^{Zn} \qquad (5.27)$$

where $\alpha cs = \sum_o^{\infty} [\alpha(E_{Cu})]^i$; $\alpha zs = \sum_o^{\infty} [\alpha(E_{Zn})]^i$

$B = R/\sigma$

$$cf = \sum_o^{\infty} [\alpha(E_{Cu})]^i \left(\frac{n-i}{n} \right)$$

$$zf = \sum_{o}^{n} [\alpha(E_{Zn})]^{i} \left(\frac{n-i}{n} \right)$$

A full derivation of equation (5.27) is given in Appendix I. Unlike the top layer model, a variety of possible surface zinc concentrations can result from equation (5.27) because the parameter, n, is not set. A series of calculations were made, giving a set of three surface zinc concentrations for various values of n. A summary of these results is given in Table 1 in Appendix II. It was decided to quote the results for two extremes, using $n = 2$ and $n = 10$ and to consider these. With $n = 2$, the profile is similar to the top layer model ($n = 1$ gives the top layer model). However, with $n = 10$, there is a much more gradual change in the zinc concentration from the enriched surface layer to the bulk which is achieved at 10 layers below the surface. It was found that the results for the three zinc concentrations changed only slightly at high values of n (i.e. $n = 8$ or above) for an alloy with the same bulk composition annealed at the same temperature, so the results at $n = 10$ were quoted. In a similar way to the top layer model, two sets of three surface zinc concentrations were calculated, one set being determined using an inter-layer spacing associated with a surface predominantly composed of (100) faces and the second set being based on a surface composed of (111) faces. The application of the linear profile model to the segregation data will be discussed after the next model is presented.

5.4.4 Exponential concentration profile model

This model is almost identical to the linear model, except that there is an exponential change in the zinc concentration from the surface layer to the layer n, at which bulk is achieved. This model can be represented mathematically as :

$$\theta_i^{Zn} = \theta_B^{Zn} + \theta_e^{Zn} \exp(-xi) \quad \text{for } 0 \leqslant i \leqslant n \tag{5.28}$$

$$\theta_i^{Zn} = \theta_B^{Zn} \quad \text{for } i > n \tag{5.29}$$

where $x = \dfrac{4.6}{n}$

Bulk composition was assumed to be reached when the surface excess of zinc was reduced to 1% of its original value by the exponential term in equation (5.28) and hence a value of x was easily found. Again, by substituting equations (5.28) and (5.29) into the basic equation, (5.18), a relation can be found which represents this model. This relation is given below :

$$\theta_o^{Zn} = \frac{B(1-\theta_B^{Zn}).\ \alpha cs - \theta_B^{Zn}.\ \alpha z\, s}{B.cf + z\, f} + \theta_B^{Zn} \tag{5.30}$$

where $cf = \sum_o^n [\alpha(E_{Cu})]^i \exp(-xi)$

$zf = \sum_o^n [\alpha(E_{Zn})]^i \exp(-xi)$

The terms αcs, αzs and B were defined after equation (5.27). This expression was derived in the same way as equation (5.27). A similar analysis to that carried out for the linear model was applied for the exponential model, and all of the comments which were made about the results of the analysis for the linear model also extend to the exponential model. The results of the application of equation (5.30) to the segregation results are shown in Table 2 in Appendix II. Again, a summary of results is quoted, using n = 2 and n = 10, and two calculations were made for each bulk alloy and anneal temperature to illustrate the difference in the results if the surface of the alloy is predominantly composed of (100) or (111) faces.

5.4.5 Discussion of the top layer, linear and exponential models

From the results of the application of the top layer, the linear profile and the exponential profile models to the peak area ratios obtained from the segregation experiments, it can be seen that none of these models is a good representation of the composition profile with depth for any of the alloys, if the criterion of a good fit being based on the surface zinc contents of a set of three being almost identical is used. In the results for the top layer model, a decrease in the surface enrichment occurs with increasing bulk composition (not including the 2% bulk alloy) for calculations made at similar anneal temperatures.

This decrease in surface enrichment with increasing bulk zinc content is in total disagreement with the trends of the peak area ratios obtained directly from the experiments. Consequently, the top layer model cannot be used to calculate surface compositions.

In the case of the linear profile and the exponential profile models, it can be seen that although the two surface zinc contents calculated from the two 2p peak area ratios agree to a reasonable extent in places, the surface composition calculated from the 3p peak area ratio does not agree with the other two. The latter composition is always smaller, and this could be attributed to the possibility that depletion layers are formed in the alloy immediately below the surface. Somorjai and Overbury[27] made a theoretical study of alloys, and showed that alloys with an exothermic heat of solution would form depletion layers. The heat of solution of zinc in copper is -9.18 kcal/mol (-38.5 kJ/mol)[117], so it is certainly possible that depletion layers do occur in brasses. Alloys with a positive heat of solution do not show this property. The form of the composition depth profile predicted by Somorjai and Overbury is shown in Figure 5.5. Consequently, models were developed which took into account the formation of depletion layers, but which were easier to handle than the profile illustrated in Figure 5.5.

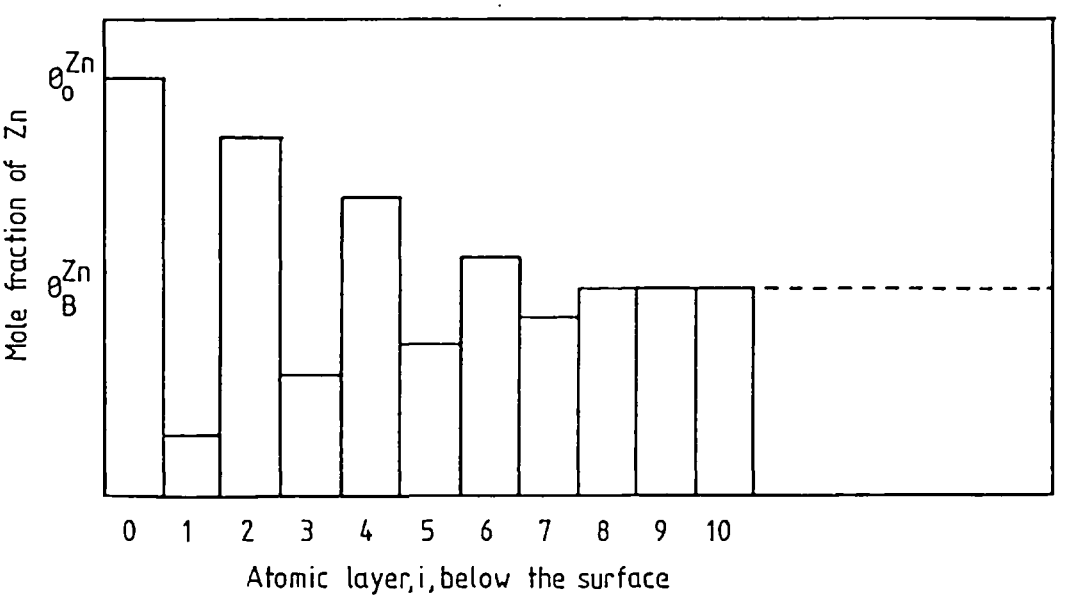


Figure 5.5. Predicted composition depth profile for an alloy with an exothermic heat of solution

5.4.6 Linear concentration profile with depletion layers

This model is similar to the linear model presented earlier over the first few layers, except that in this case, the linear change in zinc concentration finishes at a zinc concentration below that of bulk. This is illustrated in Figure 5.4. The model is represented mathematically as follows :

$$\theta_i^{Zn} = (\theta_B^{Zn} - \theta_d^{Zn}) + (\theta_e^{Zn} + \theta_d^{Zn}) \left(\frac{m-i}{m}\right) \quad \text{for } 0 \leq i \leq m \qquad (5.31)$$

$$\theta_i^{Zn} = (\theta_B^{Zn} - \theta_d^{Zn}) + \left(\frac{i-m}{n-m}\right) \theta_d^{Zn} \quad \text{for } m+1 < i < n \qquad (5.32)$$

$$\theta_i^{Zn} = \theta_B^{Zn} \quad i > n \qquad (5.33)$$

where θ_d^{Zn} is the extent of zinc depletion at the maximum point below the bulk

m is the layer at which maximum depletion is attained

n is the layer at which the bulk composition is attained.

By the usual substitution of equations (5.31), (5.32) and (5.33) into equation (5.18), the following expression can be found :

$$\theta_o^{Zn} = \frac{B(1-\theta_B^{Zn}).\alpha cs - [B.cf+zf-B.mcf-mzf]\theta_d^{Zn} - \alpha zs.\theta_B^{Zn}}{(B.cf + zf)} + \theta_B^{Zn} \qquad (5.34)$$

where $cf = \sum_o^m [\alpha(E_{Cu})]^i \left(\frac{m-i}{m}\right)$

$$zf = \sum_o^m [\alpha(E_{Zn})]^i \left(\frac{m-i}{m}\right)$$

$$mcf = \sum_{o}^{n} [\alpha(E_{Cu})]^i - \sum_{m+1}^{n} [\alpha(E_{Cu})]^i \left(\frac{i-m}{n-m}\right)$$

$$mzf = \sum_{o}^{n} [\alpha(E_{Zn})]^i - \sum_{m+1}^{n} [\alpha(E_{Zn})]^i \left(\frac{i-m}{n-m}\right)$$

The terms αcs, αzs, θ_o^{Zn}, θ_B^{Zn} and B were defined previously.

Equation (5.34) was derived in a similar manner to the equation for the linear profile model (5.27). A linear profile was assumed between the layer of maximum depletion and the layer at which bulk composition was attained. Changes in this part of the overall model would have a lesser significance on the surface compositions obtained using the model compared with changes in the profile between the surface layer and the point of maximum depletion. To simplify the overall analysis, the profile between the point of maximum depletion and the point where bulk composition was attained was not varied.

Application of the linear/depletion model gives three parameters which can be varied. These are m and n, the positions where maximum depletion and bulk composition are attained respectively, and θ_d^{Zn}, the extent of zinc depletion below the surface. As with previous models, the model was applied to the experimental results using a large variety of values of n and also of m and θ_d^{Zn}. A summary of these results is presented in Table 3 in Appendix II. The results are quoted for m = 1, m = 2 and m = 10 which illustrate the effect of two extremes of the

position of maximum depletion. Above m = 10, there is only a small change in the calculated surface compositions with increasing m. For m = 1 and m = 2, which represent the maximum depletion point being formed just below the surface, it was found that the surface compositions calculated from the two $2p_{3/2}$ peak area ratios changed only slightly with increasing values of n, the position where bulk composition is attained. However, the surface composition calculated from the 3p ratio did depend on the value of n. As n was increased, the difference between the surface compositions obtained from the $2p_{3/2}$ and the 3p ratios became smaller. At higher values of n, above n = 10, there was not much change in the surface composition calculated from the 3p ratio. As there was generally a better agreement between the three surface compositions at higher values of n, the results quoted in Table 3 for m = 1 and m = 2 are for a value of n = 10. For m = 10, which represents the maximum depletion point being much deeper below the surface, it was found that increasing values of n above n =12 did not affect the calculated surface compositions significantly, so the results are quoted for n = 16. The only parameter which has not been set yet is the extent of depletion, θ_d^{Zn}. Again, to illustrate the effect of this parameter briefly, two extremes are considered. The first extreme is with almost no depletion and this will give results which are essentially identical to the linear profile model presented in section 5.4.3. The other extreme is to assume that the depletion is such that the layer at maximum depletion

is composed of 100% copper. This latter case, with $\theta_d^{Zn} = \theta_B^{Zn}$, is quoted in Table 3. The results of the application of the linear/depletion model will be discussed after the next model has been presented.

5.4.7 Exponential concentration profile with depletion layers

This model is very similar to the previous model, except that there is an exponential change in the concentration profile between the surface layer and the point of maximum depletion instead of a linear change. Again to simplify the analysis, a linear profile was assumed between the point of maximum depletion and the point where bulk composition was reached.

The model is represented mathematically below :

$$\theta_i^{Zn} = (\theta_B^{Zn} - \theta_d^{Zn}) + (\theta_d^{Zn} + \theta_e^{Zn}) \exp(-xi) \quad \text{for } 0 \leqslant i \leqslant m \qquad (5.35)$$

$$\theta_i^{Zn} = (\theta_B^{Zn} - \theta_d^{Zn}) + (\frac{i-m}{n-m})\ \theta_d^{Zn} \qquad m+1 \leqslant i \leqslant n \qquad (5.36)$$

$$\theta_i^{Zn} = \theta_B^{Zn} \qquad i > n \qquad (5.37)$$

Again, by substituting these equations into equation (5.18), the surface composition is given by :

$$\theta_o^{Zn} = \frac{B(1-\theta_B^{Zn}).\alpha cs - [B.cf + zf - B.mcf - mzf]\theta_d^{Zn} - \alpha zs.\theta_B^{Zn}}{B.cf + zf} + \theta_B^{Zn} \qquad (5.38)$$

$$\text{where } cf = \sum_{o}^{n} [\alpha(E_{Cu})]^{i} \exp(-xi)$$

$$zf = \sum_{o}^{n} [\alpha(E_{Zn})]^{i} \exp(-xi)$$

The terms αcs, αzs, θ_o^{Zn} , θ_B^{Zn} and B were defined previously. The terms mcf and mzf are the same as they were for the linear/depletion model, and are therefore defined in the previous section.

Application of this model to the experimental results produced results which followed similar trends to the linear/depletion model, but gave greater enrichment in the surface. A summary of the results from applying this model is presented in Table 4 in Appendix II. The results are quoted for m = 2 with n = 10, and for m = 10 with n = 16 with $\theta_d^{Zn} = \theta_B^{Zn}$. These values of n,m and θ_d^{Zn} have been used in the summary for the reasons discussed in the previous section for the linear/depletion model. The results from this model for m = 1 are identical to those obtained with m = 1 in the linear/depletion model.

5.4.8 Discussion of the depletion models

Consideration of the results from applying the linear/depletion and exponential/depletion models, shows that there is a better agreement between the surface zinc contents calculated from the three peak area ratios when models which include depletion layers are applied. The results from the depletion models also show that there is a generally better agreement between the three calculated surface compositions when maximum

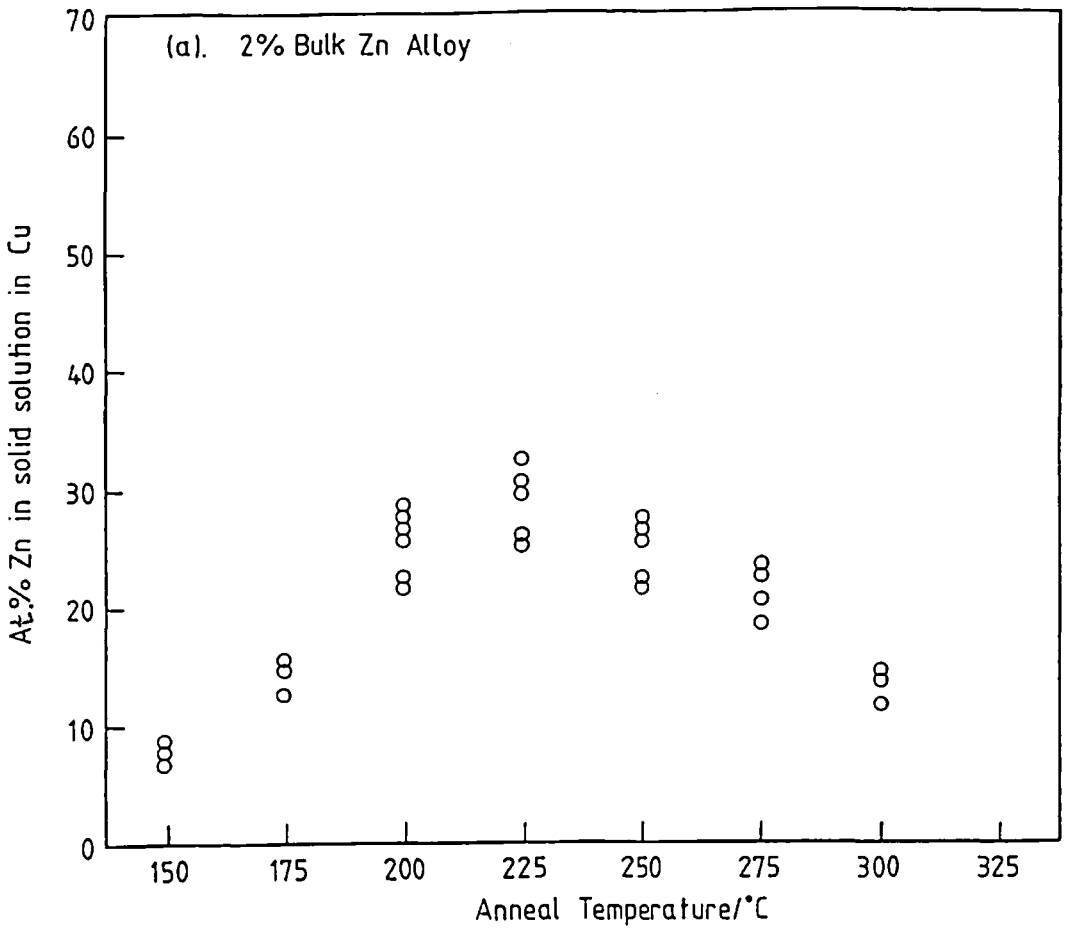
depletion is reached just below the surface (i.e. m = 1 or m = 2), except for the 30% bulk Zn alloy which will be discussed later. The better agreement for the model where maximum depletion is reached just below the surface and the predictions of Somorjai and Overbury[27] described earlier suggest that this type of model is more representative of the real profile and that the surface compositions calculated using these models will be more accurate than for the model where maximum depletion is reached at many layers below the surface. However, it is much more difficult to determine whether any one of the remaining models is more accurate than the others, as all give similar extents of agreement between the three calculated surface zinc contents. Similarly, it is difficult to tell whether the surface was predominatly composed of (100) or (111) surfaces, again because the extents of agreement are much the same. It was decided therefore to represent the surface composition as a function of annealing temperature for each alloy as a band of compositions composed of the results from three models. These models are the linear/depletion profile with m=1, n=10 and m=2, n=10 and the exponential/depletion profile with m = 2, n = 10. As it was difficult to determine whether the (100) or (111) face gave more accurate results, the values for both of these from each model were employed in the band.

In the tables for the calculated surface compositions, the results are quoted assuming that the maximum depletion layer is 100% Cu. It was found that for the 2%, 5% and 10% bulk Zn alloys, the best agreement between the three calculated surface compositions for a given anneal temperature for a given alloy was

with a maximum depletion of 100% Cu. The 30% bulk Zn alloy will be discussed later. It was also found that the surface compositions calculated from the surface sensitive peak area ratios hardly changed with changes in the extent of the maximum depletion, θ_d^{Zn}. Again it was difficult to establish what value of θ_d^{Zn} was correct for each alloy, so the results based on $\theta_d^{Zn} = \theta_B^{Zn}$ (i.e. 100% Cu) were used for the 2%, 5% and 10% bulk Zn alloys. The surface composition bands against annealing temperature for these three alloys are shown in Figure 5.6.

Despite incorporating depletion layers into the models, there is still a difference between the surface compositions calculated from the two $2p_{3/2}$ peak area ratios and that calculated from the 3p peak area ratio. There are two possible reasons for this discrepancy. The IMFPs were not necessarily accurate and this would lead to errors in the final surface compositions. Secondly, although simple models were used to represent the composition profiles, it is difficult to establish exactly what happened below the surface from the experimental data, and this will introduce a significant uncertainty which should effect the 3p peak area ratio most because it is much less surface sensitive.

In the case of the 30% bulk Zn alloy, the surface compositions calculated from the 3p peak area ratios were similar or greater than the other two, and the results for the surface zinc contents cannot be treated in the same way as in the


(a). 2% Bulk Zn Alloy
At.% Zn in solid solution in Cu
0
10
20
30
40
50
60
70
150
175
200
225
250
275
300
325
Anneal Temperature/°C

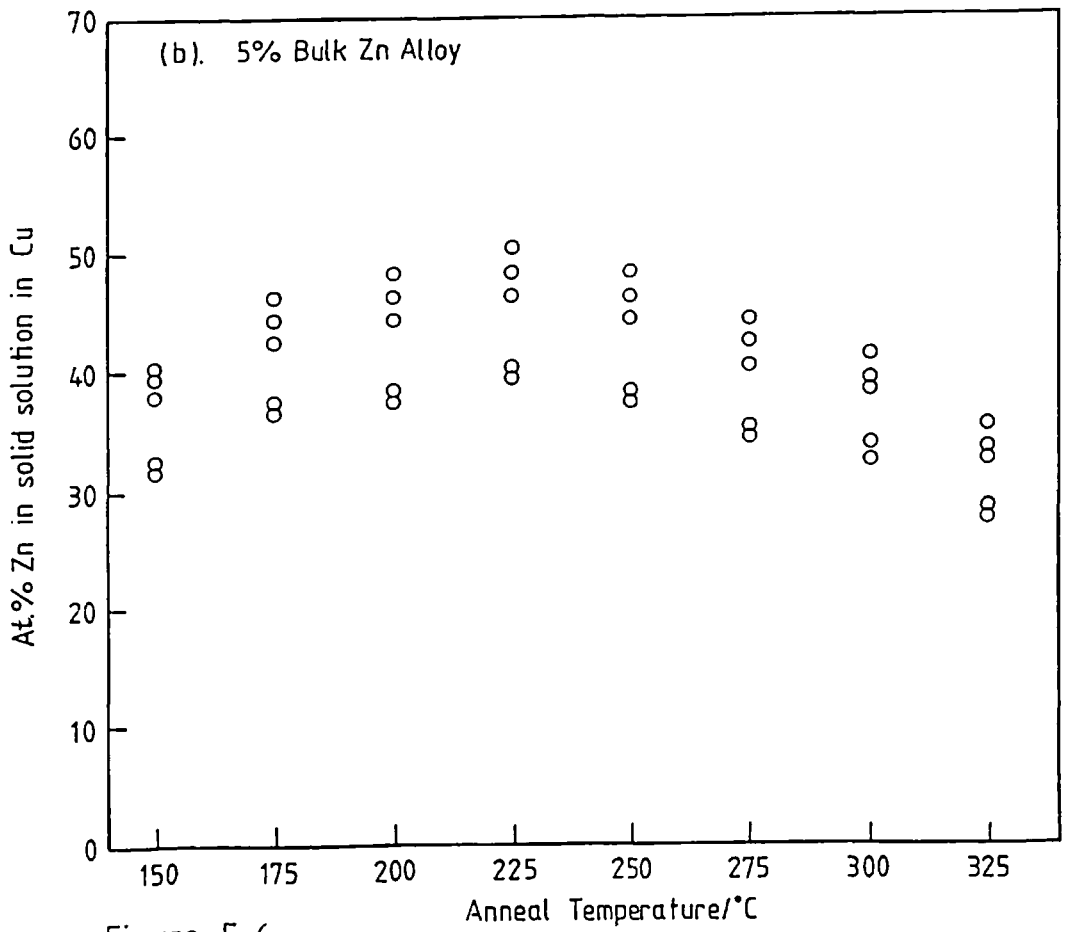

(b). 5% Bulk Zn Alloy
At.% Zn in solid solution in Cu
0
10
20
30
40
50
60
70
150
175
200
225
250
275
300
325
Anneal Temperature/°C

Figure 5.6.

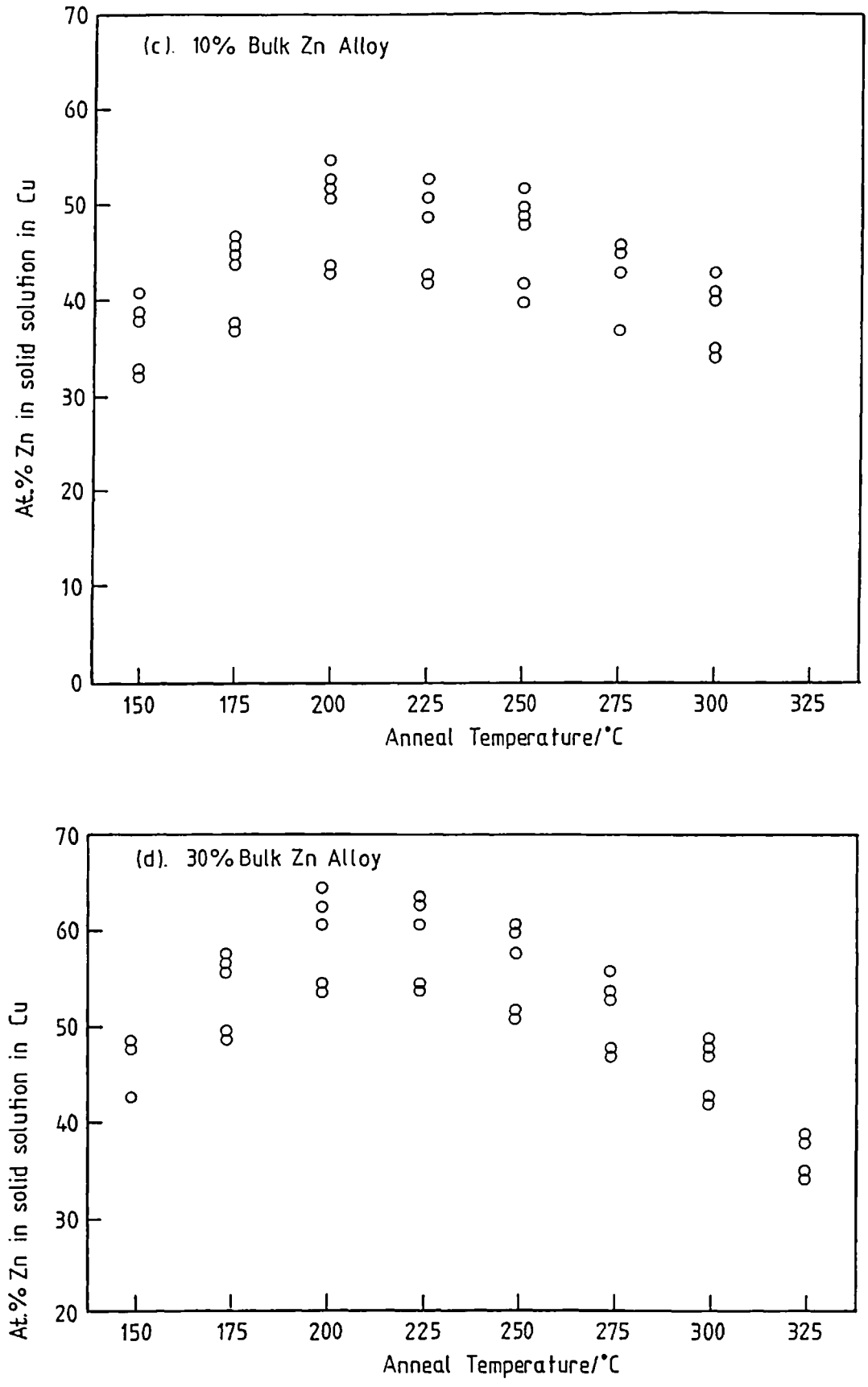


Figure 5.6. Surface compostion 'bands' as a function of annealing temperature resulting from the application of different composition depth profile models to the segregation results

previous three alloys, as the agreement criterion does not give as clear cut results as previously. It is unlikely that the linear/depletion and the exponential/depletion models with m = 10, n = 16, are correct because a comparison of the results of these models with the composition bands of the 5% and 10% bulk Zn alloys shows that the values for the 30% bulk Zn alloy are similar or less than those of the 5% and 10% bulk Zn alloys. This is in contradiction to the trends of the peak area ratios, as shown in Figure 5.1. However, the agreement between the sets of calculated surface compositions from the remaining models with $\theta_d^{Zn} = 0.3$ is not particularly good. A generally better agreement was obtained by putting $\theta_d^{Zn} = 0.2$, and the results for the linear/depletion model with m = 1, n = 10 and m = 2, n = 10 and for the exponential/depletion model with m = 2, n = 10 with $\theta_d^{Zn}=0.2$ are shown in Table 5 in Appendix II. As with the 2%, 5% and 10% bulk Zn alloys there is no real evidence to suggest that either the (100) or (111) faces give more accurate results. As a result of this, a composition band for the 30% bulk Zn alloy is shown in Figure 5.6 which uses the three models described above with $\theta_d^{Zn} = 0.2$ and incorporates surface zinc contents using both the (100) and the (111) faces.

In all four alloys, it is possible that the extent of depletion, θ_d^{Zn}, is dependent on the anneal temperature. However, it would be necessary to carry out more extensive experiments to establish this more accurately. It was felt that the experimental data from this work was insufficient to investigate

the temperature dependence of θ_d^{Zn} so θ_d^{Zn} was kept constant for each bulk alloy.

It has been shown that zinc segregates to the surface of Cu/Zn alloys. If brass is formed in methanol synthesis catalysts, then it may be that zinc segregation will determine the amount of surface zinc in the catalyst. This point will be discussed in Chapter 9, after the results of the work on the $Cu/ZnO/Al_2O_3$ catalysts have been considered.

CHAPTER 6

CO CHEMISORPTION ON POLYCRYSTALLINE COPPER, ZINC AND BRASS SURFACES

The adsorption of CO onto the catalyst surface is one of the principal stages in the methanol synthesis mechanism. If brass formation occurs in the methanol synthesis catalyst, then the CO adsorption characteristics may be altered by the presence of surface zinc which may subsequently affect the catalyst activity. The effect of brass formation on the chemisorption of CO was studied by making a comparison of CO adsorption on pure copper and a variety of brasses with different surface compositions. In all cases, the adsorption of CO was carried out with sample temperatures between 90K and 100K. These adsorption temperatures are suitable for CO adsorption, although they are slightly higher than those used previously by the majority of workers studying CO on copper.

6.1 Chemisorption of CO on polycrystalline copper

6.1.1 Uptake of CO

The uptake of CO on copper was studied by monitoring the changes in intensity of the C1s, O1s and $Cu2p_{3/2}$ peaks with increasing CO dose. The procedure used to develop the uptake curve was that the sample was initially exposed to 0.5L CO, then the C1s, O1s and $Cu2p_{3/2}$ spectra were taken and finally the adlayer was desorbed to give a TPD spectrum (see section 6.1.3). Immediately after the sample had cooled back to 90K, a 1L dose

of CO was given and again the C1s, O1s, $Cu2p_{3/2}$ and TPD spectra were taken. This process of adsorption/desorption was repeated with increasing CO doses until the uptake curve was fully developed. In all cases, CO doses were made at a pressure of 2×10^{-8} torr for the appropriate length of time. The intensity changes in the C1s, O1s and $Cu2p_{3/2}$ spectra as a function of dose are shown in Figure 6.1. It can be seen from the uptake curves that copper has an initial sticking coefficient of approximately unity and that the surface is essentially saturated after a dose of 2L. This is in general agreement with the previous results described in Chapter 2. There is evidence to suggest that there is a further gradual increase in the C1s and O1s peak intensities above a dose of 2L CO. This would correspond to the formation of the CO compression structures on the copper surface. The formation of the compression structure will be discussed further in section 6.1.3 when the desorption spectra have been presented.

A second experiment was carried out in which successive adsorption was used instead of adsorption/desorption cycles, and this gave similar results.

6.1.2 Photo-electron spectra of chemisorbed CO

The C1s and O1s peaks resulting from the adsorption of CO on a polycrystalline copper surface both gave broad spectra with widths of approximately 10eV. Typical C1s and O1s spectra of the chemisorbed CO are shown in Figures 6.2 and 6.3

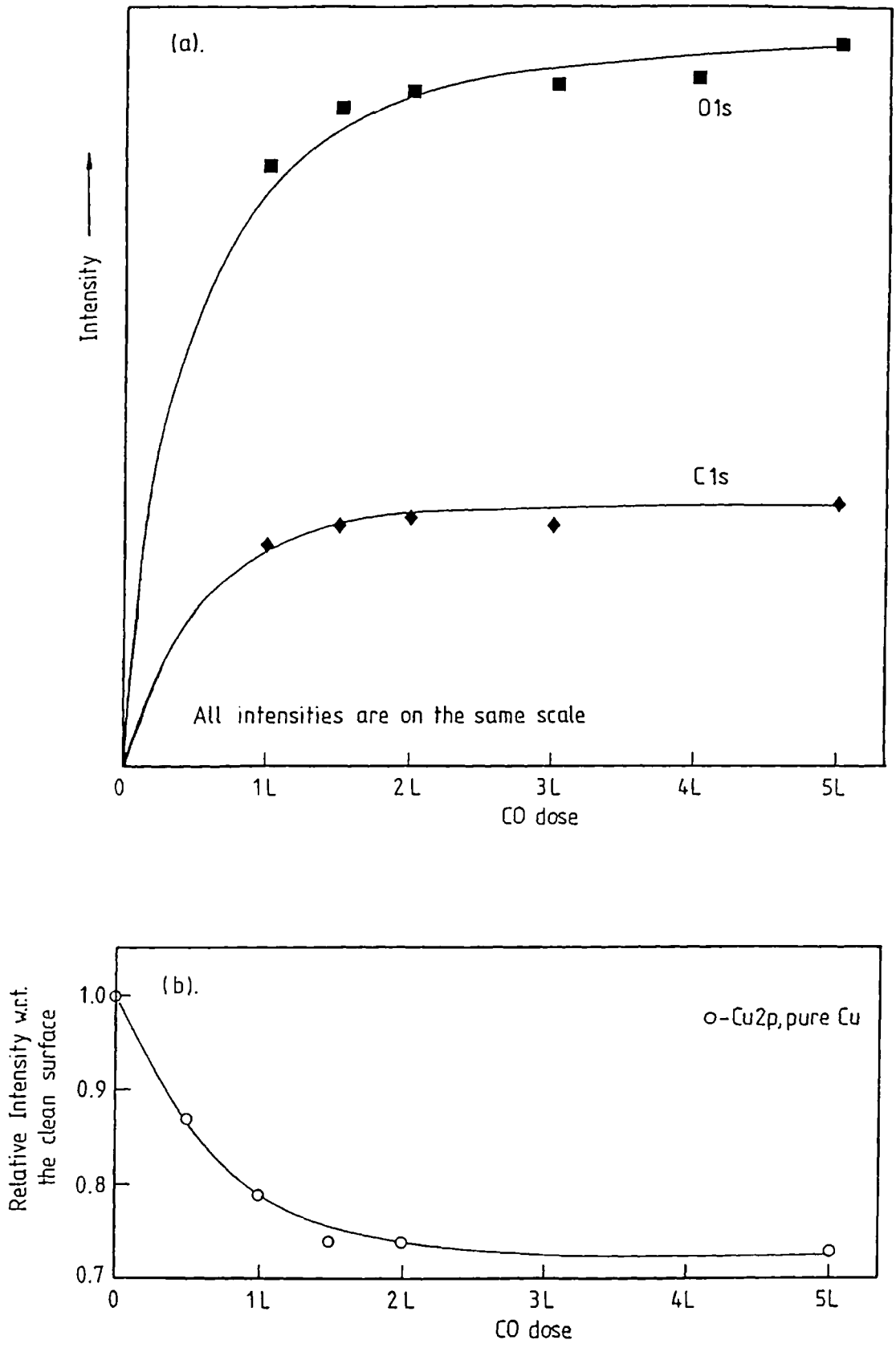


Figure 6.1. C1s,O1s & $Cu2p_{3/2}$ peak intensities as a function of CO dose on pure polyx Cu

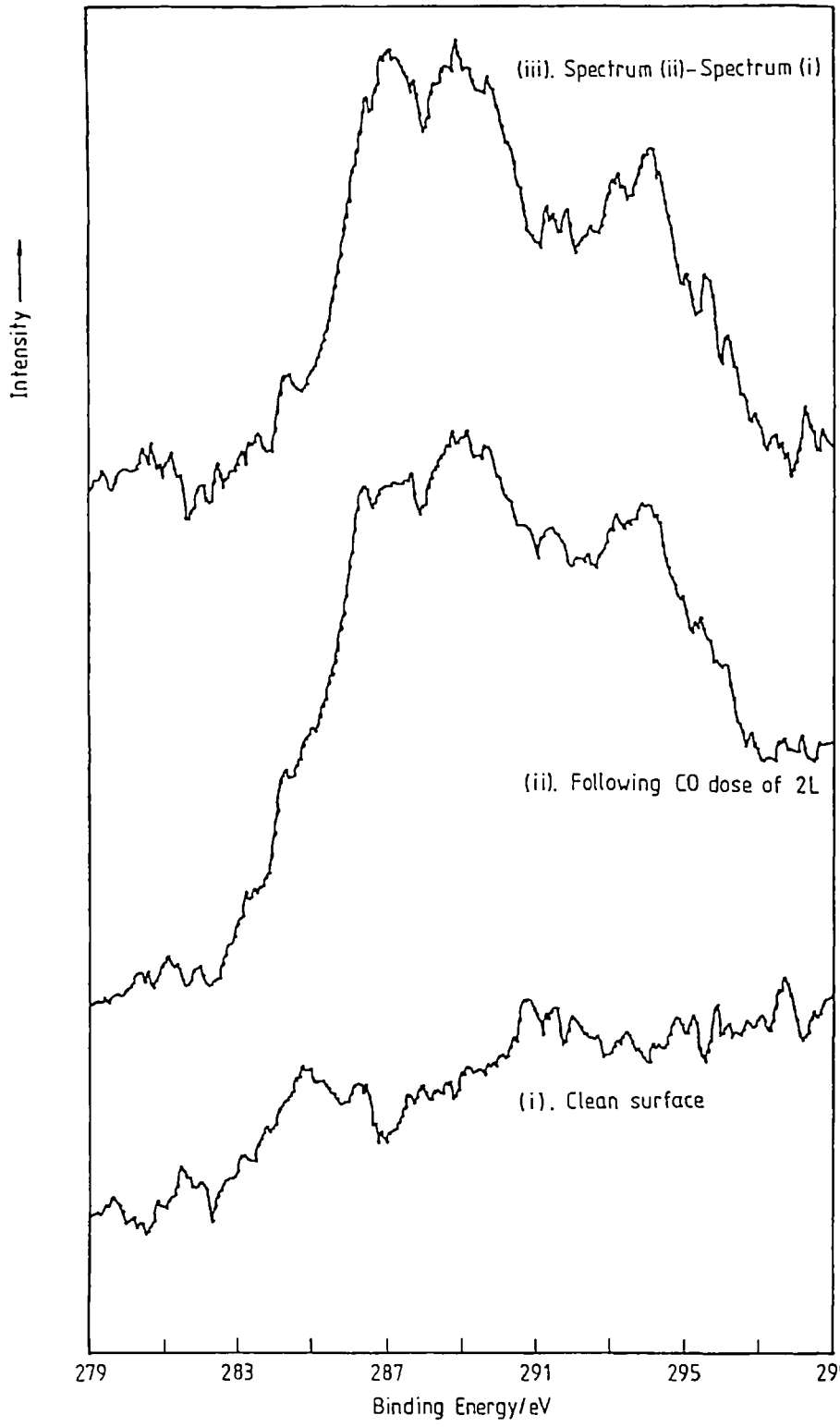


Figure 6.2. C1s spectra of CO chemisorbed on a pure polyx copper surface

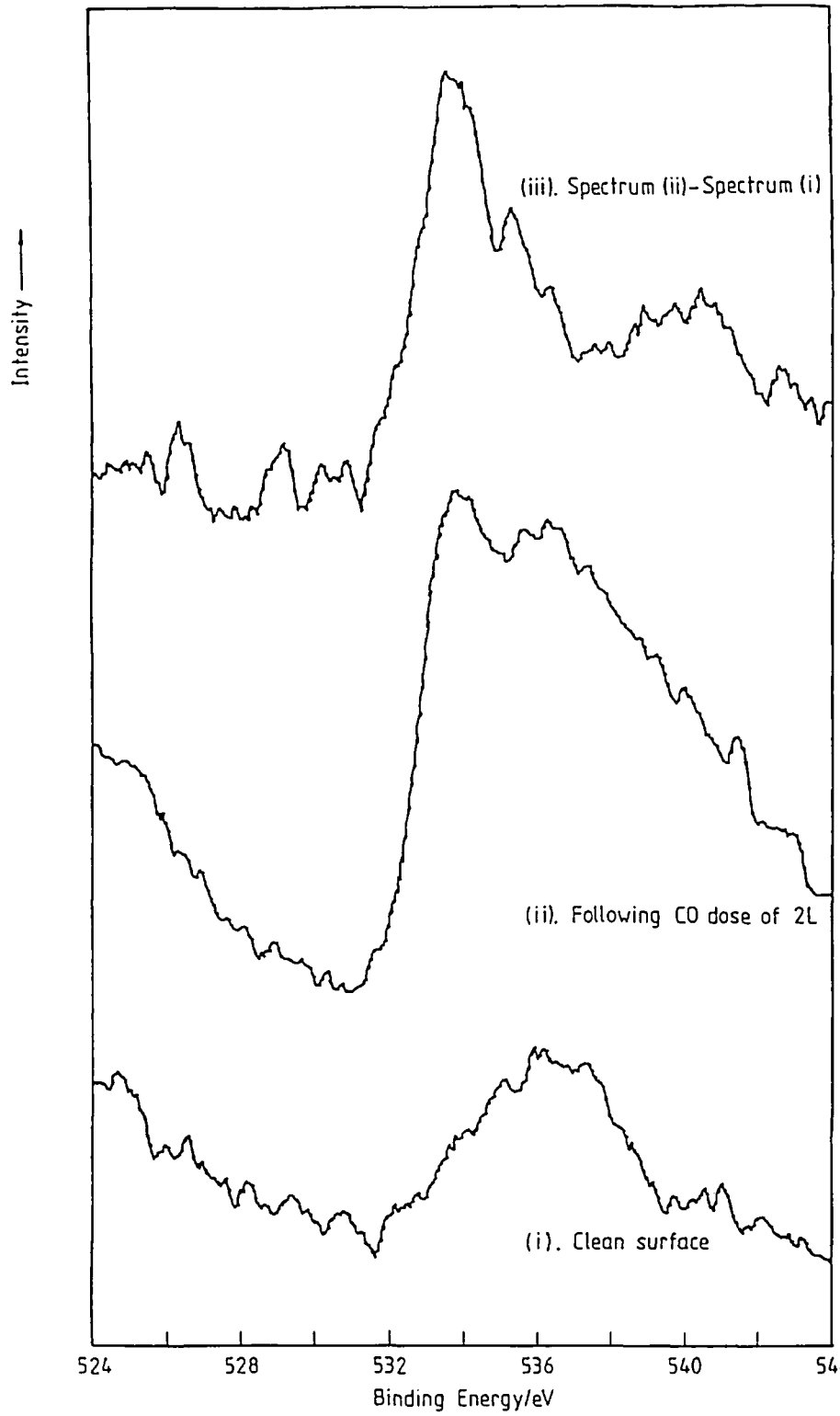


Figure 6.3. O1s spectra of CO chemisorbed on a pure polyx copper surface

respectively, along with the spectra of the clean surface. The O1s spectral region of the clean surface showed two broad peaks centred at ∿ 520eV and ∿ 536eV. These two peaks represented two copper Auger peaks, so the O1s spectrum of the adsorbed CO is also shown with these Auger peaks subtracted out. Similarly, a C1s subtraction spectrum of the adsorbed CO is also shown in Figure 6.2. The line-shape of both the C1s and O1s spectra were similar to those obtained by Norton et al[37]. This would suggest that both spectra are composed of three peaks and a closer inspection would appear to support this. An approximate deconvolution of the spectra gave characteristics as shown in Table 6.1.

TABLE 6.1 Characteristics of the C1s and O1s spectra

Peak	Binding Energy/eV	Approx. Half Width/eV
C1s (i)	286.7 ± 0.2	2.0
(ii)	289.3 ± 0.2	2.6
(iii)	293.6 ± 0.2	3.6
O1s (i)	533.5 ± 0.2	2.2
(ii)	536.1 ± 0.2	2.7
(iii)	540.2 ± 0.2	3.4

Note (i) These values are quoted following a dose of 2L CO at 90K

(ii) All B.E.s are referred to the B.E. of the $Cu2p_{3/2}$ peak at 932.8eV.

These binding energies agree favourably with those of Norton et al[37], and the higher pair of B.E.s for the C1s spectra also agree favourably with those of Isa et al[32] for their (100) surface. The discrepancy between the O1s B.E.s obtained in this work and those of Isa et al have been discussed already in Chapter 2.

The C1s and O1s spectra kept their three peak structure down to the lowest dose of CO (0.5L) and the B.E.s of the individual peaks remained essentially constant, indicating that the spectra were coverage independent. This point will be discussed further in section 6.1.3 after the CO desorption spectra have been presented.

6.1.3 Desorption of CO from polycrystalline copper surfaces

Desorption spectra were obtained following exposure of the sample to similar CO doses to those used to obtain the series of spectra for the adsorbed CO, and these are shown in Figure 6.4. It can be seen that up to 1L CO, the desorption spectra showed what appeared to be a two peak structure with the main peak having a T_{max} of 175K and the shoulder T_{max} being around 200-205K. The higher energy peak forming the shoulder appears to be excessively broad on the trailing edge, so it is difficult to state exactly where T_{max} lies. This is why a temperature range has been used to describe the T_{max} of this peak. The problem of broadening and background CO will be discussed

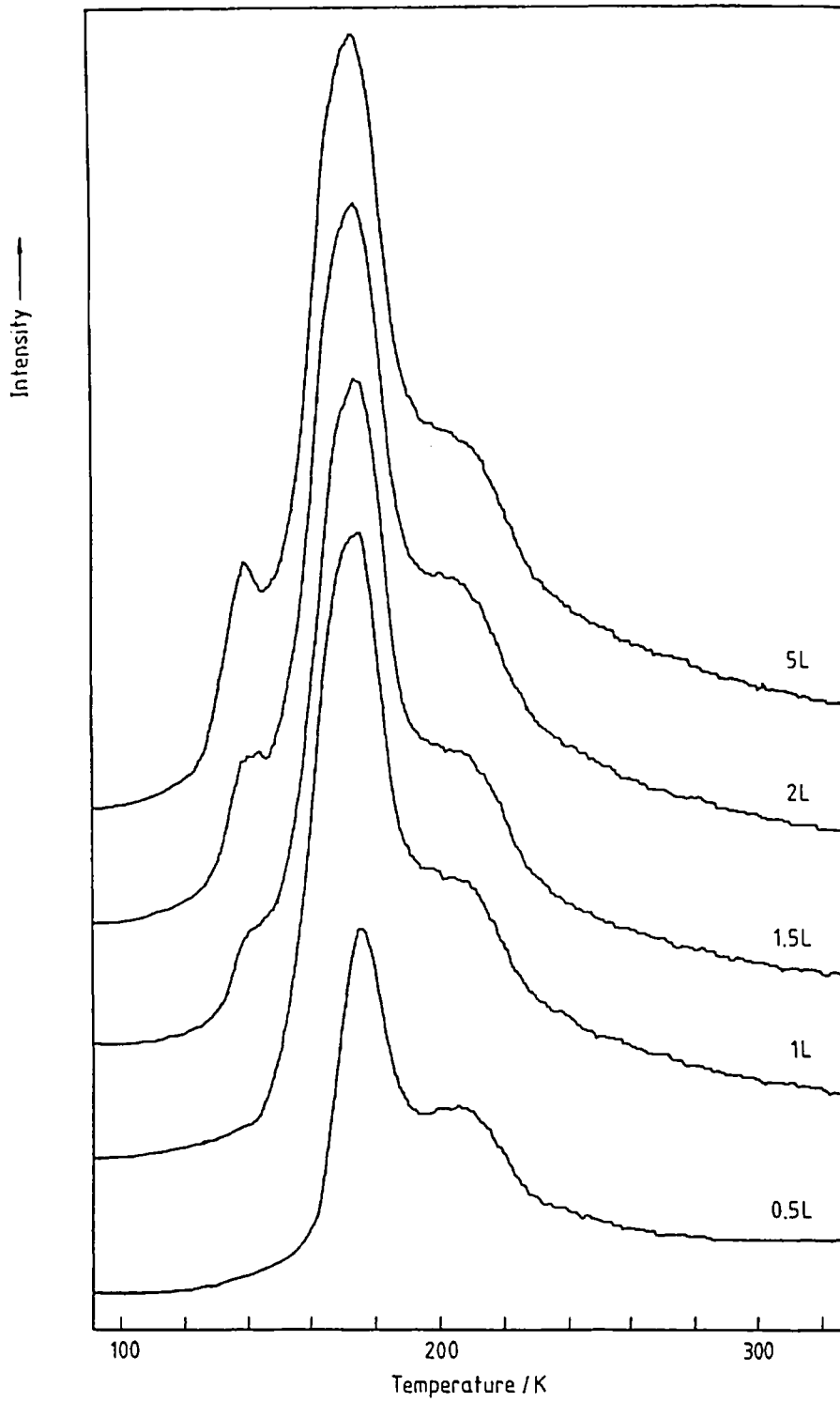


Figure 6.4. TPD spectra of CO desorbing from pure polyx copper as a function of CO dose

later in this section.

At 1.5L, a new peak appeared in the spectrum which had a T_{max} of 140K. This peak became enhanced with increasing doses of CO above 1.5L whilst there was only a slight increase in the size of the major peaks. Use of Redhead's analysis[98] to estimate the activation energy for desorption (E_d) by assuming that the pre-exp. factor was $10^{13} sec^{-1}$ gave an E_d for this peak of 37 kJ/mol. This approximate activation energy is similar to that obtained by Kessler and Thieme[50] for a weakly adsorbed state on their polycrystalline copper surface, using a work-function against temperature method. This weakly adsorbed state was interpreted by Kessler and Thieme as the CO compression structure. As a result of this, the low energy peak with a T_{max} of 140K is interpreted as the desorption of the CO which formed the compression structure. This interpretation can be supported by consideration of the uptake curves, shown in Figure 6.1. When the third, low energy, desorption peak appeared the surface was near saturation. As mentioned previously, the CO compression structure increases the coverage by a small extent after saturation coverage has almost been achieved. Secondly, a comparison of the size of the peak with a T_{max} of 140K with the main peaks shows that it corresponded to a smaller additional increase in the coverage.

The general lineshape of the desorption spectrum above 160K was similar to that obtained by Ertl et al[58] for their Cu (111) surface, but the ratio of the main peak height to the shoulder

height was different, and the spectrum in this work was broadened on the high temperature side. Ertl et al interpreted the peak with a T_{max} of 175K as the desorption of the CO which formed the compression structures. This interpretation appears to be incorrect because the peak which Ertl et al obtained at 175K was larger than the shoulder peak and this would mean that the compression structure corresponded to a greater coverage than the CO adsorbed in an ordered manner. The other piece of evidence which shows that the interpretation of Ertl et al is incorrect is the appearance of a peak at 140K at high CO coverage in the TPD spectra of this work. An approximate value of E_d for the largest peak at 175K in this work was 46 kJ/mol, and again this was found using Redhead's method. This suggests that the main peak in the desorption spectra was associated with the desorption of CO from the (111) surfaces of the sample as Kessler and Thieme found that the activation energy for desorption of CO from these surfaces was 45 kJ/mol and Ertl et al[41] found that the heat of adsorption of CO on these surfaces was 48 kJ/mol. Application of Redhead's analysis to a peak with a T_{max} of 200K to 205K gives an activation energy range of 53-55 kJ/mol. Kessler and Thieme found that the activation energy for desorption from the (100) surface was 54 kJ/mol, so the initial interpretation of the shoulder is that it is associated with CO desorption from (100) surfaces in the sample.

An attempt was made to try to isolate the high energy peak by exposing the sample to very small doses of CO, in the hope

that the high energy state would become populated first before the main state began to appear. Doses of approximately 0.025L, 0.05L, 0.075L and 0.1L were made, and the resulting desorption spectra are shown in Figure 6.5. These four spectra were obtained in a completely different experiment to those shown for the higher CO doses and have suffered from broadening to a different extent. In addition, it was difficult experimentally to reproduce the same mass spectrometer sensitivity, so a quantitative comparison between the spectra in Figure 6.4 and in Figure 6.5 cannot be made. However, the five spectra in Figure 6.4 can be compared directly as these were obtained in the same experimental run, and similarly the four spectra in Figure 6.5 can be compared directly. Consideration of the spectra obtained following small doses of CO shows that initially both the high energy (T_{max} = 200K - 205K) and the intermediate energy (T_{max} = 175K) states were populated to a similar extent. However, increasing CO dose results in the growth in the population of both states with the intermediate state growing more rapidly than the high energy state, until the intensity ratio between the intermediate state and the high energy state reached approximately 3 to 1. Population of the higher energy states first would be expected.

The principal difficulty encountered with the desorption system was, as can be seen from the spectra, the problem of background CO. The probe, as described in Chapter 4, was not the source of the problem, because a 'blank' stainless steel sample was fitted using a similar copper support wire to

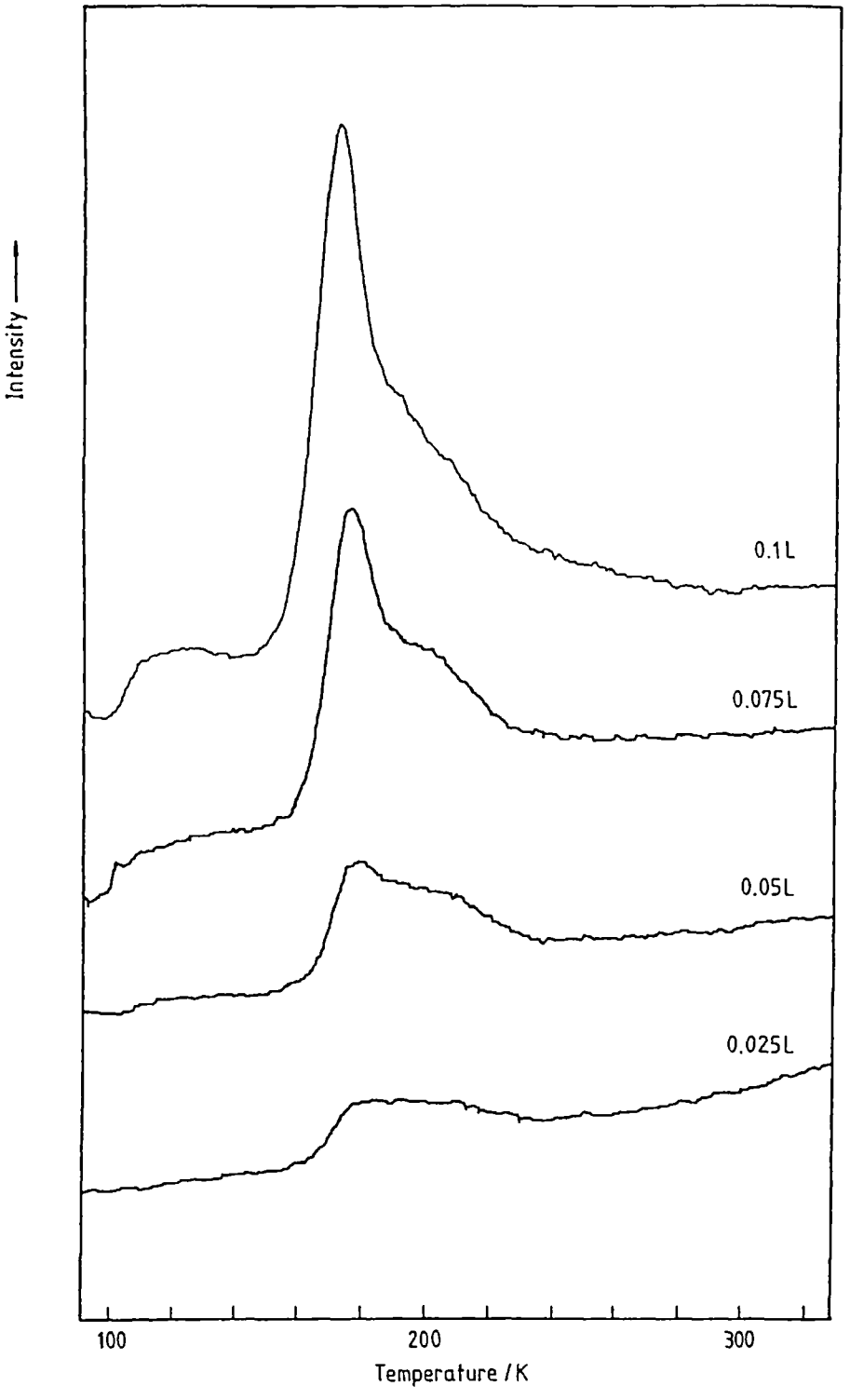


Figure 6.5. TPD spectra of CO desorbing from pure polyx copper following low CO doses (<0.1L). These spectra were obtained in a separate experiment, and are not on the same scale as those shown in Figure 6.4.

that described in Chapter 4, and an identical CO dosing and desorption experiment was carried out and this gave a completely flat desorption spectrum. The difficulty appeared to be associated with the pumping speed of the instrument. Consequently the spectra can be interpreted in a qualitative manner but no detailed quantitative analysis will be attempted because it is impossible to tell how the background CO varied during the TPD experiments. A height/area analysis of the intermediate energy peak following a 2L dose was made by extrapolation of the trailing edge of the peak so that the shoulder was excluded. The height/area method of analysis was described in Chapter 3. It was found that this method gave E_d as 23 kJ/mol and the pre-exp factor of 10^6 which illustrates a significant broadening of even the major peak. The extent of broadening can be examined by comparing the desorption spectrum obtained following a 2L dose of CO with the envelope of three peaks calculated theoretically. The height of a single peak, H, can be related to the temperature by an expression developed by Redhead[98], and this is shown below :

$$\ell n\left(\frac{H_{max}}{H}\right) = \frac{E_d}{R}\left(\frac{1}{T} - \frac{1}{T_{max}}\right) + \left(\frac{T}{T_{max}}\right)^2 \exp\left[\frac{-E_d}{R}\left(\frac{1}{T} - \frac{1}{T_{max}}\right)\right] - 1 \qquad (6.1)$$

where H_{max} is the maximum peak height.

The envelope of the three peaks is found by finding the height of each constituent peak at a particular temperature and then summing the three resulting heights. The three constituent peaks of the envelope were based on the interpretation of the desorption spectra given so far, so activation energies of 37 kJ/mol, 46 kJ/mol and 54 kJ/mol were used, and T_{max} of 140K and 175K were used for the low and intermediate energy peaks. Two values of T_{max} were used for the high energy peak, these being 200K and 205K, so the experimentally determined spectrum was in fact compared with two envelopes. This comparison is shown in Figure 6.6, where the extent of the broadening is clearly obvious. The broadening on the trailing edge of the shoulder may be partially caused by desorption of CO from high energy states such as (110) faces, higher index faces and grain boundaries.

Other sources of broadening could include the possibility that the final anneal at 300°C was not enough to remove argon ion damage, which would create high energy adsorption sites. It is also possible that a temperature gradient was created across the sample as it warmed up during desorption cycles, and this too would result in broadening. Broadening may also be caused by the interaction of the desorbing species with the walls of the instrument as described by Feulner and Menzel[120]. These workers suggested a simple method to overcome these difficulties, and it would seem necessary to implement this so that a quantitative analysis of the TPD

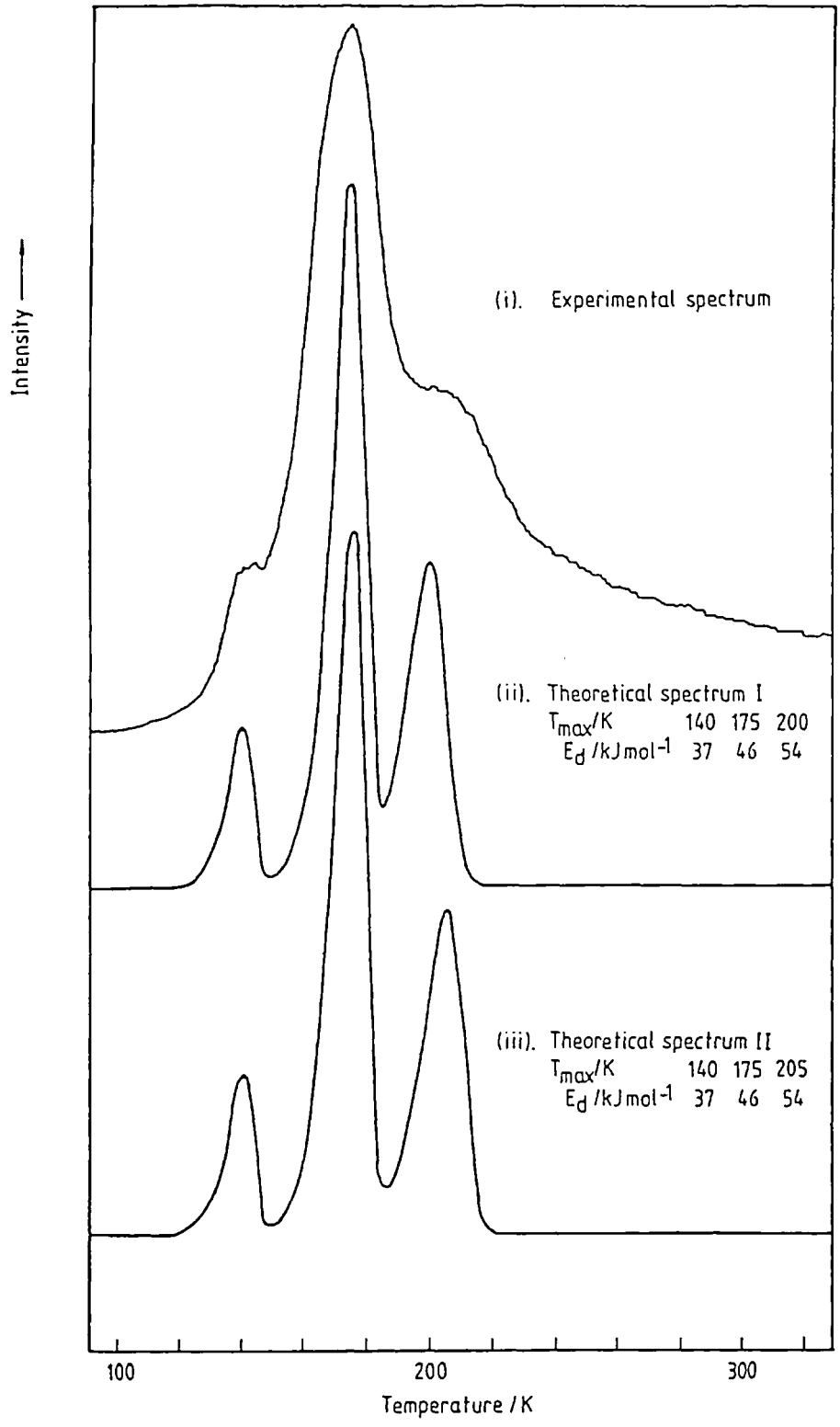


Figure 6.6. A comparison between the experimental TPD lineshape of CO desorbing from a polyx Cu surface and theoretical lineshapes derived from given values of T_{max} and E_d (see text). This comparison shows the extent of broadening of the experimental spectrum

spectra can be made in future work.

The CO desorption spectra illustrate that there is no phase change between 0.025L and 2L except for the formation of the compression structure. This is in agreement with the C1s and O1s spectra obtained from the adsorbed species. This also agrees with the view expressed by many workers [32, 37, 39, 41, 42, 46] that only one adsorbed state of CO exists on a particular crystal face apart from the compression state, and that the two higher binding energy peaks in both the C1s and O1s spectra were as a result of photo-emission induced phenomena, such as shake-up.

6.2 Chemisorption of CO on Zinc

Experiments were carried out where a zinc sample was exposed to CO at 90K. At doses up to several thousand langmuirs, no detectable CO was seen, as the C1s spectrum showed only a trace amount of residual carbon. There was a small oxygen peak, but this was attributed to the adsorption of trace impurities of either oxygen or water in the CO or from the residual gases.

6.3 Chemisorption of CO on a 30% Bulk Zn Brass

It was found that following 15 minute anneal periods at 200°C and 300°C there was no uptake of CO on the resulting surfaces at 90K, even following doses of up to several hundred langmuirs. This was the only alloy that did not take up any CO, as judged

by XPS, and so no desorption spectra were taken.

6.4 Chemisorption of CO on a 5% Bulk Zn Brass

6.4.1 Uptake of CO

In a similar manner to the copper surface, the rate of uptake of CO up to saturation was studied on the 5% bulk Zn alloy. The rate of uptake was established on two surfaces, following annealing at 200°C and 300°C. As a shorthand, a surface which has been formed following annealing of an n% bulk Zn alloy at T°C will be denoted as n%/T. The uptake curves for these two surfaces are shown in Figure 6.7. The uptake characteristics on both surfaces were similar to that of the copper surface, and the surfaces were almost saturated following a 2L dose (2×10^{-8}torr for 100 sec).

6.4.2 Photo-electron spectra of adsorbed CO

The C1s and O1s spectra resulting from adsorption of CO on the 5%/200 and 5%/300 surfaces also gave broad spectra with widths of approximately 10eV. Typical spectra are illustrated in Figures 6.8 to 6.11. The characteristics of the spectra are also similar to those obtained on pure copper, although the lineshape and noise levels make it difficult to establish where the precise peak maxima are. It would appear that the spectra are all composed of three peak structures with similar

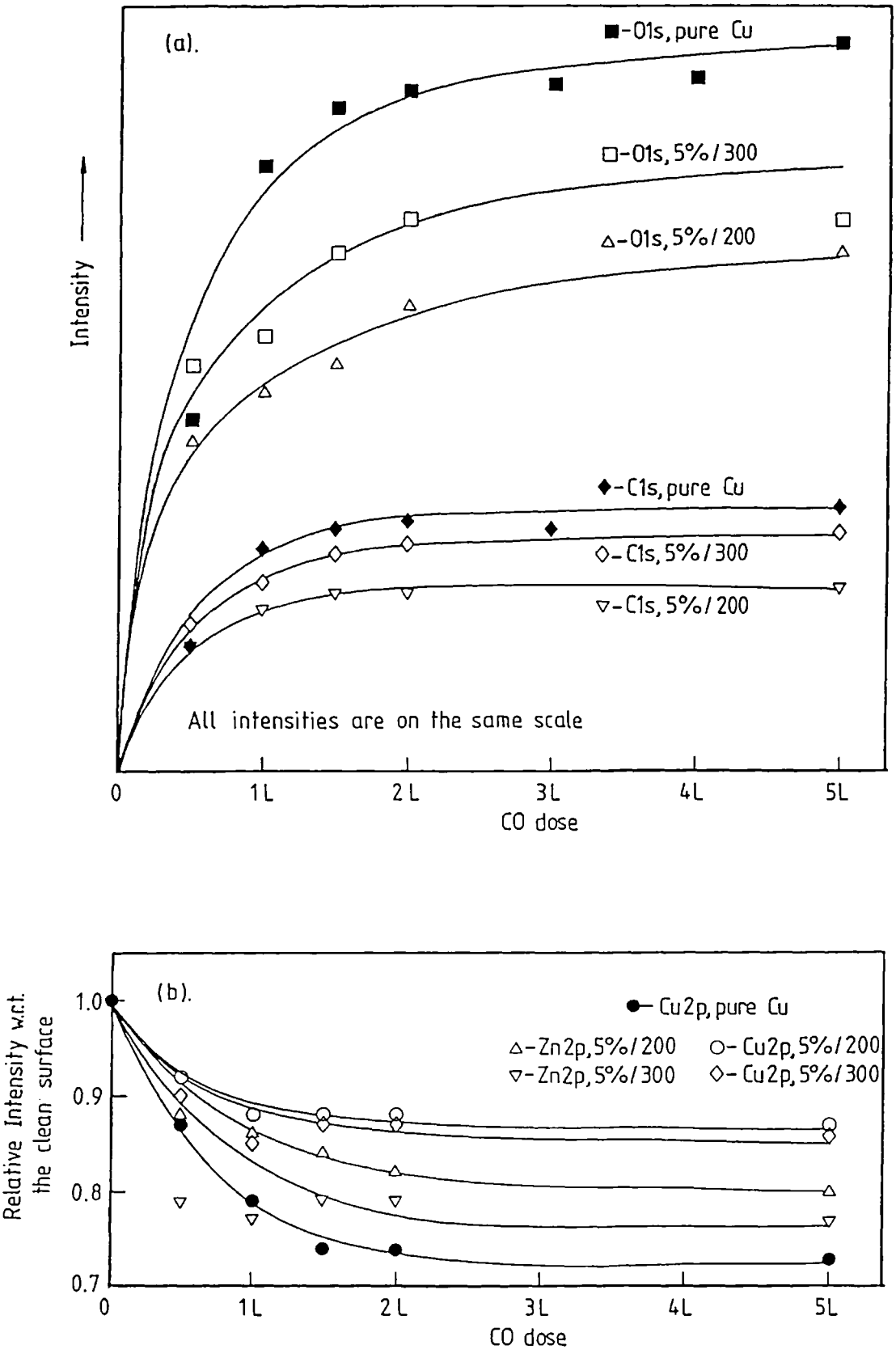


Figure 6.7. C1s,O1s & $Cu2p_{3/2}$ peak intensities as a function of CO dose on two different polyx brass surfaces (Cu intensities also shown for comparison)

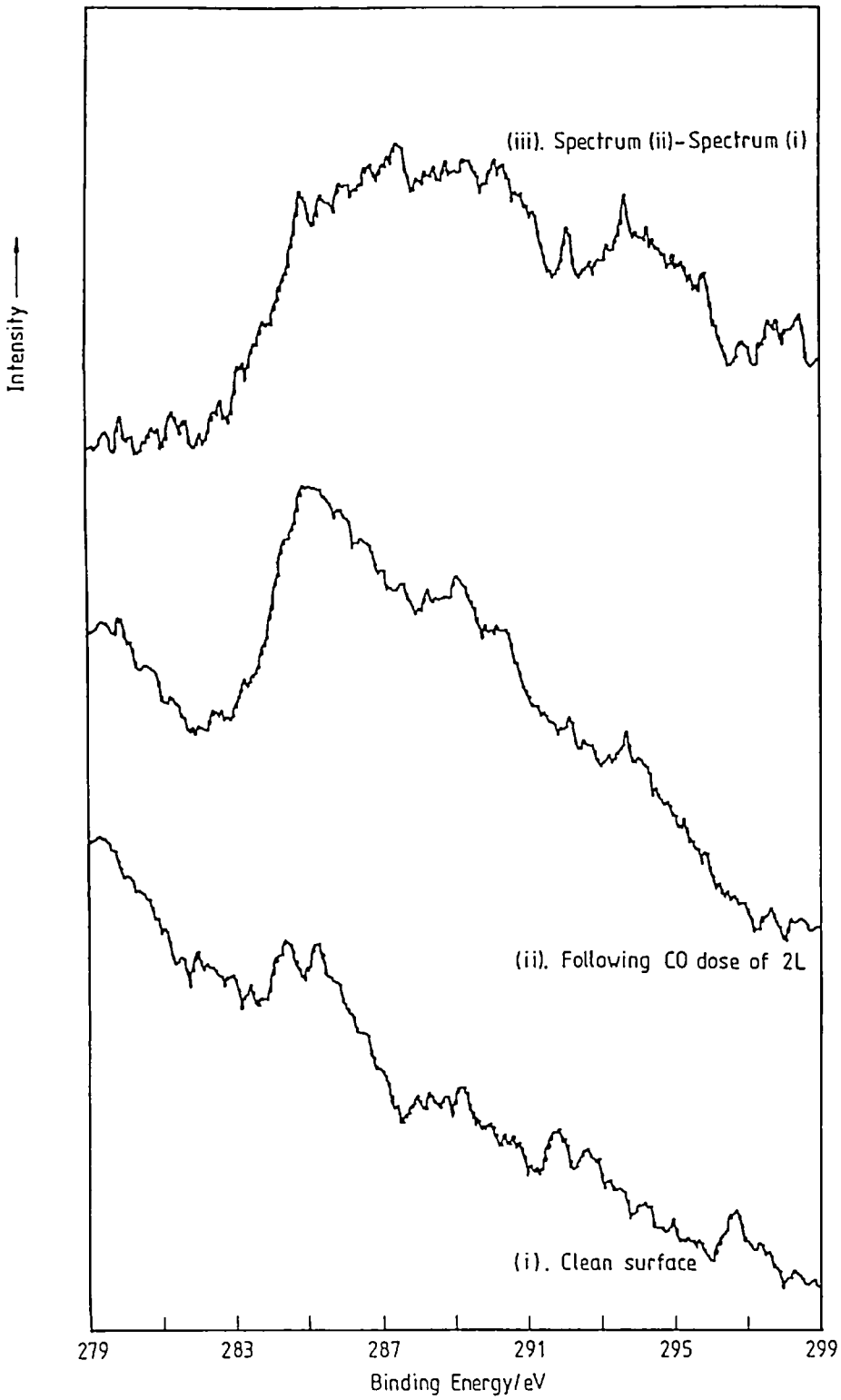


Figure 6.8. C1s spectra of CO chemisorbed on a polyx 5%/200 brass surface

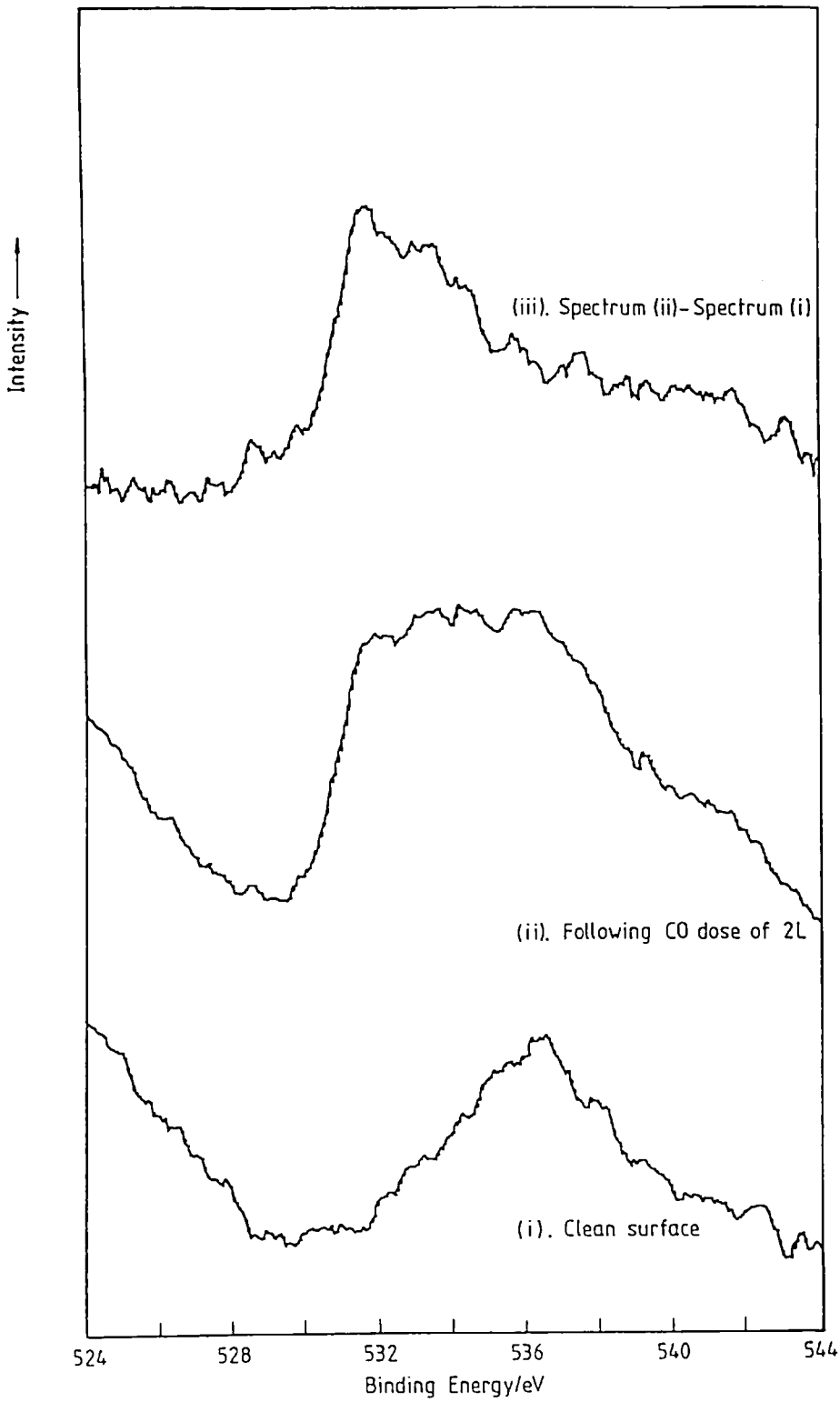


Figure 6.9. O1s spectra of CO chemisorbed on a polyx 5%/200 brass surface

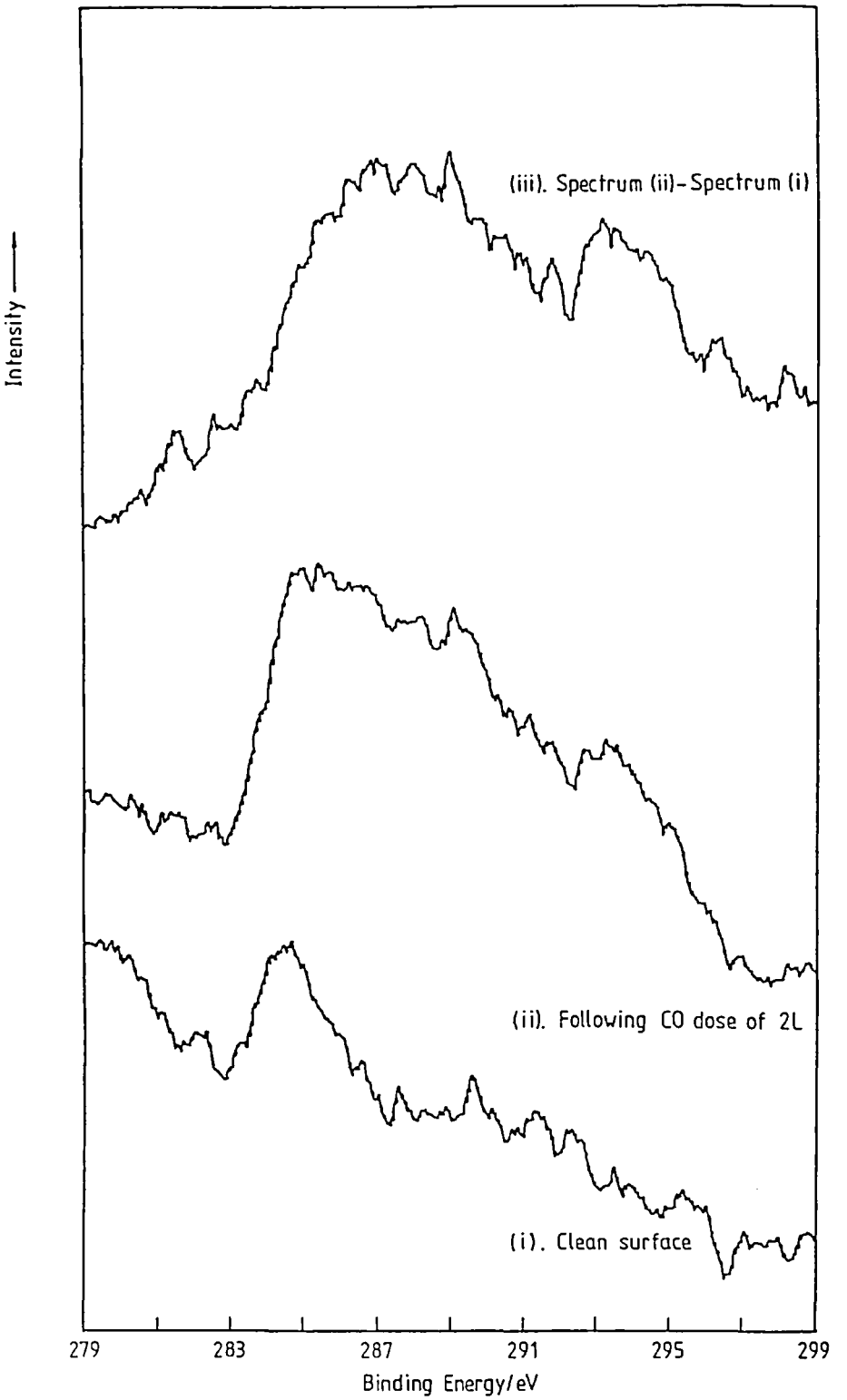


Figure 6.10. C1s spectra of CO chemisorbed on a polyx 5%/300 brass surface

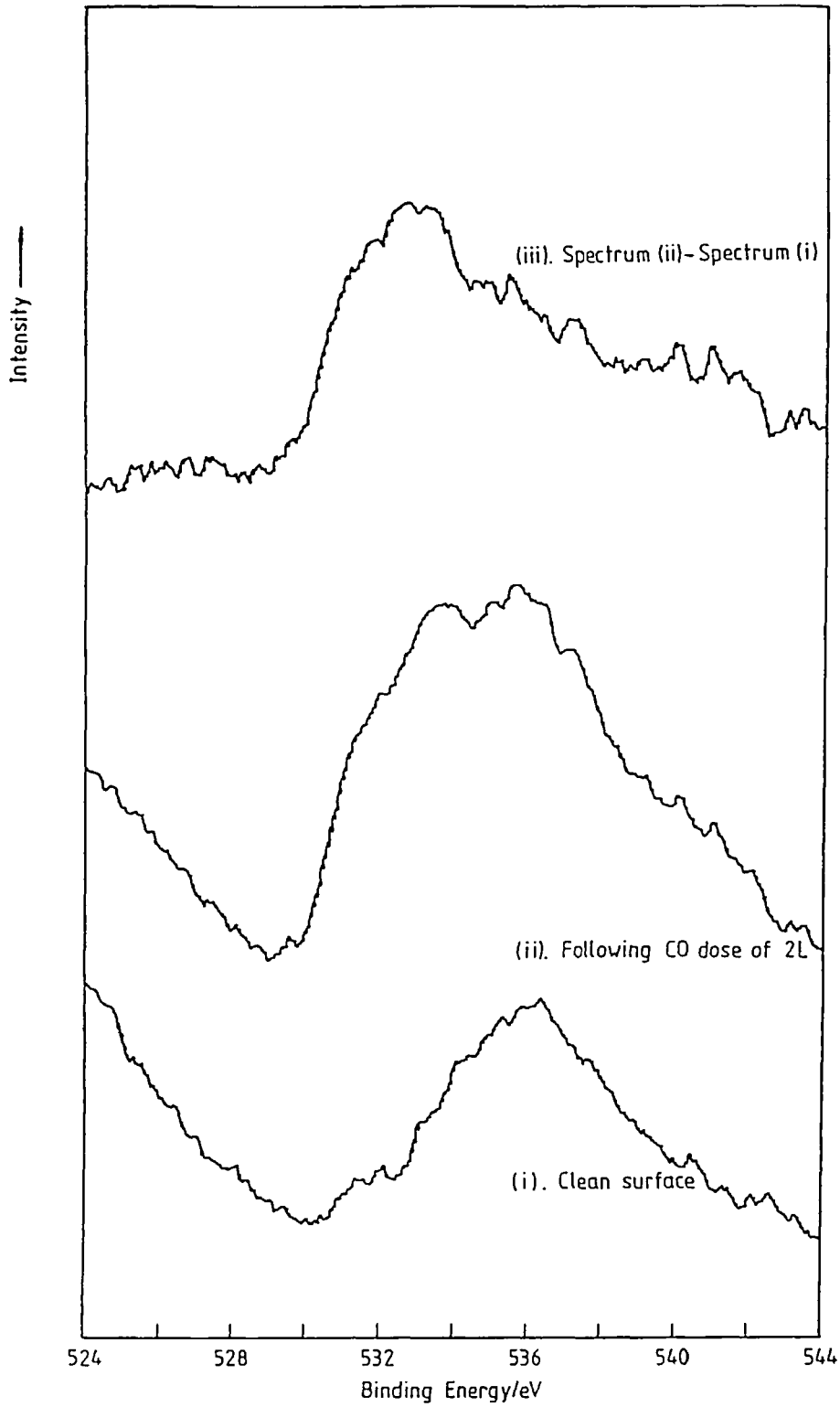


Figure 6.11. O1s spectra of CO chemisorbed on a polyx 5%/300 brass surface

binding energies to those obtained from CO adsorption on pure copper. The C1s and O1s spectra appeared to keep their three peak structure for all CO doses - this is similar to the pure copper surface.

6.4.3 Desorption of CO from a 5% Bulk Zn Brass

CO desorption spectra were obtained from the 5%/200 and 5%/300 surfaces following doses of 2L CO and these are shown in Figure 6.12. The desorption of CO from a pure polycrystalline copper surface following a dose of 2L CO is also included in the Figure as a comparison. It can clearly be seen that the presence of zinc in the surface creates additional adsorption sites which are, as would be expected, weaker than sites composed of pure copper. However, difficulties were again encountered with background CO, leading to extensive broadening, so again an extensive quantitative analysis was not carried out.

The lineshape of the whole spectrum was similar for CO desorption from both the 5%/200 and the 5%/300 surfaces illustrating that a difference in surface zinc content between around 33% and 49% did not alter the adsorption states. The effect of differing zinc contents on the desorption of CO will be discussed further after adsorption on the 2% and 10% bulk Zn alloys have been considered.

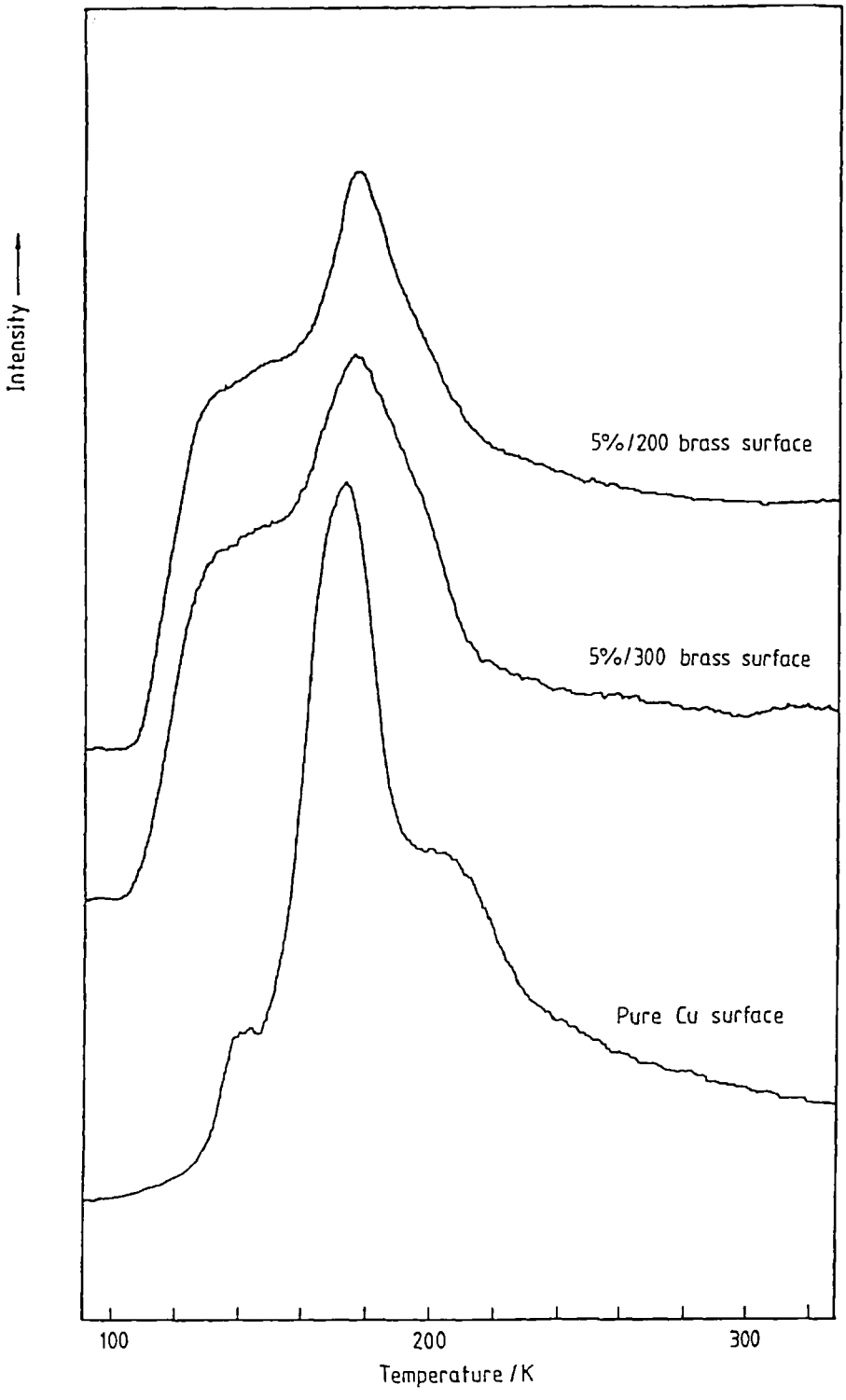


Figure 6.12. TPD spectra of CO desorbing from 5% bulk Zn polyx brasses following a dose of 2L CO

It is clear that there is a peak at around 175K. The form of the desorption spectra suggest that two peaks may exist below 175K, with approximate T_{max} of 126-130K and 145K. Above 175K, at least one extra state exists, although it is possible that more than one extra state is present. There is no firm evidence to clarify the situation above 175K. The peak at 175K will probably represent the desorption of CO from copper ensembles in the (111) faces. The peaks below 175K may be as a result of desorption from different Cu/Zn ensembles in the (111) or even the (100) faces. The peak or peaks above 175K maybe as a result of desorption of CO from Cu/Zn ensembles in the (100) faces. However, it is possible that the peaks above 175K may be caused by the interaction of the Zn atoms and the oxygen in the CO molecule creating an additional activation energy for desorption. Much more work needs to be done on the desorption of CO from brass surfaces, especially on single crystal surfaces so that the situation can be clarified and a better interpretation of the desorption spectra can be made.

The general lineshape of the desorption spectra for both the 5%/200 and 5%/300 surfaces was not significantly affected by CO coverage indicating that there was no change in the adsorption states with coverage.

6.5 Chemisorption of CO on a 10% Bulk Zn Brass

The chemisorption of CO on a 10% bulk Zn brass was studied but to a more limited extent than the 5% alloy. This sample created experimental problems, because above 250°C, significant amounts of carbon appeared at the surface. The sample proved extremely difficult to clean, so the experiments were restricted to surfaces created by annealing between 200°C and 250°C. The adsorption characteristics were established by exposing the 10%/200 and 10%/250 surfaces to 2L CO only and taking the C1s and O1s spectra and then running the thermal desorption programme.

The adsorption of 2L CO on the 10%/200 and 10%/250 surfaces produced almost identical C1s, O1s and TPD spectra, and these were similar to those obtained from the 5% alloy surfaces, except that the intensity was reduced indicating that less CO was taken up on this alloy. This will be discussed further in section 6.7.

6.6 Chemisorption of CO on a 2% Bulk Zn Brass

CO adsorbed on surfaces created by annealing a 2% bulk Zn alloy again resulted in C1s and O1s spectra which were similar to those described previously for the 5% alloy. The amount of CO taken up by this surface will be compared with the 5% and 10% alloy surfaces in section 6.7. The desorption spectra

following adsorption of 2L CO only on the 2%/200, 2%/225 and 2%/275 surfaces showed slightly different characteristics to those of the 5% and 10% alloy surfaces, and these are shown in Figure 6.13. The reason for the change in character is not immediately obvious, but it was reproducible on the 2% alloy which was used.

The presence of zinc in a copper substrate appears to create adsorption sites which are unaffected energetically by the amount of zinc in the surface layer for surface zinc contents between $\sim$ 20% and $\sim$ 55%. A similar behaviour in the desorption lineshape is observed between 120K and 175K for the 2%, 5% and 10% bulk Zn alloys. As described above, the character of the desorption spectrum lineshape from the 2% bulk Zn alloy is slightly different above 175K.

6.7 Effect of surface zinc on the amount of CO adsorbed

The effect of the presence of zinc in brass surfaces on the amount of CO taken up needs to be quantified. This relation was established by exposing brass surfaces with different zinc contents to 2L CO, which essentially represented saturation, and using the C1s and O1s intensities to represent the amount of adsorbed CO. The C1s and O1s intensities corresponding to adsorbed CO on brass surfaces with different zinc contents are given in Table 6.2. These intensities were corrected so that they corresponded to the adsorption on samples with similar

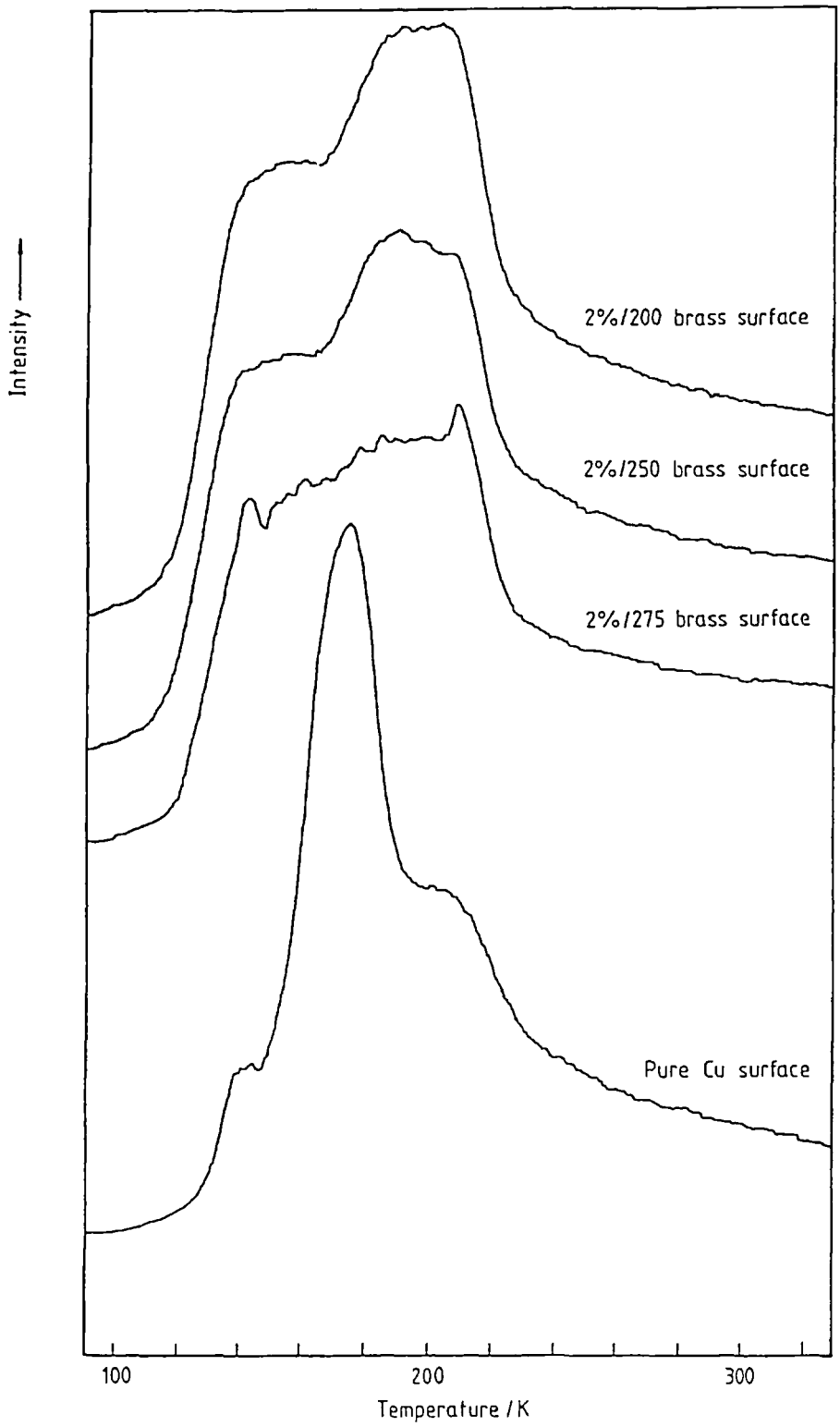


Figure 6.13. TPD spectra of CO desorbing from 2% bulk Zn polyx brasses following a dose of 2L CO

TABLE 6.2 C1s and O1s intensities following adsorption of 2L CO on brasses with different surface compositions

Bulk Comp. (% Zn)	Anneal Temp.	Peak Area Ratio	Surface Comp. (% Zn)	C1s Inten.	O1s Inten.	Relative Inten. C1s	Relative Inten. O1s
Pure Copper		0	0	1440	3920	1.0	1.0
2	200	0.17	22-29	1170	3000	0.81	0.77
2	225	0.20	25-33	1230	3160	0.85	0.81
2	275	0.14	19-24	1280	3320	0.89	0.85
2	300	0.08	12.15	1440	4240	1.00	1.08
5	250	0.33	38-49	1110	2920	0.77	0.74
5	300	0.27	33-42	1210	2840	0.84	0.72
5	325	0.22	28-36	1260	3440	0.88	0.88
10	200	0.38	43-55	950	2120	0.66	0.54
10	250	0.35	40-52	1010	2360	0.70	0.60
30	200	0.56	50-61	0	0	0	0
30	250	0.53	47-60	0	0	0	0
30	300	0.40	38-52	0	0	0	0

Note: (i) All of the C1s and O1s intensities can be compared directly.

(ii) The surface compositions are represented by the appropriate composition bands, as established in Chapter 5.

(iii) The peak area ratios are based on the $2p_{3/2}$(Mg-Kα) peaks.

total Cu and Zn intensities when clean. Relative C1s and O1s intensities were plotted against the Zn/Cu $2p_{3/2}$(MgKα) peak area ratios so that it could be seen how the uptake of CO was affected by a measured quantity which approximately represented the surface composition. The relative C1s and O1s intensities were also plotted against the appropriate surface composition bands, which were calculated and presented in Chapter 5. These two plots are shown in Figures 6.14 and 6.15 respectively. The results clearly show that increasing surface zinc content only reduces the amount of CO taken up to a small extent, and it is not until there is 25% to 30% Zn in the surface that any dramatic decrease in the CO uptake begins to occur. One interesting point that does emerge is that the 30%/300 surface does not take up CO despite only having around 40% Zn in the surface layer. This could be just experimental error, but in view of the existence of strong Zn depletion in the second layer it may be that interaction of the second layer is important in determining the amount of CO taken up.

6.8 Evidence for dissociation of CO on brass surfaces

A significant feature which appeared in the C1s and O1s spectra for the 5%/200 surface whilst performing the uptake experiment was the steady broadening of the lowest B.E. peak with increasing CO dose, suggesting that a fourth peak was appearing in both spectra. The uptake experiment was carried out by adsorption/desorption cycles, and following

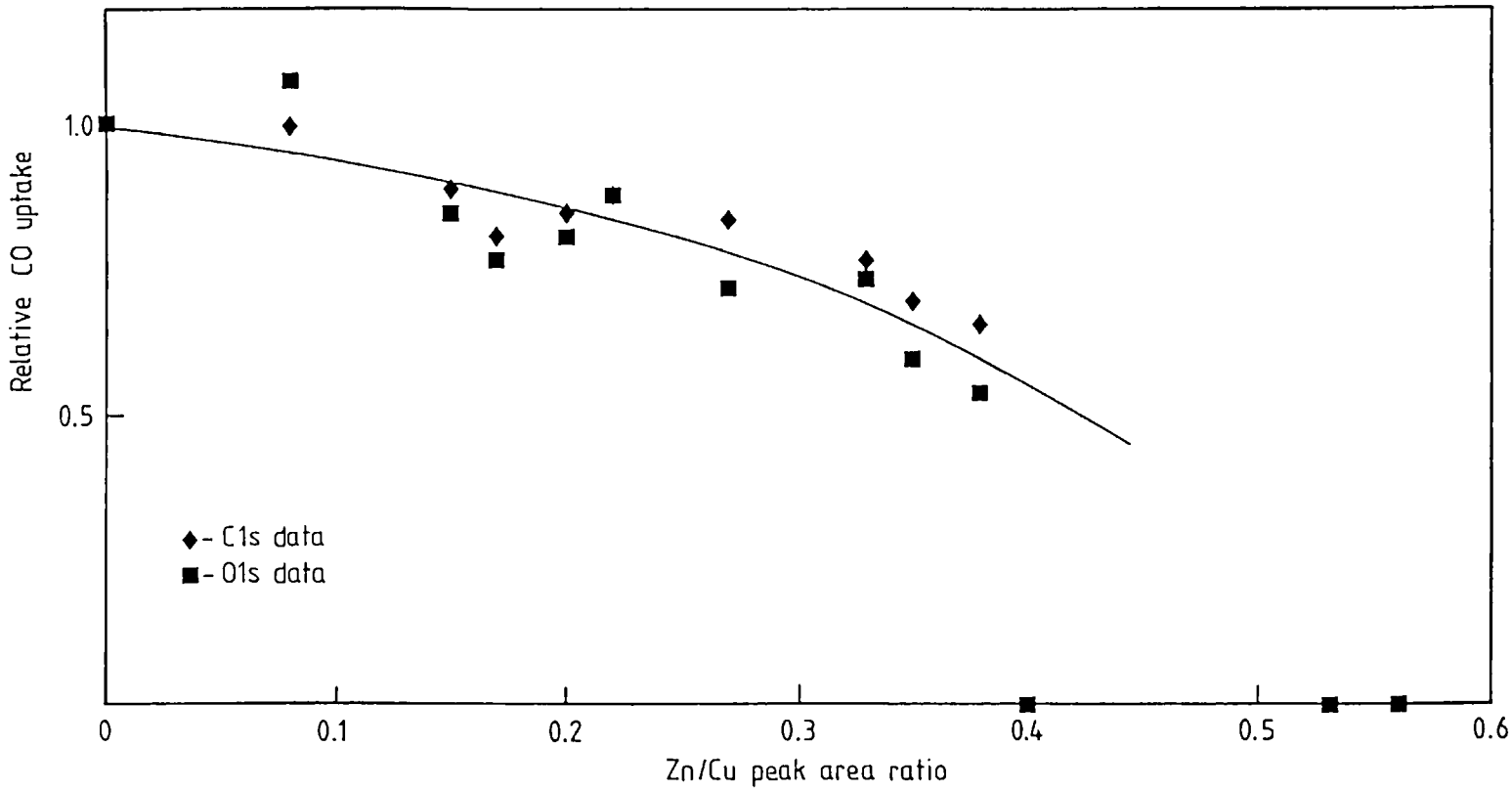


Figure 6.14. Relative C1s and O1s intensities as a function of the $2p_{3/2}$ (Mg-Kα) peak area ratios obtained from the segregation experiments

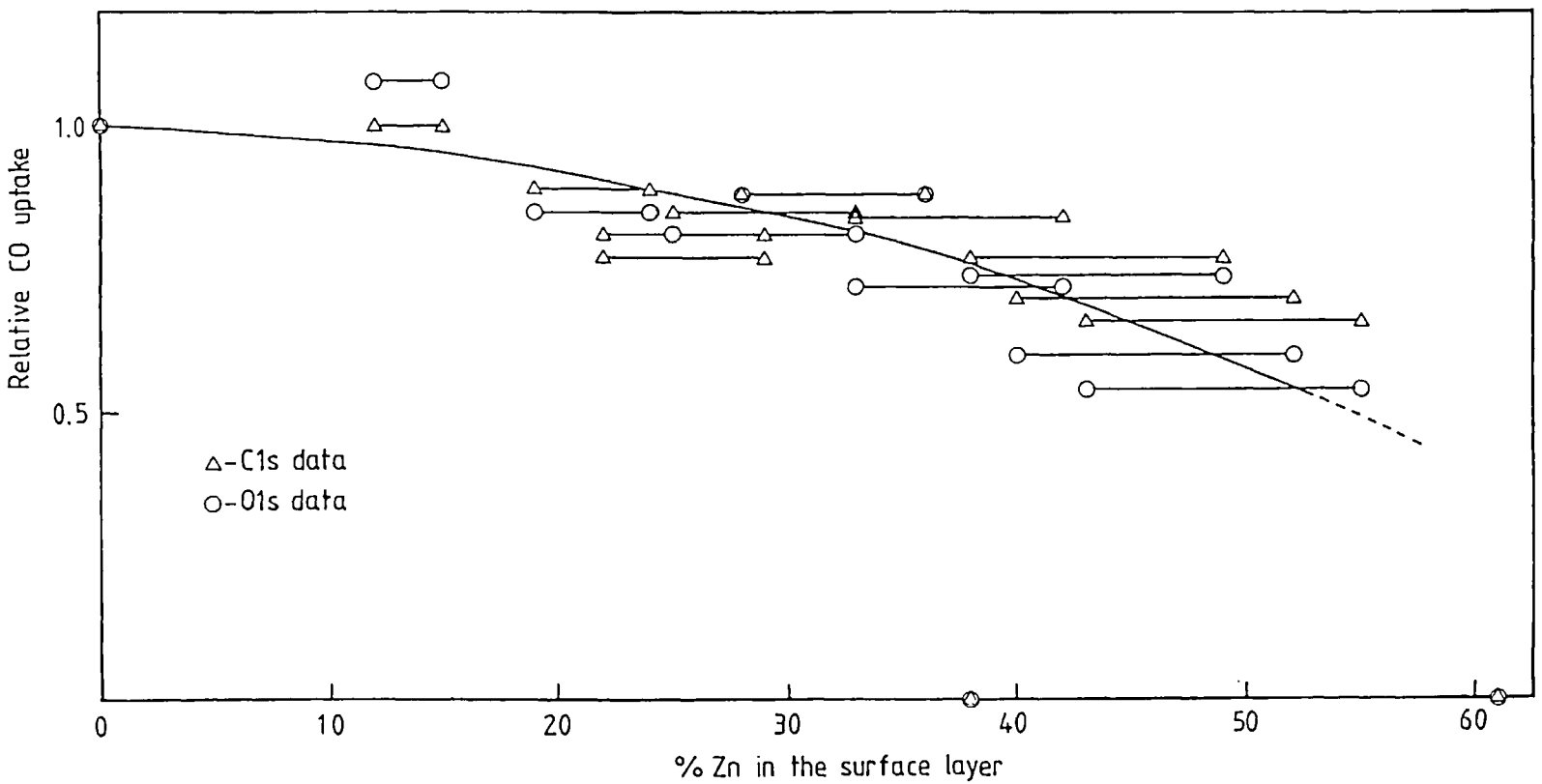


Figure 6.15. Relative C1s and O1s intensities plotted against the surface composition bands which were derived from the segregation results

desorption of the adlayer formed by the adsorption of 5L CO, the 'residual' C1s and O1s spectra were taken, and these are shown in Figures 6.16 and 6.17. It can clearly be seen that there was material left behind on the surface following desorption of the adlayer. The residual spectra were taken with the sample temperature at 90K, since it cooled rapidly after the desorption cycle was complete. The residual peaks at 90K were a single C1s peak at 284.9 (± 0.2) eV and a single O1s peak at 531.6 (± 0.2) eV. These are clearly different from the character of the C1s and O1s peaks of adsorbed CO at 90K. The ratio of these peaks after taking the relative cross-sections into account (the O1s peak has a cross-section which is 2.85 times greater than the C1s peak[113]) is 1 : 1. This result suggests that dissociated CO is left behind on the surface. The O1s binding energy of 531.6 eV can be compared with the binding energies of chemisorbed oxygen on Zn (532.0 eV [121]) and of chemisorbed oxygen on Cu (530.5 eV at 80K[122]). This suggests that the remaining oxygen was chemisorbed on both copper and zinc, but that the majority of the oxygen was on the zinc. The residual C1s peak was interpreted as adsorbed carbon on the brass surface.

The residual spectra were also taken with the sample held at room temperature, giving similar results, and at room temperature following warming of the sample to around 150°C, and these are shown in Figure 6.16. and 6.17. The intensity of both the C1s and O1s spectra decreased suggesting that some recombination

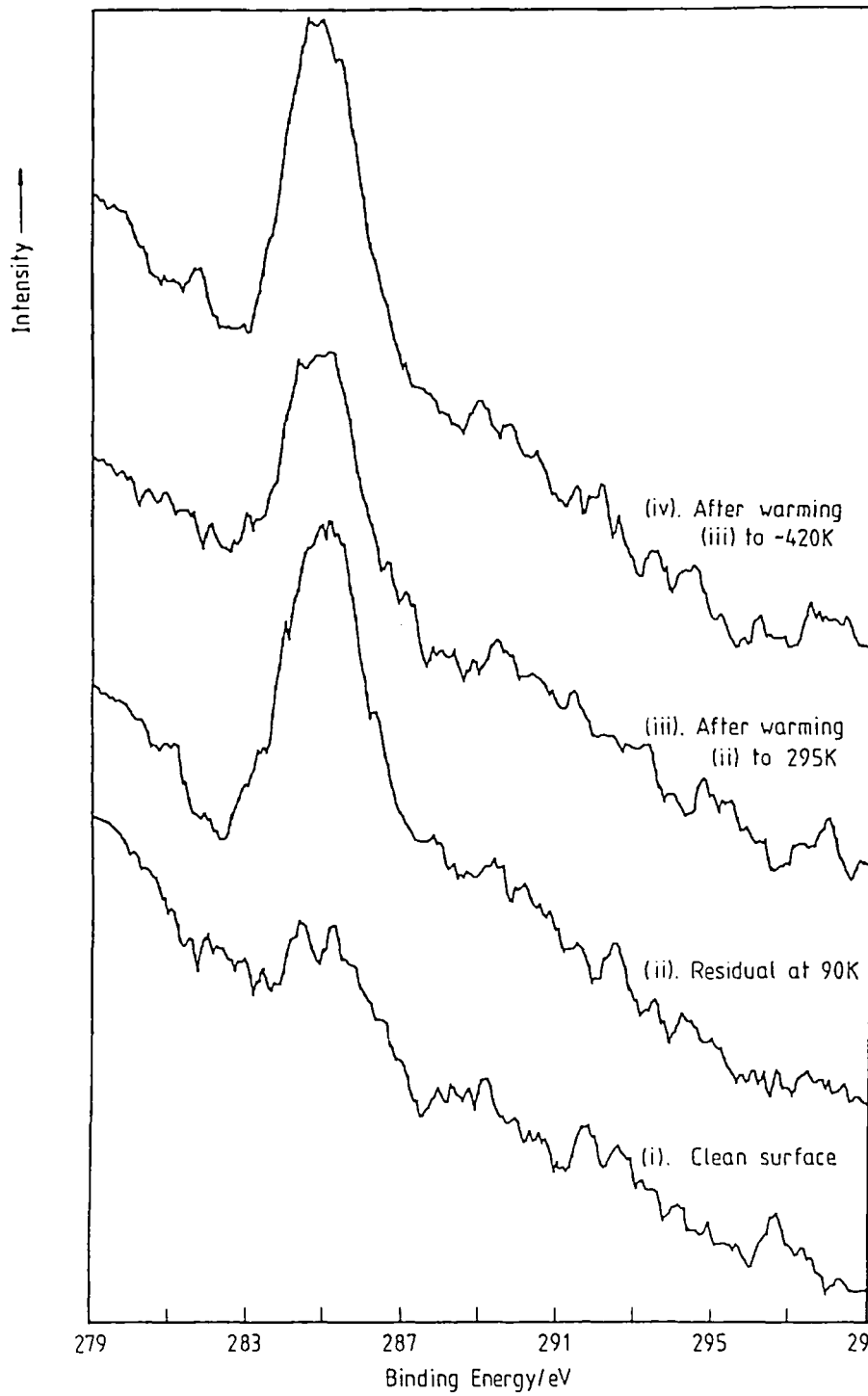


Figure 6.16. Residual C1s spectra from a 5%/200 brass surface following several adsorption/desorption cycles

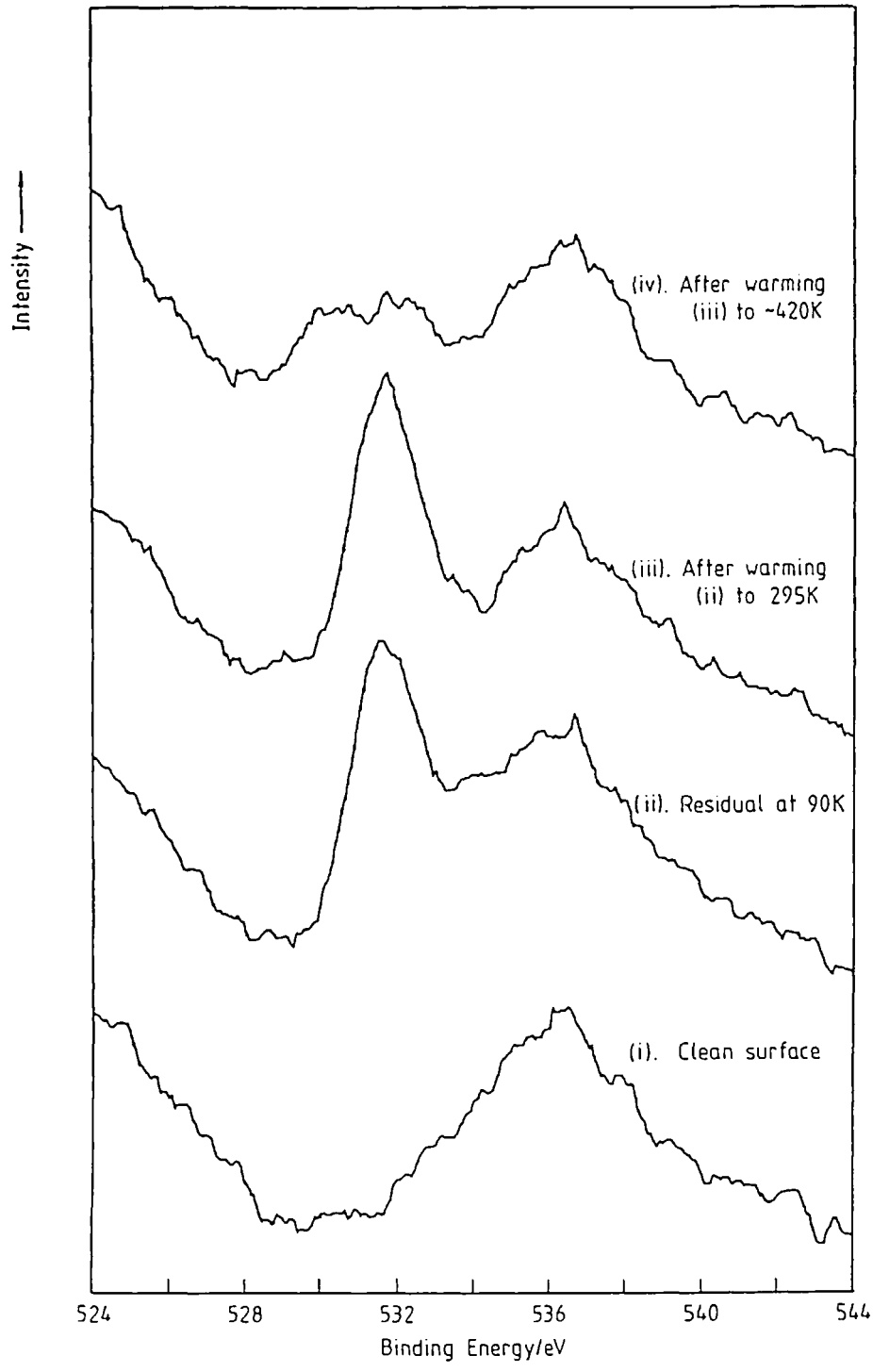


Figure 6.17. Residual O1s spectra from a 5%/200 brass surface following several adsorption/desorption cycles

of the carbon and chemisorbed oxygen occurred and subsequently desorbed as CO. The most interesting feature though was the change in the O1s spectrum where an additional peak appeared at around 530 eV. There are two possible causes for this. The first is that the increase in temperature results in additional mobility of the oxygen on the surface so that more chemisorbed oxygen on copper is formed. The second cause is the formation of ZnO which gives an O1s B.E. of 529.8 eV[121]. No significant change was observed in the Zn LMM Auger structure around 1000 eV kinetic energy which suggests that oxide formation is restricted to the surface if it is formed.

A similar broadening occurred in the lowest binding energy peak in both the C1s and O1s spectra of adsorbed CO on the 5%/300 surface following several adsorption/desorption cycles. The residual C1s and O1s spectra of the 5L CO dose adlayer following the desorption cycle in the uptake determination experiment at room temperature are shown in Figures 6.18 and 6.19. The residual C1s and O1s spectra following warming to 150°C are also shown.

The initial interpretation of the fourth peak in the C1s and O1s spectra of the adsorbed CO and the residual peaks is that some of the adsorbed CO is dissociated. Experimentally, the additional peaks representing a dissociated state did not begin to become significant until two or three adsorption/desorption cycles had been carried out. The extent of the accumulation of chemisorbed oxygen was significant. After the 5L CO dose, the amount of chemisorbed oxygen was almost equivalent to the

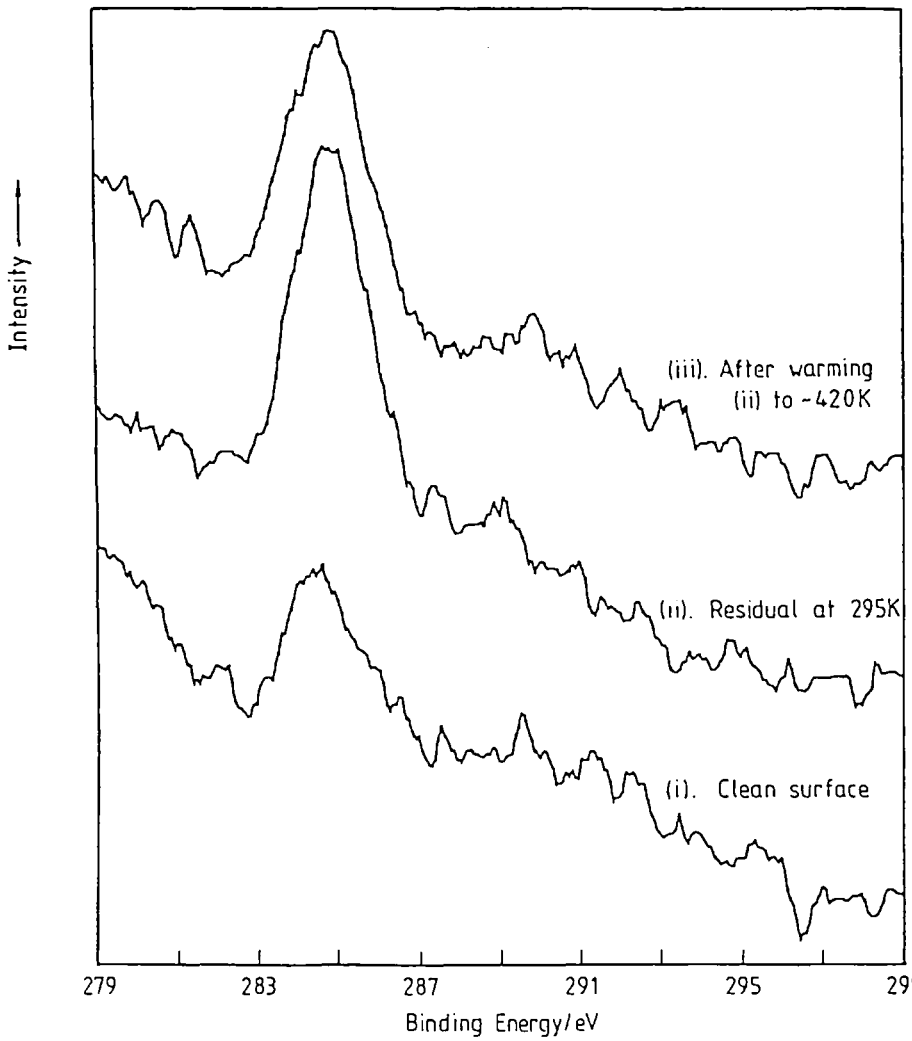


Figure 6.18. Residual C1s spectra from a 5%/300 brass surface following several adsorption/desorption cycles

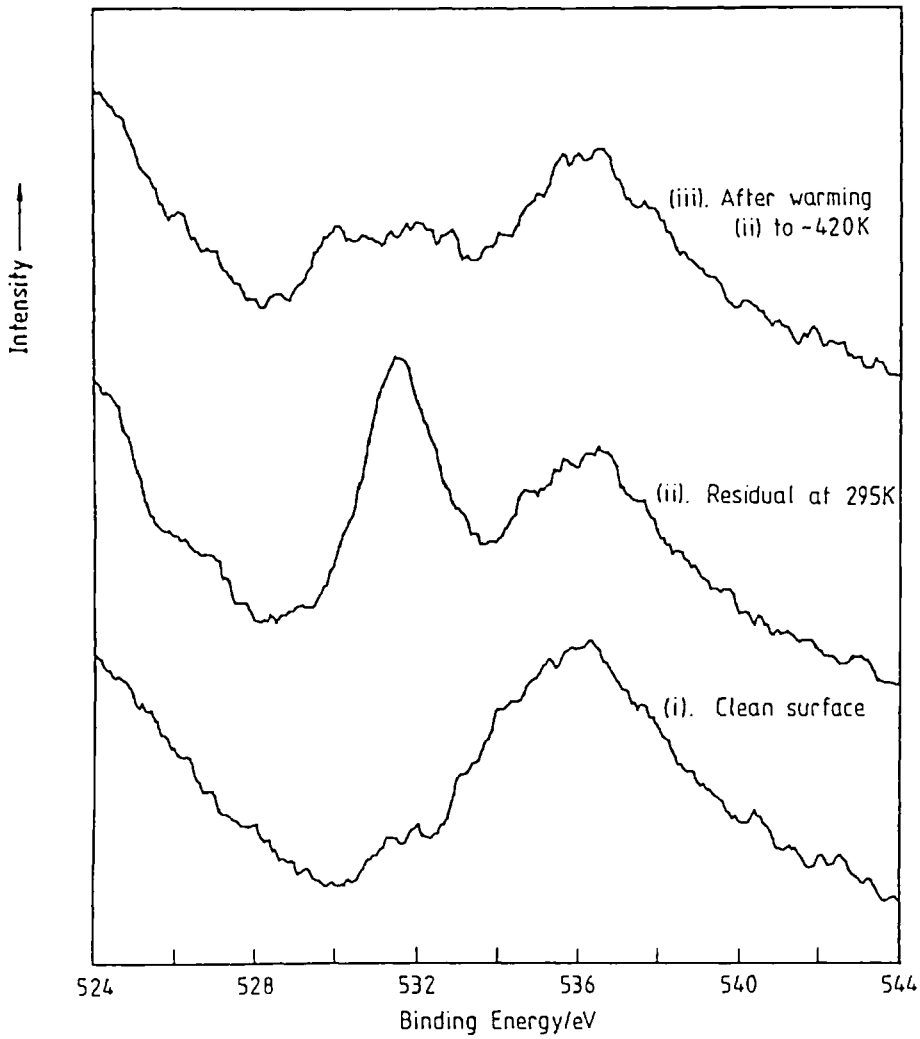


Figure 6.19. Residual O1s spectra from a 5%/300 brass surface following several adsorption/desorption cycles

amount of molecularly adsorbed CO. This was the case on both the 5%/200 and 5%/300 surfaces with the former having more chemisorbed oxygen present than the latter. The extent of dissociation will be quantified further later.

Other possible causes of the appearance of the additional oxygen peak have been considered. Oxygen contamination of the dosing gas did not exist because no mass 32 peak was present in a mass spectral analysis of the gas. Another possibility was that the oxygen peak appeared following adsorption of atomic oxygen which was formed by CO dissociation at local filaments. However an experiment was carried out where the sample was dosed with CO and then allowed to warm up with all of the local filaments being switched off. It was found that the residual Cls and Ols peaks still appeared, which ruled out dissociation of the dosing gas and the desorbing CO by hot filaments.

Dissociation on brass surfaces may also be affected by argon ion damage. In the preparation of the brass surfaces, especially those with the greatest zinc contents, the annealing temperature is generally kept below 300^{o}C and although the annealing period was 15 minutes, it was difficult to establish whether all of the argon ion damage was annealed away. Unfortunately, there was no way around this problem without affecting the surface zinc concentration.

The intensity of the residual O1s spectrum compared with that of the CO adlayer following a dose of 5L CO suggests that approximately 25-30% of the sites were occupied by the dissociated material. However, it must be remembered that the residual spectra shown in Figures 6.16-6.19 were obtained after several adsorption/desorption cycles and the significant intensity would be as a result of accumulation of the residual material following these cycles.

The presence of the residual material on the brass surfaces means that the uptake of CO as a function of dose as determined in this work may not be quite accurate for higher CO coverages because the presence of the dissociated material would reduce the number of available sites for further CO uptake. There was no easy way to overcome this difficulty if the TPD spectra were to be obtained in addition to the XPS results. The only possibility would have been to sputter and re-anneal the surface, but there was no guarantee that the same surface could be reproduced.

6.8.1 Quantification of the dissociation

The extent of dissociation was quantified by subjecting the 2%, 5%, and 10% bulk Zn alloys to a 2L dose of CO, and then taking the residual C1s and O1s spectra after desorption. It was found that no measurable dissociation took place on the 2% alloy irrespective of annealing temperature. The residual spectra following adsorption of 2L CO on the 5%/250, 5%/300 and 5%/325 surfaces are shown in Figures 6.20 to 6.25. In addition

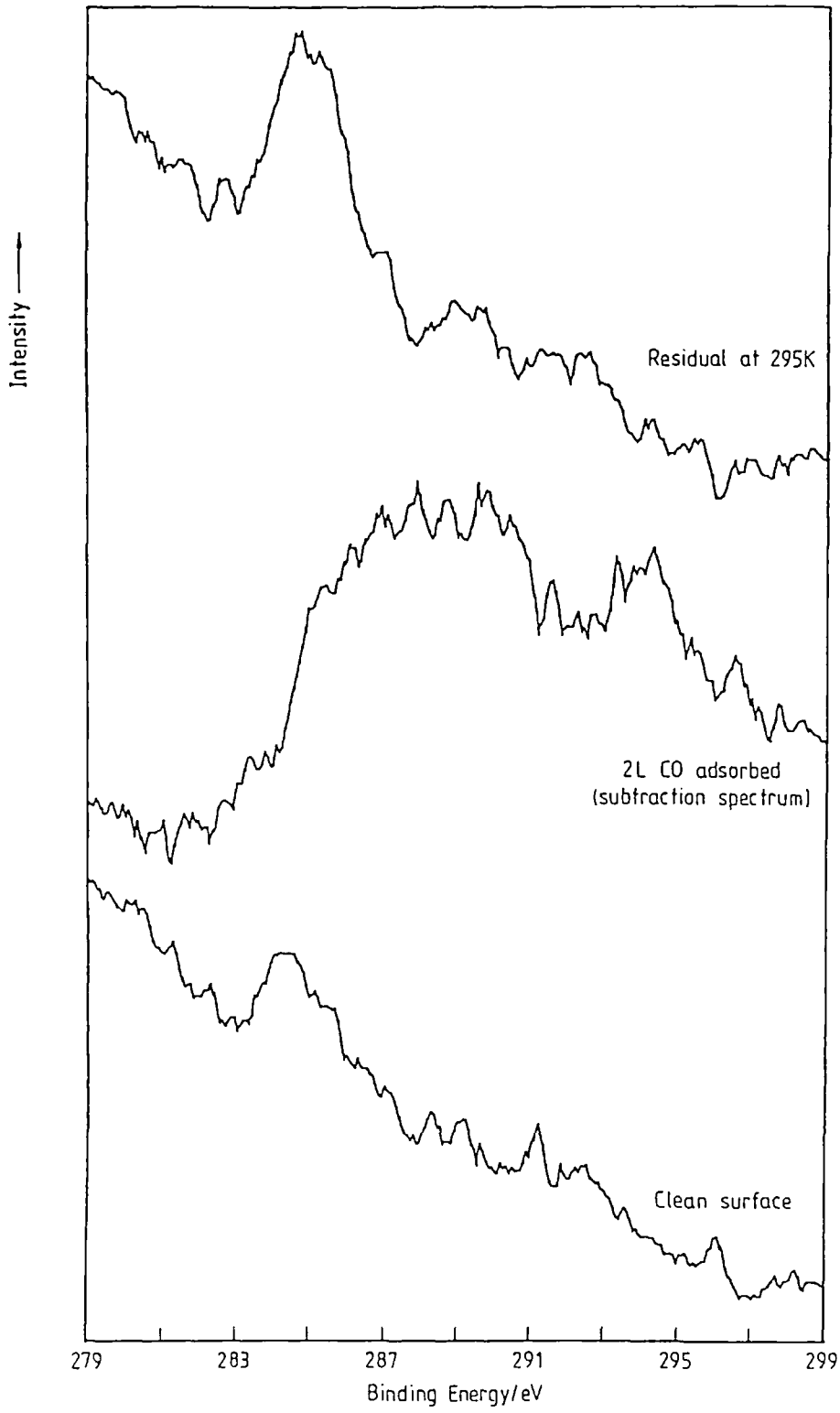


Figure 6.20. Residual C1s spectrum following adsorption of 2L CO on a 5%/250 brass surface and a subsequent desorption cycle(spectra of the clean surface and the CO adlayer are also shown for comparison).

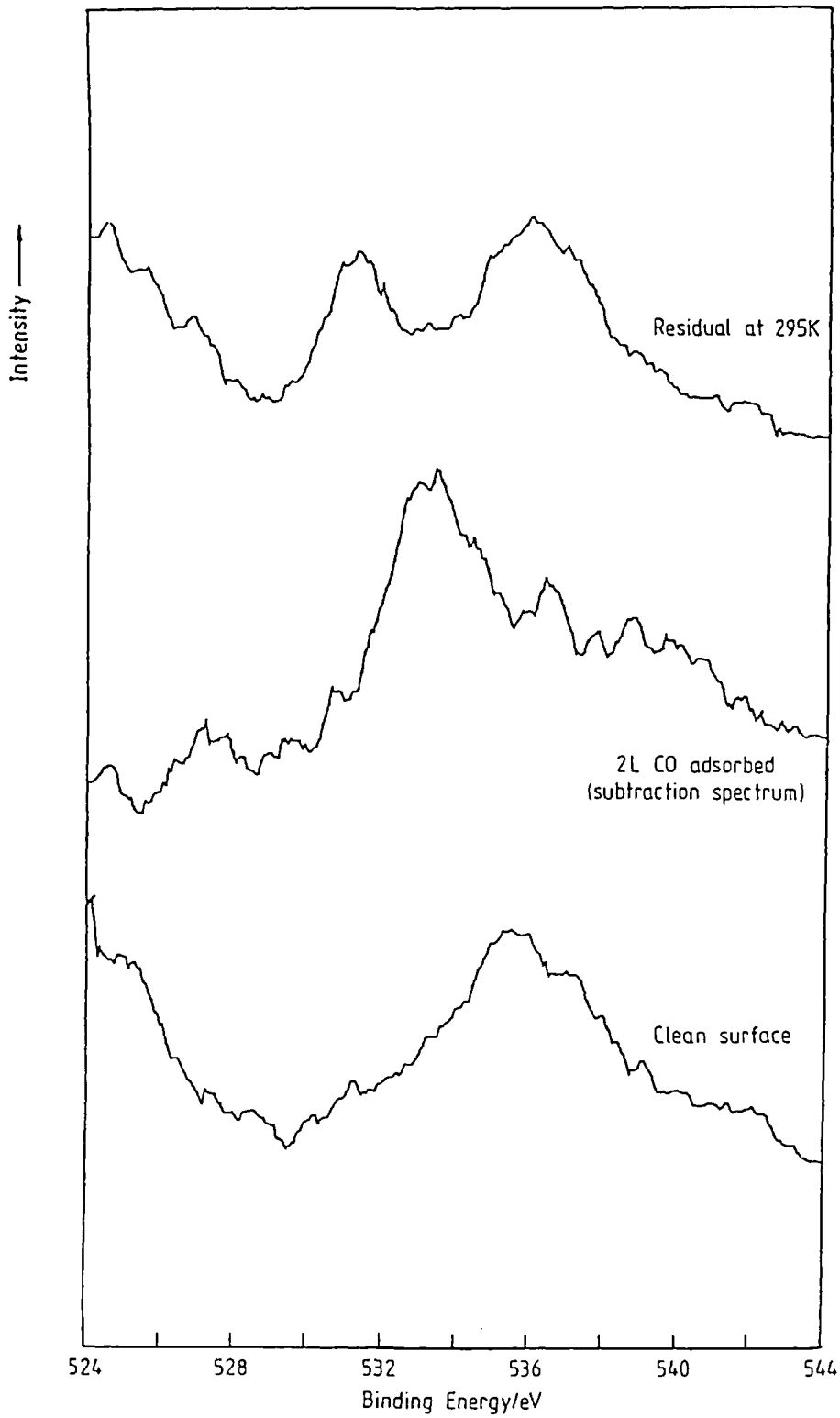


Figure 6.21. Residual O1s spectrum following adsorption of 2L CO on a 5%/250 brass surface and a subsequent desorption cycle(spectra of the clean surface and the CO adlayer are also shown for comparison).

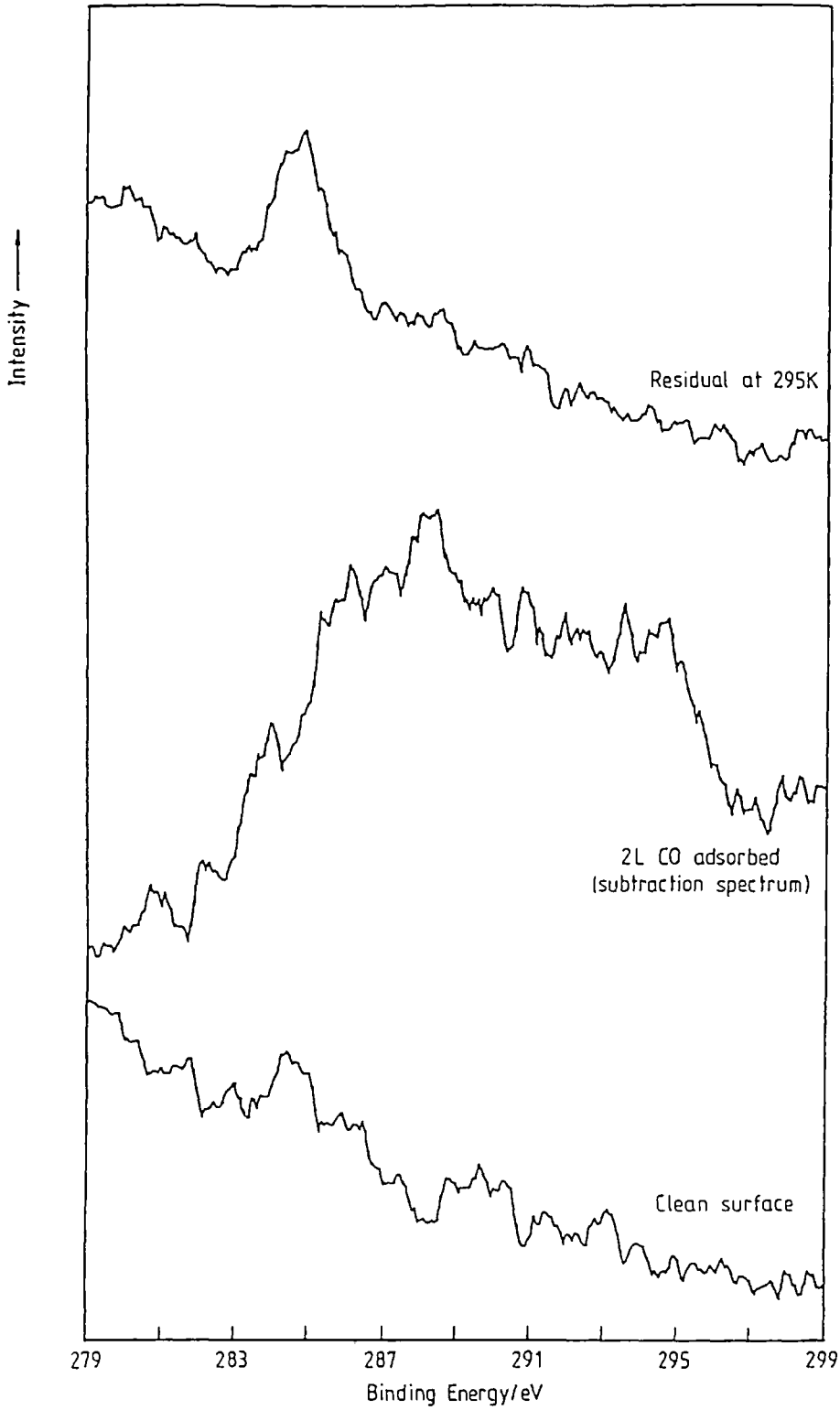


Figure 6.22. Residual C1s spectrum following adsorption of 2L CO on a 5%/300 brass surface and a subsequent desorption cycle(spectra of the clean surface and the CO adlayer are also shown for comparison).

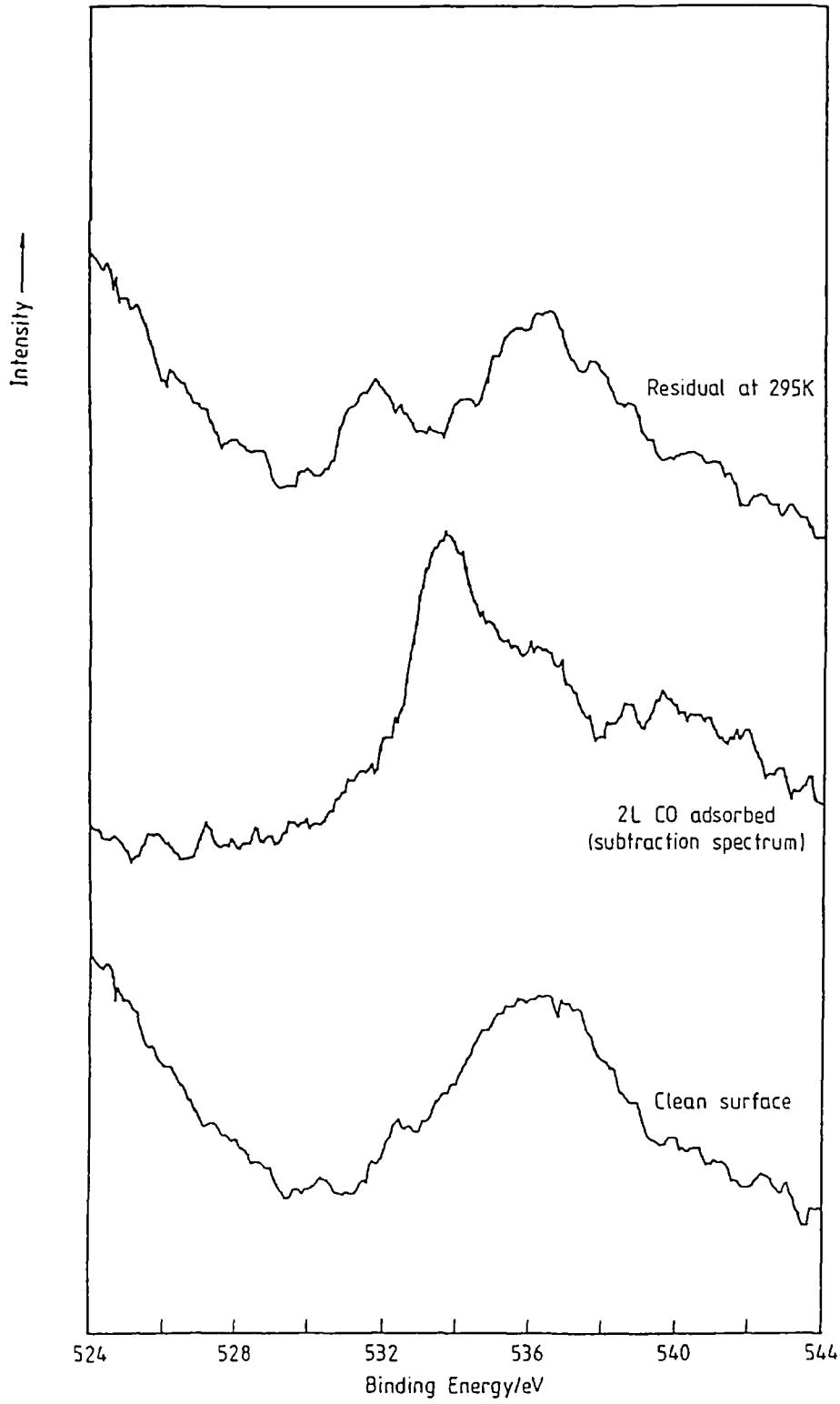


Figure 6.23. Residual O1s spectrum following adsorption of 2L CO on a 5%/300 brass surface and a subsequent desorption cycle(spectra of the clean surface and the CO adlayer are also shown for comparison).

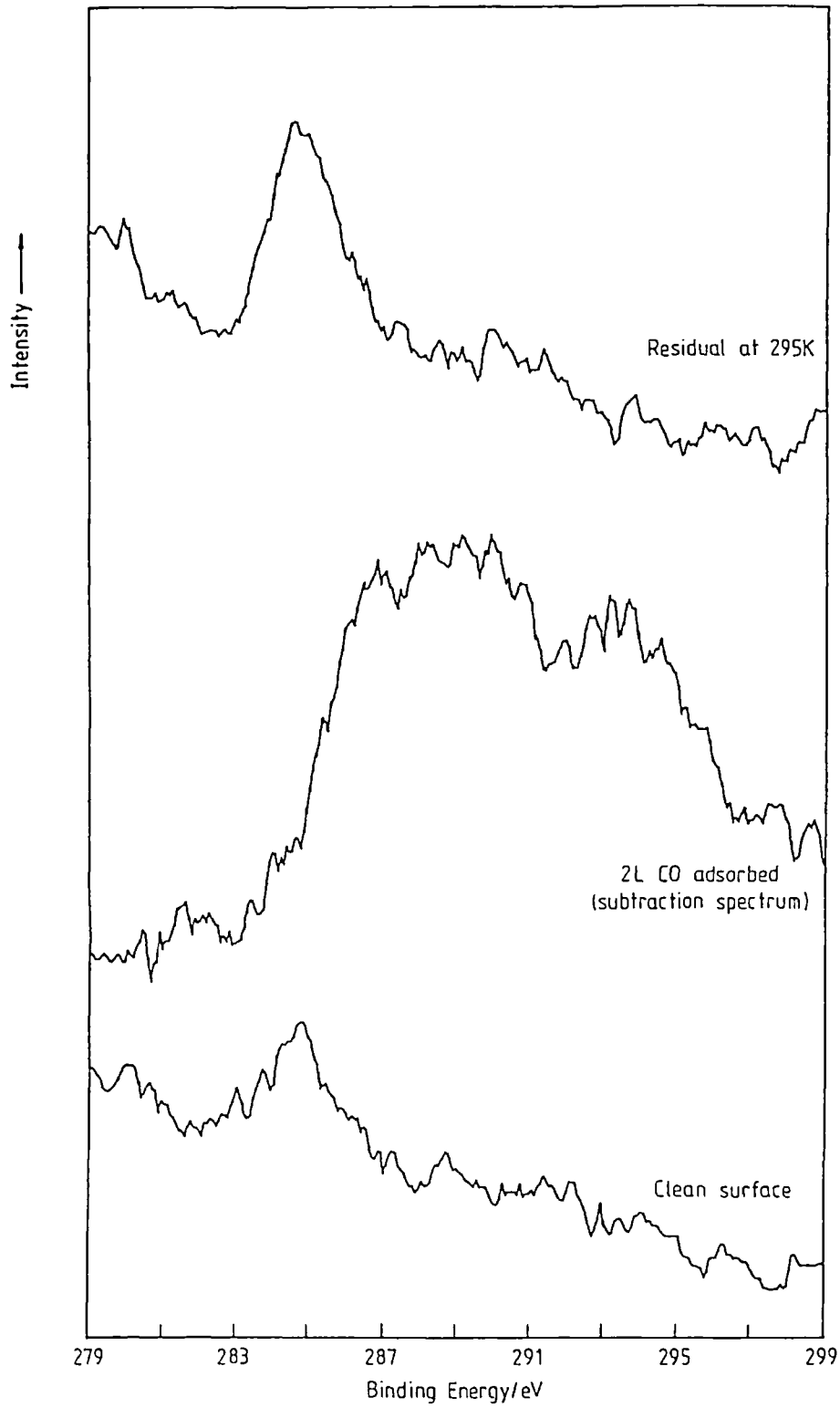


Figure 6.24. Residual C1s spectrum following adsorption of 2L CO on a 5%/325 brass surface and a subsequent desorption cycle(spectra of the clean surface and the CO adlayer are also shown for comparison).

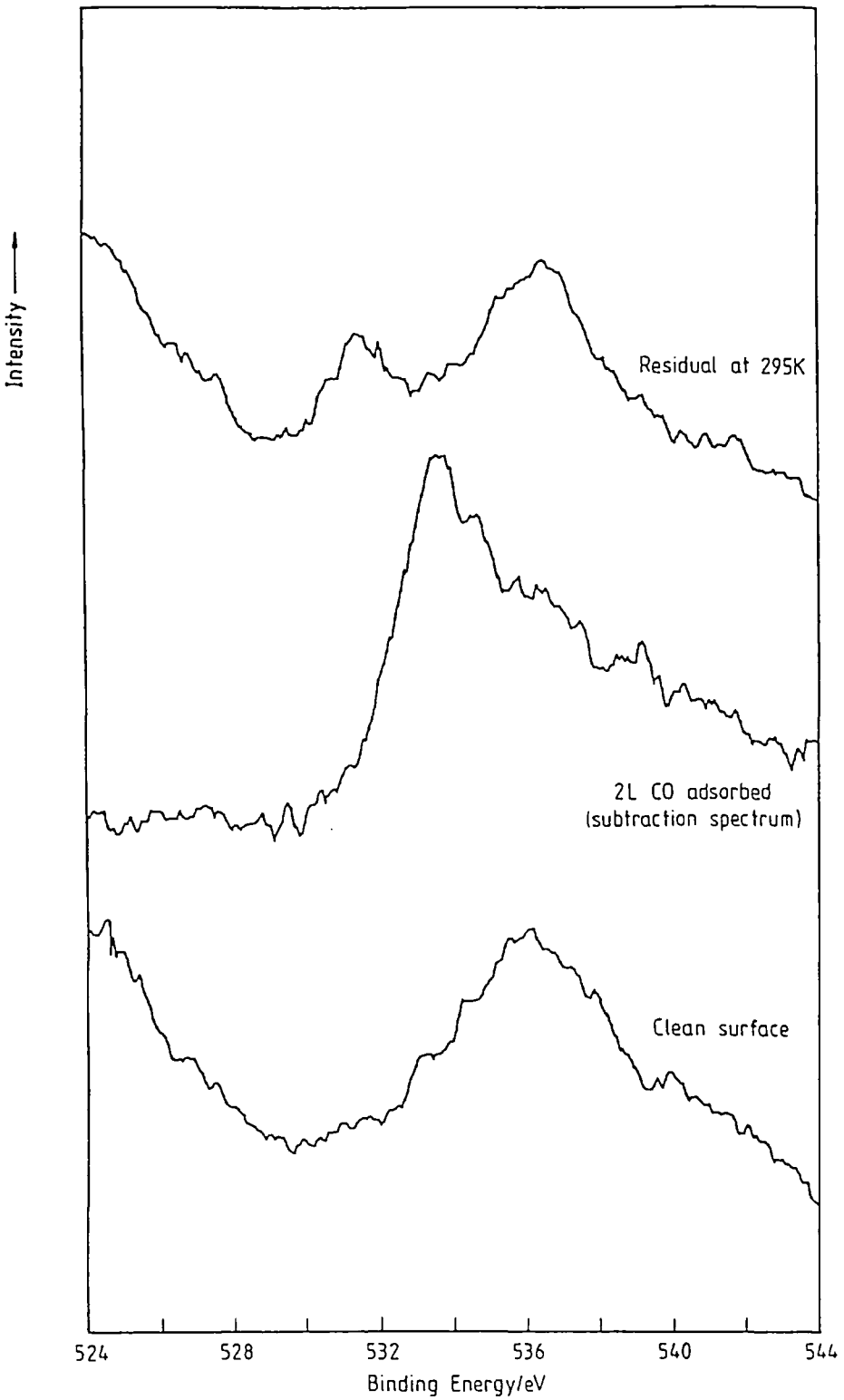


Figure 6.25. Residual O1s spectrum following adsorption of 2L CO on a 5%/325 brass surface and a subsequent desorption cycle(spectra of the clean surface and the CO adlayer are also shown for comparison).

to these, the C1s and O1s spectra of the CO adlayer following adsorption of 2L CO on the alloy surfaces are also shown for comparison. Again, a distinct O1s residual peak is formed on all three surfaces of the 5% alloy. The greatest extent of dissociation occurred on the 5%/250 surface which contained the greatest amount of Zn, and a comparison of the intensity of the O1s residual peak on this surface with that of the CO adlayer suggests that between 10% and 15% of the adsorbed CO dissociates. However the 5%/300 and 5%/325 surfaces only dissociated between 5% and 10% of the adsorbed CO.

The lineshape of the O1s spectrum of the CO adlayer shows little evidence for the presence of a fourth peak. This shows that the CO is adsorbed molecularly at 90K and only dissociates during the desorption cycle.

Residual C1s and O1s spectra obtained following adsorption of 2L CO on the 10%/200 and 10%/250 surfaces are shown in Figures 6.26 to 6.29. The O1s spectra suggest that there is a small peak around 531.5 eV indicating that a small amount of dissociation took place. However, the amount of CO taken up on the 10% alloy surfaces is much less than that on the 5% alloy surfaces and it appears that approximately 5% of the adsorbed CO dissociates during the desorption cycle. Since the extent of dissociation is dependent of Zn content, this is strong evidence for the dissociation being a property of Cu/Zn surfaces.

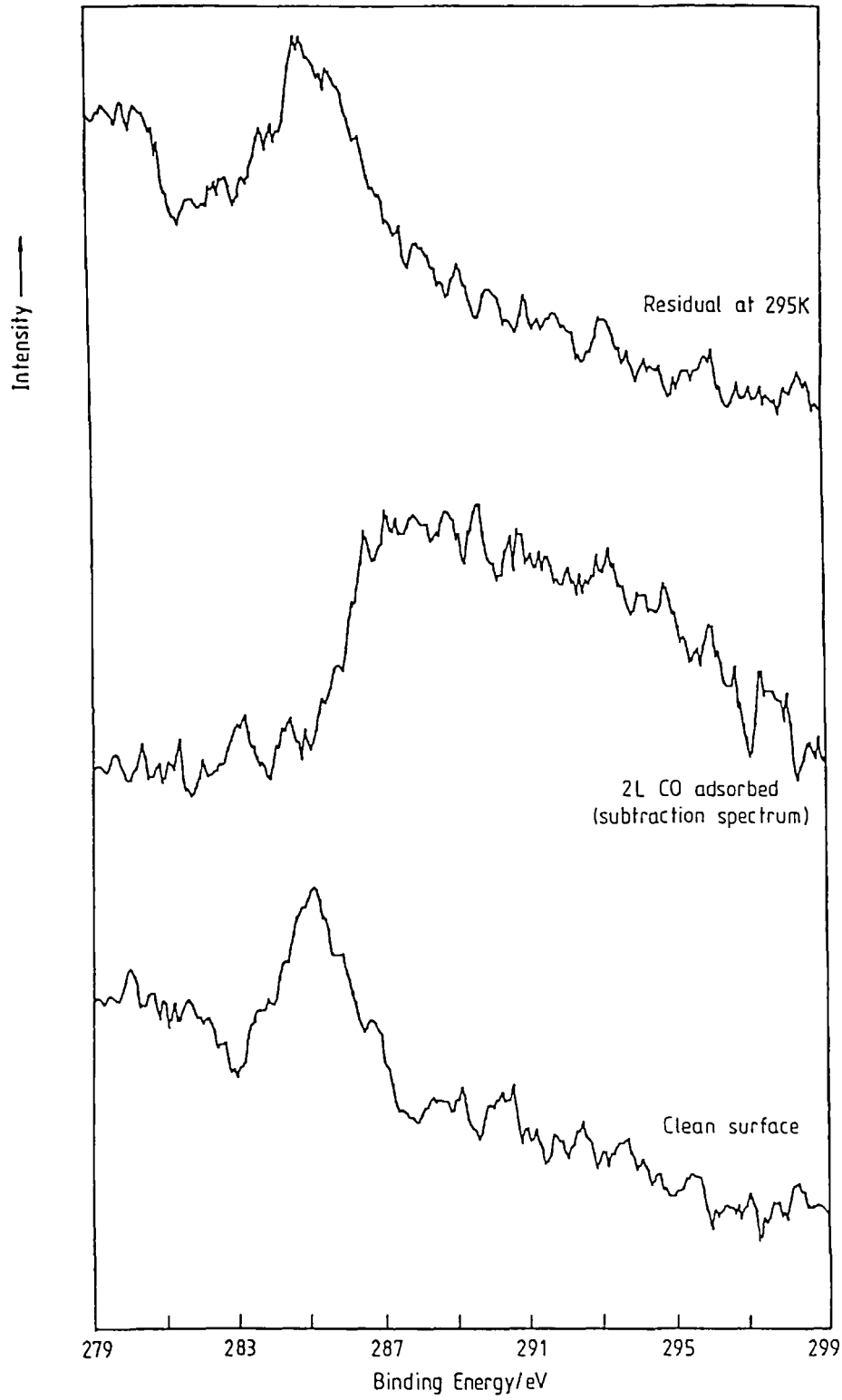


Figure 6.26. Residual C1s spectrum following adsorption of 2L CO on a 10%/200 brass surface and a subsequent desorption cycle(spectra of the clean surface and the CO adlayer are also shown for comparison).

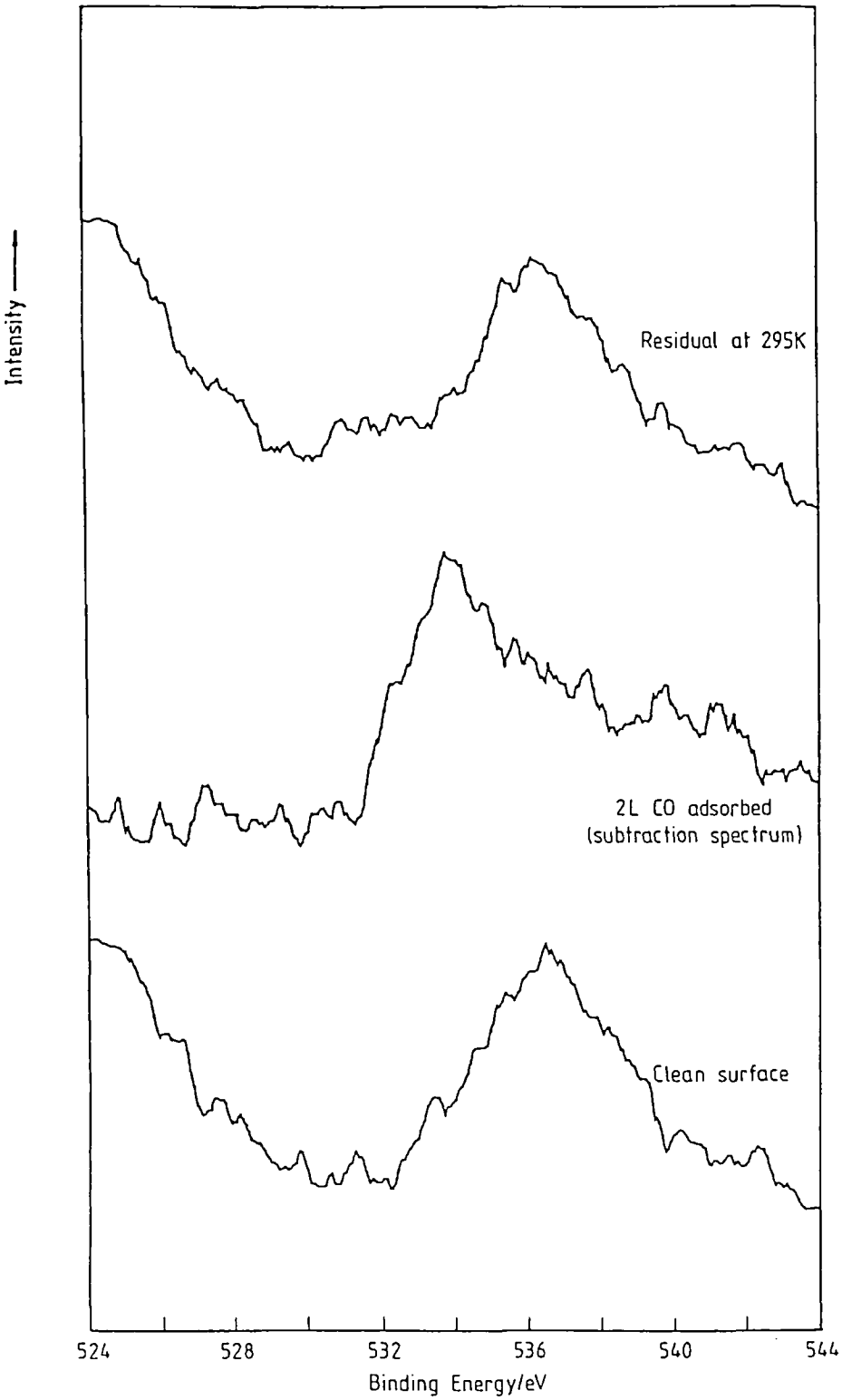


Figure 6.27. Residual O1s spectrum following adsorption of 2L CO on a 10%/200 brass surface and a subsequent desorption cycle(spectra of the clean surface and the CO adlayer are also shown for comparison).

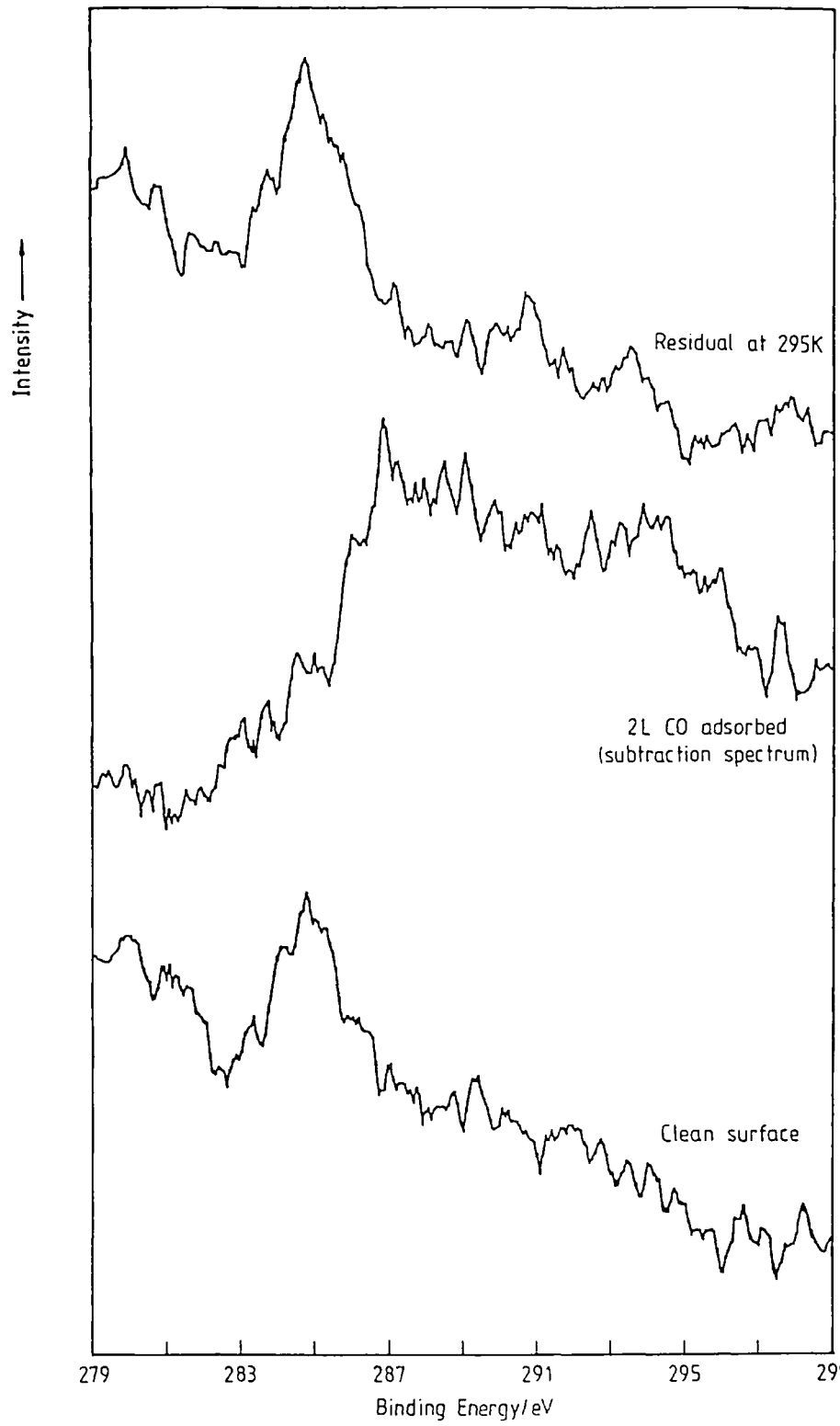


Figure 6.28. Residual C1s spectrum following adsorption of 2L CO on a 10%/250 brass surface and a subsequent desorption cycle(spectra of the clean surface and the CO adlayer are also shown for comparison).

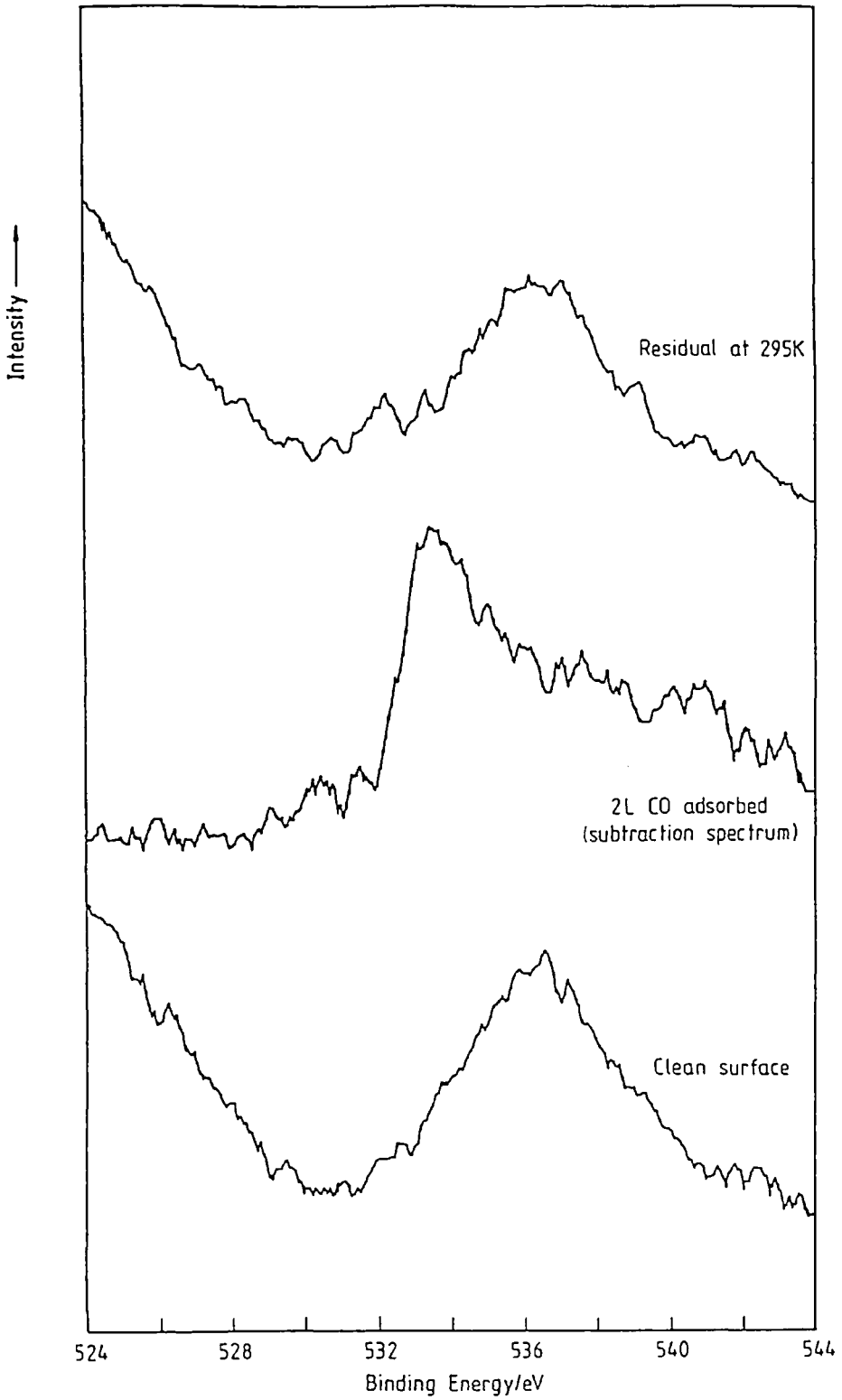


Figure 6.29. Residual O1s spectrum following adsorption of 2L CO on a 10%/250 brass surface and a subsequent desorption cycle(spectra of the clean surface and the CO adlayer are also shown for comparison).

6.8.2 Discussion

The extent of dissociation on the different brass surfaces imply that argon ion damage may not be an important factor in the dissociation process. This is because the 2% bulk Zn alloy should need a higher temperature to anneal away the argon ion damage than the 5% or 10% alloys, but no dissociation was observed on the 2% alloy. If argon ion damage was the most significant factor in the dissociation process then it would have been expected that the 2% alloy would have showed the greatest extent of dissociation.

The likelihood of CO dissociating on brass surfaces seems reasonable, because of the strong affinity of zinc for oxygen. A comparison between the dissociation energy of CO and the heat of adsorption of oxygen atoms on zinc would give an approximate idea of whether the dissociation is possible. No information appears to exist for the heat of adsorption of oxygen on zinc, so from a comparison of the heat of adsorption of oxygen on copper with the heat of formation of CuO it will be assumed that the heat of adsorption of oxygen on Zn is similar to the heat of formation of ZnO. The heat of formation of ZnO, which is -348kJ/mol[123] is much greater than the dissociation energy of CO (-111kJ/mol[124]) indicating that dissociation could be possible. However, this is only a simplistic comparison and better data would be required to establish whether dissociation is possible thermodynamically.

It has been shown that the residual peaks appear during the desorption cycles. The appearance of these peaks should be as a result of increasing the temperature of the CO adlayer rather than an effect which is directly associated with the desorption cycle. These results imply that the dissociation is an activated process, since it is unlikely that a brass surface at 90K will be capable of dissociating a CO molecule

The mechanism of dissociation of CO on brass surfaces is proposed as follows. At 90K, there is no evidence for dissociation because the C1s and O1s spectra of CO adsorbed on brass surfaces are similar to those of CO adsorbed on pure Cu. Upon warming the CO becomes vibrationally activated. If the amplitude of the bending vibration becomes large enough then it may be that the zinc can capture the oxygen atom, so breaking the C-O bond and leaving adsorbed carbon, probably on the copper.

One difficulty that does arise from these results is why the 5%/325 surface (approximately 30% Zn) dissociates CO but the 2%/200 surface (approximately 25% Zn) shows no detectable dissociation. The reason for this is not clear, although it may be that the dissociation is related to the surface crystallography.

CHAPTER 7

THE ADSORPTION OF HYDROGEN, CARBON DIOXIDE AND METHANOL

In addition to the work on CO adsorption, some initial studies were made on the adsorption of hydrogen and methanol on polycrystalline copper and brass surfaces, and of CO_2 on copper. These results have been included for the record.

7.1 Hydrogen adsorption

Copper and brass surfaces were exposed to up to 10000L of H_2 at room temperature and after the dose were cooled to approximately 200K so that a TPD spectrum could be obtained. In both cases the resulting TPD spectra showed that no hydrogen had been taken up directly from the gas phase. Attempts were made to adsorb atomic hydrogen by using local filaments as a dissociating source but no successful adsorption results were obtained.

7.2 Carbon dioxide adsorption

Polycrystalline copper and zinc surfaces were exposed to up to 100L of CO_2 at 100K. In both cases there was no evidence to suggest that CO_2 was chemisorbed by either surface because little change was observed in the C1s and O1s spectral region following the CO_2 dose.

7.3 Methanol adsorption

7.3.1 Methanol adsorption on polycrystalline copper

The adsorption of methanol on polycrystalline copper was studied at both room temperature and at 100K. At room temperature no apparent change could be seen in the C1s and O1s spectral region following exposure of the sample to 2×10^{-7} torr for up to 1000 sec (this is equivalent to 200L, without correcting for the ion gauge sensitivity factor). However at 100K, methanol was found to adsorb readily on the copper surface. Following exposure of the copper to 2×10^{-8} torr of methanol for 50 seconds (1L, uncorrected) both the C1s and O1s spectra exhibited single peaks with binding energies of 287.1 eV and 533.5 eV for the C1s and O1s peaks respectively. This can be compared to the work of Bowker and Madix[71] who obtained binding energies of 286.2 eV and 532.4 eV respectively at 140K. The reference level used by Bowker and Madix was 932.8 eV for the B.E. of the $Cu2p_{3/2}$ peak, the same as that used in this work. The adsorption experiments were repeated with different doses, and these gave binding energies which fell within a range of ± 0.2 eV. The higher binding energies and their range suggest that some methanol may have condensed on the initial chemisorbed layer so forming multilayers. Warming of the sample to room temperature resulted in the desorption of all the adsorbed methanol as the original clean spectra were recovered. This result is in agreement with that of Hofmann et al[73] who found that no adsorbed species existed at room temperature on a Cu(100) surface.

7.3.2 Methanol adsorption on a brass surface

The adsorption of methanol was carried out on a 5%/200°C surface, but the surface was created by annealing the lead contaminated 5% alloy. Although the maximum surface lead content was estimated at less than 0.1% in this 5%/200 surface, its presence means that any results could be misleading because Pb inhibits Zn segregation. However, the results are of some value since they differ from the pure copper case. Obviously, further experiments are necessary on pure brass surfaces.

Following exposure of the brass surface to 2×10^{-7} torr of methanol for up to 1000 sec at room temperature, the C1s and O1s spectral region showed little change from that of the clean surface. However, at 100K, methanol was readily adsorbed following exposures of 2×10^{-8} torr for up to 50 seconds. A dose of 2×10^{-8} torr for 25 seconds at 100K gave C1s and O1s spectra which were both characterised by a single peak at 287.6 eV and 533.9 eV respectively. These spectra are illustrated in Figures 7.1 and 7.2. On increasing the methanol dose, the binding energy was found to be coverage dependent and increased to 288.0 eV and 534.2 eV respectively following exposure to 2×10^{-8} torr for 75 seconds. This again suggests that multi-layers are being formed on top of the initial chemisorbed layer.

Warming of the adlayer to room temperature produced a different result to that on a pure polyx Cu surface. The residual C1s and

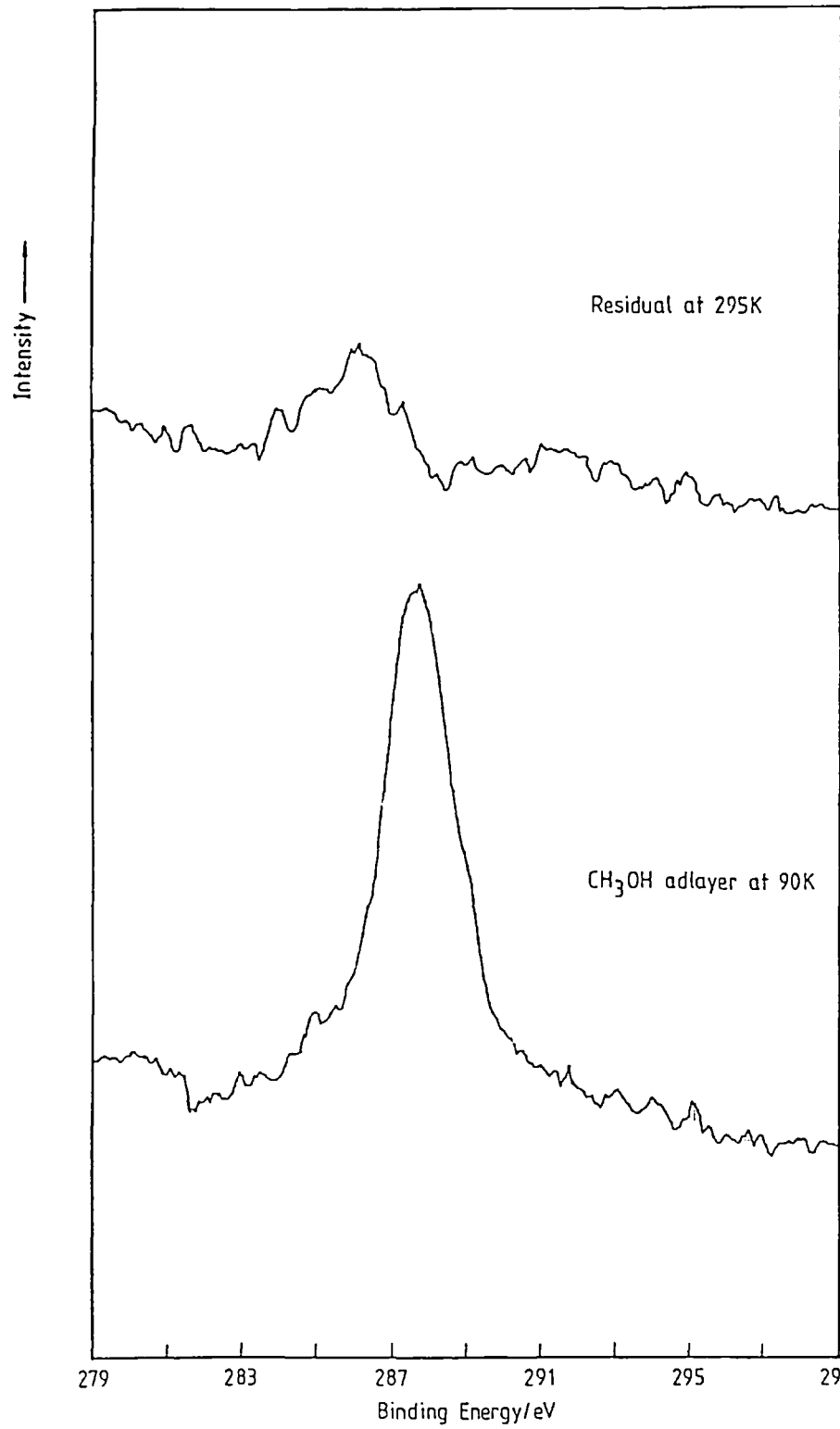


Figure 7.1. C1s spectrum of CH_3OH adsorbed on a brass surface containing ~20% Zn at 90K. The residual spectrum following warming of the adlayer to 295K is also shown

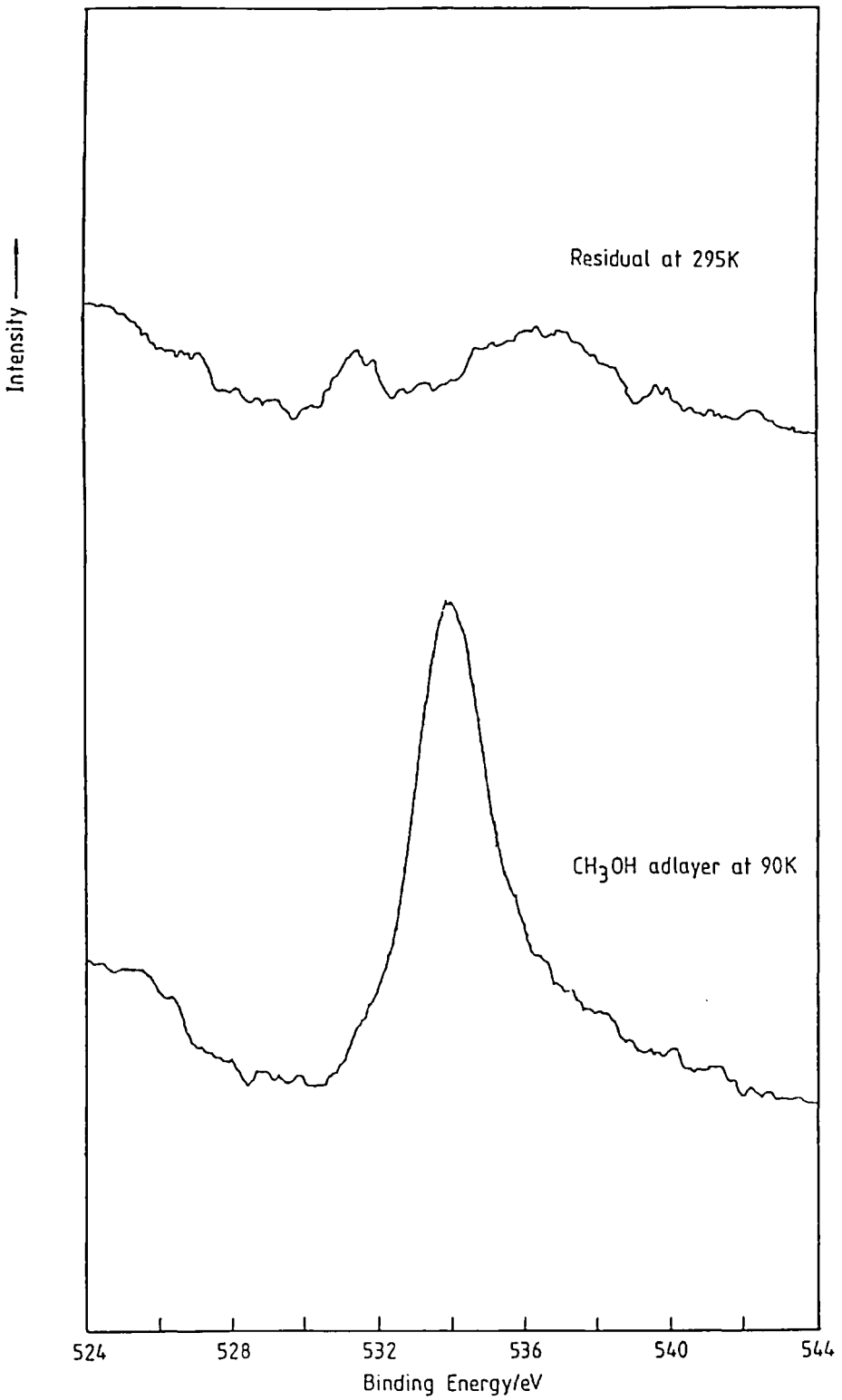


Figure 7.2. O1s spectrum of CH_3OH adsorbed on a brass surface containing ~20% Zn at 90K. The residual spectrum following warming of the adlayer to 295K is also shown

O1s spectra, taken at 100K, following exposure of the brass surface to 2 x 10^{-8} torr methanol for 50 sec at 100K and warming to room temperature show that there is some material left behind on the surface following warming. The residual spectra are shown in Figures 7.1 and 7.2. The C1s and O1s spectra of the original adlayer are also shown. The residual C1s and O1s spectra are characterised by peaks at approximately 286.0 eV and 531.4 eV respectively. The C1s binding energy is similar to that obtained by Bowker and Madix[71] upon warming their methanol adlayer at 140K to 270K, but the O1s binding energy is 0.7eV higher than that of Bowker and Madix. It may be that a methoxy species is formed which is chemisorbed via the oxygen atom to the zinc, so giving a different O1s binding energy.

However, it must be remembered that lead may be present in the surface which may give different results to pure brass surfaces. If these results can be reproduced on a lead free brass surface, then it would be significant because it would show that the presence of zinc in a copper surface results in the adsorption characteristics for methanol being modified rather than just reducing the amount of methanol taken up.

CHAPTER 8

BRASS FORMATION IN Cu-ZnO-Al_2O_3 CATALYSTS AND ITS EFFECT ON METHANOL SYNTHESIS

Methanol synthesis catalyst is loaded into a reactor in an unreduced form and has to be reduced in situ to become activated. It has been suggested that a brass phase may be formed within the catalyst during the reduction stage. No work has been reported in the literature on the effect of brass formation in Cu-ZnO-Al_2O_3 catalysts on the methanol synthesis reaction, and so to complement the surface studies, experiments were carried out on supported catalysts. The objective of these experiments was to deliberately condition the catalyst to form a brass phase with a range of zinc contents up to 20% (a level which is in excess of the normal catalyst) and to establish the effect of the brass phase on the methanol synthesis reaction.

8.1 Preparation and characterisation of the brassy catalysts

8.1.1 Preparation and conditioning

The catalyst samples used in this work were similar to a commercial methanol synthesis catalyst and had an approximate molar composition as oxide of 60% copper, 30% zinc and 10% aluminium. These catalyst samples were prepared at ICI Agricultural Division during a CASE industrial period, and this preparation is described in Appendix III. After preparation, the catalyst samples consisted of CuO, ZnO and Al_2O_3.

There have been no reports in the literature on the reduction conditions required to form brass in a 60/30/10 $Cu/ZnO/Al_2O_3$ catalyst. Van Herwijnen and De Jong[9] worked on a catalyst containing 64% Zn, 34% Cu and 2% Fe (by weight as oxides), and found that reduction over a period of 100 hours in a hydrogen stream containing 1 or 100 ppmv of water formed up to 10% Zn in solid solution in Cu at 300°C. The authors subjected their catalyst to a standard reduction procedure to reduce the CuO before conditioning to form brass. This method formed a guideline for the methanol catalyst.

In this work, the freshly prepared $CuO/ZnO/Al_2O_3$ samples were subjected to two stages of reduction, as described below.

(i) A standard pre-reduction procedure normally used to activate the catalyst.

(ii) A conditioning stage which was used to create the brassy catalysts.

The pre-reduction procedure involved temperature programming the samples from 100°C to 230°C at a linear rate of 40°C/hour in a stream of 5% hydrogen in nitrogen (5% H_2/N_2) with a GHSV of 3750 hr^{-1}. At the end of the temperature programme, the reduction was always complete as no more hydrogen was being consumed. At this point, the conditioning stage was started by raising the temperature rapidly to the desired level whilst maintaining the flow of reducing gas. The GHSV and composition of the reducing gas was left unchanged. After conditioning,

the samples were analysed in their reduced form by X-ray diffraction (XRD) to establish average crystallite sizes of the Cu and ZnO phases from line broadening and to determine the lattice constant of copper which gave the average zinc content in the brass phase. The lattice constant was found using the method of Rao and Anantharaman[125]. There is an almost linear relationship between the lattice constant and the percentage zinc in the brass phase[116], and this was used to find the average zinc content.

The objective of the experiments was to form a brass phase within the catalyst with a range of Zn compositions and also to form a brass phase which contained as much Zn as possible. Van Herwijnen and De Jong were able to form a brass phase with 10% Zn present at 300°C, so a temperature of 350°C was selected initially for the conditioning, but with a much shorter conditioning time. It was found that at this temperature that only 3% Zn in the brass phase (3% Zn in solid solution in Cu) was formed at maximum and that this level of brass formation became essentially time independent for long conditioning periods of up to 10 hours. Four samples labelled 1A, 1B, 1C, 1D, were tested, each being subjected to the standard reduction before being conditioned at 350°C for 0, 2, 4 and 6 hours respectively. The results for the brass formation and changes in average crystallite sizes with time are shown in Table 8.1 and Figures 8.1 and 8.2.

TABLE 8.1 Brass formation in Cu-ZnO-Al_2O_3 catalysts and the effect of conditioning on crystallite sizes

Sample	Treatment	%Zn in Brass phase	Cu Crystallite sizes (Å)			ZnO crystallite size (Å)
			(111) line	(200) Line	Average	
1A	Std. Rdn. only	0-1	-	-	-	-
1B	Std. Rdn. + 2hrs @ 350°C in 5% H_2/N_2	1½	85	55	70	35
1C	Std. Rdn. + 4hrs	2½	90	65	78	40
1D	Std. Rdn. + 6hrs	3	90	65	78	45
1E	Std. Rdn. + 10hrs	-	-	-	-	-
2A	Std. Rdn. only	0-1	65	45	55	35
2B	Std. Rdn. + 2hrs @ 375°C in 5% H_2/N_2	4	95	60	78	40
2C	Std. Rdn. + 4hrs	4½	100	65	83	45
2D	Std. Rdn. + 6hrs	5	100	70	85	-
2E	Std. Rdn. + 10hrs	5½	105	70	88	60
3A	Std. Rdn. only	0-1	65	60	63	30
3B	Std. Rdn. + 2hrs @ 400°C in 5% H_2/N_2	4½	105	65	85	45
3C	Std. Rdn. + 4hrs	5	105	70	88	55
3D	Std. Rdn. + 6hrs	6	110	70	90	65
3E	Std. Rdn. + 10hrs	6½	110	70	90	70
4A	Direct Rdn. @ 350°C for 2hrs	2	215	165	190	40
4B	for 4hrs	-	-	-	-	-
4C	for 6hrs	2½	235	180	208	45
4D	for 8hrs	3	235	180	208	45
5A	Std. Rdn. only	0-1	-	-	-	-
5B	Std. Rdn. + 4hrs @ 375°C in N_2 only	2½	95	70	83	40
5C	Std. Rdn. + 4hrs @ 400°C in N_2 only	1	100	70	85	40
5D	Std. Rdn. + 4hrs @ 400°C in 5% H_2/N_2	5	105	65	85	55

Notes: 5% H_2/N_2 refers to 5% hydrogen in nitrogen

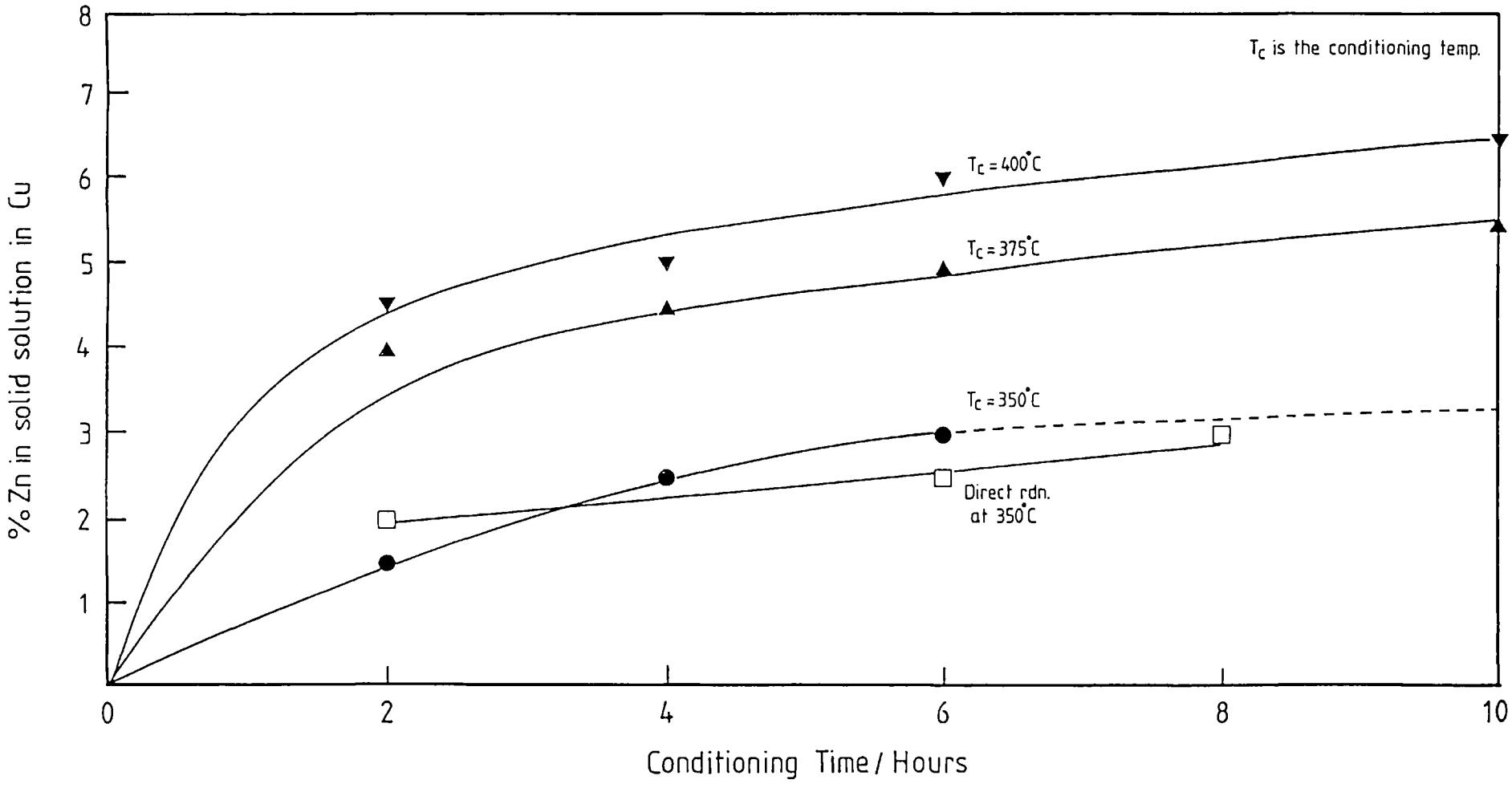


Figure 8.1. Brass Formation as a function of Conditioning Time

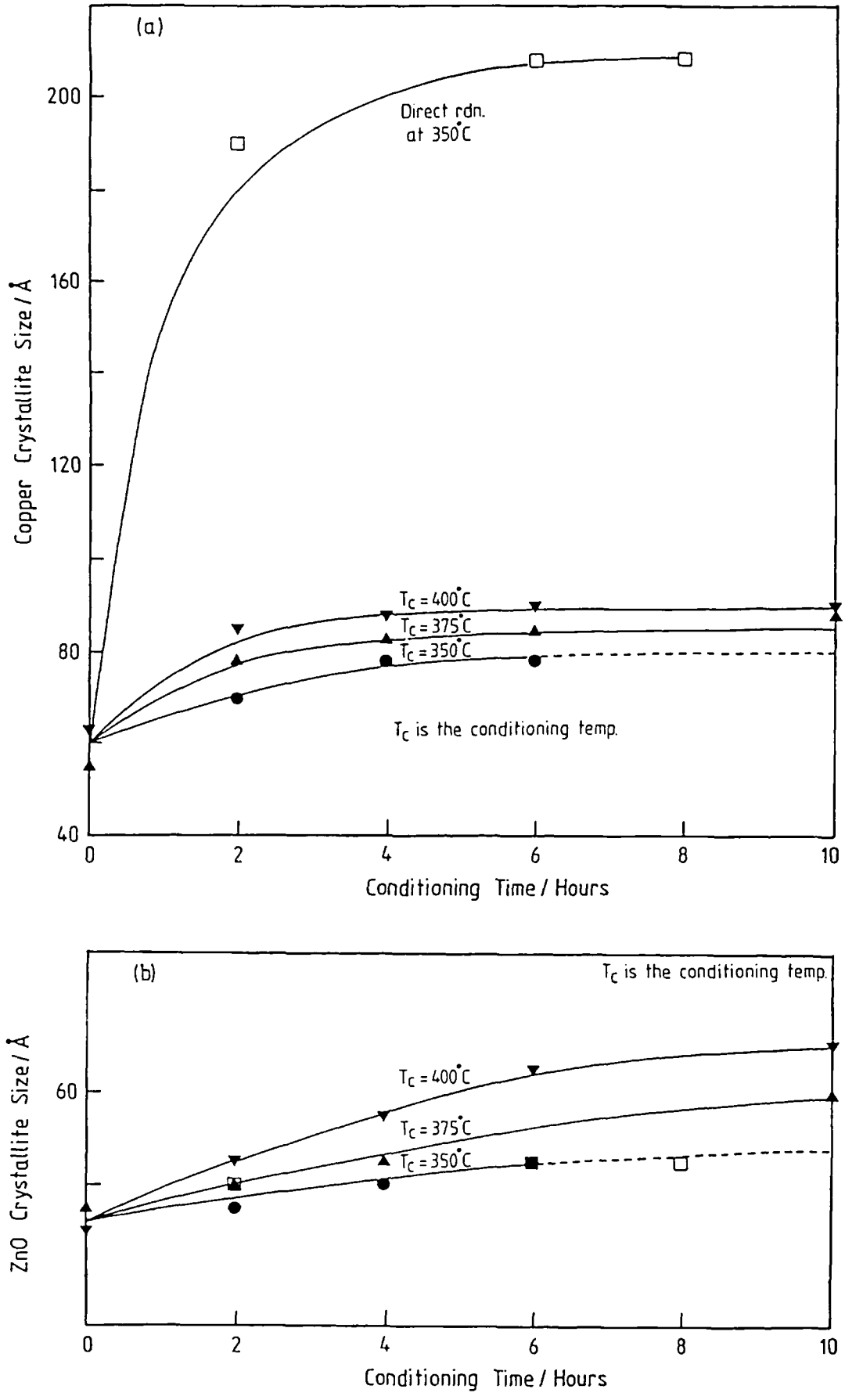


Figure 8.2. Increase in Crystallite Sizes with Conditioning Time

Two further experiments were carried out where catalyst samples were conditioned at higher temperatures in an attempt to increase the amount of zinc present in the brass phase. Five samples, labelled 2A, 2B, 2C, 2D and 2E were conditioned at 375°C for 0, 2, 4, 6 and 10 hours respectively, and a further five samples labelled 3A, 3B, 3C, 3D and 3E were again conditioned for 0, 2, 4, 6 and 10 hours, but at 400°C. In both of these experiments, a standard reduction procedure preceeded the conditioning, and in all three experiments the composition and GHSV of the reducing gas was kept constant. The effect of conditioning time on the brass formation and average crystallite sizes at 375°C and 400°C are also shown in Table 8.1 and Figures 8.1 and 8.2. The results following conditioning at 375°C and 400°C were similar to those obtained after conditioning at 350°C. The brass formation against conditioning time plots both increased rapidly at first, but at higher conditioning times, the increase in the amount of zinc dissolved in the copper became more gradual. As expected, increasing temperature led to an increasing percentage of zinc in the brass phase, with a maximum zinc content of 6.5% being reached following conditioning at 400°C for 10 hours. This result follows since the thermodynamic equilibrium moves towards brass formation with increasing temperature, as predicted in the work of Van Herwijnen and De Jong. Unlike the results of these two workers, the "equilibrium" percentage of zinc in the brass phase was achieved in only a few hours, rather than in the region of 100 hours. The reason for this is probably due to the fact that in

this work, the conditioning was carried out at a much higher temperature so that the reaction rate was increased and any diffusion limiting effects as discussed by these workers were much reduced. However, the percentage of zinc in the brass phase was much lower in this work, and the only obvious reason for this would appear to be the difference in catalyst composition, as there was less zinc oxide present in the original catalyst used in this work. It can also be seen from Figure 8.1 that at a given conditioning period, the difference in the brass formation between 400°C and 375°C was smaller by about a factor of two than that between 375°C and 350°C. The reason for this is probably associated with the increase in the copper crystallite sizes which is illustrated in Figure 8.2. It can be seen that for the same conditioning time, there was an increase in the size with increasing temperature, a result which is to be expected. An increase in crystallite size is indicative of a decrease in the surface area, and this will result in less hydrogen being adsorbed during the conditioning period when the conditioning is carried out at higher temperatures. In addition, sintering will reduce the cross-sectional area for diffusion of the Zn atoms and hence reduce the diffusion rate. Consequently, there are competing effects which determine the amount of zinc which is present in the brass phase, and a different balance between these two effects could explain the smaller increase in brass formation between 375°C and 400°C.

As expected, the copper crystallite size increased initially with conditioning time, then reached a plateau at higher conditioning times. This is clearly illustrated in Figure 8.2.

The increase of crystallite size through sintering is a disadvantage of conditioning the catalyst at high temperature. The ZnO crystallite sizes also increased with temperature and conditioning time as illustrated in Table 8.1 and Figure 8.2. The variation of the ZnO crystallite sizes will be discussed when the surface area measurements have been presented later in this chapter.

There was no conclusive evidence to suggest that there was no brass formation in the samples which were subjected to the standard reduction only (1A, 2A, 3A). The XRD results showed that a small reproducible shift in the copper peaks occurred indicating that up to 1% Zn in the brass phase could be formed. Although the shift was reproducible, the extent of the shift was not. Consequently, the percentage Zn in the brass phase for samples 1A, 2A and 3A have been recorded as 0 to 1%. In Figure 8.1, the amount of Zn at zero conditioning time has been marked as zero. This is a somewhat arbitrary choice as the real amount may lie somewhere between 0-1%.

In an attempt to form a more brassy catalyst, an experiment was carried out where the standard reduction cycle was omitted and instead the catalyst samples were rapidly heated to 350°C in dry nitrogen before the reducing gas (5% H_2/N_2) was applied. Four samples, labelled 4A, 4B, 4C, 4D, were subjected to this procedure, and were reduced for 2 hours, 4 hours, 6 hours and 8 hours respectively. The results for the brass formation and for the increase in copper crystallite sizes are shown in Table 8.1

and Figures 8.1 and 8.2. It can be seen that the extent of brass formation was similar to the samples which were subjected to the standard pre-reduction procedure and conditioned at 350°C and that a maximum average zinc content of the brass phase was also 3%. However, it can be seen that there was a drastic effect on the crystallite sizes, which were, on average, a factor of 2½ times greater than those of the samples which were pre-reduced before conditioning. This increase in the crystallite size should be reflected in the activity tests, and this will be covered in section 8.2.

A further experiment was carried out to compare the results obtained above with samples which were conditioned at 375°C and 400°C after the pre-reduction procedure, but only under nitrogen, so that the sintering could be compared without further reduction of the catalyst. Four samples labelled 5A, 5B, 5C, and 5D were pre-reduced in the usual manner. Sample 5A was not treated any further. Samples 5B and 5C were conditioned under a flow of nitrogen only for four hours at 375°C and 400°C respectively. Sample 5D was conditioned at 400°C in the usual reducing gas for 4 hours and was a repeat of sample 3C. The XRD results for sample 5D were almost identical to those of 3C, indicating that these showed a degree of reproducibility and could be treated with some certainty. The samples which were conditioned in in nitrogen (5B, 5C) had similar average copper crystallite sizes to the equivalent samples which were conditioned

in the reducing gas (i.e. 2C, 3C), suggesting that the sintering was due to thermal effects only. However, there was a reduction in the extent of brass formation in samples 5B and 5C compared with 2C and 3C. It was found that the brass phase in the sample treated at 375°C in N_2 only contained 2½% Zn, whilst that of the sample treated at 400°C in N_2 only contained 1% Zn. The reason for the presence of a significant amount of brass in the sample which was treated at 375°C could be attributed to the presence of reducing components in the nitrogen stream. However, this result does not significantly influence the general interpretation, as given later.

8.1.2 Surface Areas

All of the samples had their surface area measured by N_2 adsorption (B.E.T.) to give the total surface area and by N_2O adsorption which gave the metal surface area. The accuracy of the latter measurement will be discussed later. Before the areas were measured, the samples for area testing had to be air stabilised, because of the nature of the apparatus which was used for both types of area testing. The stabilisation was achieved by allowing a stream of nitrogen containing 1-2% oxygen to pass over the samples for approximately 20 hours at room temperature. If the samples had been immediately exposed to atmospheric conditions, the rapid oxidation of the surface copper would have created high temperatures in the samples which would have altered their character. The apparatus used for the BET measurement did not enable the samples to be re-reduced before

measuring the area. This could be a source of error.

On the N_2O adsorption apparatus, the samples could be re-reduced in situ and two measurements were made based on the unreduced weight of catalyst (i.e. air stabilised) and on the reduced weight. The results for the BET and N_2O areas are shown in Table 8.2, where both the N_2O area based on unreduced and reduced weights are presented under unreduced and reduced respectively. In general the measurements as reduced were used as these gave a truer representation of the area. In addition to these areas, the oxide areas ($ZnO + Al_2O_3$) were also found by subtracting the N_2O area from the BET area.

8.1.3 Discussion

Figure 8.3 shows the effect of conditioning time on the surface areas. It can be seen that trends do exist in the area measurements, although there are several points which appear to be anomalous. These anomalies occurred in both the B.E.T. and the N_2O adsorption measurements. The B.E.T. scatter could be attributed to the catalyst samples having their areas determined whilst remaining air stabilised. This is not the ideal way of measuring the B.E.T. areas, but was experimentally unavoidable. Similarly, the anomalies in the areas determined by N_2O adsorption could be as a result of sample oxidation then re-reduction before measurement having an effect on the catalyst.

TABLE 8.2 Catalyst Surface Areas

Sample	% Zn in Brass Phase	B.E.T. area m^3/g	Area from N_2O		'Oxide' area m^3/g	Cu Area from XRD m^3/g
			unreduc. m^3/g	reduc. m^3/g		
1A	0-1	65.4	27.8	30.8	34.6	-
1B	1½	71.8	26.4	28.5	43.3	57
1C	2½	68.6	26.5	-	42.3	51
1D	3	50.6	21.1	24.5	26.1	51
1E	-	55.3	29.2	30.1	25.2	-
2A	0-1	69.0	30.0	32.0	37.0	73
2B	4	49.1	22.3	26.3	22.8	51
2C	4½	50.9	-	25.7	24.2	48
2D	5	44.7	20.8	-	23.9	47
2E	5½	46.3	15.8	17.8	28.5	45
3A	0-1	67.9	33.0	33.9	34.0	63
3B	4½	42.9	18.5	21.4	21.5	47
3C	5	41.4	23.2	23.3	18.1	45
3D	6	40.4	22.0	22.6	17.8	44
3E	6½	46.4				44
4A	2	42.4	12.1	13.1	29.3	21
4B	-	41.6	11.9	12.8	28.8	-
4C	2½	41.5	12.6	12.8	28.7	19
4D	3	42.6	12.4	12.5	30.1	19
5A	0-1	67.9	33.6	34.5	33.4	-
5B	2½	50.1	22.9	23.9	26.2	48
5C	1	54.5	25.0	25.4	29.1	47
5D	5	49.3	17.5	18.1	31.2	50

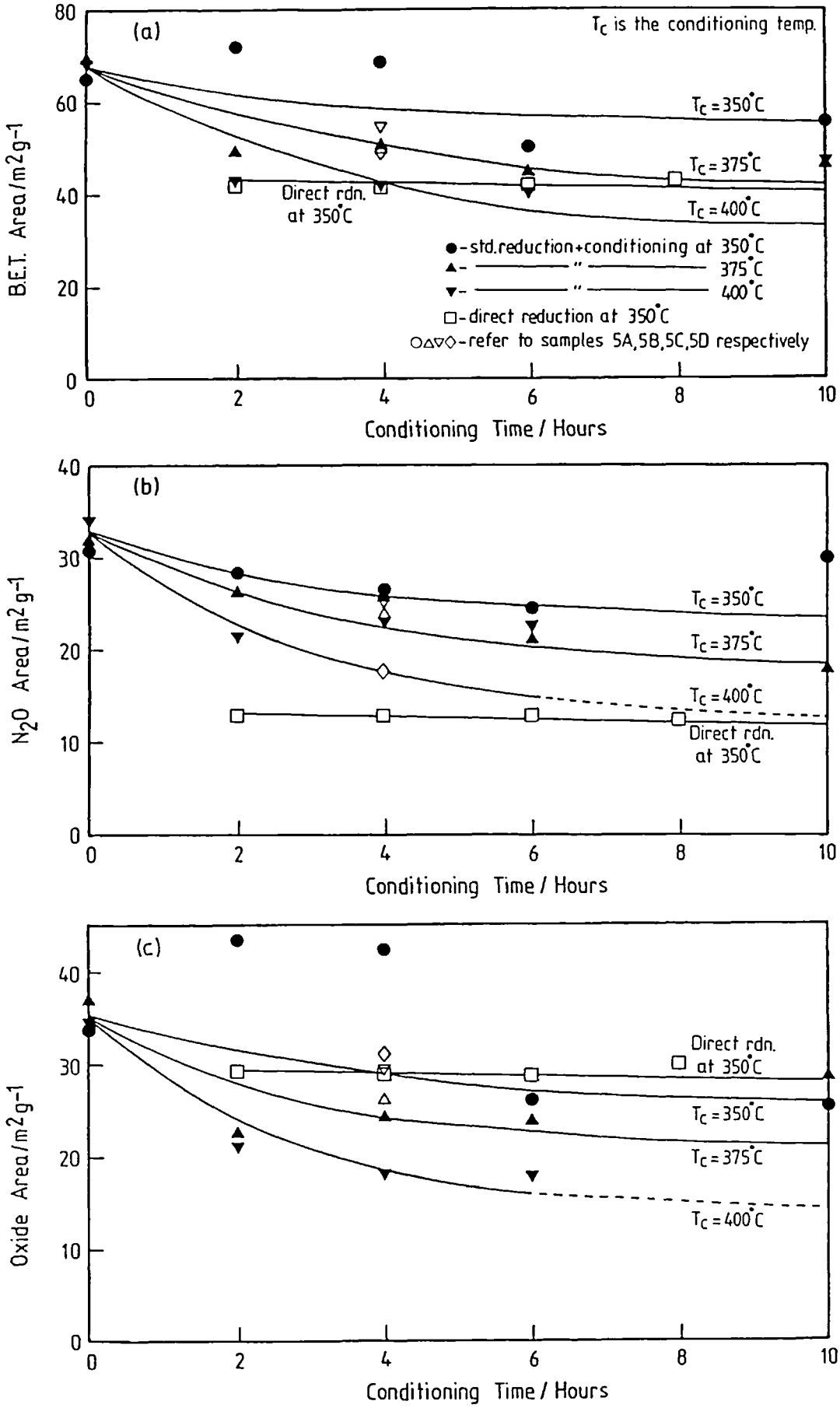


Figure 8.3. Catalyst Surface Areas as a function of Conditioning Time

The Cu areas were also calculated from the XRD crystallite sizes as a comparison with the areas obtained by N_2O adsorption. These areas were found using the expression given below and are presented in Table 8.2.

$$\text{Surface Area of reduced catalyst } (m^2/g) = \frac{6x_{Cu}}{\zeta d} \qquad (8.1)$$

where x_{Cu} is the weight fraction of Cu in the catalyst,

d is the crystallite size in $\mathring{A}$

ζ is the density of Cu.

The areas calculated from the crystallite sizes were plotted against those obtained from N_2O adsorption, and this is shown in Figure 8.4. It can be seen that there is a correlation between the two types of areas, although some scatter does exist. This is probably due to errors introduced by air stabilising and re-reducing the samples before adsorption of N_2O to determine the areas. In addition, spherical crystallites were assumed to be present to simplify the calculation. In reality, the crystallites will be of a more random shape and a shape factor is really required in Equation (8.1). Variations in the percentage of Zn in the brass phase will lead to broadening of the crystallites and again, this is not accounted for in Equation (8.1), so giving another source of error. The correlation is not linear however, for the following reason. The area measurement by N_2O adsorption is a surface technique,

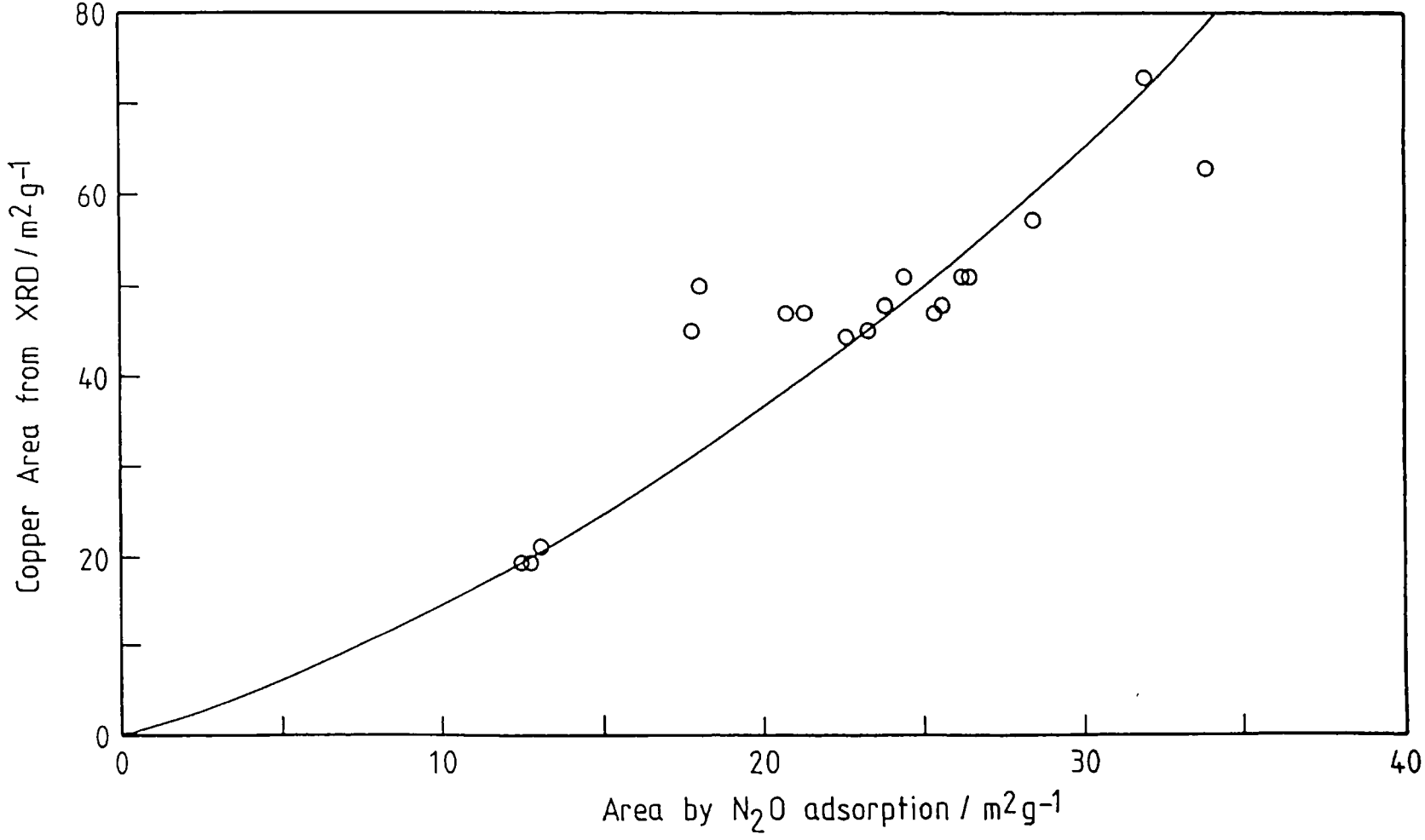


Figure 8.4. Correlation of metal areas from XRD and from N_2O adsorption

whereas the area calculated from the crystallite sizes takes into account the unexposed parts of the crystallites which are not 'seen' by the N_2O adsorption. Consequently, it would be expected that the crystallite size method would give the greater area. This was the case experimentally.

As can be seen from Figure 8.3, increasing the conditioning temperature resulted in a decrease in the three surface areas for a similar conditioning time, as would be expected. The BET and N_2O surface areas as a function of conditioning time followed similar trends for the three different conditioning temperatures. The majority of the area loss occurred in the early stages of the conditioning period and this is in agreement with the rate of increase of the copper crystallite size shown in Figure 8.2. The oxide area as a function of conditioning time also followed a similar trend. However, the most interesting features which are illustrated in Figure 8.3 are concerned with the shapes and positions of the curves for the surface area as a function of conditioning time for the samples which were reduced directly at 350°C. These curves are much flatter than the other curves, showing that little change in any of the surface areas occurred during the conditioning period above 2 hours. This suggests that almost all of the sintering occurred during the first 2 hours, but very little after that. Again this is reflected reasonably in the copper crystallite sizes. However, the position of this curve relative to the three curves representing

the samples which were conditioned after pre-reduction is not the same for the three types of surface areas. It can be seen that the surface area by N_2O which represents the metal area, is lower for the samples directly reduced at 350°C than that for the samples conditioned at 400°C following pre-reduction. This is consistent with the results for the copper crystallite sizes for these different treatments, where it was found that the former treatment gave much larger copper crystallite sizes. This result confirms that omitting the pre-reduction stage before conditioning had a drastic effect on the copper phase of the catalyst. However, the oxide surface areas for the samples reduced directly at 350°C were similar to those of the samples which were pre-reduced, then conditioned at 350°C in reducing gas, as illustrated in Figure 8.3.c. This is a significant result because it suggests that the ZnO phase was much less susceptible to the adverse conditions than the Cu phase. This is supported by considering the ZnO crystallite sizes, as shown in Figure 8.2. It can be seen that the ZnO crystallite sizes for the samples which were reduced directly at 350°C were similar to those of the samples which were conditioned at 350°C following the standard reduction for similar conditioning times. If the ZnO phase was susceptible to sintering, then it would have been expected that the ZnO crystallite sizes would have increased drastically in a similar manner to the copper crystallites. Another piece of evidence which suggests that the ZnO phase is not susceptible to sintering through thermal treatment comes from the comparison of the oxide area of sample 5C which was conditioned in nitrogen only at 400°C for 4 hours

with those of other samples. The oxide area of this sample was similar to that of sample 4C (direct reduction at 350°C) and greater than that of sample 3C which was treated in similar conditions to sample 5C, but in reducing gas instead of nitrogen. This is also reflected by the ZnO crystallite sizes of samples 1C (std. rdn. then 4 hours at 350°C in 5% H_2/N_2), 3C and 5C. The ZnO crystallite sizes of samples 1C, 4C and 5C were similar, but smaller than those of sample 3C. These results illustrate that despite the additional thermal treatment of sample 5C compared with that of samples 1C and 4C the ZnO size and area characteristics generally remained similar. However, the copper sizes and areas did not show this property. The copper crystallite size for samples 3C and 5C were almost identical, and the areas from N_2O adsorption were also similar. This is in contrast to the ZnO characteristics described above. The similar copper size and area characteristics for samples 3C and 5C were as a result of similar thermal treatment because both were conditioned at 400°C. However, sample 1C, which was conditioned at 350°C, did not suffer as much through sintering of the copper phase as samples 3C and 5C. It is interesting to consider the relation between the oxide area and metal area losses and the brass formation. For the samples which were reduced directly at 350°C a drastic reduction in the metal area occurred but there was only 2-3% Zn present in the brass phase. A comparison between samples 1C and 4C shows that for the same amount of brass formation (i.e. 2.5% Zn), the metal areas differed by a factor of almost two. Furthermore, a comparison between samples 3C and 5C shows that similar thermal treatment gave similar copper size and area characteristics,

but that the extents of brass formation were completely different. For sample 5C, only 1% Zn was present in the brass phase, whereas sample 3C had 5% Zn present. The increase in the extent of brass formation was also accompanied by a decrease in the oxide area.

The results above strongly suggest that thermal treatment is the major cause of copper sintering and that formation of a brass phase only has a minor role in metal area changes. This would be supported if a plot of the area by N_2O against brass formation results in the former being weakly dependent on the latter. This plot is shown in Figure 8.5.b. where the spread of points indicates that the metal area varies with brass formation initially, but becomes independent of brass formation at higher Zn contents. If the metal area had a significant dependence on the brass formation, a curve which was either linear or more likely, monotonically decreasing with increasing zinc content would have been expected in Figure 8.5.b.

A plot of the oxide area against brass formation, as shown in Figure 8.5.c., provides evidence to suggest that the oxide area is much more strongly dependent on brass formation, because there is an almost linear trend. This linear trend is not reflected in the plot of the oxide area against conditioning time (Figure 8.3.c.) because the brass formation tails off with increasing conditioning time.

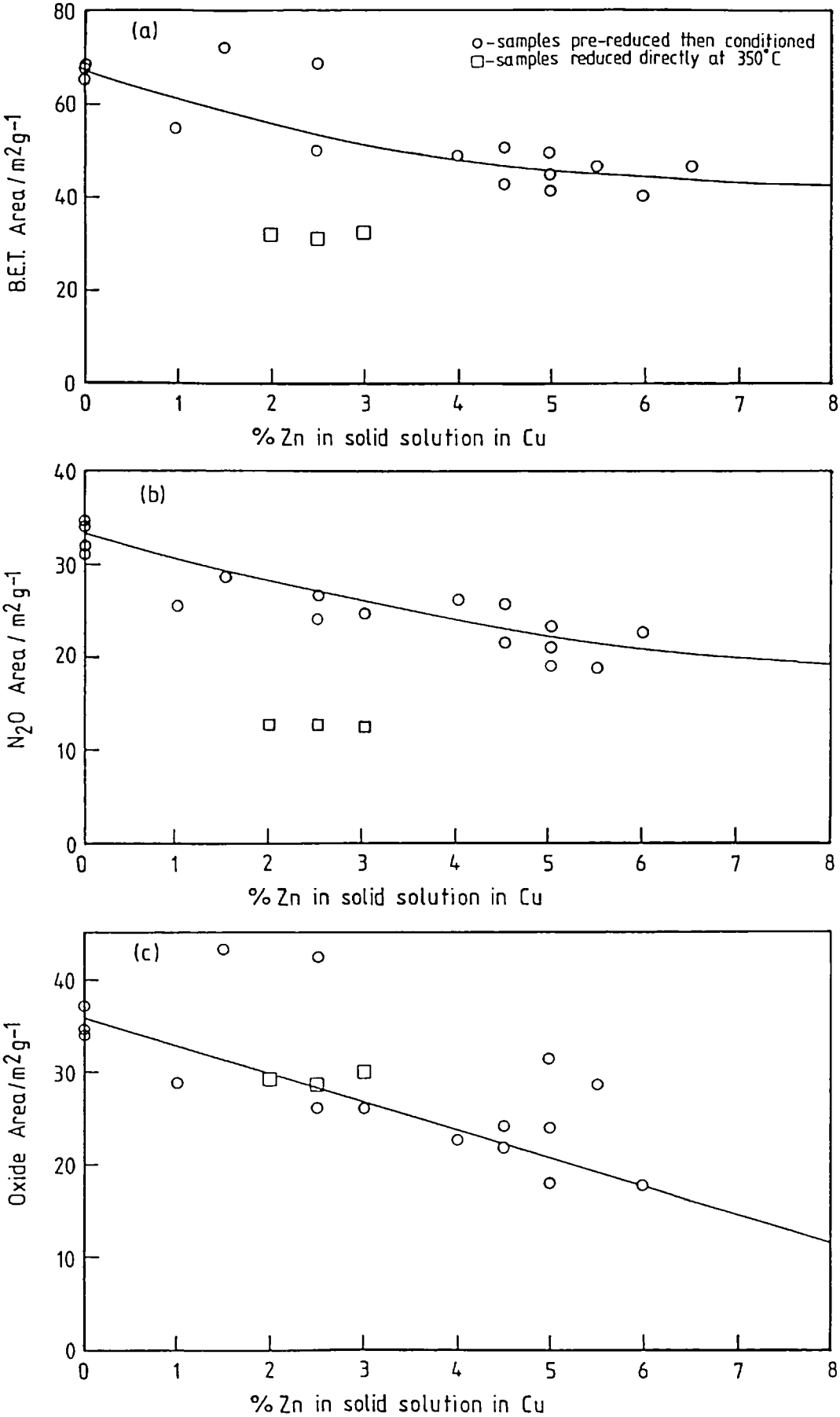


Figure 8.5. Catalyst Surface Areas as a function of Brass Formation

It can be seen in the plot of the area by N_2O adsorption against brass formation that the three points representing the samples which were reduced directly at 350°C are well separated from the majority of the remaining points, because they suffered heavy sintering. However, in the plot of oxide area against brass formation, these three points are part of the linear trend. This suggests that brass formation was the major cause of the reduction in oxide area and, as mentioned before, thermal effects only played a minor role in reducing the oxide area. The area loss of the oxide must be associated with the partial elimination of the ZnO when some of it is reduced and the resulting zinc alloys with the copper phase.

8.2 Activities of the brassy catalysts

After the treatment procedures as described in the previous section, all of the samples were then subjected to an activity test to determine the effect of brass formation and sintering on the rate of methanol formation.

The activity tests were all carried out in a conventional micro-reactor system with six separate reactors. Each reactor was charged with 2ml of treated catalyst. The gas flowrate through each reactor was set at 80 litres/hr, giving a GHSV of 40,000 hr^{-1}. In a few cases, less than 2ml of catalyst was charged, and for these, the flowrate was changed so that the GHSV was

was kept constant. The exit gas from each reactor was analysed in turn by a gas chromatograph which gave the percentage methanol in the streams leaving each reactor. An accurate rotary gas meter was also available to check the flowrates. In general, the gas flowrates were within 2 litres/hr of the required rate. The reaction conditions for the activity tests are given below :

Reaction gas composition	:	67% H_2, 10% CO, 3% CO_2, 20% N_2
Reactor pressure	:	50 atm
Reactor inlet temperature	:	234°C
Space velocity	:	40,000 hr^{-1}

The inlet temperature of 234°C gave a typical reactor temperature of approximately 250°C. For each batch of tests, four treated samples were charged into four of the reactors, whilst the remaining two were charged with 2ml of an ICI commercial methanol synthesis catalyst, in an unreduced form. These latter two catalysts were used to standardise each batch of tests so that a general comparison could be made. The micro-reactor system which was available had a maximum temperature of 350°C which meant that all of the catalyst treatment procedures to form brass were carried out in a separate unit. Consequently, the treated catalysts had to be transferred for activity testing. In some cases, the catalysts were air-stabilised, in a similar manner to that described in section 8.1 so that charging of the reactors was possible in normal atmospheric conditions. The remainder of the catalysts were charged in an unstabilised form. The possible effect of this stabilisation will be

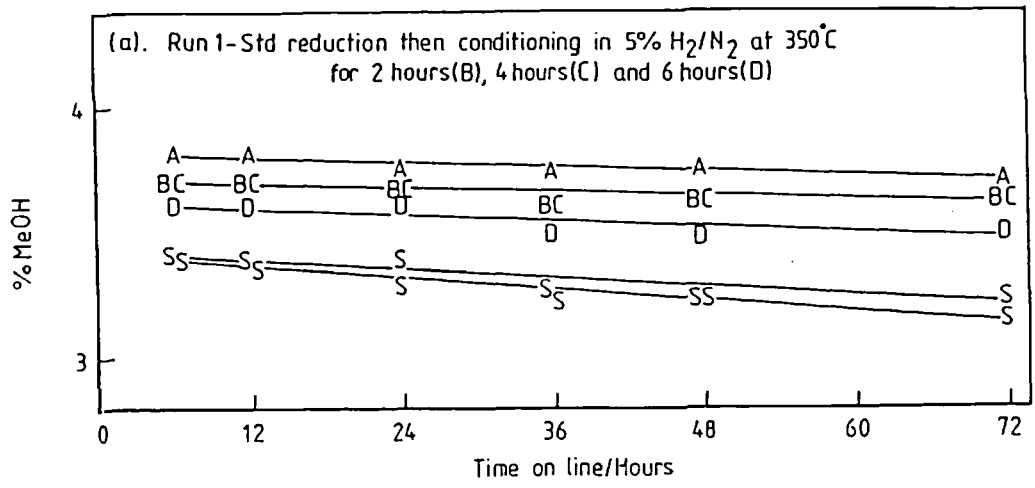
discussed later in light of the experimental results. In all cases, the standard commercial catalyst was charged in a totally unreduced form. Before the actual activity test could begin, all of the loaded samples were subjected to a standard reduction process, similar to that described in the previous section. This was done to re-reduce the air-stabilised samples, to reduce any slight oxidation of the unstabilised samples which may have occurred during charging, and to reduce the standards.

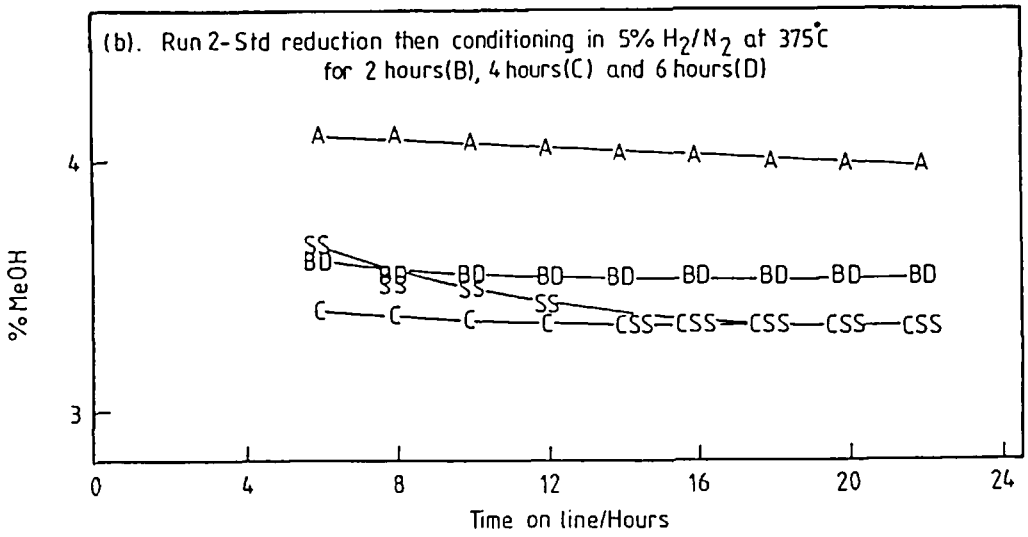
The objective of the activity tests was to determine the initial activities of all of the samples and to qualitatively assess the catalyst die-off over a period of time. In practice, the system was allowed to settle down after the reaction gas was admitted to the reactors, so that the first reliable readings usually appeared after six hours on line. Successive readings then formed the activity against time plot. A summary of the activity tests is presented in Table 8.3, where the percentage methanol in the exit streams are shown for 6 hours on line and at the end of the run. The percentage methanol against time on line plots, illustrating the catalyst die-off, are shown for Runs 1, 2, 3, 5 and 6 in Figure 8.6.

It was found that there was no evidence to correlate the extent of die-off with brass formation, as the die-off varied from run to run rather than from sample to sample. The maximum deactivation of the catalyst was around 15% over a 72 hour period, but some samples such as 1E, 2E and 3E only suffered a deactivation of

TABLE 8.3 Activity Test Results

Run no.	Sample	Charge Vol. (mls)	Charge Wgt. (gms)	Unstabilised or stabilised	% MeOH Init.	% MeOH 6hrs	% MeOH Final
1	1A	2.0	1.74	U	3.85	3.82	3.70
	1B	2.0	1.86	U	3.75	3.71	3.67
	1C	2.0	2.00	U	3.75	3.70	3.65
	1D	2.0	1.97	U	3.67	3.61	3.51
	Std.1	2.0	1.91		3.50	3.42	3.15
	Std.2	2.0	1.89		3.45	3.40	3.23
2	2A	1.5	1.38	S	4.15	4.10	3.98
	2B	1.5	1.52	S	3.65	3.60	3.52
	2C	1.5	1.52	S	3.45	3.40	3.33
	2D	1.5	1.64	S	3.75	3.60	3.55
	Std.1	1.5	1.57		3.90	3.65	3.33
	Std.2	2.0	2.17		4.05	3.65	3.33
3	3A	2.0	1.87	U	4.30	4.25	4.22
	3B	2.0	2.19	U	3.98	3.98	-
	3C	2.0	2.22	U	3.55	3.56	3.48
	3D	2.0	2.26	U	3.30	3.25	3.19
	Std.1	2.0	1.87		3.65	3.61	3.50
	Std.2	2.0	1.82		3.60	3.57	3.52
4	4A	2.0	2.00	S	-	2.10	-
	4B	2.0	1.98	S	-	2.30	-
	4C	2.0	1.92	S	-	2.10	-
	4D	2.0	1.90	S	-	2.05	-
	Std.1	2.0	2.05		-	3.80	-
	Std.2	2.0	1.97		-	3.80	-
5	5A	2.0	1.95	S	4.40	4.25	3.90
	5B	2.0	2.11	S	3.70	3.60	3.32
	5C	2.0	2.05	S	3.57	3.55	3.28
	5D	2.0	2.04	S	3.45	3.35	3.08
	Std.1	2.0	1.93		3.75	3.60	3.20
	Std.2	2.0	2.02		3.60	3.55	3.12
6	1E	2.0	2.15	U	3.90	3.90	3.82
	2E	1.7	1.57	U	3.08	3.06	2.91
	3E	2.0	2.14	U	3.35	3.33	3.21
	Std.	2.0	1.79		3.45	3.43	3.25





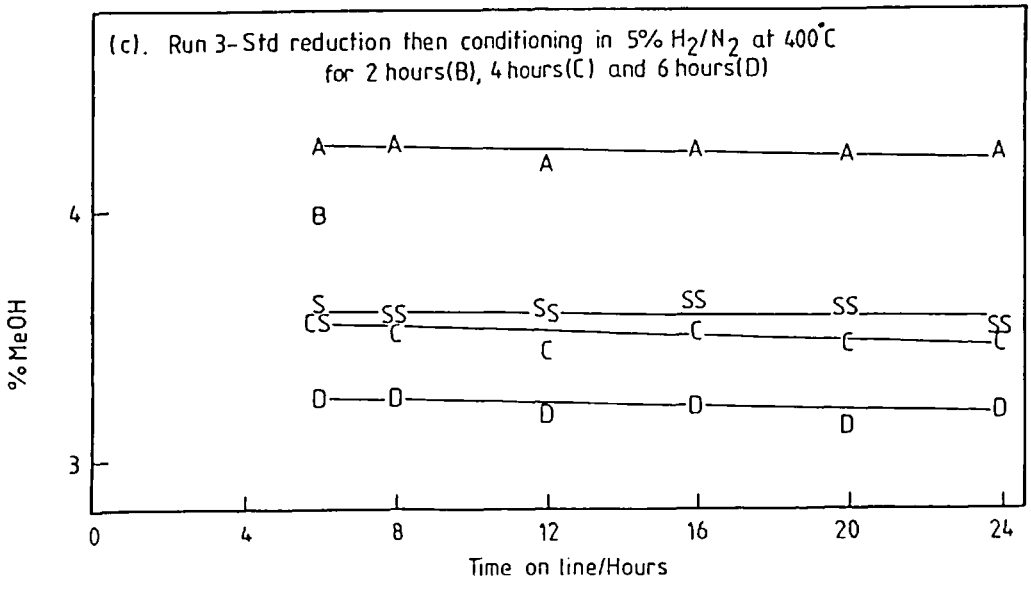


Figure 8.6. Die-off curves for the brassy catalysts

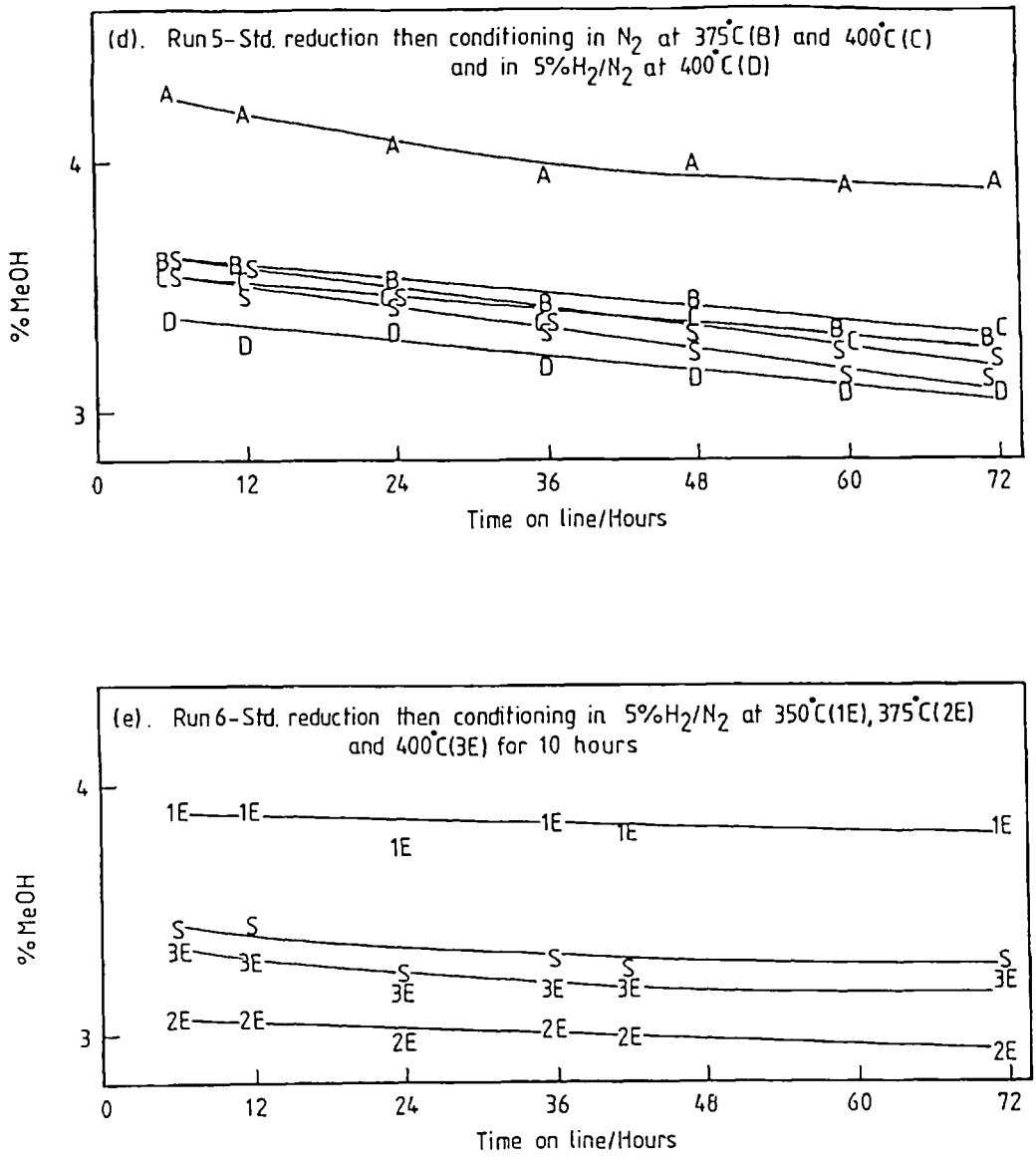


Figure 8.6. Die-off curves for the brassy catalysts

between 2% and 4%. These results lead to the conclusion that there must have been differing extents of catalyst poisons in the reaction gases during different test runs.

Although the first reliable results from the micro-reactor appeared after six hours on line, it can be seen that in some cases that there was a significant de-activation of the catalyst over the first six hours. It was decided that the effect of sintering and brass formation would be better correlated with the activity of the freshly loaded catalyst at around zero hours on line so that any poisoning effects after 6 hours on line did not come into the results. The initial activity of the freshly loaded catalyst was found by extrapolation of the die-off curves to zero time. The values for the initial percentages of methanol are also shown in Table 8.3. All of the percentage methanol figures were converted into relative activities, with the standards having an initial relative activity of 1.00. The relative activity was calculated by a method developed by ICI, which is described below. It has been shown experimentally[126] that the increase in the percentage of methanol present in the exit stream is not a linear relation of the amount of active catalyst present. This is because the methanol synthesis reaction is exothermic and an increased activity will be made greater because the heat liberated will increase the reaction rate. A curve was developed which related the percentage of methanol in the exit stream to the volume of catalyst charged, and this is shown in Figure 8.7. This graph forms the basis of the determination of the relative

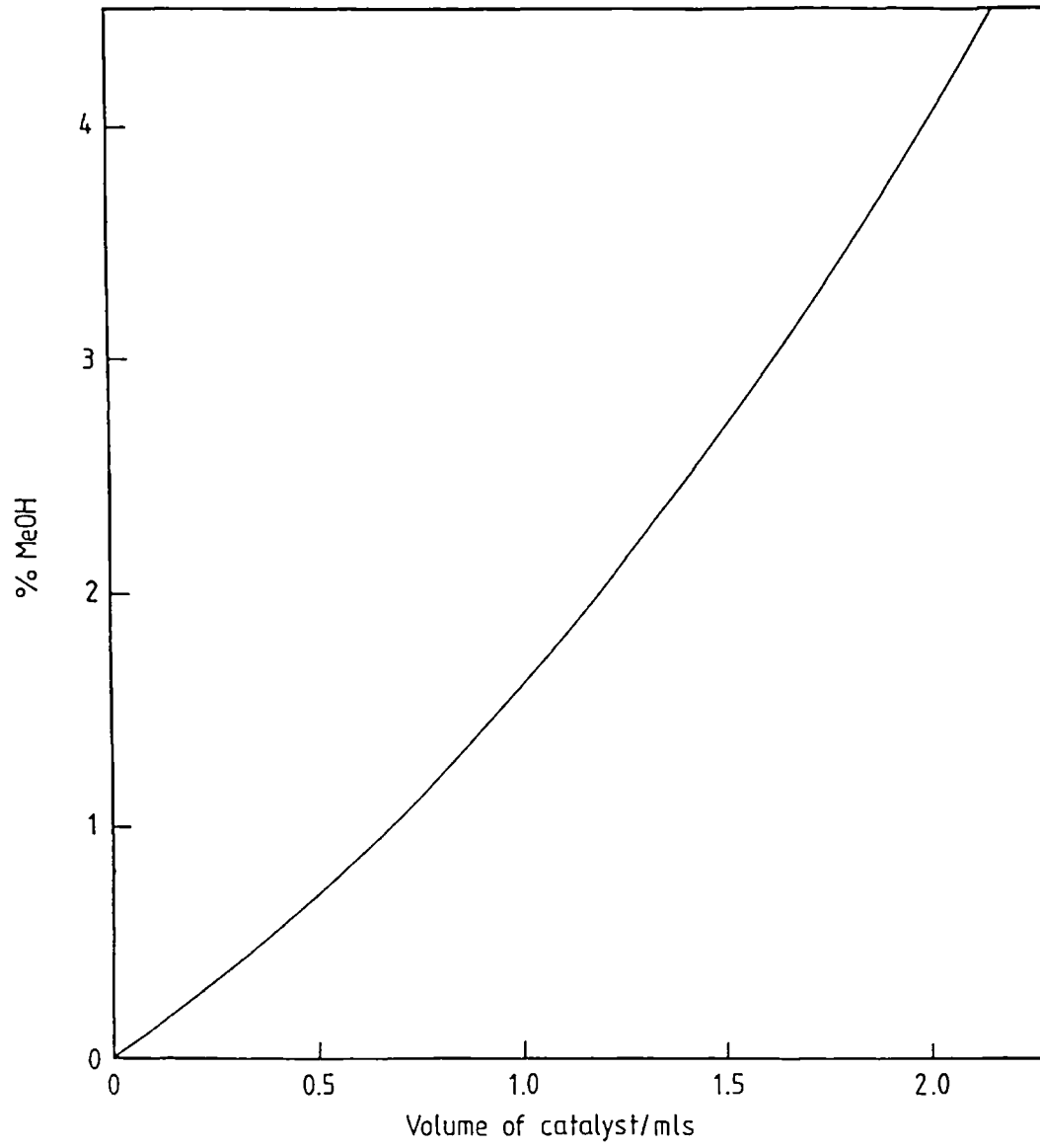


Figure 8.7. Relation between the percentage of MeOH formed and the volume of catalyst charged

activities along with the following equation below :

$$\text{Rel. Activity} = \frac{\text{mls. of sample}}{\text{mls. of std.}} \times \frac{\text{wt. of std.}}{\text{wt. of sample}} \qquad (8.2)$$

The volume of each test sample which was equivalent to the observed percentage methanol was found using Figure 8.7, along with the equivalent volumes of both standards in the batch. The initial relative activity of one of the standards was fixed at 1.00, and from this, the relative activities were then found for all of the samples in the batch including the remaining standards. The initial relative activities of the two standards were averaged and then all of the activities of the batch were adjusted so that the average of the standards was 1.00. This method of determining the relative activities of the samples takes into account the additional effect of the heat of reaction. The relative activities for all of the samples are given in Table 8.4.

It was mentioned earlier that some of the samples were loaded into the micro-reactor in an air-stabilised form. Obviously, these samples had an additional weight because they were partially oxidised compared with the samples which were loaded in reduced form. It was found experimentally by careful discharging from the micro-reactor and weighing that the weight following stabilisation was a factor of 1.04 greater than the unreduced weight. The weights of some of the unreduced samples were also checked after the activity test and these did not show any change in weight. Consequently, the relative activities of the samples loaded in an air-stabilised form were corrected

TABLE 8.4 Relative Activities and Methanol Production Rates

Run No.	Sample	Relative Activities			MeOH formation rate mol/kg catalyst.hr		
		Init.	6hrs.	Final	Init.	6hrs.	Final
1	1A	1.18	1.17	1.15	74.9	74.3	73.0
	1B	1.08	1.07	1.07	68.6	67.9	67.9
	1C	1.01	1.00	0.99	64.1	63.5	62.7
	1D	1.01	0.99	0.97	64.1	62.7	61.6
	Std.1	1.00	0.98	0.93	63.5	62.2	59.1
	Std.2		0.99	0.95		62.7	60.3
2	2A	1.24	1.23	1.20	78.7	78.1	76.2
	2B	1.02	1.01	1.00	64.8	64.1	63.5
	2C	0.98	0.97	0.96	62.2	61.6	61.0
	2D	0.97	0.94	0.93	61.6	59.7	59.1
	Std.1	1.00	0.96	0.93	63.5	61.0	59.1
	Std.2						
3	3A	1.13	1.12	1.11	71.8	71.1	70.5
	3B	0.91	0.91	-	57.8	57.8	-
	3C	0.82	0.82	0.81	52.1	52.1	51.4
	3D	0.77	0.76	0.75	48.9	48.3	47.6
	Std.1	1.00	0.99	0.97	63.5	62.7	61.6
	Std.2		1.00	1.00		63.5	63.5
4	4A	-	0.67	-	-	42.5	-
	4B	-	0.73	-	-	46.3	-
	4C	-	0.70	-	-	44.5	-
	4D	-	0.69	-	-	43.8	-
	Std.1	-	1.00	-	-	63.5	-
	Std.2	-		-	-		-
5	5A	1.20	1.17	1.10	76.2	74.3	69.9
	5B	0.98	0.96	0.90	62.2	61.0	57.2
	5C	0.98	0.97	0.92	62.2	61.6	58.4
	5D	0.96	0.94	0.89	61.0	59.7	56.5
	Std.1	1.00	0.98	0.87	63.5	62.2	55.2
	Std.2						
6	1E	0.91	0.91	0.90	57.8	57.8	57.2
	2E	0.89	0.89	0.86	56.5	56.5	54.6
	3E	0.82	0.82	0.79	52.1	52.1	50.2
	Std.	1.00	0.99	0.97	63.5	62.7	61.6

by this factor to take into account the additional weight from partial oxidation. This correction is included in the relative activities in Table 8.4.

Comparison of the activity results from batch to batch could only be made effectively if the standards gave similar percentages of methanol in the exit stream for a similar weight of standard charged. It has been shown that under typical methanol activity test conditions, the commercial catalyst gives 4.00% methanol in the reactor exit stream when 2.1gms of the catalyst is charged, and that a plot of the percentage methanol against weight of standard charged formed a similar curve to that in Figure 8.7[126]. The percentage methanol against weight of standard charged was plotted for all of the standards used in the activity tests and this is shown in Figure 8.8. It can be seen that in general the points lie close to the curve representing the experimental relation between percentage methanol and weight of standard charged. Consequently it is safe to assume that the results from batch to batch can be compared directly without further modifications. The relative activities were converted into methanol production rates, and these are shown in Table 8.4. The production rate of 2.1gms of standard catalyst was 63.5 mol/kg catalyst.hr. This figure was found assuming that the exit gas stream at the rotary gas meter was at 20°C and that the flowrate was 80 litres/hr. In all cases, the weights quoted for the standard catalyst were un-reduced weights. Consequently, a comparison between the treated catalyst and the standard could not be made directly. The calculation to determine the relative activity (equation

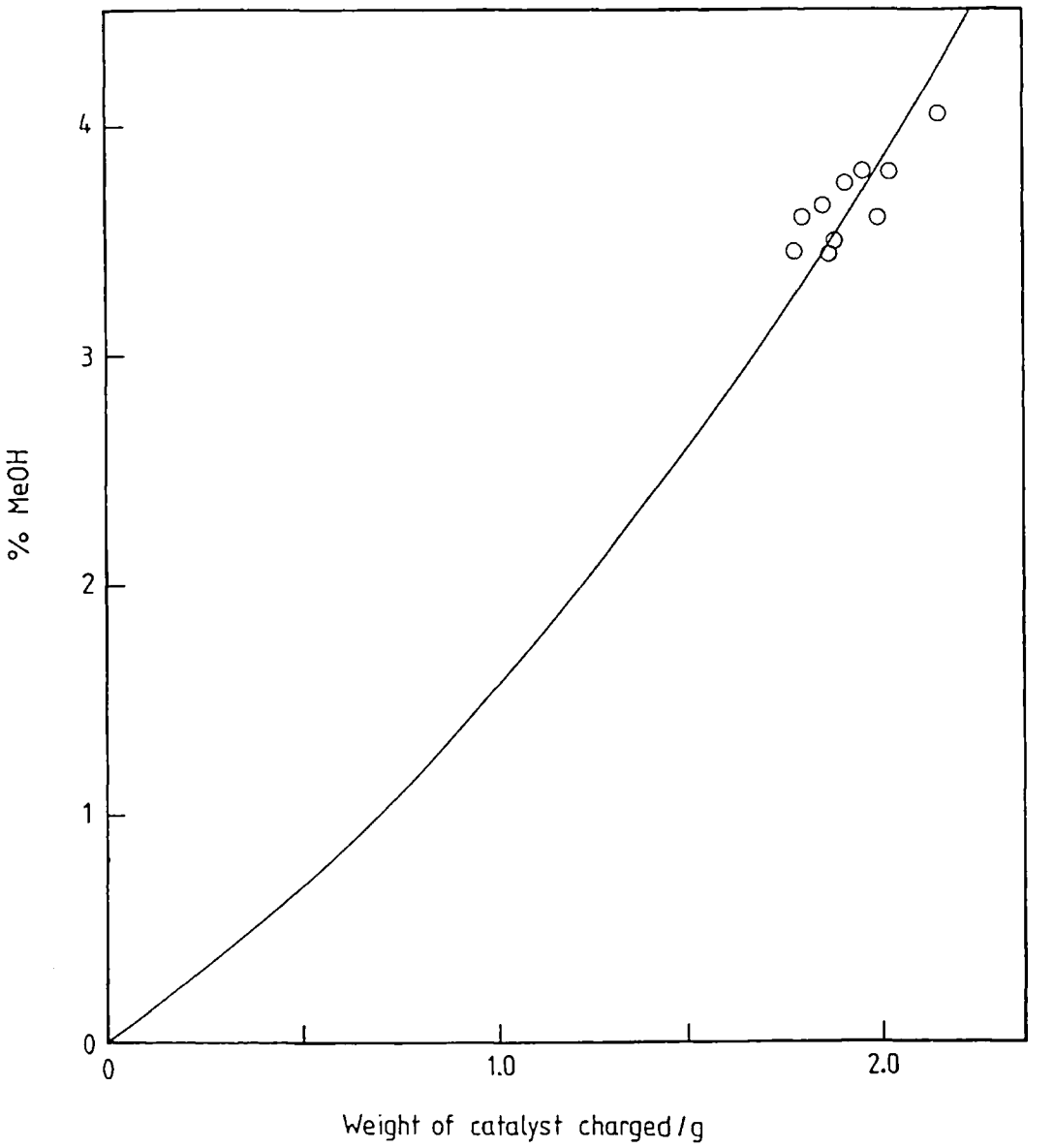


Figure 8.8. Percentage MeOH as a function of the weight of standard catalyst charged for all of the standards used in the activity tests

(8.2)) was also based on the weight of unreduced standard. The scale of relative activity is arbitrary.

8.3 Relationship between catalyst activity and surface area and brass formation

The general trends in activity changes following different catalyst treatments can be illustrated by plotting the initial relative activities against conditioning time for all of the samples, and this is shown in Figure 8.9. As expected, the activity decreases with conditioning temperature for a constant treatment time. As with previous curves involving conditioning times the three curves corresponding to the samples which were pre-reduced then conditioned decreased rapidly at first then levelled out at increasing conditioning times. Not too much information can be derived from these curves, but it is interesting to consider the four points representing the samples which were reduced directly at 350°C. The activity of these samples was 30% lower than those of the samples which were conditioned at 350°C for similar lengths of time but pre-reduced initially. It can be seen from Table 8.2 that the areas from N_2O adsorption of the samples which were pre-reduced and conditioned at 350°C were up to 2½ times greater than those for the directly reduced samples. Consequently, the observed reduction in activity was not equivalent to the reduction in the metal area. This result suggests that the copper phase is not the only active phase in the catalyst, which implies that the ZnO phase must also play a significant role in the methanol

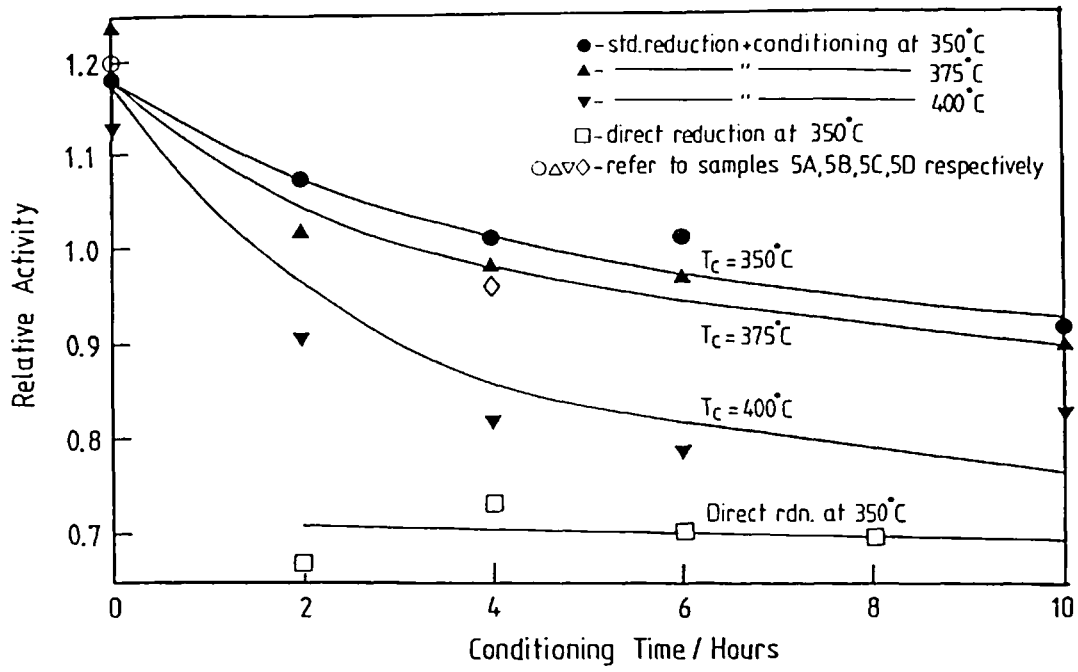


Figure 8.9. Activity as a function of conditioning time

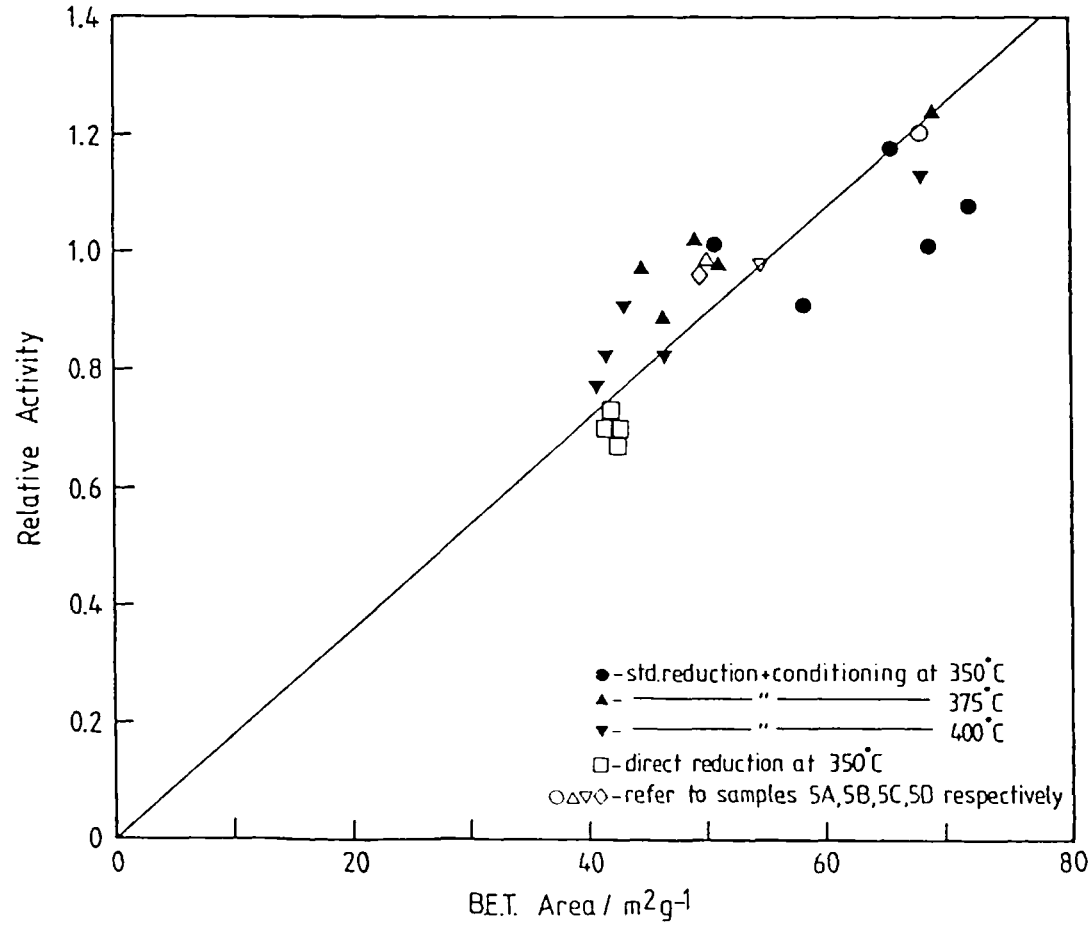


Figure 8.10. Activity as a function of B.E.T. area

synthesis reaction. Before this result is discussed more fully, it is necessary to consider the effect of surface area and brass formation on the activity.

8.3.1 Activity against total area

The initial relative activities were plotted against the B.E.T. area as shown in Figure 8.10, where it can be seen that an increase in activity occurs with increasing area. There is a reasonable linear trend to the points if a fit is made to run through the origin, and a least squares fit is shown in the Figure which includes all of the marked points. It can be seen that there is a large amount of scatter about the fit, and this again could be attributed to errors resulting from measuring the B.E.T. areas of the catalysts in an air stabilised form.

8.3.2 Activity against metal area

Consideration of a plot of activity against metal area, as shown in Figure 8.11.a. shows that the activity increases with increasing metal area, and that a linear relation would form a reasonable fit to most of the points. A least squares fit was made to all of the points using a relation of the form $a + bx$, where x is the metal area, and a and b are constants, and this is shown in Figure 8.11.a. The most important feature is that the line does not pass through the origin, but cuts the activity axis at 0.42. It has been found that catalysts made from supported copper or supported zinc oxide only do not show any

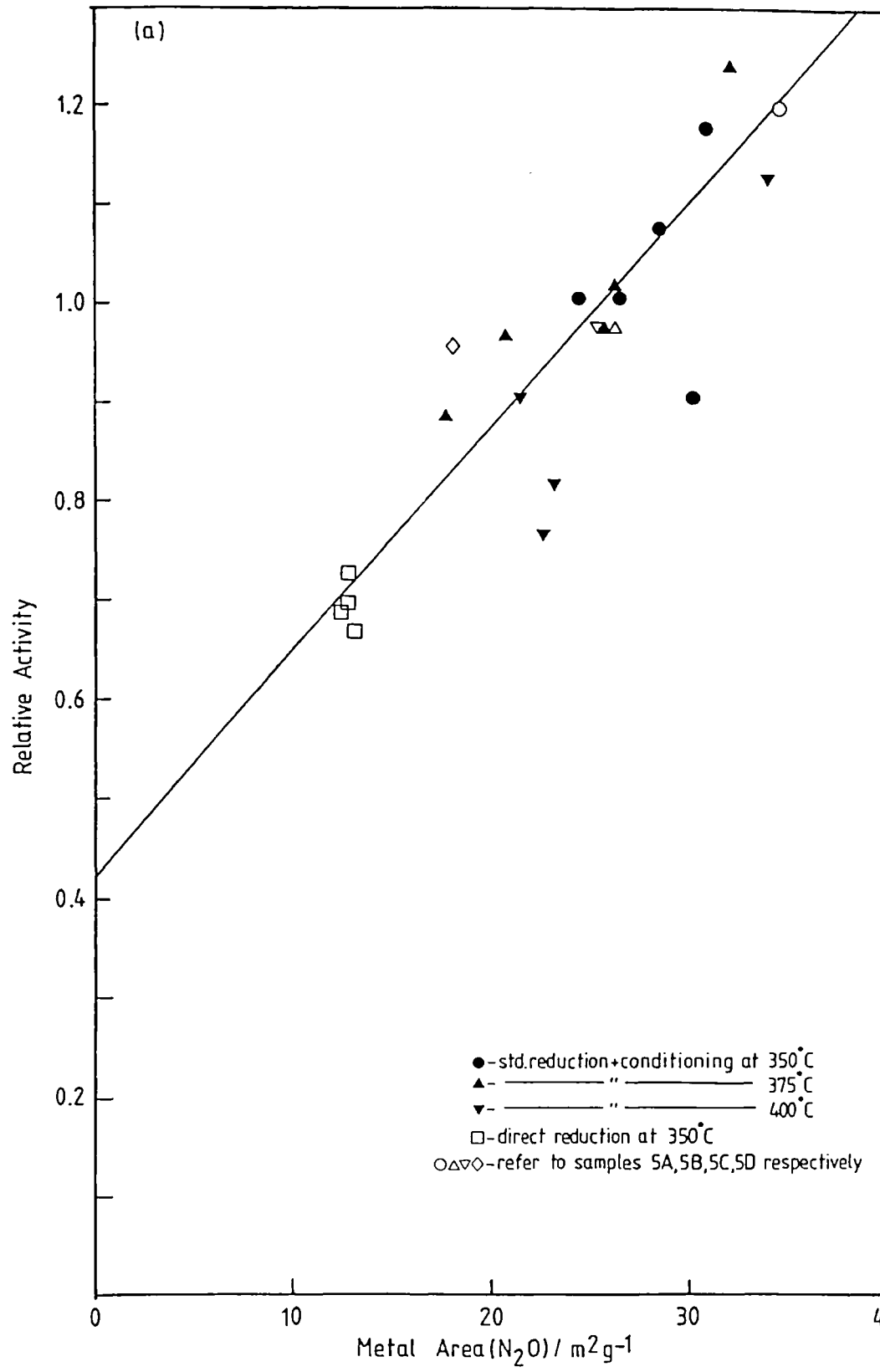


Figure 8.11.a. Activity as a function of metal area

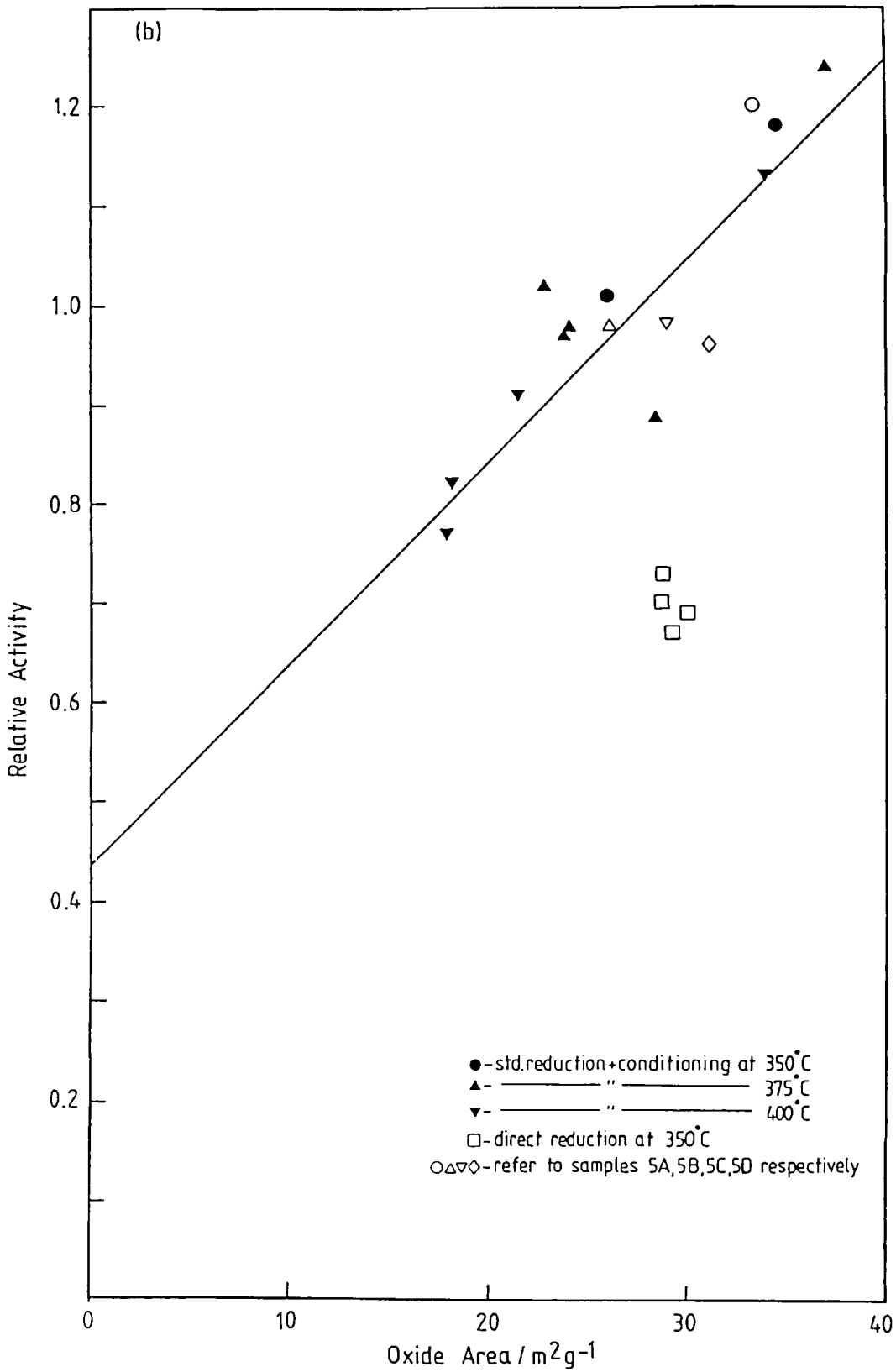


Figure 8.11.b. Activity as a function of oxide area

activity towards methanol synthesis at 250°C and 50 bar[80], so it would be expected that the relation between the activity and the metal area in Figure 8.11.a. should pass through the origin. The position of the intercept of the least squares fit cannot be explained by the standard deviation of the fit which is 0.05, and this suggests that a linear fit may not be correct. Consideration of the samples which were reduced directly at 350°C provides evidence that the activity may be related to the metal area by a power law with an exponent of between 0 and 1. The metal area of these samples decreased by a factor of 0.37 compared with the catalysts which were pre-reduced only, whereas the activity was only reduced by 0.56. The oxide area of these samples were only decreased by about 15%. This result indicates that the activity could be approximately dependent on the square root of the metal area. If this is the case, then the expected reduction of the activity would be 0.61 which is similar to the observed activity loss. In addition, consideration of the activities and metal areas in Tables 8.4 and 8.2 respectively for all of the remaining samples shows that the activity was not decreased by the same factor as the decrease in the metal area. In every case the metal area decrease was always greater. The possibility of the activity having a square root dependence on the metal area will be discussed further after the effect of the oxide area and brass formation on the activity have been considered.

Two points on the metal area plot appear to be well separated from the general trend. These two points represent

samples 3C and 3D. The separation could be due to random error, and their presence in the plot does not affect the result of the linear least squares fit cutting the activity axis at around 0.4.

An important source of uncertainty in the metal areas is concerned with what N_2O adsorption actually determined. The N_2O adsorption experiment is usually used to measure the copper surface area, but in the brassy catalysts, zinc will also be present. Zinc has a great affinity for oxygen and it is possible that the zinc could be capable of dissociating the N_2O for this reason. Consequently, any surface zinc which is present in the catalyst may adsorb the oxygen from the N_2O and so N_2O adsorption will give a value for the metal area rather than the copper surface area. The question as to whether zinc could dissociate N_2O has never been brought up in relation to $Cu/ZnO/Al_2O_3$ catalysis. It would be important to confirm whether zinc does in fact take up the oxygen during adsorption of N_2O on brass surfaces. As a result of this uncertainty, the area obtained from N_2O adsorption has been referred to as the metal area rather than the copper area. If the zinc atoms do adsorb oxygen from N_2O, the total metal area may be over-estimated. It has been shown that at saturation, one oxygen atom is adsorbed by two copper atoms[127], and this has been assumed in calculating the N_2O area. The stoichiometry for oxygen adsorption on zinc however is more likely to be one to one hence giving greater oxygen adsorption.

There is a possible reason why samples 3C and 3D are well separated from the general trend. It is interesting to note that these two points represent samples which were conditioned at 400°C for four hours and six hours respectively which are the most effective reduction conditions. These conditions, as well as forming a brass phase with 6.5% Zn, could also result in a significant amount of zinc metal being formed through oxide reduction but where some zinc remains out of solid solution with the copper. If the presence of zinc does modify the N_2O area measurement, then this would result in an activity which would seem low for the metal area associated with the catalyst.

8.3.3 Activity against oxide area

The dependence of the activity on the oxide area is shown in Figure 8.11.b. Again, it can be seen that the activity increases with increasing oxide area, and the general trend of the points gives the impression that the activity is dependent on the oxide area to a significant extent. However, the data in this plot is also affected by the deactivation through copper area loss, and this will affect the true dependence. This point is discussed further below.

As with the metal area plot, a linear relation was fitted using least squares to all of the points except for the four points representing the samples which were reduced directly at 350°C. These four points were omitted because the samples suffered significant deactivation as a result of the heavy sintering of

the copper phase and this is reflected in the oxide area plot, so the activity is low despite the high oxide area.

The least squares linear fit is illustrated in Figure 8.11.b. It can be seen that there is a significant amount of scatter about the linear fit, which could result from several sources. The oxide area includes the area of Al_2O_3 support which is inactive, so the quoted area is not truly representative of the ZnO area. The oxide area is also determined by taking the difference between the B.E.T. and N_2O areas which will introduce a significant error. It must also be remembered that the deactivation through the loss of metal area will also be reflected in the activities in the activity against oxide area plot, and this is a further cause of the scatter.

In general, the activities corresponding to the lower oxide areas will be affected by copper area loss to a greater extent than those with the higher oxide areas. In addition, the least squares fit does not pass through the origin, but cuts the activity axis at 0.44. These two points suggest that the true dependence of the activity on the oxide area will not be linear, but will take a form which approximates to a power law with an exponent between 0 and 1, and the curve representing this true dependence will lie above the linear fit illustrated in Figure 8.11.b. This dependence will be discussed after the effect of brass formation has been considered.

8.3.4 Effect of brass formation on the activity

The effect of increasing zinc content in the brass phase on the catalyst activity is illustrated in Figure 8.12. A general decrease in activity can be seen as the amount of zinc in the brass phase increases. The activity was decreased by about 33% on formation of 6% Zn in the brass phase. However, it must be remembered that the data forming this curve also included the deactivation through sintering of the copper and ZnO phases which in general became more significant with increasing brass formation. This is reflected particularly in the positions of the points representing the samples which were reduced directly at 350°C. Thus the important question as to whether the presence of the brass phase itself affected the activity of the catalyst cannot be established from a simple plot of activity against brass formation, as shown in Figure 8.12.

The activity per unit B.E.T. area was plotted against brass formation, and this is shown in Figure 8.13.a. It can be seen that the activity per unit B.E.T. area was essentially independent of brass formation. This is a very important result because it demonstrates that the formation of a brass phase did not drastically affect the catalyst activity for methanol synthesis. This is in stark contrast to the results of Van Herwijnen and de Jong[9], who found that the activity per unit B.E.T. area for the L.T. shift reaction was reduced by up to 50% following the formation of a brass phase with 6% Zn using a catalyst with 60% ZnO by weight. The general trend of the points in Figure

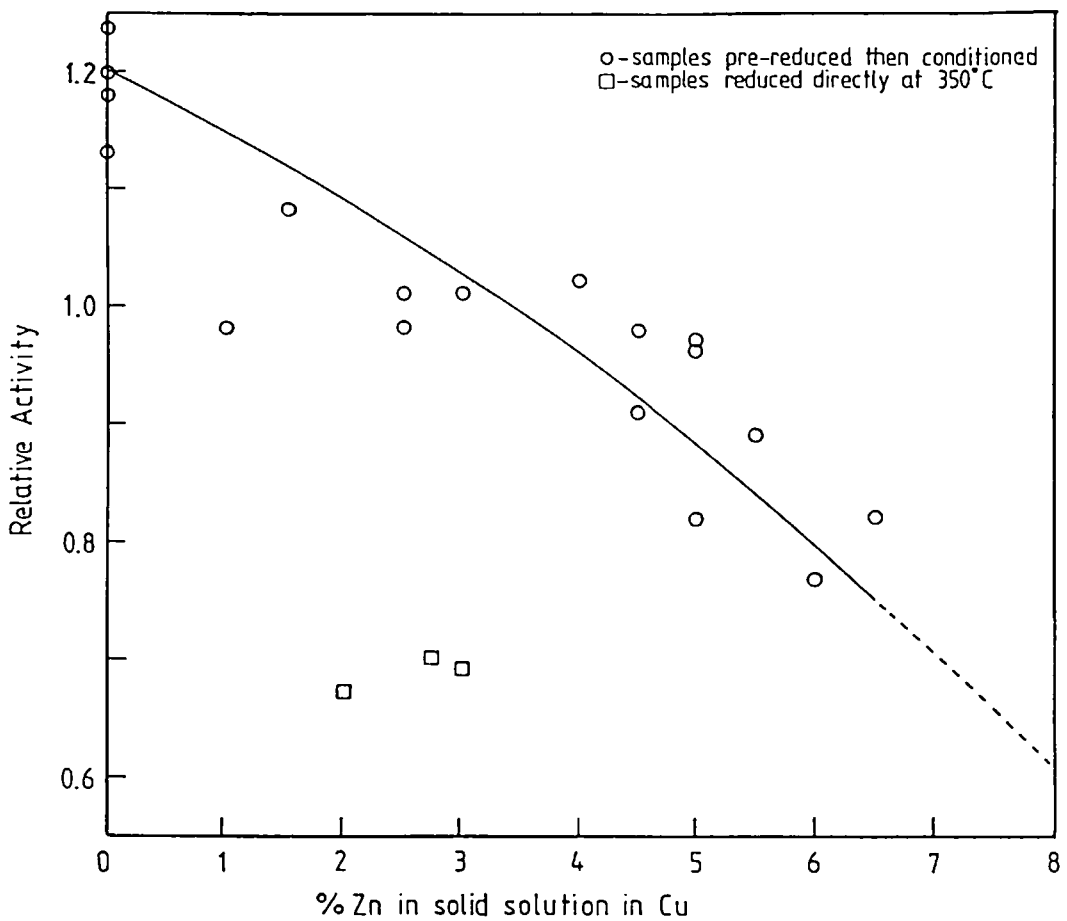


Figure 8.12. Activity as a function of brass formation

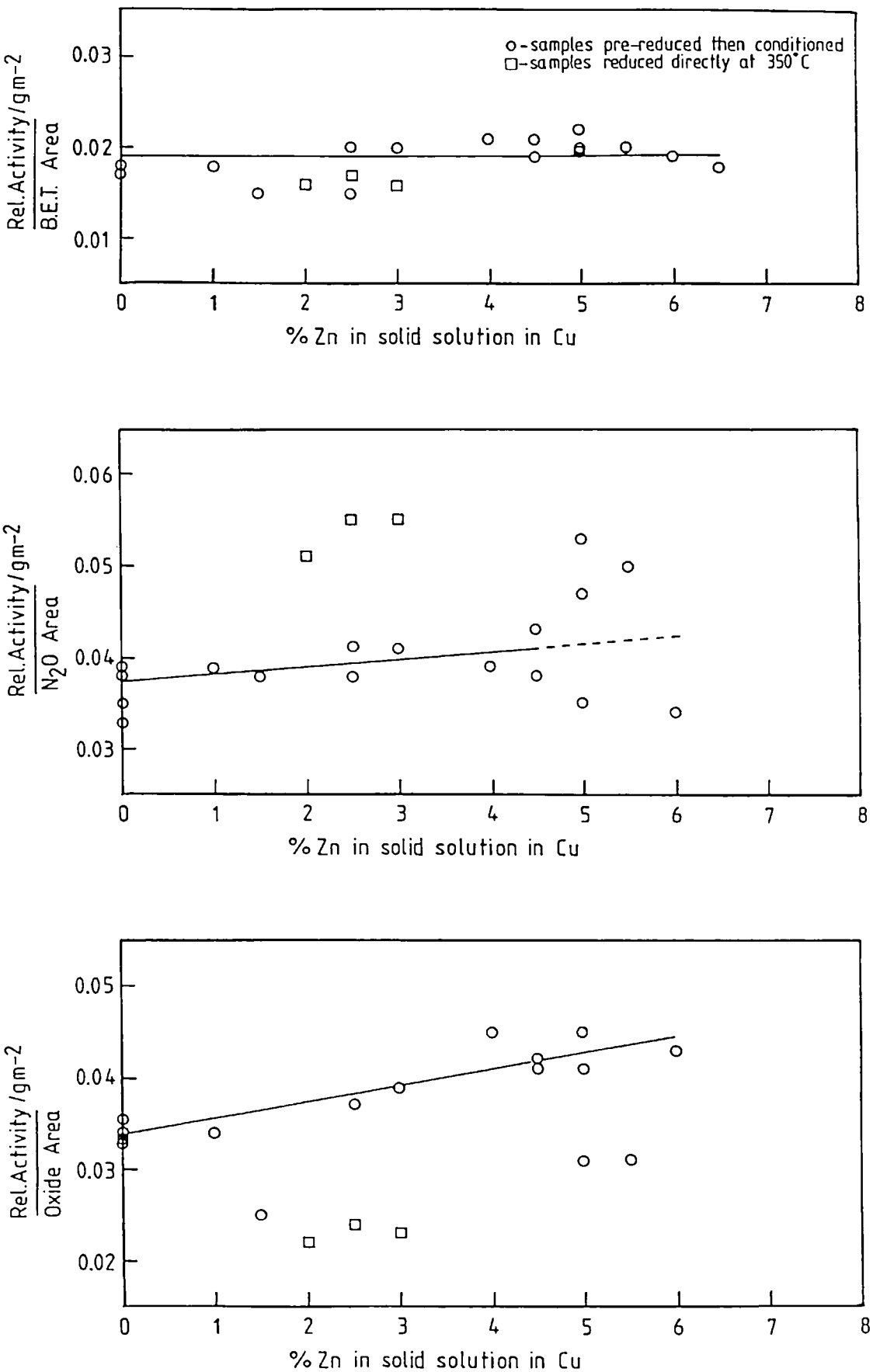


Figure 8.13. Activity per unit surface area as a function of brass formation

8.13.a indicate that there may even be a slight activation with brass formation. It is difficult to state this for certain because of the possible errors in the B.E.T. area measurements, described earlier. However, it is interesting to reconsider the plot of activity against B.E.T. area (Figure 8.10). It can be seen that the majority of the points on this plot lie above the line indicated representing the least squares fit. Furthermore, all of the points above the line represented the brassy catalysts.

The activity per unit N_2O area against brass formation is shown in Figure 8.13.b. This too showed that the activity was essentially independent of brass formation up to 4½% Zn. The points representing the samples which were reduced directly at 350°C lie above the main trend of points, and their positions give the impression that the deactivation in the samples which were reduced directly at 350°C was not linearly related to the metal area loss (see 8.3.2). Above 4½% Zn, the points on the plot are more erratically spread. It would seem that the uncertainty in what N_2O adsorption actually measures, along with the possibility that the metal areas for samples 3C and 3D were too high may be the cause of this spread.

The activity per unit oxide area was also plotted, as shown in Figure 8.13.c. , but it is difficult to establish anything conclusive from this plot because again, deactivation through copper sintering is also reflected in the plot. Nevertheless, no definite trend with brass formation can be seen.

It was mentioned earlier that some of the conditioned samples were loaded into the micro-reactors in an air-stabilised form and that some were loaded in an unstabilised form. This difference does not appear to have had any dramatic effect on the results for the activities.

8.3.5 Dependence of the activity on a function involving both the metal and oxide areas

It has been suggested that the activity may be dependent on the square root (approximately) of the metal area and that in addition, the activity may also be dependent on the oxide area. However, brass formation appears to leave the activity unaffected, so that the catalyst activity could be defined as :

$$\text{Rel. Act.} = K\,(\text{metal area})^{n_1}\,(\text{oxide area})^{n_2} \qquad (8.3)$$

where n_n, n_2 are exponents between 0 and 1,

K is a constant of proportionality.

In an attempt to clarify the suggestions made so far on the factors affecting the activity, a fresh catalyst was prepared with a molar composition of 50% Cu, 40% Zn and 10% Al as oxides so that the effect of the change in the amounts of Cu and ZnO on the activity could be assessed. The preparation method for this catalyst was similar to that used for the 60/30/10 $Cu/ZnO/Al_2O_3$ catalyst. Two samples were subjected to the usual pre-reduction procedure and then conditioned for four hours at

350°C in the usual reducing gas stream. The results for the brass formation, metal and B.E.T. areas and the activities are shown in Table 8.5.

TABLE 8.5 Characteristics and Activity of a 50/40/10 $Cu/ZnO/Al_2O_3$ catalyst

Sample	% Zn in Brass phase	BET area m^3/g	Area from N_2O		oxide area m^3/g	Relative Activity
			unreduced m^3/g	reduced m^3/g		
6A	4	53.5	15.2	16.7	38.8	0.74
6B	4	51.9	14.8	17.3	34.6	0.78
Std	-	-	-	-	-	1.00

Note: The activities can be compared directly with those in Table 8.4

The first result that comes from these samples is that the deactivation of this catalyst compared with the 60/30/10 catalyst samples which were pre-reduced only is not equivalent but less than the corresponding loss in metal area. The same result was found for all of the previous samples, as described earlier. This result gives further evidence to support the idea that the activity is related to the metal area by a power law with an exponent of between 0 and 1.

The power law dependence of the activity on the metal area was tested by adding curves to the plot of the activity against metal area which represented the activity being dependent on the metal area to the power n for different values of n. This addition is illustrated in Figure 8.14, where curves with n = 0.4, 0.5, 0.6 and 0.7 are shown. The curves are based on the de-activation of the pre-reduced 60/30/10 samples, where average values for the metal area ($33 m^2/g$) and the relative activity (1.19) for the pre-reduced samples were used. It can be seen that with the power, n, as 0.5 or 0.6, a reasonable fit to the experimental data is achieved, excluding the two points representing samples 3C and 3D which may be anomalous as described previously. A power of 0.5 to 0.6 for the metal area dependence agrees with the findings for the samples reduced directly at $350^{\circ}C$.

A least squares analysis was carried out on the results for the activities and the metal and oxide areas assuming that the activity was dependent on the metal area to the power 0.5. It was found that the activity was additionally dependent on the oxide area to the power of approximately 0.2. A plot was made of the relative activity against $(\text{metal area})^{0.5}$ $(\text{oxide area})^{0.2}$ to illustrate this dependence, and this is shown in Figure 8.15. The linear relation representing the expected activity from the $(\text{metal area})^{0.5}$ $(\text{oxide area})^{0.2}$ dependence is also shown. The two samples based on the 50/40/10 catalyst were also included in the plot. It can be seen that this relation is a reasonable

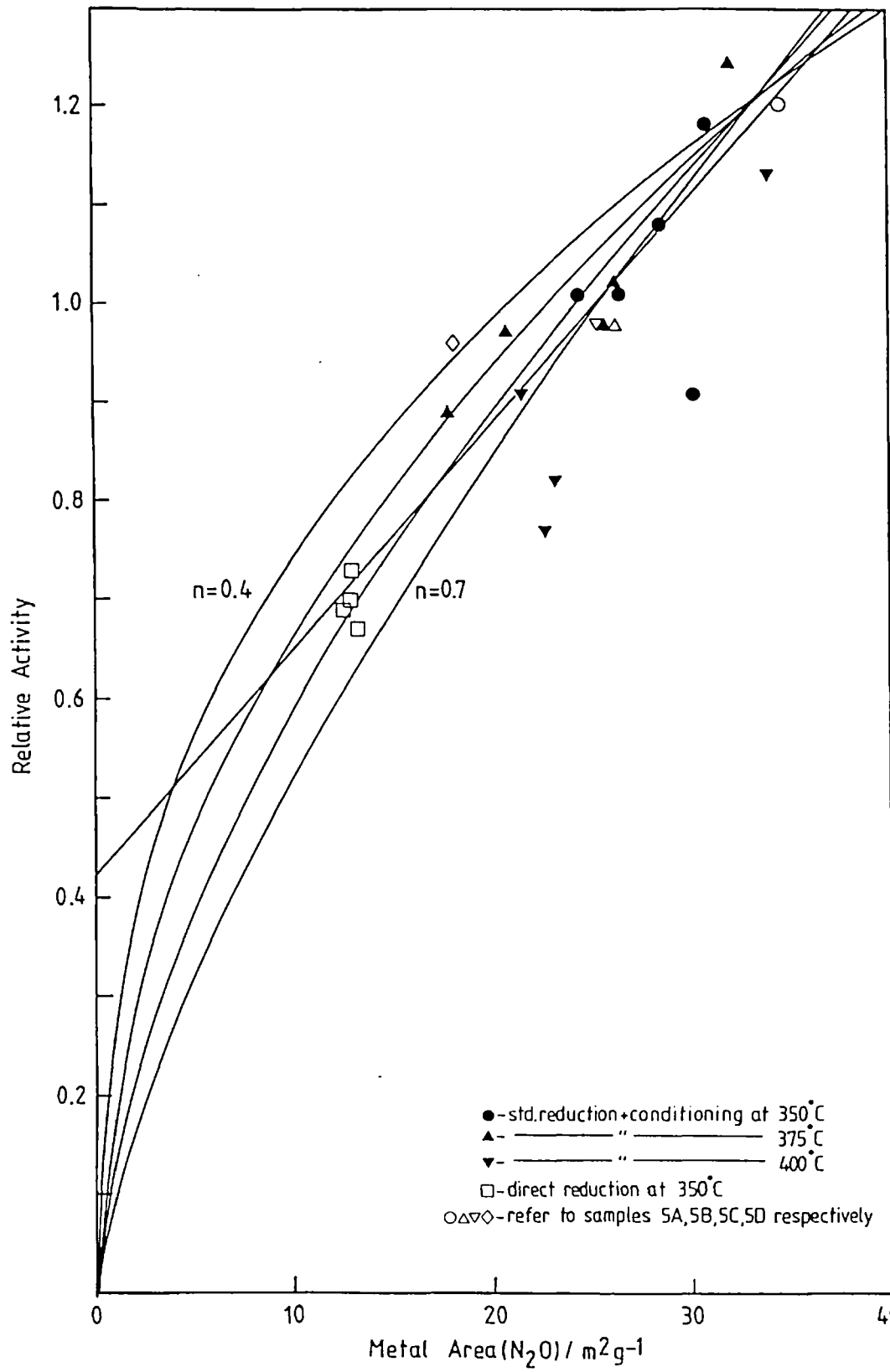


Figure 8.14. Activity as a function of (metal area)^n for values of n between 0.4 and 0.7

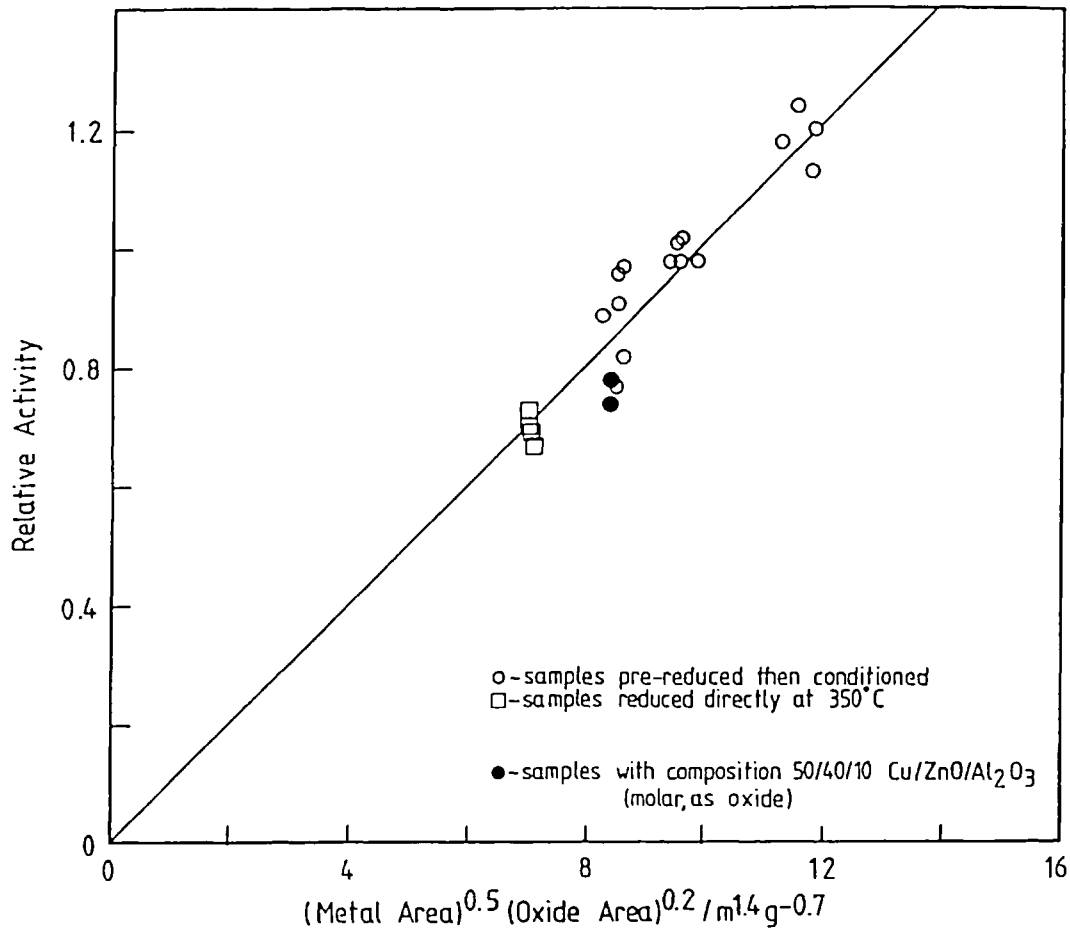


Figure 8.15. Activity as a function of (metal area)$^{0.5}$ (oxide area)$^{0.2}$

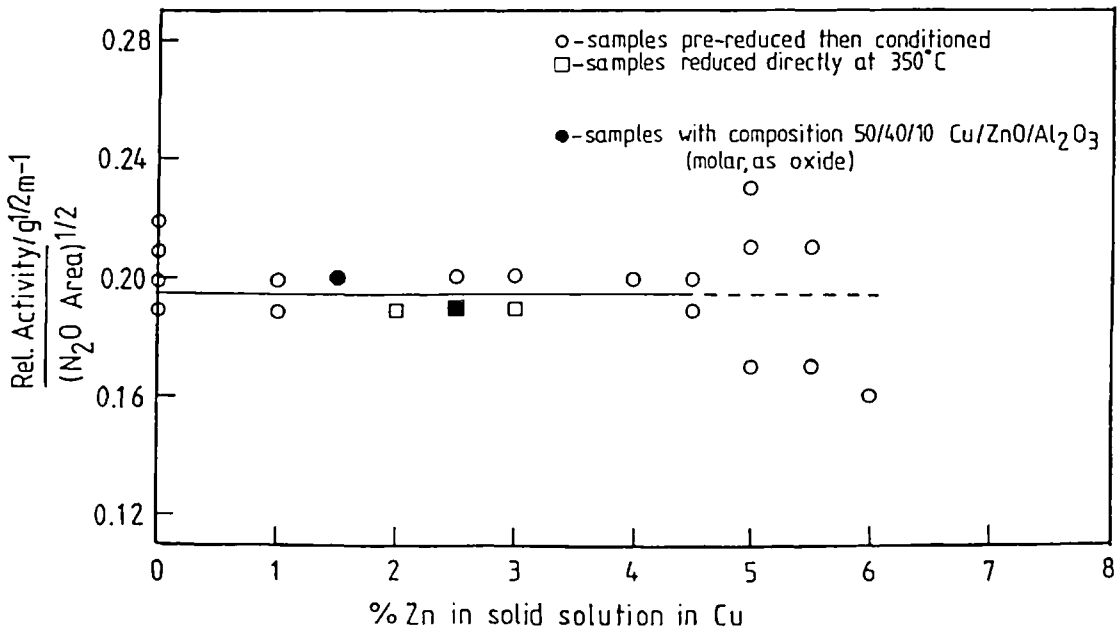


Figure 8.16. Activity per unit metal area to the power 0.5 as a function of brass formation

fit to the data, but there is some scatter which can be associated with the uncertainty involved in the measured surface areas. Both exponents in the relation above are only first approximations for similar reasons.

The results of this work clearly suggest that the ZnO area must also affect the activity of the catalyst. In general, there is an additional de-activation of the samples after the decrease in metal area to the power 0.5 has been included, and this additional deactivation is related to the extent of oxide reduction. This is reflected in the plot of the activity against (metal area)$^{\frac{1}{2}}$ (oxide area)$^{0.2}$. Although (oxide area)$^{0.2}$ appears to fit the data, it is very difficult to establish the relationship between the ZnO area itself and the activity. The oxide area is determined by taking the difference between the B.E.T. and N_2O areas and so it will include the inactive area associated with the Al_2O_3 support, and it may be that the activity has a stronger dependence on the ZnO area.

The activity per unit metal area to the power 0.5 was plotted against brass formation, as shown in Figure 8.16, so that a comparison could be made with the activity per unit metal area against brass formation plot (Figure 8.13.b.). It can be seen that the same result is obtained as before except that the points representing the samples which were reduced directly at 350°C are now part of the general trend instead of being isolated. This shows that the activity of these samples is also independent of brass formation.

8.4 Final Discussion and Summary

The principal result of this work, in summary, is that brass is formed in a 60/30/10 $Cu/ZnO/Al_2O_3$ catalyst, but does not appear to significantly affect the methanol synthesis reaction directly. However, brass formation does reduce the oxide area which should result in a small deactivation of the catalyst. The deactivation encountered in this work was principally as a result of the conditioning required to form the brassy catalysts giving a significant metal area loss.

The other major result to stem from this work is that the activity of the catalyst depends on both the ZnO area and also on the metal area. This is in contrast to the work of Klier et al[80-81] who concluded that the active phase was a Cu(I) solution in ZnO, and that copper metal was an inactive phase. The results for the samples which were directly reduced at 350°C are difficult to explain in the light of the conclusions of Klier et al. These samples were de-activated by the thermal treatment, but the ZnO phase was left almost unaffected. It would seem unlikely that the Cu(I) phase dissolved in the ZnO would sinter whilst the ZnO itself did not. It is more likely that these would sinter together. So, unless the thermal treatment affected the Cu(I)/ZnO phase in some other way, the de-activation cannot be associated with this phase. Klier et al also concluded that the ZnO phase may contain up to 16% of dissolved Cu(I). Assuming a simple model for the 60/30/10 $Cu/ZnO/Al_2O_3$ catalyst where all of the ZnO has 16% Cu(I)

dissolved in it and all the remaining copper takes the form of copper metal, then there will still be a large amount of copper metal present as only 8% of the original copper oxide will be dissolved in the ZnO phase.

It has been shown that one oxygen atom is adsorbed per two copper atoms at full coverage suggesting that Cu(I) is formed by N_2O adsorption[127]. Therefore it would seem unlikely that Cu(I) would dissociate N_2O and adsorb the oxygen. The activity showed a very significant dependence on the metal area by N_2O which implies that copper metal must be an active phase. This will be discussed further in Chapter 9.

CHAPTER 9

DISCUSSION OF RESULTS

The objective of this Chapter is to discuss the results of the previous chapters and to consider the role of brass formation in $Cu/ZnO/Al_2O_3$ catalysts on methanol synthesis and also on the low temperature shift reaction.

9.1 Segregation in brasses and its implication on the catalyst composition

In Chapter 5, it was established that for a wide range of bulk composition alloys, zinc segregated to the surface of the alloys, with the maximum surface zinc concentration occurring between 200°C and 250°C. In the experiments on the catalysts in Chapter 8, the amount of Zn in the brass phase was determined by XRD which gave the average percentage of Zn in the Cu phase of the catalyst, and represented only a bulk quantity. In light of the segregation results, it is certainly possible that the surface Zn content of the brass phase in the catalyst may be different from the bulk. The extent of surface zinc enrichment in the catalyst could be dependent on both the conditioning temperature and on the synthesis reaction temperature. For example, in the samples which were pre-reduced only, the XRD results suggested that a brass phase was formed with up to 1% Zn. If this is the case then because the final temperature of the pre-reduction cycle is 230°C, a significant amount of surface zinc may be present from consideration of the effect of annealing a 2% bulk Zn alloy at 225°C. On the other hand, the

segregation results imply that heavy evaporation should occur at 400°C, which was the highest conditioning temperature used in the experiments. If the segregation results are directly applicable to the catalyst at 400°C, then it would be expected that the surface of the brass phase would contain very little zinc. However, the synthesis reaction temperature of approximately 250°C could mean that the extent of zinc enrichment in the catalysts after conditioning is modified by effectively re-annealing the catalysts at the reaction temperature.

A direct application of the segregation results to predict surface zinc contents of the brass phase in the catalyst is difficult to justify in reality, because the segregation results were obtained in vacuo whilst the catalyst was conditioned at just above atmospheric pressure (1.25 atm) in 5% H_2 in N_2 (5% H_2/N_2), and this may have an effect on the segregation characteristics. There is evidence which tends to suggest that heavy evaporation did not occur whilst conditioning at high temperatures. Inspection of the reactors in which the conditioning was carried out showed that no noticeable discolouration through zinc deposition had occurred. In addition, consideration of the oxide area against conditioning time plot (Figure 8.3.c) shows that the area loss tails off at higher conditioning times. If evaporation was taking place then the last Zn in the brass phase would be constantly replenished by further reduction of the ZnO so that the thermodynamic equilibrium brass composition could be maintained. Consequently a continuous reduction in the oxide area with conditioning time would have been expected.

The exact extent of surface zinc enrichment in the brass phase of the catalyst is difficult to establish from the XRD and segregation results because the latter were found using a semi-infinite alloy whereas the copper phase of the catalyst which forms brass is a dispersion of crystallites which are typically 60-90Å in diameter. In the latter case, the small crystallite size may limit the extent of segregation. Clearly no firm statement can be made about the surface zinc content in the brass phase of the catalyst, but it probably lies between the value measured by XRD and that predicted by the segregation studies.

9.2 Dependence of the activity on metal area

The results of Chapter 8 clearly showed that the activity of the conditioned catalysts was dependent on the metal area. This is easily understood if the metallic phase is the active phase. However, the metal area loss was caused by sintering during the conditioning processes, and this suggests that the activity is related to the particle size. If the activity is directly proportional to the metal area then this would indicate a basic structure insensitivity. Any deviation from the linear dependence would suggest some structure dependence.

This discussion is based on the metallic phase being active, and the dependence on the metal area also needs to be discussed assuming that the active phase is Cu(I) dissolved in ZnO,

as proposed by Klier et al[80-82]. There are some possible reasons why a dependence of the activity on the metal area could be observed if Cu(I) was the active phase. The first of these is that the amount of Cu(I) is directly related to the metal area. If this is the case, then the experimentally observed relationship would hold. A second possibility is connected with whether the Cu(I) phase can be reduced in 5% H_2/N_2 at 350-400°C. If this were so, then providing the reduction was irreversible, the catalyst would suffer a loss in activity owing to the reduction in the number of Cu(I) sites. This effect would then result in an apparent relationship between the activity and the metal area since the metallic phase sinters whilst the number of Cu(I) sites is being reduced. A third possibility is that sintering of the ZnO phase reduces the number of Cu(I) sites, so that there is an apparent relationship between the activity and the metal area. However, there is not a strong dependence of the activity on oxide area as would be expected if ZnO sintering was a significant cause of loss of activity although the true dependence of activity on ZnO area cannot be established from this work as the support area is also included in the measured oxide area.

Consideration of the activity against metal area plot in Chapter 8 (Figure 8.11.a) shows that a straight line is a good fit to all of the points but that the best fit cuts the activity axis at approximately 0.4. A possible explanation of this is that there was a constant error in the activity measurements

or that the surface areas by N_2O were under estimated. However, the surface areas by N_2O would have to be increased by approximately $20m^2/g$ before the best fit passed through the origin, and this error seems to be excessive to be the cause of the observed offset of a linear activity against metal area dependence. As stated previously, the activity against metal area plot would be expected to pass through the origin because ZnO is essentially inactive towards methanol synthesis at 250°C and 50 bar. In Chapter 8, it was shown that a relation where the activity was dependent on the square root of the metal area was a reasonable fit to the points in Figure 8.11.a. and which passed through the origin. If this relationship is a true one, then it has some important implications if the metallic phase is the active phase, and these will now be discussed.

The square root of the metal area suggests that the activity could be dependent on the particle size with structure dependence or that the activity depends on a characteristic length. In the former case, it may be that changes in particle size leads to a change in the crystallographic structure and that this influences the activity. In the latter case, it may be that the physical separation of two adsorbed species where one is adsorbed on the metallic phase and the other on the ZnO phase is important if the migration of the two species across the surface to form an intermediate is a rate determining step.

Sintering of the metallic phase and indeed the ZnO phase would increase the separation between adsorption sites on separate phases. However, whether the square root relation would apply to $Cu/ZnO/Al_2O_3$ catalysts which are pre-reduced but not conditioned and which have had their metal area adjusted by varying the catalyst composition remains to be determined.

If the Cu(I) in ZnO phase is the active phase, then if the square root dependence is true then this would require the activity to be dependent on the square root of the number of Cu(I) sites. There is no obvious reason why this should be so which suggests that either the Cu(I) theory or the square root relation is not correct.

9.3 Effect of brass formation and conditioning on the activity

The results of Chapter 8 clearly show that brass formation in $Cu/ZnO/Al_2O_3$ catalysts has little effect on the catalyst activity for methanol synthesis. The possible reasons behind this will be discussed for the case where the metallic phase is active and where the Cu(I) in ZnO phase is active.

9.3.1 Metallic phase

The results in Chapter 6 show that for the surface zinc contents in the range of interest for the brass phase of the catalyst, the uptake of CO is only reduced by approximately 5%. This result suggests that brass formation does not affect the methanol synthesis reaction if the uptake of CO is the rate

determining step. The TPD spectra for CO on brass surfaces show that the adsorbed CO is taken up in more weakly bound states at the expense of the higher energy states. It may be that the reduction in CO uptake on the brass surfaces may be countered by an increase in the reaction rate, because the CO is more weakly bound and hence more reactive/mobile. However the adsorbed CO would have to be involved in the rate determining step and this is not necessarily the case. Hence, this explanation may not correctly account for the independence of activity on brass formation.

If both the metal and oxide areas are active then it may be that brass formation could also lead to a re-dispersion of ZnO in the following manner. If the presence of CO_2 in the synthesis reaction gas is capable of re-oxidising the surface zinc in the brass phase back to the oxide, then brass formation would lead to a good dispersion of the oxide on the metal phase which in itself may result in a locally improved activity. This effect may counter-balance the loss in metal area and may indeed be beneficial.

9.3.2. Cu(I) in ZnO

If Cu(I) in ZnO is the active site in methanol synthesis, then brass formation in the inactive copper phase would not be expected to have any effect on the methanol synthesis reaction, as is observed in this work.

Although the independence of the activity on brass formation itself can be explained where the Cu(I) sites are the active sites, the effects of the conditioning processes may discount the Cu(I) active site theory. During conditioning the catalyst is subjected to reducing conditions to reduce the ZnO. It would appear that the dissolved Cu(I) in ZnO can also be reduced to inactive metal, based on the observations of Klier et al[80,82]. However it is difficult to assess the extent of Cu(I) reduction following conditioning at 400°C in 5% H_2 in N_2 (5% H_2/N_2) for several hours. If most of the Cu(I) is irreversibly reduced then the catalyst should become inactive after conditioning. This is not observed in this work. It would seem important to study the variation in Cu(I) with conditioning and then establish how much Cu(I) remained in the ZnO phase compared with a catalyst that was pre-reduced only If the Cu(I) is absent after conditioning and after activity testing then this would disprove the Cu(I) active site theory.

9.4 Mechanistic Implications from the brassy catalysts for methanol synthesis and the L.T. Shift

Although it has been shown in this work that brass formation appears to leave the methanol synthesis reaction unaffected, the work of Van Herwijnen and De Jong[9] showed that brass formation in a 34% Cu, 64% Zn and 2% Fe (by weight as oxides) catalyst resulted in a significant deactivation of the L.T. shift reaction. To understand this difference it is necessary to consider some of the proposed mechanisms for methanol synthesis and the L.T. shift reaction.

It seems well accepted from the literature that a formate is formed as the intermediate in the L.T. shift reaction and Van Herwijnen et al[128,129] suggest that the decomposition of the formate is the rate determining step. Klier et al produced a mechanism where the formate was a common intermediate for both the methanol synthesis and L.T. shift reactions[130]. Decomposition of the formate to CO_2 and subsequently H_2 gave the forward shift reaction and hydrogenation of the formate formed methanol via a formyl intermediate. This mechanism is illustrated in Figure 9.1 for the case where Cu(I) is assumed to be the active site. It is possible that this mechanism could also apply to the metallic phase if this is the active phase. The work of Bowker, Madix, Wachs and Ying on the adsorption of methanol, formaldehyde and formic acid on Cu(110) shows that a formate can be detected on metal surfaces and this was described in Chapter 2.

Some Russian work on methanol synthesis using reactant gas compositions of 5%/16%/73% of CO_2,CO and H_2 respectively (+6% N_2) has produced evidence that the methanol synthesis reaction proceeds via a CO_2 intermediate[131, 132]. It was suggested that CO_2 was formed by the forward shift reaction by the interaction of CO and water vapour in the reaction gases. An experiment was performed where the reaction gas was purified to remove CO_2 and H_2O and it was found that this resulted in no methanol production, illustrating that methanol cannot be formed by the

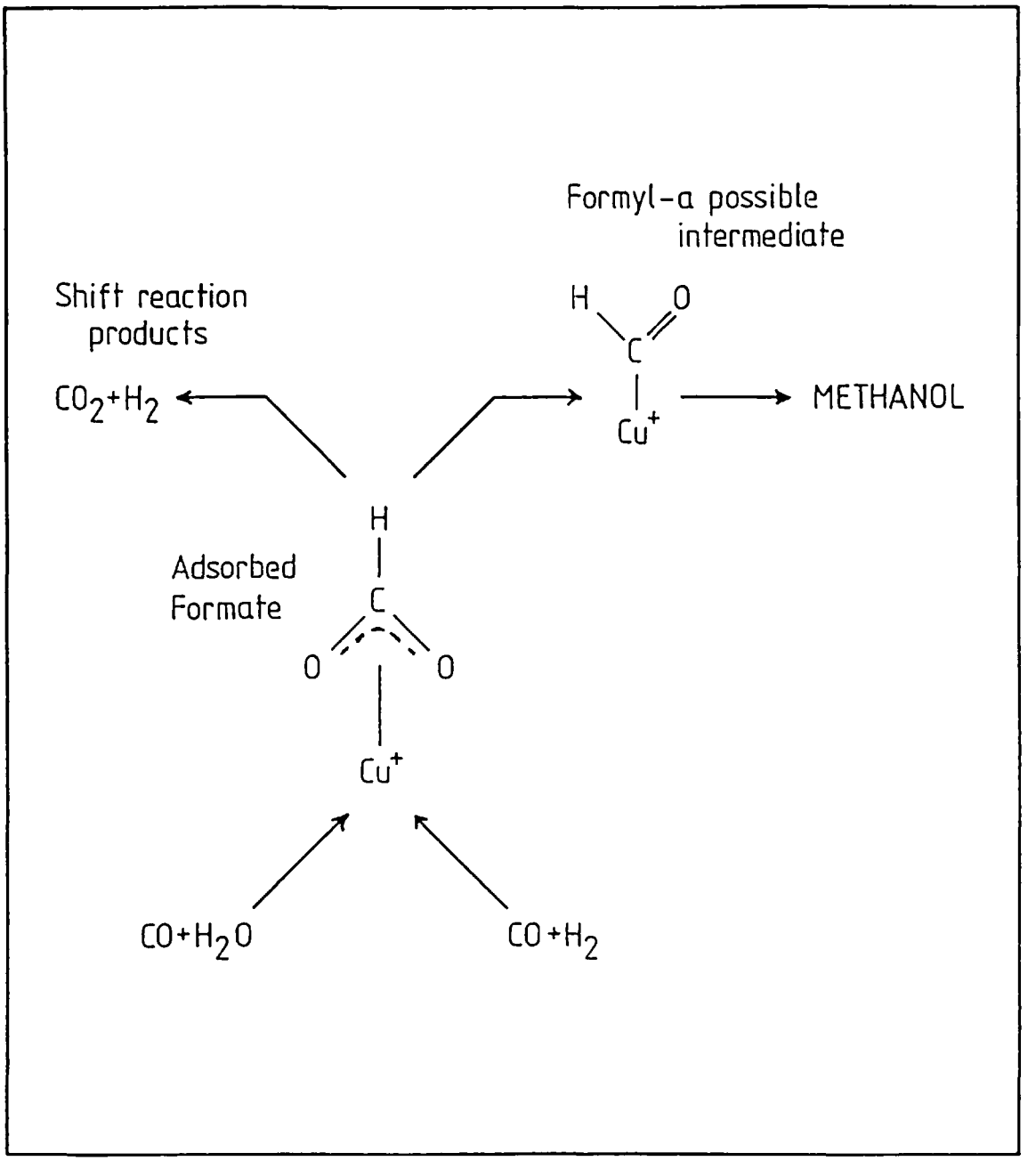


Figure 9.1. A possible reaction mechanism to form methanol or the L.T.Shift products via a common intermediate, as proposed by Klier et al [130], where Cu^+ is assumed to be the active site

direct hydrogenation of CO. Further work by Kagan et al[133] showed that methanol could be synthesised from CO_2 itself. This was also established by Klier[82]. However, the rate of formation of methanol from CO_2 only was much less than that from a CO/CO_2 mixture which was principally composed of CO. It may be that the formate is formed directly from CO_2. Assuming that the formate is a common intermediate for the methanol synthesis and the L.T. shift reactions, then the different effects of brass formation on the activity of the reactions suggests that either the formation of the formate or the decomposition/ hydrogenation of the formate is the rate determining step. The results of Van Herwijnen et al[128, 129], suggest that the step on from the formate is rate determining in the L.T. shift reaction. Whether hydrogenation of the formate is rate determining in methanol synthesis is unclear. The possible effect of brass formation on the hydrogenation and decomposition of the formate will therefore be considered. It has not been established conclusively yet whether the metallic phase or the Cu(I) in ZnO phase is active, so both of these will be discussed.

(i) Metallic Phase

If the metallic phase is active, then conditioning changes the copper phase to a brass phase giving zinc in some sites. The presence of this zinc would have to affect the decomposition of the formate to CO_2 whilst leaving the hydrogenation process unaffected. If this is not the case, then a loss in activity with brass formation would be expected in both the methanol

synthesis and the L.T. shift reactions, and the fact that the reactions are affected differently would suggest that the same intermediate could not be formed in both reactions.

On the assumption that the formate intermediate is common to both reactions, there is one possible explanation of why the L.T. shift reaction is de-activated by brass formation whilst methanol synthesis is not. It is possible that the formate adsorbed on a Cu-Zn site could be bound more strongly than on a pure copper site because of the interaction between the oxygen atoms in the formate and the zinc. It may even be that the formate is bound to the surface via the zinc instead of the copper. This should result in the formate being more difficult to decompose to CO_2 so reducing the rate of the L.T. shift reaction. This work has shown that the rate of methanol formation is preserved despite the formation of brass and consequently this explanation only holds if the formation of brass and the strengthening of the binding of the formate does not affect the hydrogenation of the intermediate. Whether the hydrogenation is affected or not is unclear. However, it would be of interest to investigate the adsorption of formic acid on brass surfaces by XPS, UPS and TPD to establish how the formate species is bound and whether it is bound more strongly on brass surfaces than on copper surfaces. This would show whether strengthening of the binding of the formate could be the source of the activity loss with brass formation for the L.T. Shift reaction.

(ii) Cu(I) in ZnO Phase

In the case where Cu(I) in ZnO is the active phase, brass formation should not directly affect either methanol synthesis or the L.T. shift reactions because the brass is formed in the inactive metallic phase. Consequently, there is no apparent reason why brass formation should affect one reaction but not the other. The only possibility is that the ZnO phase is affected in some way by the conditioning process. It has already been established that the conditioning results in oxide area loss and that it also partially reduces the ZnO, but there is no obvious reason why these should result in the L.T. shift reaction suffering a loss in activity whilst leaving methanol synthesis unaffected. Whatever effect conditioning had on the Cu(I) phase, it would be expected to affect both reactions.

9.4.1 Other mechanistic implications

The results of the Russian work[131-133] suggests that methanol synthesis proceeds via a CO_2 intermediate which is created by adsorbed CO being converted to CO_2 by the forward shift reaction. The results of this work and those of Van Herwijnen and De Jong[9] on the differing effects of brass formation on methanol synthesis and the L.T. shift reactions suggest that methanol synthesis does not proceed via a forward shift reaction because if it did then a significant de-activation with brass formation would be expected for the methanol synthesis reaction if the L.T. shift is the rate determining step. However, Russian work[133] strongly suggests

that CO is not directly hydrogenated and so the CO_2 intermediate must be formed in some other way. Another possibility is that the adsorbed CO is in fact converted to CO_2 by removal of a surface oxygen from the ZnO lattice. If this is the case then it may be that the CO_2/CO and the H_2O/H_2 ratios control the extent of ZnO defection. If these ratios both tend to zero then the number of defects in the ZnO will increase, leaving fewer lattice oxygens to take part in the reaction mechanism and therefore resulting in a loss in activity. If the CO_2/CO and H_2O/H_2 ratios were both zero, corresponding to the experiment described earlier where the reaction gas was purified so that no CO_2 or H_2O was present then this could produce a completely defected ZnO phase, leaving no lattice oxygens. If oxidation of CO to CO_2 by the ZnO lattice oxygens is a fundamental step in the methanol synthesis reaction, then a fully defected ZnO phase should leave the catalyst completely inactive. This has been observed experimentally.

9.5 Dissociation of CO by brass surfaces and its implications in methanol synthesis

In Chapter 6, evidence was produced which suggested that CO dissociation was possible on brass surfaces. As a result of CO being split into carbon and chemisorbed oxygen, it would be expected that the methanol synthesis reaction on brassy catalysts should produce a significant amount of impurities in the product stream. The presence of the carbon and oxygen would lead to methane production by hydrogenation of the carbon and also the production of higher alcohols may be possible. Unfortunately,

the product streams from the micro-reactors used in the activity tests (Chapter 8) were not analysed fully so further experiments will need to be carried out on the brassy catalysts to examine whether by-products are produced to any significant extent upon creating the brass phase.

Although the brassy catalysts form up to 6.5% Zn in the brass phase, the standard catalyst has been shown to contain between 0-1% Zn in the brass phase by XRD. If it is assumed that the surface zinc content is similar to the XRD bulk value then CO dissociation would only occur in trace proportions, which is consistent with observed selectivities. Even if the surface zinc content is higher than the XRD bulk value, the selectivity should be preserved because the results of Chapter 6 showed that no noticeable CO dissociation occurred on a 2% bulk Zn alloy.

9.6 Final Summary and Conclusions

The principal conclusions of this work are summarised below.

9.6.1 Segregation in Brasses

(i) It was found that segregation of zinc to the surface of brass foils did occur giving a significant amount of zinc enrichment in the surface layer. This result was reproduced for four different bulk composition alloys ranging from 2% Zn to 30% Zn.

(ii) The surface zinc content as a function of temperature for a constant annealing period passed through a maximum at temperatures between 200-250°C. Above the maximum, zinc evaporation started to become significant. Consequently the surface composition was determined by a balance between segregation of zinc from the bulk and evaporation of segregant from the surface.

(iii) A calculation to establish the surface composition of each alloy at different annealing temperatures showed that up to 30% Zn was present in the surface layer of the 2% bulk Zn alloy whilst up to 60% Zn was present in that of the 30% bulk Zn alloy.

(iv) Analysis of the experimental results suggested that whilst zinc enrichment of the surface occurred, annealing created zinc depletion immediately below the surface in all four alloys. The results suggested that the layer below the surface was the most heavily depleted layer with up to 100% Cu being present.

9.6.2 Adsorption of CO on polycrystalline Cu, Zn, and Cu/Zn surfaces

(i) Adsorption of CO on polyx Cu surfaces was found to occur with an initial sticking probability of approximately unity. This is in agreement with

previous results.

(ii) At least two adsorption states could be observed on the Cu surface, the major state being sites based on (111) surfaces. The second state was of higher energy and was possibly as a result of the presence of (100) faces. At higher coverages, a third adsorption state appeared with an energy of 37 kJ/mol^{-1} which was interpreted as the compression state.

(iii) No evidence was found to suggest that CO was chemisorbed on Zn surfaces.

(iv) The presence of zinc in a copper substrate did not affect the rate of CO uptake (the sticking probability) since the uptake curve for the Cu/Zn surfaces as a function of CO dose was similar to that of the Cu surface.

(v) The presence of zinc in a copper substrate did not have a significant effect on the uptake of CO at low surface zinc concentrations (i.e. less than 10% Zn). It was only at higher surface zinc concentrations that the amount of CO taken up began to be affected more dramatically. The uptake was reduced to negligible amounts with approximately 60% Zn in the surface layer.

(vi) The TPD spectra of CO from polycrystalline copper and brass surfaces showed that the presence of surface zinc created at least one additional adsorption site for CO compared with a pure copper surface. The Cu/Zn adsorption sites are of lower energy than sites composed of pure copper.

(vii) An interesting result to stem from the CO adsorption study was that a brass surface appears to be capable of dissociating CO. This process does not occur whilst exposing brass surfaces at 90K to CO, but appears after a desorption cycle. This shows that raising the sample temperature causes the dissociation and it is therefore an activated process occurring between 90K and 220K. The dissociation appears to be a property of Cu/Zn surfaces since the extent of CO dissociation depends on the amount of zinc which is present in the surface.

9.6.3 Conditioning of $Cu/ZnO/Al_2O_3$ catalysts to form brass

(i) Conditioning of $Cu/ZnO/Al_2O_3$ catalysts in a stream of 5% H_2 in N_2 between 350°C and 400°C created up to 6.5% Zn in solid solution in the copper. The brass was formed principally in the first 4 hours of conditioning. After this the amount of Zn in solid solution in Cu remained constant. The conditioning also led to sintering and therefore a reduction in the metal area. There was also a reductio

in the oxide area following conditioning, but this appeared to be dependent on the extent of brass formation rather than through sintering.

(ii) The segregation results do not necessarily predict the surface composition of the brassy phase in the conditioned $Cu/ZnO/Al_2O_3$ catalysts. The actual composition probably lies between the value from XRD and that predicted by the segregation results.

(iii) The activity of the conditioned catalysts was found to be approximately dependent on the square root of the metal area. This result suggests that the catalyst activity could be surface sensitive. Alternatively, the square root of metal area suggests that the activity is dependent on a characteristic length and so the activity may be related to the particle size.

(iv) The formation of low zinc content bulk brass of less than 10% Zn in $Cu/ZnO/Al_2O_3$ catalysts does not appear to have a net effect on the rate of methanol synthesis.

(v) The result that the uptake of CO is essentially unaffected by the presence of Zn in a copper surface does not necessarily explain the apparent independence of methanol synthesis rate on brass formation since the L.T. Shift reaction involves

CO adsorption and this is de-activated by brass formation.

(vi) The independence of the rate of methanol synthesis on brass formation suggests that a formate intermediate may not be common to both the methanol synthesis and L.T. Shift reaction mechanisms.

(vii) The apparent independence of the rate of methanol synthesis on brass formation and the de-activation of the L.T. Shift reaction from brass formation suggests that the L.T. Shift is not an intermediate stage in the methanol synthesis reaction mechanism. However, L.T. Shift will occur as a side reaction.

(viii) It would seem unlikely that Cu^+ sites form part of the active phase of $Cu/ZnO/Al_2O_3$ catalysts, but there is no conclusive proof of this. If Cu^+ was active then some activity loss would be expected following irreversible reduction of the Cu^+ to copper metal by the relatively severe reduction conditions used to create the brassy catalysts. It is also difficult to explain to square root dependence of the activity on metal area in terms of a Cu^+ theory.

ADDENDUM

Since this work was completed, two interesting results have been established.

(i)

It has been found that the B.E.T. area of the $Cu/ZnO/Al_2O_3$ catalysts is not significantly affected by making the area measurement with the catalysts in an air stabilised form compared with those made with catalysts in a reduced state.

(ii)

Work by Higgs[135] has shown that the area by N_2O adsorption for $Cu/ZnO/Al_2O_3$ catalysts with a similar composition to those used in this work shows a linear dependence with activity. The catalysts of Higgs were pre-reduced only, with no conditioning to create a brassy phase being carried out. The activity of the pre-reduced catalysts of Higgs compared very favourably with those of the catalysts which were pre-reduced only in this work, giving confidence in the activity results obtained in this work.

REFERENCES

1. A. L. Waddams in 'Chemicals from Petroleum', 4th Edition John Murray, 1978.

2. H. H. Kung, Catal. Rev. Sci. Eng., 22(2), 235 (1980).

3. C. D. Chang and A. J. Silvestri, J. Catal., 47, 249 (1977).

4. Chemical and Engineering News, 31 Jan. 1977, p.11.

5. P. J. Denny and D. A. Whan, in 'Catalysis' (Specialist Periodical Report), The Chemical Society, 1978, vol. 2, p.46.

6. V. Ponec, Catal. Rev. Sci. Eng., 18(1), 151 (1978)

7. D. R. Stull, E. F. Westrum Jnr. and G. C. Sinke in 'The Chemical Thermodynamics of Organic Compounds', Wiley, New York, 1969.

8. G. Natta in 'Catalysis', Reinhold, New York, 1955, vol. 3,p.349

9. T. Van Herwijnen and W. A. De Jong, J. Catal., 34, 209 (1974).

10. R. J. Madix, Surf. Sci., 89, 540 (1979).

11. W. M. H. Sachtler and G. J. H. Dorgelo, J. Catal., 4 654 (1965).

12. W. M. H. Sachtler and R. Jongepier, J. Catal., 4,665 (1965).

13. W. M. H. Sachtler and R. A. Van Santen, Adv. Catal., 26, 69 (1977).

14. L. S. Shield and W. W. Russell, J. Phys. Chem., 64, 1592 (1960)

15. J. G. Stark and H. G. Wallace in 'Chemistry Data Book', 2nd Ed., John Murray, 1982, p.50.

16. V. Ponec, Catal. Rev. Sci. Eng., 11, 41 (1975).

17. see (13) and (16).

18. K. Y. Yu, D. T. Ling and W. E. Spicer, J. Catal., 44, 373 (1976).

19. D. T. Quinto, V. S. Sundaram and W. D. Robertson, Surf. Sci., 28, 504 (1971).

20. H.J. Mathieu and D. Landolt, Surf. Sci., 53, 228 (1975).

21. C. R. Helms, J. Catal., 36, 114 (1975).

22. C. R. Helms and K. Y. Yu, J. Vac Sci. Tech., 12 (1), 276 (1975).

23. R. Bouwman, L. H. Toneman and A. A. Holscher, Surf. Sci., 35, 8 (1973).

24. G. Maire, L. Hilaire, P. Legare, F. G. Gault and A. O'Cinneide, J. Catal. 44, 293 (1976).

25. C. T. H. Stoddart, R. L. Moss and D. Pope, Surf. Sci., 53, 241 (1975).

26. M. P. Seah, J. Phys. F., 3, 1538 (1973).

27. G. A. Somorjai and S. H. Overbury, Faraday Disc. Chem. Soc., 60, 279 (1975).

28. R. Bouwman and P. Biloen, Surf. Sci., 41, 348 (1974).

29. P. Webber, C. E. Rojas, P. J. Dobson and D. Chadwick, Surf. Sci., 105, 20 (1981).

30. D. A. King, Surf. Sci., 47, 384 (1975).

31. J. C. Tracy, J. Chem. Phys . 56, 1248 (1972).

32. Sadoon A. Isa, R. W. Joyner and M. W. Roberts, J. C. S. Faraday I, 74, 546 (1978).

33. K. Horn, M. Hussain and J. Pritchard, Surf. Sci., 63, 244 (1977).

34. Sadoon A. Isa, R. W. Joyner and M. W. Roberts, J. C.S. Chem. Comm., 11, 377 (1977).

35. M. A. Chesters and J. Pritchard, Surf. Sci., 28, 460 (1971).

36. E.F.W. Thurston, Trans. Faraday Soc. 64, 2181 (1968).

37. P. R. Norton, R. L. Tapping and J. W. Goodale, Surf. Sci., 72, 33 (1978).

38. J. Pritchard, J. Vac. Sci. Tech., 9 (2), 895 (1972).

39. P. R. Norton and R. L. Tapping , Chem. Phys. Lett., 38(2) 207(1976).

40. See for example, T. A. Carlson, in 'Photo-electron and Auger Spectroscopy', Plenum Press, New York, 1975, p.241, and references therein.

41. H. Conrad, G. Ertl, J. Kuppers and E. E. Latta, Solid State Comm., 17, 613 (1975).

42. C. L. Allyn, T. Gustafsson and E. W. Plummer, Solid State Comm., 24, 531 (1975).

43. J. E. Demuth and D. E. Eastman, Solid State Comm., 18, 1497(1976).

44. Y. Jugnet and Tran Minh Duc, Chem. Phys. Lett., 58, 2, 243 (1978).

45. J. Kanski, L.Ilver and P. O. Nilsson, Solid State Comm., 26, 339 (1978).

46. J. C. Fuggle, E. Umbach, D. Menzel, K. Wandelt, C. R. Brundle, Solid State Comm., 27, 65 (1978).

47. R. P. Messmer, S. H.Lamson and D. R. Salahub, Solid State Comm., 36, 265 (1980).

48. O. Gunnarsson and K. Schonhammer, Phys. Rev. Lett , 41, 1608 (1978).

49. R. P. Messmer, S. H. Lamson and D. R. Salahub, Phys, Rev. B., 25(6), 3576 (1982).

50. J. Kessler and F. Thieme, Surf. Sci., 67, 405 (1977).

51. S. Andersson, Solid State Comm., 21, 75 (1977).

52. A. B. Anderson, Surf. Sci., 62, 119 (1977).

53. P. Hollins and J. Pritchard, Surf. Sci. 89, 486 (1979).

54. M. Bowker - unpublished results.

55. R. J. Madix, Adv. Catal., 29, 1 (1980).

56. I. E. Wachs and R. J. Madix, J. Catal., 53, 208 (1978).

57. I. E. Wachs and R. J. Madix, Surf. Sci., 84, 375 (1979).

58. J. C. Vickermann, K. Christmann and G. Ertl., J. Catal., 71, 175 (1981).

59. R. W. Joyner, C. S. McKee and M. W. Roberts, Surf. Sci., 26, 303 (1971).

60. A. F. H. Ward, Proc. Roy. Soc. A., 133, 506 (1931).

61. D. O. Hayward and B. M. W. Trapnell in 'Chemisorption', Butterworths, London, 1964.

62. T. Kwan, J. Res. Inst. Catalysis (Hokkaido), 1, 96 (1949).

63. O. Beeck. A. E. Smith and A. Wheeler, Proc. Roy. Soc. A., 177, 62, (1940).

64. B. M. W. Trapnell, Proc. Roy. Soc. A., 218, 566 (1953).

65. G. L. Kington and J. M. Holmes, Trans. Faraday Soc., 49, 417 (1953).

66. J. Pritchard and F. C. Tompkins, Trans. Faraday Soc., 56, 540 (1960).

67. C. S. Alexander and J. Pritchard, J. Chem. Soc., Faraday Trans. I., 68 , 202 (1972).

68. J. Pritchard, Nature 205, 1208 (1965).

69. Isao Kojima, Makoto Kiyomiya and Iwas Yasumori, Bull. Chem. Soc. Jpn., 53, 2123 (1980).

70. M. Bowker - unpublished work.

71. M. Bowker and R. J. Madix, Surf. Sci., 95, 190 (1980).

72. R. J. Madix, CRC. Crit. Rev. Solid State Mat. Sci., 7 (2) 143 (1978).

73. P. Hoffman, C. Mariani, K. Horn and A. M. Bradshaw, Proc. 4th Int. Conf. Solid State Surf. (Ed. D . A. Degras and M. Costa), Cannes. 1980. vol. I, p.541.

74. D. H. S. Ying and R. J. Madix, J. Catal. 61, 48 (1980).

75. M. Bowker and R. J. Madix, Surf. Sci., 102 542 (1981).

76. M. Smutek, S. Cerny and F. Buzek, Adv. Catal. 24, 343 (1975).

77. T. S. Nagarjunan, M. V. C. Sastri and J. C. Kuriacose, J. Catal., 2, 223 (1963).

78. M. Bowker, H. Houghton and K. C. Waugh, J. C. S. Faraday Trans. I., 77, 3023 (1981).

79. A. Baranski and J. Galuszka, J. Catal, 44, 259 (1970).

80. R. G. Herman, K. Klier, G. W. Simmons, B. P. Finn, J. B. Bulko and T. P. Kobylinski, J. Catal 56,407 (1979).

81. S. Mehta, G. W. Simmons, K. Klier and R. G. Herman, J. Catal., 57,339 (1979).

82. K. Klier, V. Chatikavanij , R. G. Herman and G. W. Simmons, J. Catal., 74,343 (1982)

83. R. W. Joyner, Surf. Sci., 63,291 (1977).

84. M. W. Roberts, Adv. Catal., 29,55 (1981).

85. W. N. Delgass, T. R. Hughes and C. S. Fadley, Catal. Rev. Sci. Eng., 4,179(1971).

86. See for example - K. Siegbahn, C. Nordling, A. Fahlman, R. Nordberg, K. Hamrin, J. Hedman, G. Johansson, T. Bergmark, S. E. Karlsson, I. Lindgren and B. Lindberg, 'ECSA - Atomic, Molecular and Solid State Structure studied by means of Electron Spectroscopy' Nov. Act. Reg. Sci. Upsaliensis(IV), 20, Almqvist and Wiksells, Uppsala (1967).

87. S. Evans in 'Handbook of X-Ray and U.V. Photo-electron Spectroscopy', (Ed. D. Briggs), Heyden, 1977, p.121.

88. M. Johansson, J. Hedman, A. Bendtsson, M. Klasson and R. Nillson, J. Electr. Spect., 2, 295 (1973).

89. R. J. Bird and P. Swift, J. Elect. Spectr., 21,227 (1980).

90. A. F. Orchard in 'Handbook of X-Ray and U.V. Photo-electron Spectroscopy', (Ed. D. Briggs), Heyden, 1977, p.1.

91. M. P. Seah and W. A. Dench, Surf. and Interface Anal., 1(1),2(1979).

92. D. R. Penn, J. Electr. Spectr., 9,29 (1976).

93. D. Briggs in 'Handbook of X-Ray and U.V. Photo-electron Spectroscopy (Ed. D. Briggs), Heyden, 1977, p.153.

94. C. J. Powell and P. E. Larson, Appl. Surf. Sci., 1, 186 (1978).

95. P. T. Dawson and P. C. Walker in 'Experimental Methods in Catalytic Research' (Ed. R. B. Anderson and P. T. Dawson), Academic Press, 1976, vol.III, p.211.

96. T. E. Madey and J. T. Yates, Surf. Sci., 63, 203 (1977).

97. G. Ehrlich, J. Appl. Phys., 32 (1), 4 (1961).

98. P. A. Redhead, Vacuum, 12,203 (1962).

99. J. L. Falconer and R. J. Madix, Surf. Sci., 48, 393 (1975).

100. J. L. Falconer and R. J. Madix, J. Catal., 48, 262 (1977).

101. A. Cassuto and D. A. King, Surf. Sci., 102, 388 (1981).

102. D. Edwards Jnr., Surf. Sci, 49, 393 (1975).

103. R. P. Webb, S. E. Donnelly and D. G. Armour, Vacuum, 27, 559 (1977).

104. D. Edwards Jnr. Vacuum, 26, 91 (1976).

105. D. Edwards Jnr. J. Vac. Sci. Tech., 11(6), 1141 (1974).

106. C. R. Brundle, M. W. Roberts, D. Latham and K. Yates, J. Electr. Spectr., 3, 241 (1974).

107. A. Barrie in 'Handbook of X-Ray and U.V. Photo-electron Spectroscopy', (Ed. D. Briggs), Heyden, 1977, p.79.

108. J. McCarty, J. L. Falconer and R. J. Madix, J. Catal., 30,235 (1973).

109. D. A. King, Surf. Sci., 64,43 (1977).

110. See for example :(31),(32),(35),(44),(71), and(75).

111. J. Pritchard, Surf. Sci., 79,231 (1979).

112. P. R. Webber and D. Chadwick, Surf. Sci., 94, L151 (1980).

113. J. H. Scofield, J. Electr. Spectr. , 8, 129 (1976).

114. S. Evans, R. G. Pritchard and J. M. Thomas, J. Electr. Spectr., 14, 341 (1978).

115. M. A. Karolewski, PhD Thesis, Imperial College, 1983.

116. W. B. Pearson in 'A Handbook of Lattice Spacings and Structures of Metals and Alloys', Pergamon Press, 1958, p.619.

117. N. F. Mott in 'Metallic Solid Solutions', (Ed. J. Friedel and A. Guinier), W. A. Benjamin Inc., New York, 1963, p.1.

118. M. Szymonski, Appl. Phys., 23, 89 (1980).

119. R. J. Madix, Catal. Rev. Sci. Eng., 15 (2), 293 (1977).

120. P. Feulner and D. Menzel, J. Vac. Sci. Tech., 17(2), 662 (1980).

121. D. Briggs, Faraday Disc. Chem. Soc., 60, 81 (1975).

122. M. J. Braithwaite, R. W. Joyner and M. W. Roberts, Faraday Disc. Chem. Soc., 60, 89 (1979).

123. Lange's Handbook of Chemistry, 12th Edition (Ed. John A. Dean), McGraw Hill, p.9-63.

124. J. G. Stark and H. G. Wallace in 'Chemistry Data Book', 2nd Edition, John Murray, 1982 p.34.

125. S. Srinivasa Rao and T. R. Anantharaman, Current Science, 32, 262 (1963).

126. ICI - unpublished work.

127. J. J. F. Scholten in 'Preparation of Catalysts', (Ed. B. Delmon, P. Grange, P. Jacobs and G. Poncelet), Elsevier, 1979, vol. III, p.685.

128. T. Van Herwijnen and W. A. De Jong, J. Catal., 63,83 (1980).

129. T. Van Herwijnen, R. T. Guczalski and W. A. De Jong, J. Catal., 63, 94 (1980).

130. K. Klier - unpublished work; see also K. Klier, Adv. Catal. 31, 243 (1982).

131. A. Ya. Rozovskii, Yu. B. Kagan, G. I. Lin, E. V. Slivinskii, S. M. Loktev, L. G. Liberov and A. N. Bashkirov, Kinet. Katal. 16(3), 810 (1975).

132. Yu. B. Kagan, A. Ya. Rozovskii, L. G. Liberov, E. V. Slivinskii, G. I. Lin, S. M. Loktev and A. N. Bashkirov, Doklady Akademii Nauk SSSR, 224 (5), 1081 (1975).

133. Yu. B. Kagan, G. I. Lin, A. Ya. Rozovskii, S. M. Loktev, E. V. Slivinskii, A. N. Bashkirov, I. P. Naumov, I. K. Khludenev, S. A. Kudinov and Yu. I. Golovkin, Kinet. Katal., 17(2), 440 (1976).

134. R. Gorte and L. D. Schmidt, Surf. Sci., 76, 559 (1978).

135. V. Higgs - unpublished work.

APPENDICES

APPENDIX I

1. Derivation of the expression for surface zinc content from the linear concentration profile model.

The basic equation relating the measured peak area ratio to the composition of each layer and the IMFPs is :

$$R = \sigma \frac{\sum_{o}^{\infty} \theta_i^{Zn} \left[\alpha(E_{Zn})\right]^i}{\sum_{o}^{\infty} \theta_i^{Cu} \left[\alpha(E_{Cu})\right]^i} \qquad \text{(A.1.)}$$

The linear model can be represented mathematically as :

$$\theta_i^{Zn} = \theta_B^{Zn} + \theta_e^{Zn} \left(\frac{n-i}{n} \right) \qquad \text{for } 0 \leqslant i \leqslant n$$

$$\theta_i^{Zn} = \theta_B^{Zn} \qquad \text{for } i > n$$

Substituting these two relations into equation (A.1.) gives :

$$R = \frac{\sigma \sum_{o}^{\infty} \theta_B^{Zn} \left[\alpha(E_{Zn})\right]^i + \sigma \sum_{o}^{n} \theta_B^{Zn} \left(\frac{n-i}{n} \right) \left[\alpha(E_{Zn})\right]^i}{\sum_{o}^{\infty} (1-\theta_B^{Zn}) \left[\alpha(E_{Cu})\right]^i - \sum_{o}^{n} (1-\theta_B^{Zn}) \left(\frac{n-i}{n} \right) \left[\alpha(E_{Cu})\right]^i} \qquad \text{(A.2.)}$$

By putting : $B = R/\sigma$

$$\alpha cs = \sum_{o}^{\infty} \left[\alpha(E_{Cu})\right]^i \quad , \quad \alpha zs = \sum_{o}^{\infty} \left[\alpha(E_{Zn})\right]^i$$

and rearranging equation (A.2.) for the excess surface zinc content, θ_e^{Zn}, the following expression results :

$$\theta_e^{Zn} = \frac{B(1-\theta_B^{Zn}).\alpha cs - \theta_B^{Zn}.\ \alpha zs}{B\sum_o^n(\frac{n-1}{n})[\alpha(E_{Cu})]^i + \sum_o^n(\frac{n-1}{n})[\alpha(E_{Zn})]^i}$$

The total surface zinc mole fraction θ_o^{Zn} is given by

$\theta_B^{Zn} + \theta_e^{Zn}$, so the final expression becomes :

$$\theta_o^{Zn} = \frac{B(1-\theta_B^{Zn})\alpha cs - \theta_B^{Zn}.\ \alpha zs}{B.cf + zf} + \theta_B^{Zn} \qquad (A.4.)$$

where $cf = \sum_o^n(\frac{n-1}{n})[\alpha(E_{Cu})]^i$

$zf = \sum_o^n(\frac{n-1}{n})[\alpha(E_{Zn})]^i$

APPENDIX II

Tables of surface compositions calculated from the application of different depth profile models to the segregation results

Tables showing the mole fraction of zinc in the surface layer are presented. Three values are given against each anneal temperature for a particular profile and these have been derived from the three experimentally measured peak area ratios. Tables have been presented for different values of n and m. These two parameters were defined in Chapter 5, section 5.4.

TABLE 1

Calculated surface compositions from the linear profile model

(i) 2% Bulk Zn

a) n = 2

TABLE 1.1

Peak Pair	(100) Face			(111) Face		
	2p(MgKα)	2p(AlKα)	3p(MgKα)	2p(MgKα)	2p(AlKα)	3p(MgKα)
Anneal temp.						
150°C	0.06	0.05	-0.01	0.07	0.06	-0.01
175°C	0.12	0.10	0.03	0.12	0.11	0.03
200°C	0.21	0.17	0.04	0.22	0.18	0.04
225°C	0.24	0.18	0.05	0.25	0.19	0.05
250°C	0.21	0.18	0.05	0.22	0.19	0.05
275°C	0.18	0.16	0.03	0.18	0.17	0.03
300°C	0.11	0.09	-0.01	0.11	0.09	-0.01
325°C	-	-	-	-	-	-

b) n = 10

TABLE 1.2

Peak Pair	(100) Face			(111) Face		
	2p(MgKα)	2p(AlKα)	3p(MgKα)	2p(MgKα)	2p(AlKα)	3p(MgKα)
Anneal temp.						
150°C	0.05	0.04	0.01	0.05	0.04	0.01
175°C	0.09	0.07	0.03	0.09	0.07	0.03
200°C	0.16	0.11	0.03	0.16	0.12	0.03
225°C	0.18	0.12	0.04	0.18	0.12	0.04
250°C	0.16	0.12	0.04	0.15	0.12	0.04
275°C	0.13	0.11	0.03	0.13	0.11	0.03
300°C	0.08	0.06	0.01	0.08	0.06	0.01
325°C	-	-	-	-	-	-

(ii) 5% Bulk Zn

a) n = 2

TABLE 1.3

	(100) Face			(111) Face		
Peak Pair	2p(MgKα)	2p(AlKα)	3p(MgKα)	2p(MgKα)	2p(AlKα)	3p(MgKα)
Anneal Temp.						
150°C	0.30	0.24	0.09	0.30	0.26	0.09
175°C	0.34	0.30	0.14	0.35	0.33	0.14
200°C	0.35	0.32	0.18	0.36	0.35	0.18
225°C	0.37	0.33	0.18	0.38	0.35	0.19
250°C	0.36	0.33	0.18	0.37	0.35	0.18
275°C	0.32	0.29	0.12	0.33	0.31	0.12
300°C	0.30	0.26	0.10	0.31	0.28	0.10
325°C	0.25	0.19	0.04	0.26	0.21	0.04

b) n = 10

TABLE 1.4

	(100) Face			(111) Face		
Peak Pair	2p(MgKα)	2p(AlKα)	3p(MgKα)	2p(MgKα)	2p(AlKα)	3p(MgKα)
Anneal Temp.						
150°C	0.23	0.17	0.07	0.22	0.18	0.07
175°C	0.26	0.21	0.10	0.26	0.21	0.10
200°C	0.26	0.22	0.11	0.26	0.23	0.12
225°C	0.28	0.22	0.12	0.28	0.23	0.12
250°C	0.27	0.22	0.11	0.27	0.23	0.11
275°C	0.24	0.20	0.08	0.24	0.20	0.08
300°C	0.23	0.18	0.08	0.23	0.19	0.08
325°C	0.19	0.14	0.05	0.19	0.14	0.11

(iii) 10% Bulk Zn

a) n = 2

TABLE 1.5

	(100) Face			(111) Face		
Peak Pair	2p(MgKα)	2p(AlKα)	3p(MgKα)	2p(MgKα)	2p(AlKα)	3p(MgKα)
Anneal Temp.						
150°C	0.27	0.25	0.08	0.27	0.27	0.08
175°C	0.32	0.28	0.11	0.32	0.30	0.11
200°C	0.38	0.32	0.13	0.38	0.34	0.13
225°C	0.36	0.30	0.14	0.37	0.32	0.16
250°C	0.35	0.30	0.14	0.36	0.32	0.14
275°C	0.31	0.24	0.11	0.32	0.26	0.11
300°C	0.29	0.23	0.03	0.29	0.25	0.03
325°C	-	-	-	-	-	-

b) n = 10

TABLE 1.6

	(100) Face			(111) Face		
Peak Pair	2p(MgKα)	2p(AlKα)	3p(MgKα)	2p(MgKα)	2p(AlKα)	3p(MgKα)
Anneal Temp.						
150°C	0.22	0.20	0.09	0.22	0.20	0.09
175°C	0.26	0.21	0.11	0.25	0.22	0.11
200°C	0.29	0.23	0.11	0.29	0.24	0.11
225°C	0.28	0.22	0.12	0.29	0.23	0.13
250°C	0.28	0.23	0.12	0.28	0.23	0.12
275°C	0.25	0.19	0.10	0.25	0.20	0.10
300°C	0.23	0.18	0.07	0.23	0.19	0.07
325°C	-	-	-	-	-	-

(iv) 30% Bulk Zn

a) n = 2

TABLE 1.7

	(100) Face			(111) Face		
Peak Pair	2p(MgKα)	2p(AlKα)	3p(MgKα)	2p(MgKα)	2p(AlKα)	3p(MgKα)
Anneal Temp.						
150°C	0.28	0.26	0.14	0.28	0.27	0.13
175°C	0.35	0.31	0.17	0.34	0.33	0.16
200°C	0.39	0.37	0.24	0.39	0.38	0.24
225°C	0.39	0.25	0.27	0.39	0.37	0.26
250°C	0.37	0.31	0.17	0.37	0.32	0.19
275°C	0.33	0.27	0.10	0.32	0.28	0.09
300°C	0.28	0.19	0.05	0.27	0.20	0.04
325°C	0.20	0.18	-0.01	0.19	0.19	-0.02

b) n = 10

TABLE 1.8

	(100) Face			(111) Face		
Peak Pair	2p(MgKα)	2p(AlKα)	3p(MgKα)	2p(MgKα)	2p(AlKα)	3p(MgKα)
Anneal Temp.						
150°C	0.29	0.28	0.22	0.28	0.28	0.22
175°C	0.33	0.31	0.23	0.33	0.32	0.23
200°C	0.37	0.34	0.27	0.36	0.35	0.27
225°C	0.36	0.33	0.28	0.36	0.34	0.28
250°C	0.35	0.31	0.23	0.34	0.31	0.23
275°C	0.32	0.28	0.20	0.32	0.29	0.20
300°C	0.28	0.23	0.18	0.28	0.24	0.17
325°C	0.23	0.23	0.14	0.22	0.23	0.14

TABLE 2

Calculated Surface Compositions for the Exponential profile model

(i) 2% Bulk Zn

a) n = 2

TABLE 2.1

	(100) Face			(111) Face		
Peak Pair	2p(MgKα)	2p(AlKα)	3p(MgKα)	2p(MgKα)	2p(AlKα)	3p(MgKα)
Anneal Temp.						
150°C	0.07	0.06	-0.02	0.07	0.06	-0.02
175°C	0.13	0.12	0.03	0.14	0.13	0.03
200°C	0.25	0.21	0.04	0.26	0.22	0.04
225°C	0.28	0.22	0.06	0.29	0.23	0.06
250°C	0.24	0.22	0.06	0.25	0.23	0.06
275°C	0.21	0.19	0.04	0.21	0.20	0.04
300°C	0.12	0.10	-0.01	0.13	0.11	-0.01
325°C	-	-	-	-	-	-

b) n = 10

TABLE 2.2

	(100) Face			(111) Face		
Peak Pair	2p(MgKα)	2p(AlKα)	3p(MgKα)	2p(MgKα)	2p(AlKα)	3p(MgKα)
Anneal Temp.						
150°C	0.06	0.05	-0.00	0.06	0.05	0.00
175°C	0.10	0.09	0.03	0.10	0.09	0.03
200°C	0.19	0.14	0.03	0.19	0.15	0.03
225°C	0.21	0.15	0.04	0.22	0.16	0.04
250°C	0.18	0.15	0.04	0.19	0.16	0.04
275°C	0.16	0.13	0.03	0.16	0.14	0.03
300°C	0.10	0.07	0.00	0.10	0.08	0.00
325°C	-	-	-	-	-	-

(ii) 5% Bulk Zn

a) n = 2

TABLE 2.3

Peak Pair	(100) Face			(111) Face		
	2p(MgKα)	2p(AlKα)	3p(MgKα)	2p(MgKα)	2p(AlKα)	3p(MgKα)
Anneal Temp.						
150°C	0.34	0.29	0.10	0.35	0.31	0.11
175°C	0.39	0.36	0.16	0.41	0.39	0.17
200°C	0.41	0.39	0.21	0.42	0.41	0.22
225°C	0.43	0.39	0.22	0.45	0.42	0.22
250°C	0.41	0.39	0.21	0.43	0.42	0.22
275°C	0.37	0.34	0.14	0.38	0.37	0.14
300°C	0.35	0.31	0.11	0.36	0.33	0.12
325°C	0.29	0.23	0.04	0.30	0.24	0.04

b) n = 10

TABLE 2.4

Peak Pair	(100) Face			(111) Face		
	2p(MgKα)	2p(AlKα)	3p(MgKα)	2p(MgKα)	2p(AlKα)	3p(MgKα)
Anneal Temp.						
150°C	0.26	0.21	0.08	0.27	0.22	0.08
175°C	0.30	0.26	0.12	0.31	0.27	0.12
200°C	0.31	0.27	0.14	0.31	0.29	0.15
225°C	0.33	0.28	0.15	0.33	0.29	0.15
250°C	0.31	0.28	0.14	0.32	0.29	0.15
275°C	0.28	0.24	0.10	0.29	0.26	0.10
300°C	0,27	0.22	0.09	0.27	0.23	0.09
325°C	0.23	0.17	0.04	0.23	0.18	0.04

(iii) 10% Bulk Zn

a) n = 2

TABLE 2.5

Peak Pair	(100) Face			(111) Face		
	2p(MgKα)	2p(AlKα)	3p(MgKα)	2p(MgKα)	2p(AlKα)	3p(MgKα)
Anneal Temp.						
150°C	0.30	0.29	0.08	0.31	0.31	0.08
175°C	0.36	0.32	0.11	0.37	0.34	0.11
200°C	0.43	0.36	0.13	0.44	0.39	0.13
225°C	0.41	0.34	0.14	0.42	0.37	0.17
250°C	0.40	0.35	0.14	0.41	0.37	0.15
275°C	0.35	0.28	0.11	0.36	0.30	0.11
300°C	0.32	0.26	0.02	0.33	0.28	0.01
325°C	-	-	-	-	-	-

b) n = 10

TABLE 2.6

Peak Pair	(100) Face			(111) Face		
	2p(MgKα)	2p(AlKα)	3p(MgKα)	2p(MgKα)	2p(AlKα)	3p(MgKα)
Anneal Temp.						
150°C	0.25	0.22	0.09	0.25	0.24	0.09
175°C	0.29	0.24	0.11	0.29	0.26	0.11
200°C	0.34	0.28	0.12	0.34	0.29	0.12
225°C	0.33	0.26	0.13	0.33	0.28	0.14
250°C	0.32	0.27	0.13	0.32	0.28	0.13
275°C	0.28	0.22	0.11	0.28	0.23	0.10
300°C	0.26	0.21	0.05	0.26	0.22	0.05
325°C	-	-	-	-	-	-

(iv) 30% Bulk Zn

a) n = 2

TABLE 2.7

Peak Pair	(100) Face			(111) Face		
	2p(MgKα)	2p(AlKα)	3p(MgKα)	2p(MgKα)	2p(AlKα)	3p(MgKα)
Anneal Temp.						
150°C	0.28	0.25	0.10	0.27	0.27	0.09
175°C	0.35	0.32	0.13	0.35	0.33	0.12
200°C	0.41	0.38	0.22	0.41	0.40	0.22
225°C	0.41	0.36	0.26	0.41	0.38	0.25
250°C	0.38	0.31	0.13	0.38	0.33	0.13
275°C	0.33	0.26	0.05	0.33	0.27	0.04
300°C	0.27	0.17	-0.01	0.26	0.17	-0.02
325°C	0.18	0.16	-0.10	0.17	0.16	-0.11

b) n = 10

TABLE 2.8

Peak Pair	(100) Face			(111) Face		
	2p(MgKα)	2p(AlKα)	3p(MgKα)	2p(MgKα)	2p(AlKα)	3p(MgKα)
Anneal Temp.						
150°C	0.28	0.27	0.18	0.28	0.28	0.18
175°C	0.34	0.31	0.20	0.33	0.32	0.20
200°C	0.38	0.35	0.26	0.38	0.37	0.25
225°C	0.38	0.34	0.27	0.38	0.35	0.27
250°C	0.36	0.31	0.20	0.36	0.32	0.20
275°C	0.32	0.27	0.15	0.32	0.28	0.15
300°C	0.28	0.21	0.12	0.27	0.22	0.11
325°C	0.21	0.20	0.07	0.21	0.21	0.06

TABLE 3

Calculated Surface Compositions for the Linear/Depletion Model

(i) 2% Bulk Zn

a) m = 1, n = 10

TABLE 3.1

Anneal Temp.	(100) Face			(111) Face		
	2p(MgKα)	2p(AlKα)	3p(MgKα)	2p(MgKα)	2p(AlKα)	3p(MgKα)
150°C	0.09	0.09	0.02	0.09	0.09	0.02
175°C	0.15	0.15	0.07	0.16	0.16	0.07
200°C	0.28	0.24	0.09	0.29	0.26	0.08
225°C	0.31	0.25	0.10	0.33	0.27	0.11
250°C	0.27	0.25	0.10	0.28	0.27	0.11
275°C	0.23	0.22	0.08	0.24	0.24	0.08
300°C	0.14	0.13	0.02	0.15	0.14	0.02
325°C	-	-	-	-	-	-

b) m = 2, n = 10

TABLE 3.2

Anneal Temp.	(100) Face			(111) Face		
	2p(MgKα)	2p(AlKα)	3p(MgKα)	2p(MgKα)	2p(AlKα)	3p(MgKα)
150°C	0.07	0.07	0.02	0.08	0.07	0.02
175°C	0.13	0.12	0.06	0.13	0.12	0.06
200°C	0.22	0.19	0.06	0.23	0.20	0.06
225°C	0.25	0.20	0.08	0.26	0.21	0.08
250°C	0.22	0.20	0.08	0.23	0.21	0.08
275°C	0.19	0.17	0.06	0.19	0.19	0.06
300°C	0.12	0.10	0.02	0.12	0.11	0.02
325°C	-	-	-	-	-	-

c) m = 10, n = 16

TABLE 3.3

Anneal Temp.	(100) Face			(111) Face		
	2p(MgKα)	2p(AlKα)	3p(MgKα)	2p(MgKα)	2p(AlKα)	3p(MgKα)
150°C	0.05	0.04	0.01	0.05	0.05	0.01
175°C	0.09	0.07	0.03	0.09	0.08	0.03
200°C	0.16	0.12	0.04	0.16	0.12	0.04
225°C	0.18	0.12	0.04	0.18	0.13	0.04
250°C	0.16	0.12	0.04	0.16	0.13	0.04
275°C	0.13	0.11	0.03	0.13	0.11	0.03
300°C	0.08	0.06	0.01	0.08	0.07	0.01
325°C	-	-	-	-	-	-

(ii) 5% Bulk Zn

a) m = 1, n = 10

TABLE 3.4

Anneal Temp.	(100) Face			(111) Face		
	2p(MgKα)	2p(AlKα)	3p(MgKα)	2p(MgKα)	2p(AlKα)	3p(MgKα)
150°C	0.40	0.36	0.20	0.41	0.39	0.18
175°C	0.45	0.44	0.27	0.47	0.48	0.23
200°C	0.47	0.47	0.32	0.49	0.50	0.28
225°C	0.49	0.48	0.32	0.51	0.51	0.28
250°C	0.47	0.47	0.32	0.49	0.51	0.28
275°C	0.43	0.42	0.24	0.45	0.45	0.21
300°C	0.40	0.38	0.21	0.42	0.41	0.19
325°C	0.34	0.30	0.13	0.36	0.32	0.12

b) m = 2, n = 10

TABLE 3.5

Anneal Temp.	(100) Face			(111) Face		
	2p(MgKα)	2p(AlKα)	3p(MgKα)	2p(MgKα)	2p(AlKα)	3p(MgKα)
150°C	0.32	0.28	0.15	0.33	0.30	0.14
175°C	0.37	0.34	0.20	0.38	0.37	0.18
200°C	0.38	0.36	0.24	0.39	0.39	0.21
225°C	0.40	0.37	0.24	0.41	0.40	0.22
250°C	0.38	0.37	0.24	0.39	0.39	0.21
275°C	0.35	0.33	0.18	0.36	0.35	0.16
300°C	0.33	0.30	0.16	0.34	0.32	0.15
325°C	0.28	0.23	0.10	0.29	0.25	0.09

c) m = 10, n = 16

TABLE 3.6

Anneal Temp.	(100) Face			(111) Face		
	2p(MgKα)	2p(AlKα)	3p(MgKα)	2p(MgKα)	2p(AlKα)	3p(MgKα)
150°C	0.23	0.18	0.09	0.23	0.18	0.08
175°C	0.26	0.22	0.11	0.26	0.22	0.11
200°C	0.27	0.23	0.13	0.27	0.24	0.12
225°C	0.28	0.23	0.13	0.28	0.24	0.13
250°C	0.27	0.23	0.13	0.27	0.24	0.12
275°C	0.25	0.21	0.10	0.25	0.21	0.09
300°C	0.23	0.19	0.09	0.23	0.20	0.09
325°C	0.20	0.15	0.06	0.20	0.15	0.06

(iii) 10% Bulk Zn

a) m = 1, n = 10

TABLE 3.7

Anneal Temp.	(100) Face			(111) Face		
	2p(MgKα)	2p(AlKα)	3p(MgKα)	2p(MgKα)	2p(AlKα)	3p(MgKα)
150°C	0.39	0.42	0.27	0.41	0.45	0.27
175°C	0.46	0.45	0.30	0.47	0.49	0.31
200°C	0.53	0.50	0.32	0.55	0.54	0.33
225°C	0.51	0.48	0.32	0.53	0.52	0.37
250°C	0.50	0.49	0.30	0.52	0.52	0.34
275°C	0.45	0.41	0.30	0.46	0.44	0.30
300°C	0.41	0.40	0.20	0.43	0.43	0.20
325°C	-	-	-	-	-	-

b) m = 2, n = 10

TABLE 3.8

Anneal Temp.	(100) Face			(111) Face		
	2p(MgKα)	2p(AlKα)	3p(MgKα)	2p(MgKα)	2p(AlKα)	3p(MgKα)
150°C	0.32	0.33	0.21	0.33	0.35	0.21
175°C	0.37	0.36	0.23	0.38	0.38	0.24
200°C	0.43	0.39	0.25	0.44	0.42	0.25
225°C	0.42	0.38	0.26	0.43	0.40	0.28
250°C	0.40	0.38	0.26	0.42	0.41	0.26
275°C	0.37	0.32	0.23	0.37	0.34	0.23
300°C	0.34	0.31	0.15	0.35	0.33	0.16
325°C	-	-	-	-	-	-

c) m = 10, n = 16

TABLE 3.9

Anneal Temp.	(100) Face			(111) Face		
	2p(MgKα)	2p(AlKα)	3p(MgKα)	2p(MgKα)	2p(AlKα)	3p(MgKα)
150°C	0.23	0.21	0.12	0.23	0.22	0.12
175°C	0.27	0.23	0.14	0.27	0.24	0.14
200°C	0.30	0.25	0.14	0.30	0.26	0.15
225°C	0.30	0.24	0.15	0.30	0.25	0.16
250°C	0.29	0.24	0.15	0.29	0.25	0.15
275°C	0.26	0.21	0.13	0.26	0.21	0.14
300°C	0.24	0.20	0.10	0.24	0.21	0.10
325°C	-	-	-	-	-	-

(iv) 30% Bulk Zn

a) m = 1, n = 10

TABLE 3.10

Anneal Temp.	(100) Face			(111) Face		
	2p(MgKα)	2p(AlKα)	3p(MgKα)	2p(MgKα)	2p(AlKα)	3p(MgKα)
150°C	0.53	0.62	0.64	0.55	0.66	0.65
175°C	0.61	0.69	0.68	0.63	0.74	0.69
200°C	0.68	0.76	0.78	0.70	0.81	0.80
225°C	0.67	0.74	0.82	0.70	0.79	0.83
250°C	0.64	0.68	0.68	0.67	0.73	0.70
275°C	0.59	0.63	0.59	0.61	0.67	0.60
300°C	0.53	0.53	0.53	0.54	0.56	0.53
325°C	0.43	0.52	0.44	0.44	0.55	0.44

b) m = 2, n = 10

TABLE 3.11

Anneal Temp.	(100) Face			(111) Face		
	2p(MgKα)	2p(AlKα)	3p(MgKα)	2p(MgKα)	2p(AlKα)	3p(MgKα)
150°C	0.44	0.50	0.51	0.45	0.53	0.51
175°C	0.50	0.55	0.53	0.52	0.58	0.54
200°C	0.55	0.60	0.61	0.57	0.64	0.62
225°C	0.55	0.59	0.63	0.57	0.62	0.64
250°C	0.53	0.54	0.54	0.54	0.58	0.54
275°C	0.49	0.50	0.47	0.50	0.53	0.47
300°C	0.43	0.43	0.42	0.44	0.45	0.42
325°C	0.35	0.41	0.35	0.36	0.44	0.35

c) m = 10, n = 16

TABLE 3.12

Anneal Temp.	(100) Face			(111) Face		
	2p(MgKα)	2p(AlKα)	3p(MgKα)	2p(MgKα)	2p(AlKα)	3p(MgKα)
150°C	0.32	0.33	0.31	0.32	0.34	0.32
175°C	0.36	0.36	0.33	0.36	0.37	0.33
200°C	0.40	0.39	0.36	0.40	0.41	0.37
225°C	0.40	0.38	0.38	0.40	0.40	0.38
250°C	0.38	0.36	0.33	0.38	0.37	0.33
275°C	0.35	0.33	0.29	0.35	0.34	0.30
300°C	0.32	0.28	0.27	0.32	0.30	0.27
325°C	0.26	0.28	0.23	0.26	0.29	0.24

TABLE 4

Calculated Surface Compositions for the Exponential/Depletion Model

(i) 2% Bulk Zn

a) m = 2, n = 10

TABLE 4.1

Anneal Temp.	(100) Face			(111) Face		
	2p(MgKα)	2p(AlKα)	3p(MgKα)	2p(MgKα)	2p(AlKα)	3p(MgKα)
150°C	0.09	0.08	0.02	0.09	0.09	0.02
175°C	0.15	0.14	0.07	0.15	0.15	0.07
200°C	0.26	0.23	0.08	0.27	0.25	0.08
225°C	0.30	0.24	0.10	0.31	0.26	0.10
250°C	0.26	0.24	0.10	0.27	0.26	0.10
275°C	0.22	0.21	0.07	0.23	0.23	0.08
300°C	0.14	0.12	0.03	0.14	0.13	0.03
325°C	-	-	-	-	-	-

b) m = 10, n = 16

TABLE 4.2

Anneal Temp.	(100) Face			(111) Face		
	2p(MgKα)	2p(AlKα)	3p(MgKα)	2p(MgKα)	2p(AlKα)	3p(MgKα)
150°C	0.07	0.06	0.02	0.07	0.06	0.02
175°C	0.11	0.10	0.05	0.11	0.10	0.05
200°C	0.19	0.15	0.05	0.20	0.16	0.05
225°C	0.22	0.16	0.06	0.22	0.17	0.06
250°C	0.19	0.16	0.06	0.19	0.17	0.06
275°C	0.16	0.14	0.05	0.17	0.15	0.05
300°C	0.10	0.08	0.02	0.10	0.09	0.02
325°C	-	-	-	-	-	-

(ii) 5% Bulk Zn

a) m = 2, n = 10

TABLE 4.3

Anneal Temp.	(100) Face			(111) Face		
	2p(MgKα)	2p(AlKα)	3p(MgKα)	2p(MgKα)	2p(Alkα)	3p(MgKα)
150°C	0.38	0.34	0.19	0.40	0.37	0.17
175°C	0.43	0.42	0.25	0.45	0.45	0.22
200°C	0.45	0.44	0.30	0.47	0.48	0.26
225°C	0.47	0.45	0.31	0.49	0.49	0.27
250°C	0.45	0.45	0.30	0.47	0.48	0.26
275°C	0.41	0.40	0.23	0.43	0.43	0.20
300°C	0.39	0.37	0.20	0.40	0.39	0.18
325°C	0.33	0.28	0.13	0.34	0.31	0.12

b) m = 10, n = 16

TABLE 4.4

Anneal Temp.	(100) Face			(111) Face		
	2p(MgKα)	2p(AlKα)	3p(MgKα)	2p(MgKα)	2p(AlKα)	3p(MgKα)
150°C	0.28	0.23	0.13	0.29	0.25	0.12
175°C	0.32	0.28	0.16	0.32	0.30	0.15
200°C	0.33	0.30	0.19	0.33	0.32	0.17
225°C	0.35	0.31	0.19	0.35	0.32	0.17
250°C	0.33	0.30	0.19	0.34	0.32	0.17
275°C	0.30	0.27	0.15	0.31	0.29	0.13
300°C	0.28	0.25	0.13	0.29	0.26	0.12
325°C	0.24	0.19	0.09	0.25	0.21	0.08

(iii) 10% Bulk Zn

a) m = 2, n = 10

TABLE 4.5

Anneal Temp.	(100) Face			(111) Face		
	2p(MgKα)	2p(AlKα)	3p(MgKα)	2p(MgKα)	2p(AlKα)	3p(MgKα)
150°C	0.38	0.40	0.26	0.39	0.43	0.27
175°C	0.44	0.43	0.29	0.45	0.47	0.30
200°C	0.51	0.48	0.31	0.52	0.52	0.32
225°C	0.49	0.46	0.33	0.51	0.50	0.36
250°C	0.48	0.47	0.33	0.49	0.50	0.33
275°C	0.43	0.40	0.29	0.45	0.42	0.29
300°C	0.40	0.38	0.20	0.41	0.41	0.20
325°C	-	-	-	-	-	-

b) m = 10, n = 16

TABLE 4.6

Anneal Temp.	(100) Face			(111) Face		
	2p(MgKα)	2p(AlKα)	3p(MgKα)	2p(MgKα)	2p(AlKα)	3p(MgKα)
150°C	0.28	0.28	0.18	0.29	0.29	0.18
175°C	0.32	0.30	0.20	0.33	0.31	0.20
200°C	0.37	0.33	0.21	0.38	0.35	0.22
225°C	0.36	0.32	0.22	0.37	0.33	0.24
250°C	0.35	0.32	0.22	0.36	0.34	0.22
275°C	0.32	0.27	0.20	0.32	0.29	0.20
300°C	0.30	0.26	0.14	0.30	0.28	0.14
325°C	-	-	-	-	-	-

(iv) 30% Bulk Zn

a) m = 2, n = 10

TABLE 4.7

Anneal Temp.	(100) Face			(111) Face		
	2p(MgKα)	2p(AlKα)	3p(MgKα)	2p(MgKα)	2p(AlKα)	3p(MgKα)
150°C	0.52	0.61	0.64	0.54	0.65	0.65
175°C	0.60	0.67	0.67	0.62	0.72	0.68
200°C	0.66	0.74	0.76	0.68	0.79	0.78
225°C	0.65	0.72	0.80	0.68	0.76	0.81
250°C	0.62	0.67	0.68	0.65	0.71	0.69
275°C	0.57	0.61	0.59	0.59	0.65	0.60
300°C	0.51	0.52	0.53	0.53	0.55	0.54
325°C	0.42	0.51	0.44	0.43	0.54	0.45

b) m = 10, n = 16

TABLE 4.8

Anneal Temp.	(100) Face			(111) Face		
	2p(MgKα)	2p(AlKα)	3p(MgKα)	2p(MgKα)	2p(AlKα)	3p(MgKα)
150°C	0.39	0.43	0.46	0.40	0.46	0.47
175°C	0.45	0.47	0.48	0.45	0.50	0.49
200°C	0.49	0.52	0.53	0.50	0.55	0.54
225°C	0.49	0.50	0.55	0.50	0.53	0.56
250°C	0.47	0.47	0.48	0.47	0.50	0.49
275°C	0.43	0.43	0.43	0.44	0.46	0.44
300°C	0.39	0.37	0.39	0.39	0.40	0.40
325°C	0.32	0.37	0.34	0.32	0.39	0.35

TABLE 5

Calculated surface compositions for the 30% Bulk Zn alloy with 10% Zn in the maximum depletion layer

(i) Linear Depletion model with m = 1, n = 10

TABLE 5.1

	(100) Face			(111) Face		
Anneal Temp.	2p(MgKα)	2p(AlKα)	3p(MgKα)	2p(MgKα)	2p(AlKα)	3p(MgKα)
150°C	0.45	0.50	0.46	0.45	0.53	0.46
175°C	0.53	0.56	0.49	0.54	0.60	0.50
200°C	0.59	0.63	0.59	0.61	0.68	0.60
225°C	0.59	0.61	0.63	0.60	0.65	0.64
250°C	0.56	0.56	0.50	0.57	0.60	0.50
275°C	0.50	0.50	0.40	0.52	0.53	0.41
300°C	0.44	0.41	0.31	0.45	0.43	0.34
325°C	0.34	0.39	0.25	0.35	0.42	0.25

(ii) Linear Depletion model with m = 2, n = 10

TABLE 5.2

	(100) Face			(111) Face		
Anneal Temp.	2p(MgKα)	2p(AlKα)	3p(MgKα)	2p(MgKα)	2p(AlKα)	3p(MgKα)
150°C	0.39	0.42	0.38	0.39	0.44	0.39
175°C	0.45	0.47	0.41	0.46	0.50	0.41
200°C	0.50	0.52	0.48	0.51	0.55	0.49
225°C	0.50	0.51	0.51	0.51	0.54	0.52
250°C	0.47	0.47	0.41	0.48	0.49	0.42
275°C	0.43	0.47	0.34	0.44	0.45	0.35
300°C	0.38	0.35	0.30	0.39	0.37	0.30
325°C	0.30	0.34	0.23	0.31	0.36	0.23

(iii) Exponential/Depletion model with m = 2, n = 10

TABLE 5.3

	(100) Face			(111) Face		
Anneal Temp.	2p(MgKα)	2p(AlKα)	3p(MgKα)	2p(MgKα)	2p(AlKα)	3p(MgKα)
150°C	0.44	0.49	0.46	0.45	0.52	0.46
175°C	0.52	0.55	0.49	0.53	0.59	0.50
200°C	0.57	0.62	0.58	0.59	0.66	0.59
225°C	0.57	0.60	0.62	0.59	0.64	0.63
250°C	0.54	0.55	0.50	0.56	0.58	0.50
275°C	0.49	0.49	0.41	0.50	0.52	0.41
300°C	0.43	0.40	0.35	0.44	0.43	0.35
325°C	0.34	0.39	0.26	0.34	0.41	0.26

APPENDIX III

Preparation of the $Cu/ZnO/Al_2O_3$ Catalysts

The catalyst was prepared by reverse batch precipitation at 65°C. A solution of 1.5M Na_2CO_3 was steadily added to a 1M solution (both solutions at 65°C)of mixed nitrates until the pH reached 6.5. The resulting solution was aged at 65°C for 1 hour. The mixed nitrates contained Cu, Zn and Al in the appropriate molar ratios to give a 60/30/10/ $Cu/ZnO/Al_2O_3$ catalyst. The resulting slurry was filtered and washed until the sodium level was below 8ppm. This is equivalent to approximately 1% Na_2O. The filter cake was dried at 120°C for 16 hours, and calcined at 300°C for 6 hours. A sample was taken for analysis and the catalyst composition is shown in Table I.

The calcined cake was crushed and 2% by weight of graphite was added. The resulting powder was subjected to a pelleting process which gave pellets with a density of 2000 kg/m^3. These pellets were ground and sieved between 18 and 25 B.S.S. mesh sieves (0.853mm and 0.599mm respectively) to give the catalyst granules to be used in the experiments.

A similar procedure was followed to prepare a 50/40/10 $Cu/ZnO/Al_2O_3$ catalyst, and the composition of the calcined cake is shown in Table I.

TABLE 1

CATALYST COMPOSITIONS

	Nominal catalyst composition	
Analysis	60/30/10	50/40/10
% CuO	63.3	46.2
% ZnO	31.2	46.2
% Al_2O_3	5.2	7.4
ppm NiO	<70	<70
ppm Fe_2O_3	320	340
ppm Na_2O	590	650
ppm MgO	58	150
ppm K_2O	78	140
ppm CaO	240	720
% Sulphur	<0.01	<0.01
% Chlorine	0.01	0.02
% Loss at 900°C	15.1	13.9

TEM and XRD analysis of the 60/30/10 (nominal) filter cake

TEM appears to show that the precipitate contains many quite well formed needles ∿ 1500Å - 3500Å long and some laths up to ∿2000Å long. Some hexagonal shaped plates up to ∿5000Å across and occasional poorly crystalline material are also visible.

XRD shows that the major phase is malachite (120 peak breadth 0.7°, peak height x breadth 19.3 and the $\bar{2}01$ peak indicates that ∿ 25% Zn in solid solution). Some fairly crystalline hexagonal phase was also seen.